Cape Peninsula University of Technology

Development of new FSP method for enhancing the mechanical properties of FSW and TIG welded dissimilar aerospace aluminium alloy joints

by

SIPOKAZI MABUWA

Thesis submitted in fulfillment of the requirements for the degree

Doctor of Engineering: Mechanical Engineering

under Mechanical and Mechatronic Engineering Department

in the Faculty of Engineering and the Built Environment at the Cape Peninsula University of Technology

Supervisor: Dr V. Msomi

Co-Supervisor: Dr O. Nemraoui

Bellville
March 2022

DECLARATION

I, Sipokazi Mabuwa, declare that the contents of this dissertation/thesis represent my unaided work and that the dissertation/**thesis** has not previously been submitted for academic examination towards any qualification. Furthermore, it represents my own opinions and not necessarily those of the Cape Peninsula University of Technology.

15 March 2022

Signed **Date**

ABSTRACT

The main aim of this study was to develop a new friction stir processing method to enhance the mechanical properties of the FSW and TIG-welded AA6082-T651/AA8011-H14 dissimilar aluminium alloy joints. The processing conditions used included friction stir processing under normal (air at room temperature) and underwater (submerged) at room temperature. The dissimilar plates were first welded using the tungsten inert gas welding (TIG) and the friction stir welding (FSW) techniques, taking into consideration the material positioning. The first batch was welded with the AA6082-T651 alloy on the advancing side, while the AA8011-H14 was positioned on the retreating side. The second batch was welded with the AA8011-H14 on the advancing side and AA6082-T651 on the retreating side. A similar pattern was followed during the friction stir processing of the aforementioned welded joints. This was done to evaluate the impact of material positioning on the microstructure and mechanical properties of the said joints.

The welded and friction stir processed (FSP) plates were cut and prepared for different tests. The tests conducted include the x-ray diffraction analysis, chemical composition, macrostructure and microstructure analysis, tensile tests, fractographic analysis, flexural tests and hardness tests. The test results of the said joints produced distinctive FSP conditions were studied comparatively. The FSW and TIG-welded average mean grain sizes preceding FSP were 23.247 µm and 31.765 µm respectively. The post-FSP results revealed greatly refined nugget zone microstructural grain sizes under both FSP conditions applied. The submerged FSP TIG-welded (SFSP-TIG) average mean grain size was 4.24 µm, while the normal FSP TIG-welded (NFSP-TIG) average mean grain size was 10.373 µm. The TIG-welded joints had a maximum ultimate tensile strength (UTS) of 85.42 MPa with a maximum yield strength of 68.336 MPa and tensile strain of 23.889 %. The NFSP-TIG showed a maximum UTS of 89.777 MPa with a maximum yield strength of 71.822 MPa, while the SFSP-TIG had a maximum UTS of 90.25 MPa with a yield strength of 72.2 MPa. The maximum tensile strain rates of the same were 27.994 % and 28.829 % respectively. The tensile results correlated with the grain sizes obtained. The nugget zone maximum average Vickers hardness of the TIG-welded joints was found to be 58.5 HV while the NFSP-TIG one was 61.5 HV and the 69 HV of the SFSP-TIG. The fracture surface morphology correlated with the strain rate results with the TIG-welded joints showing a brittle nature of fracture and the FSP specimens under both conditions showing a ductile behaviour.

The normal friction stir processed FSW (NFSP-FSW) joints average nugget zone mean grain size was significantly refined to 12.475 µm and the submerged friction stir processed FSW (SFSP-FSW) joints to 5.611 µm. The FSW joints had a maximum UTS of 84.444 MPa with a yield strength of 67.555 MPa and a strain rate of 23.035%. The NFSP-FSW maximum UTS was 89.611 MPa with a yield strength of 71.289 and strain rate of 24.609 %, while for the SFSP-FSW joints was 92.511 MPa with a yield strength of 74.004 MPa and a strain rate of 25.975 %. The nugget zone maximum average Vickers hardness was found to be 48 HV for the FSW joints, 53 HV for the NFSP-FSW joints and 61 HV for the SFSP-FSW joints. The fracture surface morphology for the FSW and FSP joints all showed a ductile behaviour with the SFSP-FSW joints showing more ductility. With regards to specimen positioning the positioning of the harder alloy AA6082-T651 on the advancing side and the weaker strength alloy AA8011-H14 on the retreating side resulted in improved results than when the AA8011-H14 alloy was positioned on the advancing side.

ACKNOWLEDGEMENTS

To God be the glory, He is and will always be my source of strength. Indeed if God is for us who can be against us.

To the woman, I once was 'you are visible, your dreams do matter and there are no limitations.'

Special gratitude goes to my supervisors Dr Msomi and Dr Nemroui. To Dr Msomi who has been my academic mentor as well, I thank God we crossed paths, your encouragement, support and availability towards my postgraduate journey didn't go unnoticed. Thank you so much for having faith in me even when there were times I lost mine in me. May God continue to bless you and your family abundantly. May you also continue to be a blessing to other students who wish to walk this journey of research.

I would like to thank my colleagues, Mr Vuyani Moni the former CPUT senior laboratory technician for granting me unlimited access to the laboratories used for this study, Miss Shaheeda Petersen, for assistance in the preparation of etchants, Mr Zukile Cobothwana for the manufacturing of the FSW/P tool, Mr Mark Jenkins for assistance in TIG-welding of my plates, Rafique Williams and Fransisco Fredrics for landing a hand whenever necessary and the entire workshop staff for the moral support.

Special gratitude also goes to Mrs Miranda Waldron of the University of Cape Town, for assisting me with SEM during the entire duration, she never complained, this could not have been possible without your help. I would also like to thank Dr. Remy Bucher from the iThemba laboratories for the X-ray diffraction analysis tests for my samples.

To the women who I consider my blessings Ngeniswa Ngalo, Nondumiso Ngalo, Zintathu Ngalo, Zoleka Ngalo, Nompumezo Ngalo and Nosintu Ngalo thank you so much for the love and encouragement. Not forgetting my sister-in-law Nomfundiso Mabuwa you have been amazing, I will forever be grateful for your never-ending support. To my friends this couldn't have been possible without your never-ending emotional support, you were tolerant with me throughout the journey.

My heartfelt gratitude also goes to my kids for always fuelling me to focus, they knew sleep time for them meant study time for mommy, they even used to remind me on the days that they would see me going to bed instead of studying. To my husband Zanoxolo Mabuwa thank you so much for invoking me from my comfort zone and for allowing me to take this journey, I will forever be grateful. To Vuyokazi Mzingelwa, thank you so much for always being my very own cheerleader, in my darkest hours during this journey you were always there, you never complained no matter what time of the day I felt overwhelmed you were always there for me.

My sincere gratitude goes to the **Cape Peninsula University of Technology** for paying my tuition fees, the conference committee for funding the Material Science and Technology (MST) 2019 conference expenses. Last but not least thank you so much for financing all my journal article publication charges.

DEDICATION

To my kids Isipho Angela Mabuwa, Esihle Samuel Mabuwa and Qhawe Kamva Mabuwa, every time I looked at you I knew I had to do this for you, if not for myself.

LIST OF PAPERS

The thesis includes the following supplements

Supplement 1
Mabuwa, S.; Msomi, V. Comparative analysis between normal and submerged friction stir processed friction stir welded dissimilar aluminium alloy joints. *Journal of Materials Research and Technology*, 9(5), **2020**, pp. 9632-9644, https://doi.org/10.1016/j.jmrt.2020.06.024.

Supplement 2
Mabuwa, S.; Msomi, V. Review on friction stir processed TIG and friction stir welded dissimilar alloy joints. *Metals*, 10(1), **2019**, 142, https://doi.org/10.3390/met10010142.

Supplement 3
Mabuwa, S.; Msomi, V. The impact of submerged friction stir processing on the friction stir welded dissimilar joints. *Materials Research Express,* 7, **2020**, pp. 096513, https://doi.org/10.1088/2053-1591/abb6b6.

Supplement 4
Mabuwa, S.; Msomi, V. Fatigue behaviour of the multi-pass friction stir processed AA8011-H14 and AA6082-T651 dissimilar joints. *Engineering Failure Analysis*, 118, **2020**, pp. 104876, https://doi.org/10.1016/j.engfailanal.2020.104876.

Supplement 5
Mabuwa, S.; Msomi, V. The Influence of Multiple Pass Submerged Friction Stir Processing on the Microstructure and Mechanical Properties of the FSWed AA6082-AA8011 Joints. *Metals*, 10(11), **2020**, pp. 1429, https://doi.org/10.3390/met10111429.

Supplement 6
Msomi, V.; Mabuwa, S. Effect of material positioning on fatigue life of the friction stir processed dissimilar joints. *Materials Research Express*, 7, **2020**, 106520, https://doi.org/10.1088/2053-1591/abc18c.

Supplement 7
Mabuwa, S.; Msomi, V. The impact of material positioning towards the friction stir welded dissimilar aluminium alloy joints. *Recent Patents on Mechanical Engineering*, 14(2), **2020**, pp. 252-259, https://doi.org/10.2174/2212797613999201.

Supplement 8
Mabuwa, S.; Msomi, V.; Muribwathoho, O.; Motshwanedi, S.S. The microstructure and mechanical properties of the friction stir processed TIG-welded aerospace dissimilar aluminium alloys. *Materials Today: Proceedings*, 46(1), **2021**, pp. 658-664, https://doi.org/10.1016/j.matpr.2020.11.588.

Supplement 9
Msomi, V.; Mabuwa, S.; Muribwathoho, Motshwanedi, S.S. Effect of tool geometry on microstructure and mechanical properties of submerged friction stir processed AA6082/AA8011 joints. *Materials Today: Proceedings*, 46(1), **2021**, pp. 638-644, https://doi.org/10.1016/j.matpr.2020.11.580.

Supplement 10
Msomi, V.; Mabuwa, S.; Merdji, A.; Muribwathoho, O.; Motshwanedi, S.S.; Microstructural and mechanical properties of submerged multi-pass friction stir processed AA6082/AA8011 TIG-welded joint. *Materials Today: Proceedings*, 45(6), **2021**, pp. 5702-5705, https://doi.org/10.1016/j.matpr.2021.02.504.

Supplement 11

Mabuwa, S.; Msomi, V.; Analysis of mechanical properties between submerged and normal multiple-pass friction stir processing of the FSWed dissimilar aluminium joints. Materials Today: Proceedings, 45(6), **2021**, pp. 5400-5404, https://doi.org/10.1016/j.matpr.2021.02.101.

Supplement 12
Msomi, V.; Mabuwa, S.; Optimization of normal and submerged FSP parameters for dissimilar aluminium joints using Taguchi technique, Materials Science Forum, 1034, **2021**, pp. 207-218, http://dx.doi.org/10.4028/www.scientific.net/MSF.1034.207.

Supplement 13
Mabuwa, Sipokazi, and Msomi, Velaphi. The effect of FSP conditions towards microstructure and mechanical properties of the AA6082/AA8011 TIG-welded joint. *Materials Research Express*, 8(6), **2021**, 066514, https://doi.org/10.1088/2053-1591/ac0735.

Supplement 14
Verma, S.; Msomi, V.; Mabuwa, S.; Merdji,A.; Misra, J.P.; Batra, U.; Sharma, S. Machine learning application for evaluating the friction stir processing behavior of dissimilar aluminium alloys joint. Journal of Materials: Design and Applications, **2021**, pp. 1-14, https://doi.org/10.1177/14644207211053123.

TABLE OF CONTENTS

Contents

LIST OF FIGURES

LIST OF TABLES

GLOSSARY

Terms/Acronyms/Abbreviations	Definition/Explanation
CPUT	Cape Peninsula University of Technology
FSW	Friction Stir Welding
FSP	Friction Stir Processing
TIG	Tungsten Inert Gas
SFSP-TIG	Submerged Friction Stir Processed TIG-Welded
NFSP-TIG	Normal Friction Stir Processed TIG-Welded
SFSP-FSW	Submerged Fiction Stir Processed FSW
NFSP-FSW	Normal Friction Stir Processed FSW
UTS	Ultimate Tensile Strength
SFSP	Submerged Friction Stir Processing
IMC's	Intermetallic Compounds
HAZ	The Heat-Affected Zone
TWI	The Welding Institute
Al	Aluminium
TMAZ	Thermo-Mechanically Affected Zone
NZ	Nugget Zone
PMZ	Partially Melted Zone
BM	Base Material
WM	Weld Metal
WN	Weld Nugget
ASTM	American Society for Testing and Materials
TEM	Transmission Electron Microscopy
SEM	Scanning Electron Microscope
UFG	Ultrafine Grain
HV	Hardness Vickers scale
SZ	Stir Zone
MIG	Metal Inert Gas welding

EDS	Energy Dispersive X-Ray Spectroscopy
EBSD	Electron Backscatter Diffraction
HCl	Hydrochloric Acid
FZ	Fusion Zone
AS	Advancing Side
UFS	Ultimate Flexural Strength
MFS	Maximum Flexural Strain
RS	Retreating Side
AS	Advancing Side

NOTATIONS

English Symbol

C	Celsius

Greek Symbols

°	Degree
µm	Micrometer
β	Mg-Si Precipitates
θ	Theta

Units

g	Gram
kN	Kilo Newton
ml	Milliliter
mm	Millimeter
min	Minute
MPa	Mega Pascal
RPM	Revolutions Per Minute
s	Seconds
V	Volt
A	Amps
cm^3	Centimeter cubed

CHAPTER ONE

INTRODUCTION

1.1 Introduction

A Chinese military leader in the early 1700s discovered a curious metal ornament in the tomb of Chou-Chu, which was analysed to contain approximately 85% aluminium. The production of this metal was a mystery [1-2]. Following several attempts to reproduce this metal, the first person to succeed in reproduction was Hans Christian Oersted at Copenhagen, Denmark, in 1825. This successful reproduction of aluminium was achieved by heating aluminium chloride with potassium. However, the produced sample was impure. In 1827, a German chemist, Friedrich Wöhler, perfected the method and obtained pure aluminium for the first time by combining potassium with sodium. The name *aluminium* was derived from the Latin name for alum, *alumen,* meaning bitter salt [3].

Over the last thirty years, the global production of aluminium has nearly doubled from 15 million tons per year in 1980, to 30 million tons per year in 2005 [4]. The combination of beneficial properties like high strength-to-weight ratio and good ductility makes aluminium one of the most economical and desired metallic materials for a wide range of engineering applications [5]. For example, aluminium alloys are used extensively within the transportation industry. This is because aluminium has a low density of 2.7 g/cm^3 as well as an attractive balance of mechanical properties, which make the material ideal for efficiency improvements in automotive and aerospace components [6]. The benefit of using aluminium material in building structures is that aluminium is lighter in weight which reduces power consumption. Aluminium and its alloys also have good corrosion resistance, good workability, high thermal and electrical conductivity, an attractive appearance and intrinsic recyclability. In fact, the versatility of aluminium makes it the most widely used metal after steel [7].

Pure aluminium possesses very weak material properties. To improve such, other materials like copper, manganese, silicon, magnesium, magnesium plus silicon, zinc and lithium are primarily alloyed to produce an aluminium alloy with high mechanical properties [7,9]. The fusion of the mentioned metals results in the formation of two classes of aluminium: the wrought and cast groups. The wrought group consists of nine classes, presented in Table 1. However, the main focus of this study is on the 6xxx and 8xxx, specifically the AA6082-T651 and AA8011-H14 grades. The 6xxx series alloys have excellent fabricability. AA6082-T651 is an Al-Mg-Si alloy with sufficient plasticity for extrusions and containing very high relative strength [10-11]. The AA6082 alloy is applicable in light aircraft, especially homemade ones. The AA6082 is very light in weight, with relatively high strength, easily welded and manipulated making it ideal for fuselage and wings material. The AA6082 replaces the AA6061 and the AA6063 in many aerospace engineering applications [12].

Table 1: Wrought aluminium alloys [5,8].

Series	Elements	Characteristics	Application
1xxx	99% Al	Exceptional formability, corrosion-resistant and electrical conductivity	Packaging and foil, roofing, cladding, low strength corrosion resistant vessel and tanks
2xxx	Al-Cu-Mg (1–2.5% Cu) Al-Cu-Mg-Si (3–6% Cu)	High strength at room and elevated temperature	Highly stressed parts, aerospace, structural items, heavy-duty forging, heavy goods vehicles, cylinder heads, pistons
3xxx	Al-Mn-Mg	High formability and corrosion resistance with medium strength	Packaging, roofing and cladding. Chemical drums and tanks, process and food handling equipment
4xxx	Al-Si	Good flow characteristic, moderate strength	Filler metal, cylinder heads, engine blocks, valve bodies and architectural purposes
5xxx	Al-Mg (1–2.5% Mg) Al-Mg-Mn (3–6% Mg)	Excellent corrosion resistance, toughness, weldability and moderate strength	Cladding, vessel hull, superstructures, structural members, vessel and tanks, vehicle rolling stock, architectural application
6xxx	Al–Mg-Si	High corrosion resistance, excellent extrudability, moderate strength	High strength structural members, vehicle rolling stock, marine application, architectural application
7xxx	Al-Zn-Mg Al-Zn-Mg-Cu	Very high strength, high toughness	High strength structural members, heavy section aircraft forging, military bridging, armour plate, heavy goods vehicle and rolling stock extrusions
8xxx	Al-Li-Cu-Mg	Heat treatable, high conductivity, strength, hardness	Thinner gauge applications, electrical applications, aerospace, bearing applications
9xxx	Reserved for future use		

The 8xxx series is widely used due to its low density. AA8011-H14 is an Al-Fe alloyed grade consisting of moderate strength with excellent corrosion resistance, high ductility and a reflective appearance [13]. The 8xxx is used on the upper and lower body of planes' wing skin, floor sections and on supporting members of the fuselage structures [9]. The mentioned grades are both applicable in aerospace engineering. The mentioned aluminium alloys were chosen due to the increasing demand for the joining of dissimilar aluminium alloys in many industries, including automotive and aerospace engineering [14,15]. This, therefore, makes the joining of dissimilar materials imperative and unavoidable. It is a well-known fact that rivets are the preferred joining technique in aerospace engineering applications. One reason for this preference is that welding thin sections is very finicky and difficult. Material properties are often compromised in the process. However, Kashaev et al. [14] have acknowledged the growing interest in the use of welding techniques instead of rivets in joining aluminium alloys in aerospace applications.

The dominating welding methods include the fusion welding technique called tungsten inert gas (TIG) welding and the emerging solid-state technique called friction stir welding (FSW). These techniques are highly recommended, especially in the joining of soft materials with low melting temperatures [16]. However, joining dissimilar aluminium alloys using fusion welding

techniques like TIG is quite challenging due to the low melting point and low hardness of aluminium. The use of such a technique also results in coarse-grained microstructures, large distortions that are initiated by the shrinkage in the weld metal and heat-affected zones (HAZ) [17]. Moreover, the heat experienced by the material during welding results in extensive softening in the HAZ. The softening results in the deterioration of mechanical properties [18]. FSW has been a proven solution for giving better results than TIG welding [19-20]. However, most industries still use TIG welding. Additionally, the joining of dissimilar materials generally come with drawbacks like the formation of brittle intermetallic compounds (IMCs), porosities, solidification cracking and thermal residual stresses which result in poor mechanical properties [21-22]. It is undeniable that quality improvement is increasingly in demand. This is where the friction stir processing technique emerges as a viable solution.

The friction stir processing (FSP) technique is a variant of FSW, which was developed by Mishra et al. [23]. Unlike FSW though, the FSP technique does not join materials together but modifies the microstructure, homogeneity and densification of the material [24-25]. FSP significantly improves joint properties like hardness, wear-resistance and ductility while preventing defects caused by material melting [26-27]. There are many reasons why the FSP technique comes highly recommended as a method to enhance the properties of a surface or joint. The mechanical and tribological properties of the nugget zone can be controlled by adjusting the tool pin and shoulder diameter or length, or both. This occurs by changing the tool rotation speed, tool traverse speed, tilt angle and vertical force [27-29]. Compared to other material processing techniques, FSP is the only method where the processed depth can be controlled simply by adjusting the length of the tool pin [28,30]. Furthermore, FSP is an energy-efficient green processing technique, a fully automated process with good dimensional stability [30].

Managing the heat generation during FSP is critical, for surplus heat could melt the material, especially the soft series like the 1xxx and the 8xxx [31]. The surplus heat escalates grain growth and deterioration of the joint properties. Effective cooling was determined as a solution for the removal of surplus heat and it results in ultra-fine grain structure [32]. This effective cooling is known as submerged friction stir processing (SFSP). The SFSP technique adopts the same principle as the FSP technique but differs in the operating medium. During the SFSP process, the material to be processed and the FSP tool remain under a submerged environment [33-34]. The submerged environment could be water [34], a combination of methanol, dry ice and water [35], copper backing plate [36] or even nitrogen [37-38]. A SolidWorks diagram of the SFSP is depicted in Figure 1.1.

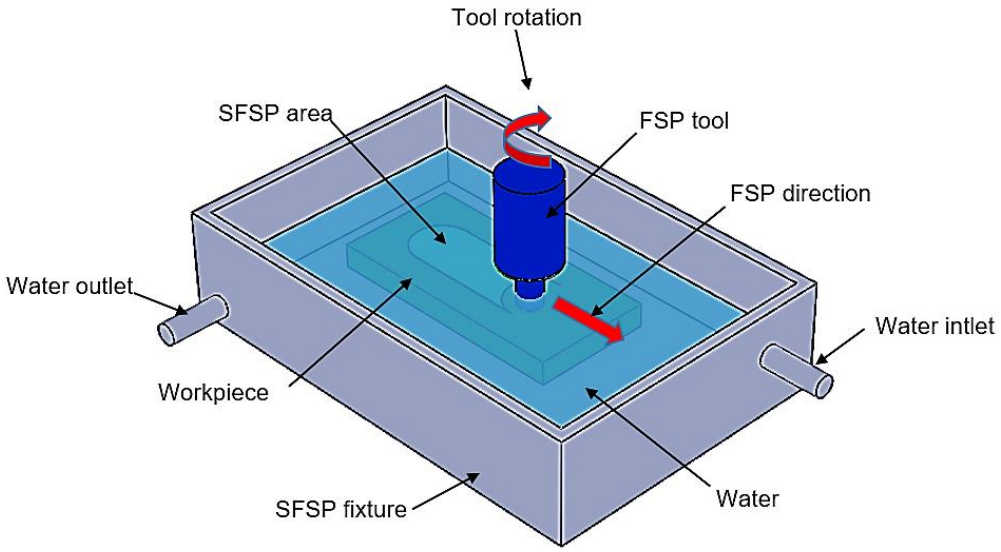

Figure 1.1: SolidWorks diagram of the underwater friction stir process.

1.2 Problem statement

It is evident that the fabrication of dissimilar materials is slowly emerging as a norm; it is difficult to find a component made of a single material, especially in automotive and aerospace engineering applications. Therefore, the joining of dissimilar materials, in general, is inevitable, as ever-advancing technology suggests the production of new structures and components from various materials and alloys. New components are therefore quite possible by combining the two mentioned aluminium alloys. This present study explore the development of the new FSP method to enhance the mechanical properties of FSW and TIG-welded AA8011-H14/AA6082-T651 dissimilar aluminium alloy joints.

1.3 Research background

Over the years, since the existence of FSP, several studies have investigated the effects of various process parameters like traverse speed and tool rotation, tool tilt angle, tool geometry, number of passes and additional cooling methods. Tool rotational speed and tool traverse speed control the material flow and heat input during FSP and have a significant impact on the microstructure of the stir zone [39]. Karthikeyan and Kumar [40] employed FSP on the AA6063-T6 plate to evaluate the relationship between process parameters and mechanical properties of the nugget zone. Varying axial forces and using tool feeds and tool rotational speeds, results revealed that FSP materials have lower tensile strength and ductility at the lowest axial force of 8 kN, but reach peak values once the axial force is increased to 10 kN. However, they fall with a further increase of axial force to 12 kN. The optimised parameters for sound results were determined as an axial force of 10 kN, a tool feed of 40.2 mm/min and a tool rotational speed of 1400 rpm. These results concur with others obtained in the literature [41-43].

FSP has been successfully used for many applications. For example, FSP can be used for microstructural modification for cast materials. Sekban et al. [44], evaluating the impact of FSP on a low carbon structural steel, found that the hardness of the alloy increased from 140 HV to 240 HV, as an increase due to the significantly refined microstructure caused by the severe plastic deformation and dynamic recrystallization. The yield and tensile strength increased

while the ductility decreased after FSP. Likewise, wear resistance also improved. Similar findings were found in the literature [45]. Wang et al. [46], for example, applied FSP on the Mg-6Zn-1Y-0.5Zr casting. FSP resulted in the dissolution and dispersion of the intergranular eutectic I-phase (Mg_3Zn_6Y). The hot deformation during FSP transformed the I-phase to W ($Mg_3Zn_3Y_2$) phase. Significant grain refinement was reported, which in turn improved tensile strength, yield strength and ductility. Similar findings on the intriguing grain structure refinement and improvement of mechanical properties were reported in the literature [47-52].

FSP has been successfully proven as a useful method for the preparation of superplastic materials. Superplasticity refers to a material with high elongation without showing necking when the material is stretched under certain conditions [53]. For a material to be deemed superplastic, it must have an elongation that is greater than 500% and grain size less than 10 µm [53-54]. Mishra et al. [28] were the first to use FSP for the preparation of superplasticity by applying FSP on the AA7075 alloy with the aim of achieving high strain rate superplasticity. Post-FSP, the average grain size obtained was 3.3 ± 0.4 µm. This conveyed the best superplasticity: an elongation of over 1000% was obtained at 1×10^{-2} S^{-1} and 490°C. Since then numerous studies were reported, as including in the literature [54-58].

FSP is applicable in the fabrication of surface composites via reinforced particles. The surface composite reinforced additives – in the form of powder, fibres or platelets – are most commonly filled into specially milled grooves [59-62]. The B_4C reinforced composite coating was fabricated on the surface of the Ti-6Al-4V alloy utilising FSP [63]. FSP resulted in 134 times improved wear resistance in comparison to the base material one. However, the hardness of the coating was doubled. As the direct wear of the matrix was notably reduced by the presence of B_4C particles, the wear mechanism reduced the coefficient of friction from 0.20 to 0.06. Nitinkumar et al. [64] enhanced the ballistic resistance of the AA7005 alloy by adding titanium diboride (TiB_2) and B_4C ceramic reinforced particles, with results showing that the surface hardness of the composite post-FSP was 70 HV higher than the base material one. A 1.6 times higher ballistics mass efficiency factor of the surface composite compared to the base material one was obtained. Several studies used various kinds of reinforced particles, including silicon carbide (SiC) [65], graphene (GNPs) [66], carbon nanotube (CNT) [67], and aluminium oxide (Al_2O_3) [68].

Fabrication of in-situ composites can also be achieved utilising FSP. The in-situ method provides thorough mixing of the introduced powder with plasticized substrate metal as a result of a complex quasi-viscous material flow at temperatures below melting point [69]. There are several existing in-situ composite combinations obtained using FSP, including aluminium copper (Al-Cu) [70], aluminium copper oxide (Al-CuO) [71], aluminium magnesium copper oxide (Al-Mg-Cuo) [72], aluminium nickel (Al-Ni) [73] and aluminium titanium (Al-Ti) [74]. You et al. [71] fabricated the aluminium based in-situ FSP composite using the Al-CuO powder mixtures. The nanometre-sized Al_2O_3 and Al_2Cu particles were used as composite reinforcements, with outcomes revealing that the FSPed specimen consisted of a cluster of Al_2O_3 nanoparticles identified as amorphous. The FSPed composite had an average grain size approximated to 1 µm which resulted in the composite having superior tensile strength and ductility in comparison to the base material. The results obtained correlated with ones obtained by other researchers, including Golmohammadi et al. [75], Mahmoud et al. [76] and Wang et al. [77].

The FSP is versatile, such that Miles et al. [78] employed the method to repair a tapered crack on the 304L stainless steel plate. The feasibility of FSP was demonstrated using a series of randomly sequenced cracks of various widths. The results denoted that FSP only managed to close the cracks with a narrow start and widening, but created voids on the cracks with a too wide crack at the start. In four of six different crack cases, the UTS of the processed specimens were greatly improved when compared to the base material. The increase in the UTS was a result of the stir zone refined grain structure. However, due to the hardness inhomogeneity, the elongation of the same specimens showed a decline compared to the base material one. The hardness correlated with the stir zone grain size as stipulated in the Hall-Petch relationship. Similarly, observations were conveyed by Al-Badour et al. [79] where FSP was used to repair a crack of the AA6061 6 mm thick plate.

Recently there have been several studies of FSP to enhance the mechanical properties of previously solid-state and fusion-welded joints. Mehdi and Mishra [80] evaluated the effect of the FSP technique on the microstructure and mechanical properties of the TIG-welded AA6061/AA7075 joints. The results showed that the FSPed TIG-welded joints had a higher UTS than the TIG-welded joints. The hardness of the TIG-welded joint was higher than the FSPed TIG-welded joints. The microstructural grain size decreased significantly post-FSP. The FSP approach was used to enhance the performance of the magnesium AZ31 alloy joint [81]. FSP was employed using a different tool than the one for the fabrication of the joint. That, therefore, resulted in a two-layered structure also known as the twining effect. The weakened strain in deformation, together with the strengthening effect of the twin lamellae, improved the mechanical properties.

Extensive research has also been conducted on the FSP variant SFSP following an initial study by Sakurada et al. [82] who was the first to utilise the underwater process on the basis of welding. The AA6061 alloy served as a base material. Results showed that it was possible to generate enough friction for processing even though the workpieces were underwater. The stirred region of the underwater weld joint showed a finer microstructure in comparison to the one exposed to room temperature air conditions. The elongation of the underwater joints was lower than the air. The results also revealed a hardness increase in AA6061 from 60 HV to 90 HV which led to a joint efficiency increase of 33%. Hoffman and Vecchio [83] introduced the same method as a processing technique rather than welding. The SFSP method was utilised to create an ultra-fine grain structure of the AA6061 alloy. The use of water as an operating medium during FSP resulted in the dramatic reduction of conductive heat flow compared to when FSPed under normal conditions. The grain size average was notably reduced to below 200 nm on the SFSP joint. Since then, many researchers have applied the SFSP for the same applications as FSP under normal conditions.

Darras and Kishta [84] friction stir processed AZ31 magnesium alloy in normal and submerged conditions to analyse the differences in tensile properties, grain structure, power consumption and thermal fields. The average grain size of 18.9 µm, 15.9 µm and 13.3 µm was obtained for FSP in the air, submerged in hot water and cold water, respectively. The most grain refinement was in cold water FSP conditions. The thermal results revealed the peak temperature for weld in the air as highest at 477 K. In the case of cold and hot water joints, it was 385 K and 433 K, respectively. The time spent for the processing was 16.5s, 7s and 4s for FSP in air, submerged in hot water and cold water. The results made evident that SFSP not only reduces the temperature but also reduces the time spent processing the material. The uniform heat absorption capacity of water results in a higher temperature gradient (along transverse and

longitudinal weld axes) and a higher cooling rate in underwater friction stir welds as compared to air-cooled welds [17].

Based on the work noted thus far in the available literature, it is clear that FSP has the ability to enhance the properties of a single material surface as well as previously welded joints for various alloys, not solely aluminium. However, there was little or no traceable literature of the previous work where SFSP was used as the post-processing technique on FSW and TIG-welded dissimilar joints. This present study explore the optimised conditions for the performance of FSP on the FSW and TIG-welded AA8011-H14/AA6082-T651 dissimilar joints. The submerged FSP AA8011-H14/AA6082-T651 dissimilar joints will then compared to those produced under normal FSP conditions.

1.4 Research aim and objectives

The main aim of the study was to develop a new FSP method that can be used in the enhancement of the mechanical properties of the FSWed and TIG-welded AA6082/AA8011 dissimilar joint. This aim was achieved through the following objectives:

i. Two dissimilar aluminium alloy plates were welded using the TIG and FSW techniques.
ii. These welded dissimilar plates were then friction stir processed using the vertical milling machine used to perform FSW.
iii. Submerged (underwater) and normal (room temperature) FSP conditions were applied.
iv. The influence of the different FSP conditions on the said joints was compared.

1.5 Thesis outline

Chapter One presents the introduction, background, research objectives and review of relevant literature of FSP. Chapter Two presents detailed literature relevant to the study and a summary of this reviewed literature. Chapter Three presents the details about experimental setup and performances. Chapter Four presents the results and discussions of the tests conducted, whereby the NFSP-TIG results are compared to the SFSP-TIG ones and the NFSP-FSW to the SFSP-FSW results. Chapter Five presents the study's conclusions based on results obtained. Recommendations are offered for future work in relation to the study. The thesis outline is depicted in Figure 1.2.

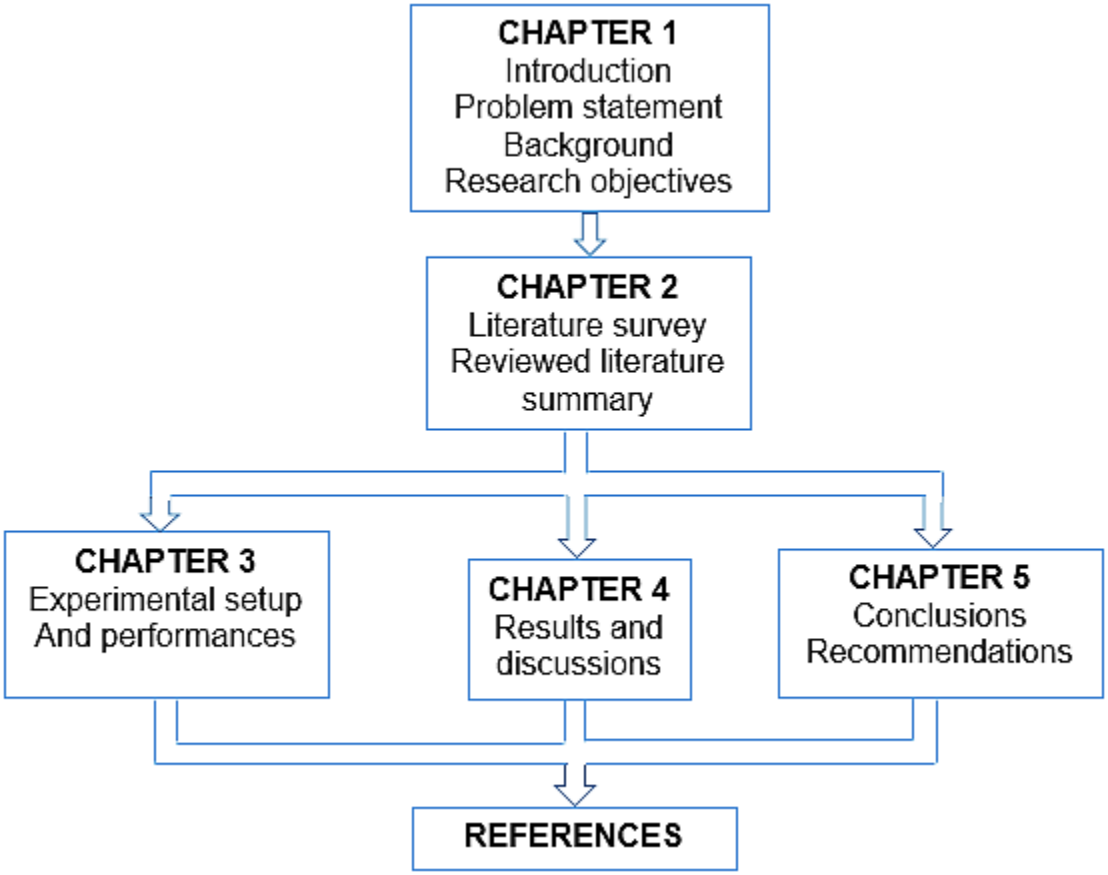

Figure 1.2: Thesis outline.

CHAPTER TWO

LITERATURE REVIEW

This chapter presents a detailed literature review related to the study at hand. The main focus is based on three subtopics which form the core of this study: friction stir welding, TIG welding and friction stir processing of aluminium alloys.

2.1. Friction stir welding of dissimilar aluminium alloys

The welding parameters during FSW of dissimilar aluminium alloys have a great influence on the characteristics of the welded zone. Welding parameters can be categorised as machine parameters (traverse speed, axial force, tool tilt angle and rotational speed) and the tool parameters (that is, tool material, shoulder diameter, pin diameter, pin length and pin geometry) [85]. Gowthaman and Saravanan [86] used FSW to join AA2024 and AA7075 alloys to evaluate the effect of welding parameters with varying tool rotational speeds between 1000 rpm and 1400 rpm, tool traverse speeds between 20 mm/min and 40 mm/min with a constant axial force of 4 kN. The microstructural results at high tool rotational speed reveal the presence of coarsening grains due to high heat input and dynamic recrystallization in the deformed zone. The UTS increased as the welding speed decreased. However, Kailainathan et al. [87] determined that the tensile strength beyond the tool rotational speed of 1200 rpm depreciates due to the distortion in the weld region caused by higher rotational speeds.

The material positioning and tool offset are vital for improving mechanical properties and reduction of weld defects in FSW of dissimilar alloys [88-91]. The AA6061-T6 was friction stir welded (FSWed) to the AA8011-H14 to investigate the impact of material positioning and tool offset [92]. The welding parameters include a tool rotational speed of 1070 rpm, tool traverse speed of 50 mm/min and a tool tilt angle of 2°. The positioning of the softer alloy AA8011-H14 on the advancing side of the tool, with a tool offset of 1 mm produced better joint properties. The tensile test results showed a maximum UTS of 77.8 MPa and an elongation of 21.96%, while the hardness was independent of the varied process parameters. A uniformly distributed grain structure was found on the weld zone. Several reports in the literature agreed with the positioning of the softer material on the advancing side of the tool, regardless of the dissimilar aluminium combinations [87,89,93-95]. According to Lee et al. [96], and based on the findings obtained on the analysis of the FSWed A356 and AA6061 results, the stir zone was dominated by the material on the retreating side. Conversely, the outcome of the study by Priya et al. [97] where the AA2219 and AA6061 were joined using FSW, revealed that the stir zone is instead dominated by the material on the advancing side.

Mahmoud et al. [98] investigated the influence of material positioning and welding parameters on the microstructural and thermomechanical issues of the FSWed AA6061/A390 weld. The varying tool rotational speed was used with A390 on the retreating side and AA6061 on the advancing side. The results indicated that the average grain size was larger when the A390 was positioned on the advancing side but smaller when the same alloy was placed on the retreating side. This was due to the particle stimulated nucleation and the temperature experienced by the weld. The strain rate on stir zone grain size was higher when the AA6061 was located on the advancing side. Similar observations were highlighted by Dinaharan et al. [99]. Several studies reported that the material with higher strength should be placed on the advancing side [100-105]. In the light of all the referenced studies, it is clear that material

positioning during FSW of dissimilar aluminium alloys is circumstantial and dependent on the welding parameters [106]. Table 2.1 samples the above reviewed literature, highlighting the core parameters used.

Table 2.1: FSW of dissimilar aluminium (TRS-tool rotational speed, TTS-tool traverse speed, RS-retreating side, AS-advancing side, NS-not specified, TPD-tool pin diameter, TPS-tool pin shape, TPL-tool pin length, TSD-tool shoulder diameter)

Material used	FSW tool	Welding parameters	Material positioning	Comments	Ref.
AA2024 AA7075	Material: AISI H13 TPS: straight cylindrical TPD: 6 mm TPD: 20 mm TPL:15 mm	Optimum TRS:1000 rpm TTS: 20 mm/min Tilt angle 7° axial force: 4 kN	AS: AA2024 RS: AA7075	Maximum UTS: 214.23 MPa YS: 191.98 MPa Elongation: 5.25%	[86]
AA8011 AA6063	Material: High carbon high steel TPS: hexagonal TPD: 5 mm TSD: 20 mm	Tool tilt angle: 2° Optimised: TRS: 1200 rpm TTS: 60 mm/min Axial force: 10 kN	Optimum: AS: AA8011 RS: AA6063	Maximum UTS: 134 MPa Maximum hardness 18 BHN	[87]
AA8011-H24 AA6061-T6	Material: D2 steel TPS: hexagonal TPD: 6 mm TPL: 5.7 mm TSD: 18 mm	Tool tilt angle: 2° TRS: 1200 rpm TTS: 50 mm/min Plunge depth: 2 mm	Optimum: AS: AA8011-H24 RS: AA6061-T6	Maximum UTS: 90.08 MPa Elongation: 13.2%	[93]
A356 AA6061	NS	TRS: 1600 rpm TTS: 87-167 mm/min Tool tilt angle: 3°	AS: AA6061 RS:A356	Maximum UTS: 192 MPa YS: 105 MPa Microhardness: 75 HV	[96]
AA2219 AA6061	Material: tool steel TPS: tapered TPD: 5 mm TPL: 4.8 mm TSD: 15 mm	Tool tilt angle: 2° TRS: 1600 rpm WS: 40 mm/min Tool offset: 1 mm (optimised)	AS: AA6061 RS: AA2219	Maximum UTS 312 MPa YS: 303 MPa Hardness: 140 HV	[97]

FSW was employed to join the AA1050-H14 and AA5083-H111 to compare the microstructure and mechanical properties of the specimens extracted at different weld positions (start, middle and end) [107]. The welding parameters included a tool rotational speed of 1000 rpm, traverse speed of 30 mm/min and a tool tilt angle of 2°. FSW was performed using a tool made of high-speed steel with a tool shoulder diameter of 20 mm, pin diameter of 6 mm, pin length of 5.8 mm and a threaded pin profile. The specimens extracted from the start of the weld had low tensile properties in comparison to those extracted from the middle and end of the weld. The UTS of all specimens was lower than that of the AA5083-H111 BM but closer to the AA1050-H14. All specimens showed a ductile fracture failure characterised by the presence of dimples. Similar findings were reported in the literature [108]. Yadav et al. [109] conducted a study on the FSW of AA1100 and AA6101-T6 alloys using an H13 cylindrical tool profile, with tool parameters including a shoulder diameter of 18 mm, pin diameter of 3 mm and a pin length of 4.8 mm. The welding parameters were a tool rotation of 1500 rpm and a tool traverse speed

of 30 mm/min. The macrostructure obtained revealed a tunnel defect on the joint surface. The tensile test results were found to pose a UTS closer to the AA1100 BM but lower than that of the AA610-T6 BM.

A microstructural analysis on the FSWed AA5052/AA6061 dissimilar joints was added in the literature [110]; results indicated that both materials showed a similar texture at the interface region of the nugget despite non-rigorous mixing of the materials. The tensile properties of the dissimilar joint were better than of the AA5052 alloy (weaker strength) but lower than of the AA6061 (stronger strength) alloy. In a similar study using aluminium grades to fabricate a dissimilar FSWed joint analysing the effect of material locations [111], results reported different material mixing patterns depending on the locations of the used BM. However, adequate mixing only occurred when the AA5052-H32 alloy was placed on the advancing side and the AA6061-T6 on the retreating side compared to the inverse. The microhardness of the HAZ of the AA5052-H32 had the lowest value under both material positioning scenarios. Moreover, the tensile test specimens all fractured on the HAZ of the same alloy.

Kan et al. [112] investigated the microstructure and mechanical properties of the friction stir welded AA2219 and AA7475 similar and dissimilar aluminium alloy joints. The micro store results suggested a nugget zone with a significantly refined grain structure due to dynamic recrystallization instigated by the plastic deformation. The UTS of the dissimilar joint was lower than those of similar joints due to the non-homogeneous movement of the materials caused by the difference in the physical and mechanical properties. The similar joints were more ductile than the dissimilar joints which had lower elongation. The TMAZ of the retreating side for all the joints contained the minimum hardness due to thermal softening. According to Amancio-Filho et al. [113], studying the tensile properties of the AA2024 and AA6056 FSWed joints, results revealed thermal softening of the base materials caused by the poor tensile strength. Moreover, the joint efficiency was at 56% of the AA2024 BM and 90% of the AA6056 BM. Similar behaviour was reported in the literature [114-115].

Numerous studies on dissimilar aluminium FSW have been conducted with regards to material flow, microstructural evolution and mechanical properties behaviour. Niu et al. [116], for example, evaluated the cyclic behaviour of the FSWed dissimilar AA2024-T351/AA7075-T65, with welding parameters of 600 rpm for tool rotational speed and a traverse speed of 150 mm/min. Uniaxial symmetric push-pull cyclic deformation tests were performed at room temperature. A stepwise increase strain amplitude of 0.1 to 0.6 was applied until the fracture at a strain rate of $1 \times 10{-}2$, 3 × 10-3 and 1 × 10-3 s-1. The cut-off limit was 1000 cycles for each level. Results indicated that the strength of the joint after 500 cycles at 0.5 strain amplitude was equated to that of the AA2024 base material. The formation of dislocation was found on the HAZ of AA2024. The cyclic hardening of the joints improved as the strain rate decreased.

Wang et al. [117] performed a grain structure analysis on the FSWed AA5052-O and AA6061-T6 dissimilar joint. The findings mentioned a discovery of numerous dislocations and precipitates present on the TMAZ and nugget zone. A theory based on dislocation arrangements was proposed to describe the function of dislocation cell structures in strain rate hardening [118]. Cyclic deformation comprises frequent back-and-forth dislocation motions at high cyclic stress resulting in the formation of dislocation of substructures like cell structures and persistent slip bands [116,119]. The cyclic deformation strain rate influences plastic strain which therefore results in material damage [116,119,120]. Several researchers conveyed

cyclic hardening during cyclic fatigue/deformation of both similar and dissimilar aluminium FSWed joints [114,121-122]. During the joining of dissimilar alloys, brittle intermetallic compounds (IMCs) are a typical phenomenon [106]. Giraud et al. [102] expressed that the formation of IMCs in the interface of two materials is difficult to control. Furthermore, the IMCs could influence the mechanical properties negatively due to the brittle nature they pose.

2.2 TIG welding of dissimilar aluminium alloys

A feasibility study on the TIG welding of dissimilar aluminium alloys AA2124 and AA7075 was conducted by Bindu et al. [123] with varying currents employed and a filler AA5356 alloy. With macrographs used for inspection of the weld produced at different currents, it was inferred that weldments at 100 amps were satisfactory. SEM analysis performed on open crack samples determined that the weldments consisted of intergranular fractures due to the segregation of the second phase along the grain boundaries. The hardness of the weld zone was significantly increased. An analysis of mechanical properties of TIG-welded dissimilar aluminium alloy AA2024 and AA6063 by Vijay et al. [124], with parameters of varying gas flow rate, voltage current and root gap and a single butt V-joint, showed an increase in tensile strength of the joint as the current and root gap increased. The hardness of the joint increased as the root gap increased to 1-1.5 mm and the gas flow rate of 18-20 L/min.

Wang et al. [125] employed the TIG welding technique to fabricate a single and double-sided joint of the AA7005-T6 and the AA5006-O of a ring stiffed closed cylindrical shell. The study parameters are presented in Table 2.2. The tensile tests results showed a UTS of 78.87% and yield strength of 97.24% of the AA5005-O BM. The elongation was 84.29% of the AA7005-T6 BM. The fusion zone, consisting of coarse grain size at high heat input, suggested that higher heat input potentially leads to complete dissolution of the strengthening precipitates in the fusion zone, which will result in deterioration of tensile strength and hardness. In the HAZ of the AA7005-T6, there was an emphasised hardening and softening zone as well as the solid solution precipitates of the Rayleigh brilliant η' ($MgZn_2$) phase.

Safari et al. [126] investigated the tensile properties of the TIG-welded AA6061-T6/AA7075-T6 dissimilar joints using a 1 mm narrow gap between the plates during the butt welding. The process parameters included an alternative current of 200 A, a gas flow rate of 25 ml/min and a voltage of 15 V. The ER4043 with a 2.4 mm diameter served as a filler metal. The ER4043 has a high content of silicon which favours the penetration of molten metal in the welding zone. Additionally, silicon also increases the fluidity of the melt [127]. Argon was used as a shielding gas. The tensile properties of the dissimilar joint obtained were UTS of 110 MPa, yield strength of 100 MPa and elongation of 1.8%. All obtained tensile properties were lower compared to the BM ones. This was substantiated as caused by the precipitation hardening properties of the T6 heat treatment which were dissolved due to high heat generated during the TIG welding process. Similar findings were reported by Patil et al. [128] using the same aluminium alloy grade with the same T6 condition.

Ishak et al. [129] subjected the AA6061/AA7075 to TIG welding to prove the conviction that filler wire has a significant impact on joint strength. Two different filler metals – ER4043, which has a high silicon content, and ER5356, which has a high magnesium content – were subjected to several tests, including visual appearance, microstructure and hardness tests. The results revealed that welding using filler ER5356 produced deeper penetration compared to filler ER4043. The use of ER5356 resulted in a penetration depth of 1.74mm and 0.9mm of

penetration was accomplished when using ER4043. Microstructures at different zones of dissimilar TIG joints (such as the fusion zone, the PMZ and the HAZ) were identified. The ER5356 had a finer average FZ grain size of 11.4 μm, while the filler ER4043 was 19.5μm. The hardness also followed the same grain size pattern with the ER5356 filler specimens higher than the filler ER4043 ones. Overall, the specimens TIG-welded using the ER5356 filler yielded better joints compared to ER4043 ones.

The AA6082/AA8011 were butt-welded using TIG welding to investigate deformation behaviour during tensile testing [130]. The UTS and yield strength reportedly increased as the current increased. The use of different filler material diameters had a minimal effect on the UTS. The hardness of the dissimilar joint increased significantly at the current of 80 A and gas flow rate of 6 L/min compared to the AA8011 BM. The mechanical properties of the AA5083/AA6061 pulsed TIG-welded dissimilar joints were evaluated [131]. Varying process parameters were applied to obtain optimised parameters. The tensile test results showed a UTS of 213 MPa, yield strength of 176 MPa and elongation of 12%. SEM analysis of the post-tensile specimens revealed a ductile dimple rupture from excessive heat and impurities which hindered micro-level weld integrity.

Sayer et al. [132] evaluated the microstructure and mechanical properties of the TIG-welded AA2014/AA5083 dissimilar joints with a V joint configuration with a 2 mm gap between the plates. Two passes of the TIG-welds was applied on one side. The welding parameters used are presented in Table 2.2. The microstructural results of the fusion zone showed a nonhomogeneous coarse grain distribution compared to AA2014 and AA5083-O base materials. The UTS of 175 MPa was obtained for the dissimilar joint AA2014/AA5083 with a yield strength of 128 MPa and elongation of 2.6%. The tensile properties achieved were lower than both BMs. The tensile specimens fractured in the welded region. SEM analysis revealed a brittle nature of the fracture with the hardness sharply decreasing 84 HV towards the HAZ region of the AA2014 side from severe heat input. However, the hardness increased in the fusion zone on the AA2014 side, followed by a decrease at the weld centre, due to the high silicon content of the filler material.

ER4043 filler wire was used during the TIG welding of the AA5083-H111/AA6061-T6 alloys [133], with welding parameters presented in Table 2.2. The microstructure was primarily dominated by fairly coarse columnar grain structure. Defects like micropores and cavities were detected. The tensile property results included a UTS of 133 MPa, elongation of 4% and a joint efficiency of 35.38%. The hardness of the dissimilar joint was approximately 105 HV which was more than the AA5083-H111 BM but less than the AA6061-T6 BM. The increase in hardness was due to the formation of the large magnesium silicon (Mg_2Si) precipitates. Similar research was found in the literature [134-136].

Table 2.2: TIG welding of aluminium alloys (WC-welding current, WS-welding speed, PT-plate thickness, Q-gas flow rate, FZ-fusion zone, YS-yield strength, V-voltage, F-frequency, FW-filler wire, NS-not specified).

Material used	Welding parameters	Comments	Ref.
AA7005-T6 AA5005-O	Q:24 L/min V: 25 V WC: 260 A WS: 200 mm/min PT: NS FW: ER5356	Maximum UTS: 281.08 MPa YS: 157.33 MPa Elongation: 11.43% Hardness: 86 HV	[125]
2AA8011 AA6063	Q:25 L/min V: 15 V WC: 260 A WS: 200 mm/min PT: 6 mm FW: ER4043	Maximum UTS: 110 MPa YS: 100 MPa Elongation: 1.8%	[126]
AA5083-O AA6061-T651	Optimised: Pulse frequency: 2 Hz V: 13.2 V WC: 175 A WS: 155 mm/min PT: 6.35 mm FW: ER5356	Maximum UTS: 213 MPa, YS: 176 Mpa Elongation: 12%	[129]
AA2014 AA5083-O	WS: NS V: 14 V WC: 140-150 A Q: 10 L/min PT: 5 mm FW: ER4043	Maximum UTS: 175 MPa YS: 128 Mpa Elongation: 2.6% Microhardness: 84 HV	[132]
AA5083-H111 AA6061-T6	WS: 150 mm/min V: 16 V WC: 200 A Q: 40 L/min PT: 5 mm FW: ER4043	Maximum UTS 133 MPa Elongation 4% Hardness: 105 HV	[134]

2.3 Friction stir processing of welded aluminium alloy joints under normal conditions

Fuller and Mahoney [137] employed FSP to modify the microstructure and mechanical properties of the AA5083-H321/AA5356 dissimilar metal inert gas (MIG). Four specimens were examined: the BM, the weld toe FSP advancing and retreating side of the FSP tool, and the weld crown. Microstructural results revealed a fine grain structure on the FSPed region consisting of smaller constituent particles. The particles found in the arc weld nugget, HAZ and BM were the Mg_2Si and the A_6(Fe Mn). FSP resulted in the strengthening of grain sizes due to grain refinement and precipitate strengthening. The application of FSP improved UTS of the fusion welded joint from 259 MPa to 306 MPa and yield strength from 162 MPa to 193 MPa. However, the elongation declined from 36% to 33%. The increase in tensile strength was due to the dynamic recrystallization that occurred during FSP leading to the grain refinement. The fatigue strength of about 10^7 cycles was higher compared to the fusion-welded one during the four-point bending fatigue analysis.

The impact of FSP on the TIG-welded dissimilar AA6061/AA7075 joint was explored by Mehdi and Mishra [138], with different wire fillers (ER4043 and ER5356) used to produce the TIG-welded joints prior to FSP. The results showed the UTS and hardness improved with an increase of the tool rotational speed. However, residual stress declined under increased tool rotation. The resulting residual stress of 71 MPa was obtained for the TIG-welded joint at the FZ for filler ER4043 while the FSPed TIG-welded one was 37 MPa. The fractured tensile specimens showed large and quasi-cleavage with sharp edges for both fillers on the TIG-welded specimens, while the FSPed ones consisted of fine dimples in the nugget zone. That, therefore, represented better mechanical properties. The microstructural grain size ranged from 3.2-4 μm. The grain sizes were determined as inversely proportional to the tool rotational speed. The ER5356 and tool rotational speed were found to results in better results. The impact of FSP on the microstructure and mechanical properties of the AA6061-T6/AA7075 TIG-welded joints were examined [80]. The tensile tests revealed that the UTS and microhardness of the FSPed TIG-welded dissimilar joint were higher than the TIG-welded joint. The grain size refinement was responsible for the improvements in the tensile properties. The obtained microhardness was 105 HV, UTS of 255 MPa with an elongation of 29.2%.

Divereddy et al. [139], subjecting the TIG-welded AA2014 joint to FSP for the evaluation of microstructure and mechanical properties of the joint, used FSP parameters of a tool traverse speed of 1200 rpm and a tool traverse speed of 1.1 mm/s. The application of FSP resulted in the elimination of defects that were present prior like voids, gas pores and porosities. The grain structure was transformed from coarse to equiaxed homogeneous grain structure. The tensile properties were greatly improved as a result of the significantly refined microstructure. The hardness of the FSPed TIG-welded joint was higher than the TIG-welded joint. Similarly, the AA5083-H111 TIG-welded joints were FSPed to modify the joint properties [140]. The application of FSP increased flexural strength and tensile strength, an increase due to the refined microstructure post-FSP. The ductility of the FSPed TIG-welded joints was also improved. SEM analysis also revealed the best-reduced dimple sizes in comparison to the TIG-welded ones.

The FSWed AAA1050-H14/ AA6082-T651 dissimilar joint was FSPed to evaluate the effect of material positioning on the mechanical properties of the joint [141]. A comparative analysis on the FSW and FSPed FSW with AA1050-H14 considered the different material positioning (advancing retreating side) to assess optimised conditions. The microstructure showed a significant grain refinement during FSW, and FSP was achieved when the AA1050 was positioned on the retreating side and the AA6082-T651 on the advancing side. However, when comparing the grain sizes of the nugget zones, the FSPed ones showed very fine grain size compared to the FSWed ones. The grain refinement improved the tensile strength of FSPed joints more than of the FSWed ones. Likewise, the hardness of the FSPed was greatly improved. The SEM of the FSPed joints showed more ductility than the FSWed ones. Similar findings on the impact of FSP on the FSW joint were reported in the literature [142-143].

According to Da Silva et al. [144], after applying FSP on the MIG-welded AA6082-T6 joints with and without reinforcement, the microstructure for the FSPed MIG joints had the finest grain structure with and without reinforcements compared to the MIG ones. The improvement was due to the geometric modification and removal of the defects that were present in the MIG grain structure like porosity and lack of wetting in the weld zone. However, the FSPed MIG weld with reinforcements had a finer grain structure than the FSPed without reinforcements. Therefore, the FSPed MIG with reinforcements resulted in better tensile properties. The FSP

technique improved the mechanical and fatigue behaviour of the AA5083-H111 MIG-welded joints [145]. Two different stress ratios (R=0 and R=-1) under constant loading were employed during the fatigue tests, with fatigue strength significantly improved due to the refinement of the microstructure grains, removal of porosities and the reduction in stress concentration. However, a minimal increase in hardness and decrease in elongation of the tensile specimens were reported. Similar findings were reported in the literature [146-147].

The influence of FSP on the TIG-welded AA2024/AA6082-T6 joints was studied by Mehdi and Mishra [148]. Varying tool rotational speed and a constant tool traverse speed of 25 mm/min were applied to reach optimised process parameters. The microstructure revealed that FSP transformed the coarse grain dendritic structure produced by the TIG-welded joint to a fine grain one. The refinement of the grain structure resulted in significantly improved hardness of the FSPed TIG-welded joint compared to the TIG-welded one. Similarly, the UTS and elongation of the FSPed TIG-welded joint were higher than the TIG-welded joint. The examination of the TIG-welded dissimilar AA7075/AA6061 joints processed using varying tool rotational speeds was added in the literature [149]. The tool rotational speeds were varied from 700 rpm to 1000 rpm using increments of 100, while the tool traverse speed was maintained at 70 mm/min at a tool tilt of 1°. The maximum tensile strength was improved by 78.57% at 1100 rpm compared to the TIG-welded joints. A ductile fracture characterised by the cleavage facets, large dimples and teared ridges were reported on the fracture surface analysis of the post-tensile test specimens. The FSPed joints had superior wear resistance compared to the TIG-welded joints.

Kianezhad and Raouf [150] used a single-pass FSP to improve the properties of the TIG-welded AA5083 joints using the Al_2O_3 particles. The tensile properties post-FSP showed an increase of 29% in the yield strength, a UTS increase of 18% and impact energy increase of 56% compared to the TIG-welded ones. A fracture surface analysis revealed a ductile classification fracture while the TIG-welded one revealed a brittle fracture. The ductility was due to the uniform distribution of reinforcement particles and the greatly refined microstructure. Saad et al. [151] demonstrated that the TIG-welded AA7020 joint hardness could be improved using the FSP technique: hardness of the FSPed TIG-welded joint was improved by 118.5% compared to the TIG-welded joint one and 103.6% compared to the base material one. Similar findings on the improvement of the TIG-welded joints using FSP were reported in the literature [152]. Table 2.3 presents a sample of the referenced summary of FSP of welded aluminium alloy joints to show the various tool and process parameters applied.

Table 2.3: FSP of welded aluminium alloy joints (TRS-tool rotational speed, TTS-tool traverse speed, RS-retreating side, AS-advancing side, NS- not specified, TPD-tool pin diameter, TPS-tool pin shape, TPL-tool pin length, TSD-tool shoulder diameter, El-elongation).

Material used	FSP tool	Welding parameters	Material positioning	Comments	Ref.
AA5083-H321 AA5356	Material: H13 tool steel TPS: Conical tapered TPD: 6.35-4.6 mm TSD: 11 mm TPL: 3 mm	TRS: 1600 rpm TTS: 40 mm/min NP: 2	AS: 5083 RS:5356	MIG UTS: 259 MPa YS: 162 MPa EL: 36% FSP UTS: 306 MPa YS: 193 MPa El: 33%	[137]

AA2014	Material: EN 31 TPS: cylindrical, TPD: 6 mm TSD: 18 mm TPL: 2 mm	Tool tilt angle: 3° Optimised: TRS: 1200 rpm TTS: 1.1 mm/s Axial force: 10 kN	NA	TIG UTS: 200 MPa, Hardness: 80 HV FSPed TIG UTS 180 MPa, HV 115 HV	[139]
AA5083	Material: H13 steel, TPS: Threaded, TPD: 6 mm TSD: 18 mm TPL: 5.8 mm	Tool tilt angle: 2° TRS: 1000 rpm TTS: 60 mm/min Axial force: 4 kN	NA	TIG UTS: 155 MPa El: 8% Hardness: 85 HV FSPed TIG UTS 250 MPa El: 23% Hardness: 95 HV	[140]
AA1050-H14 AA6082-T651	Material: H13 steel TPS: Spiral TPD: 7 mm TSD: 20 mm TPL: 5.8 mm	Tool tilt angle: 2° TRS: 1200 rpm TTS: 40 mm/min Axial force: 4.5 kN	Optimised AS: AA1050-H14 RS: AA6082-T651	FSW UTS: 80.1 MPa YS: 54.9 MPa El: 20.7% Hardness: 50 HV FSPed FSW UTS 83.2 MP YS: 61.1 MPa El: 23.6 Hardness: 80 HV	[141]
AA6082	Material: H13 tool steel TPS: threaded TPD: 4 mm TSD: 20 mm TPL: 2.9 mm	Tool tilt angle: 2.5° TRS: 1500 rpm TTS: 240 mm/min NP: 4	NA	MIG (R) UTS: 221 MPa, Efficiency: 67% Hardness: 85 HV FSP MIG (R) UTS: 225 MPa Efficiency: 68% Hardness: 80 HV	[144]
AA6082-T6 AA2024	Material: EN31, TPS: cylindrical, TPD: 6 mm TPL: 2 mm TSD: 18 mm	Tool tilt angle: 2° Optimised: TRS: 1200 rpm TTS: 25 mm/min Axial force 6 kN	AS: AA2024 RS: AA6063	TIG UTS: 204.2 MPa El: 4.5% Hardness: 57 HV FSPed TIG UTS 223.7 MPa El: 7.1% Hardness: 65 HV	[148]

2.4 Submerged friction stir processing of aluminium alloy joints

Feng et al. [153] investigated the effect of SFSP on the microstructure of the AA2219 plate. FSP application resulted in a nugget zone having a significant grain size reduction from 17 μm of the base material to 1.1 μm. The grain size decreased as the tool rotational speed decreased. The nugget zone softening also decreased as the heat input decreased. The formation of the equilibrium θ precipitates resulted in a decrease in the hardness of the nugget zone. As the tool rotational speed increased, the hardness of the nugget zone decreased. The refinement of the grain size, however, did not prevent the yield strength from decreasing from 107 MPa to 35 MPa. This was substantiated as caused by the T6 strengthening precipitate sensitivity to heat. The hardness behaviour was based on the antagonism between the material softening caused by the over-ageing of the precipitates and the microstructure grain refinement strengthening.

An analysis on the microstructure and mechanical properties of the FSPed AA2014 plate under different cooling conditions was conducted [154], with the FSP condition as air (normal) and water. The nugget zone SFSP microstructure showed a fine equiaxed and misoriented grain

structure with an average of 1.9 to 3.1 µm, while the base material ones showed a large coarse grain size. Regardless of the FSP conditions, FSP produced significantly reduced grains and second phase particle size. Grains with random orientation were also found in the nugget zone. The intensity of texture in the nugget zone was improved due to rapid cooling, suggesting that a different mechanism of grain refinement might have occurred through the discontinuous dynamic recrystallization. Furthermore, the increase in cooling rate improved the FSPed microhardness and UTS specimens.

SFSP was used to enhance the superplastic behaviour of the AA7075 alloy [155]. The submerged medium used included normal room temperature air and hybrid conditions such as compressed air, water and carbon dioxide ($CO_{2)}$ for a variety of cooling rates. The lowest processing temperature was obtained under the CO_2 conditions. However, the nugget zones of all the FSP conditions were confirmed as consisting of fine equiaxed grain sizes. A higher cooling rate was reported on the hybrid FSP condition samples which resulted in a significant grain reduction of the specimens. This phenomenon hindered the nugget zone grain coarsening. Amongst the hybrid conditions, the CO_2 had the most refined grain size of 1.96 µm. The same specimen had a significantly improved elongation of 572% due to the enticing grain size, resulting from low heat input during FSP. Similar studies were added to the literature [156-157] where water was used as a cooling medium to obtain a fine grain structure of AA7075 alloy.

Mehrain et al. [158] investigated the impact of various FSP conditions (air, dry-ice, water and liquid nitrogen) on the microstructure and corrosion of the aluminium magnesium alloy AA5052-H32. Process parameters included varying tool rotational speeds and tool traverse speeds with a constant tool tilt angle of 2.5°. The results showed significant grain refinement from 49.4 to 1 µm due to the controlled FSP conditions which posed a detrimental impact on the electrochemical behaviour due to the corrosion phenomenon wherein grain boundaries were activated. The annealed SFSPed Al-Mg alloy under tool rotation of 800 rpm and tool traverse speed was reported as an inferior electrochemical property with the highest corrosion rate of 0.01814 mm/year. Similarly, Khodabakhshi et al. [159], assessing the impact of SFSP (air, water with dry ice and liquid nitrogen) on the microstructure and mechanical properties of the same alloy AA5052, confirmed an average grain size of 3.6 µm under air, 1.2 µm for water mixed with dry ice and 200 nm for liquid nitrogen. The hardness followed the same trend as that of grain sizes with maximum hardness found on the liquid nitrogen FSP condition and minimum on the FSP air. Similar behaviour was also established on the UTS.

Many other studies have shown that employing cooling during FSP results in ultra-fine microstructure grain sizes (UFG) [160-161,164-169]. The UFG structures, in turn, bring significantly improved tensile strength and wear resistance [160-161]. The UFG is acknowledged as possible only in SFSP conditions since during the NFSP the plastic strain and frictional heat cause a dynamic recrystallization (DRX) mechanism which limits the grain refinement to 2-3 µm [23, 162-163]. The UFG in the SFSP nugget zone is promoted by the forced cooling [169]. Table 2.4 presents a sample of the SFSP parameters and outcomes.

Table 2.4: SFSP of aluminium alloy joints (TRS-tool rotational speed, TTS-tool traverse speed, AGS- average grain size, NS- not specified, TPD-tool pin diameter, TPS-tool pin shape, TPL-tool pin length, TSD-tool shoulder diameter, El-elongation).

Material	SFSP tool	Welding parameters	Material positioning	Comments	Ref.

AA2219-T6	Material: Standard tool steel TPS: Pinless TSD: 22 mm TPL: 3 mm	TRS: 600-1000 rpm TTS: 200 mm/min Tool tilt angle: 2.5°	AS: 5083 RS:5356	BM AGS: 17 µm YS: 107 MP Hardness: 138 HV SFSP AGS: 1.1 µm YS: 35 MPa Hardness: 100 HV	[153]
AA7075	Material: M2 steel TPS: Conical, TPD: 6-3 mm TSD: 20 mm TPL: 6 mm	Tool tilt angle: 2° Optimised: TRS: 765 rpm TTS: 31.5 mm/s Axial force: 10 kN	NA	Optimised condition: FSP-CO_2 SFSPed CO_2 AGS: 1.96 µm El: 572% UTS 180 MPa HV 115 HV	[155]
AA5052 H32	Material: H13 hardened steel TPS: Threaded TPD: 5 mm TSD: 18 mm TPL: 4 mm	Tool tilt angle: 2.5° TRS: 800-1400 rpm TTS: 50-200 mm/min Axial force: 4 NS	NA	BM AGS: 49.4 µm SFSPed AGS: 1 µm.	[156]
AA5052-H32	Material: H13 steel TPS: Threaded, TPD: 5 mm SD: 20 mm TPL:4 mm	Tool tilt angle: 2.5° TRS: 1400 rpm TTS: 50 mm/min Axial force: NS NP: 4	NA	BM AGS: 49.4 µm Hardness: 51 HV UTS: 180 MPa YS: 68 MPa El: 29.5% *SFSP (optimised)* AGS: 200 nm UTS: 279 MPa YS: 168 MPa El: 21% Hardness: 165 HV	[159]
AA6061-T6	Material: H13 steel, TPS: Threaded TPD: 4 mm TSD: 20 mm TPL:6 mm	Tool tilt angle: 2.5° TRS: 50-2000 rpm TTS: 12- 800 mm/min Axial force: NS NP: 4	NA	BM AGS: 80 µm, Hardness: 90 HV SFSP optimised AGS:	[166]

2.5 Summary

In all the work that has been performed thus far, the bulk of the focus has concerned NFSP and SFSP as enhancement techniques of single surfaces on aluminium alloys. Moreover, the common mechanical properties analysed include the tensile test, fatigue and microhardness. These properties are studied in correlation with the microstructure. Limited literature was reported where NFSP was employed as a post-weld processing technique for TIG and FSW dissimilar weld joints. However, there was no traceable literature where SFSP was employed on the TIG and FSW welded dissimilar joints. The focus of this present study will be based on using NFSP and SFSP as a post-processing technique to the dissimilar welded joints produced by TIG and FSW. The mechanical properties of the NFSP joints will be compared with those of the SFSP to determine the FSP conditions with better joint quality.

CHAPTER 3

EXPERIMENTAL SETUP AND PERFORMANCE

This chapter focuses on the description and discussions of the equipment utilised in conducting the experiments associated with the study at hand. This includes the welding techniques for fabricating the joints that were later subjected to FSP. The chosen welding techniques employed to fabricate the weldments were TIG welding and the FSW. The welding conditions applied are detailed in this chapter. The specifications regarding the experiments performed on the FSPed weldments are also discussed in detail in this chapter.

3.1 Welding setup

The following equipment was used in producing the welds:

- guillotine shear master cutting machine;
- TIG machine; and
- friction stir welding machine.

3.1.1 Guillotine shear master cutting machine

Figure 3.1.1 displays the guillotine shear master machine which is known for its versatility. The model of the machine was the TA Shear Master brand. The guillotine, as commonly referred to, is applicable for cutting alloys and sheet metals with a maximum thickness of 6 mm. For cutting purposes, the material to be cut must be marked to the desired dimensions for alignment. The plate or sheet is then positioned on the machine bed, with the markings aligned with the cutting blade. Once the plate is in position, the blade is lowered by either pressing the foot pedal or the start button on the left hand to execute the cutting. The offcut piece then falls into the provided receiver box.

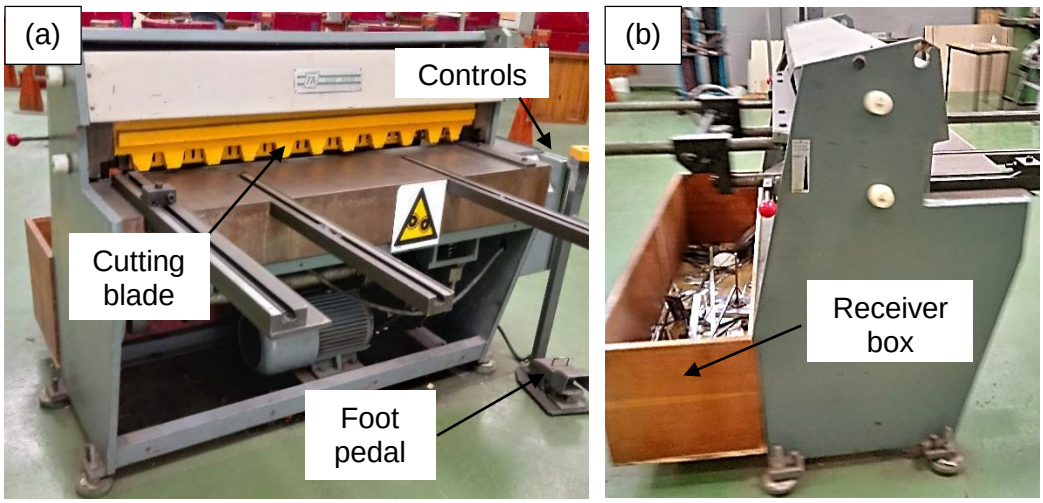

Figure 3.1.1: Guillotine shear master cutting machine: (a) front view; (b) side view.

3.1.2 TIG welding equipment

Figure 3.1.2 illustrates the JAVWELD TIG welding machine. During TIG welding, the electrode is charged with enough voltage to create an arc with the part and enough amperage to

generate the necessary heat to melt the parts that must be welded together. Once the little pool of molten metal has been created, the metal filler can be added. This is to fill up the space between the parts and to strengthen the joint. Once the rhythm is established, the filler is added and spread with the torch. The finished typical pattern of this technique resembles stacked coins. However, when joining thick plates, it is ideal to bevel the edges to a V-shaped gap between the pieces to ensured the deep penetration of the weld [170].

Figure 3.1.2: TIG welding machine.

3.1.3 Friction stir welding machine

The LAGUN FA. 1-LA conventional milling machine (see Figure 3.1.3) was successfully converted into a friction stir welding machine. The FSW machine consists of X, Y and Z bed movement controls. The FSW technique works by placing the two work pieces on the bed of the fixture. To avoid movement during the process, the mechanical clamps and bolts fasten the work pieces tightly. The head is lowered until the rotating tool pin is inserted at the centre of the two materials or required offset distance until the tool shoulder face contacts the abutting edges. The tool is made of two components, the pin (probe) and the shoulder, which is relatively large in diameter. The length of the pin is usually closely matched to the thickness of the workpiece [171]. The rotating tool pin creates frictional heat causing the material to melt plastically. Once sufficient heat has been generated, the rotating tool then traverses forward leaving a continuous joint behind until the end of the plates where the tool is unplugged leaves an exit hole.

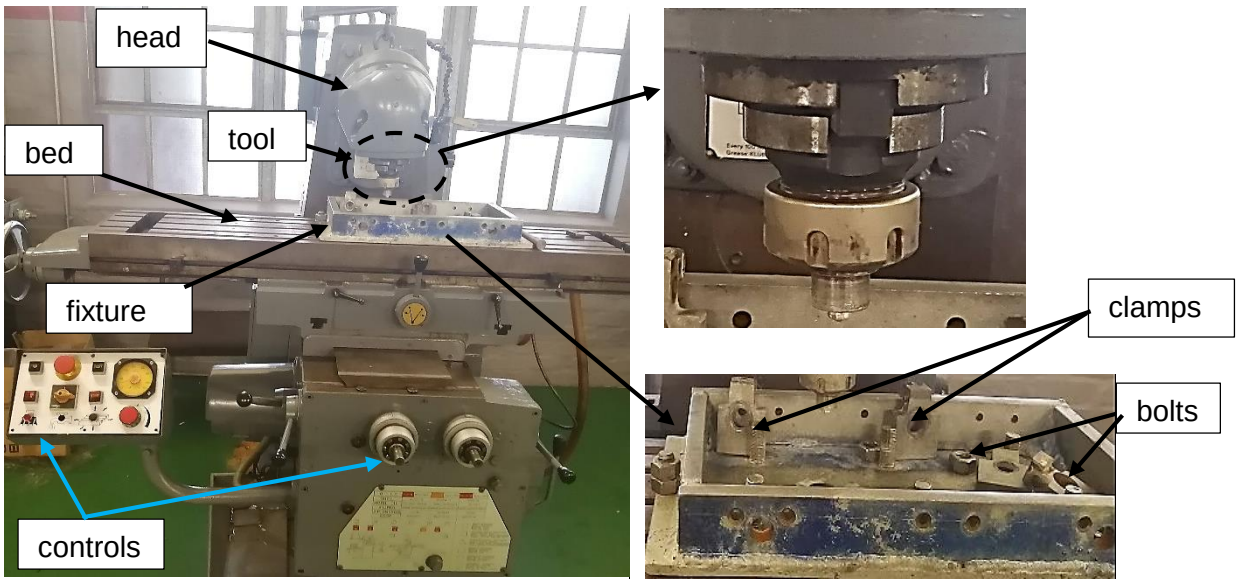

Figure 3.1.3: FSW machine.

3.2 Welding performance

AA6082-T651 and the AA8011-H14 aluminium alloy plates with a 6 mm thickness were utilised in this study. Table 3.2(a) presents the chemical composition of the materials used while Table 3.2(b) presents the mechanical properties. The plates were cut using the guillotine machine to the dimension of 250×55×6 mm. Figure 3.2(a) shows the dimensioned plate diagram. The dissimilar plates combination sample is shown in Figure 3.2(b). The dimensions were chosen based on the dimensions of the FSW fixture bed. The dissimilar aluminium alloy plates were joined using the two previously mentioned welding techniques, i.e. FSW and TIG welding techniques. The welded joints were later FSPed using the FSW machine.

Table 3.2: (a) Chemical position of the materials wt% [172].

	Mg	Zn	Ti	Cr	Si	Mn	Fe	Ni	Cu	Al
AA6082-T651	1.229	0.544	0.040	0.000	1.211	0.330	0.679	0.095	0.028	Bal
AA8011-H14	0.549	0.622	0.027	0.028	0.375	0.758	1.332	0.105	0.051	Bal

Table 3.2: (b) Mechanical properties of the materials [173].

	Tensile Strength (MPa)	Yield Strength (MPa)	Elongation (%)	Hardness
AA8011	94.1	76	40.17	33.5 HV
AA6082-T651	308	270	25.42	89.6 HV

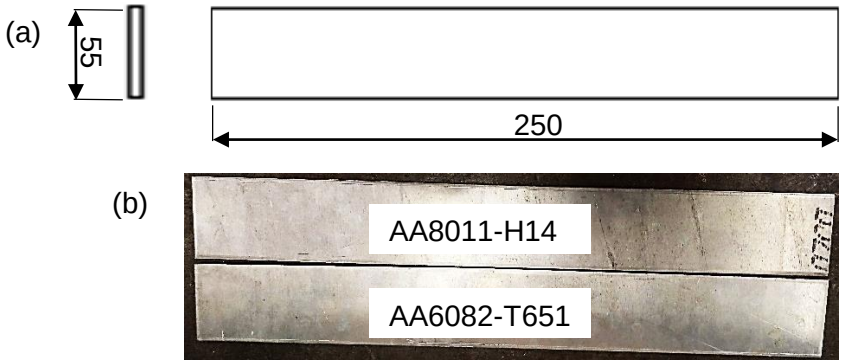

Figure 3.2: (a) Plate with dimensions in mm; (b) dissimilar combination sample.

3.2.1 TIG welding process

The TIG welding technique was used to fabricate a dissimilar joint of the AA8011-H14 and AA6082-T651 plates. Prior to the application of TIG welding, the edges of the plates were prepared such that they had dissimilar combinations for a 60° double V-shaped groove. The double V-shaped groove is advisable for thick metals where welding can be performed on both sides as it uses less filler material than a single wide V-shaped joint. Other benefits of using a double V-shaped groove are to balance in the welding residual stresses and to minimise weld distortion [170, 174]. Argon gas was used as a shielding gas, selected because of the benefits it possesses: it is a noble gas, it keeps welds clean and pure, it is not flammable nor corrosive and it prevents oxidation [174]. Prior to TIG welding, acetone was used to clean the dirt and contamination on the surfaces to be welded. The steel wire brush removed the oxide layer.

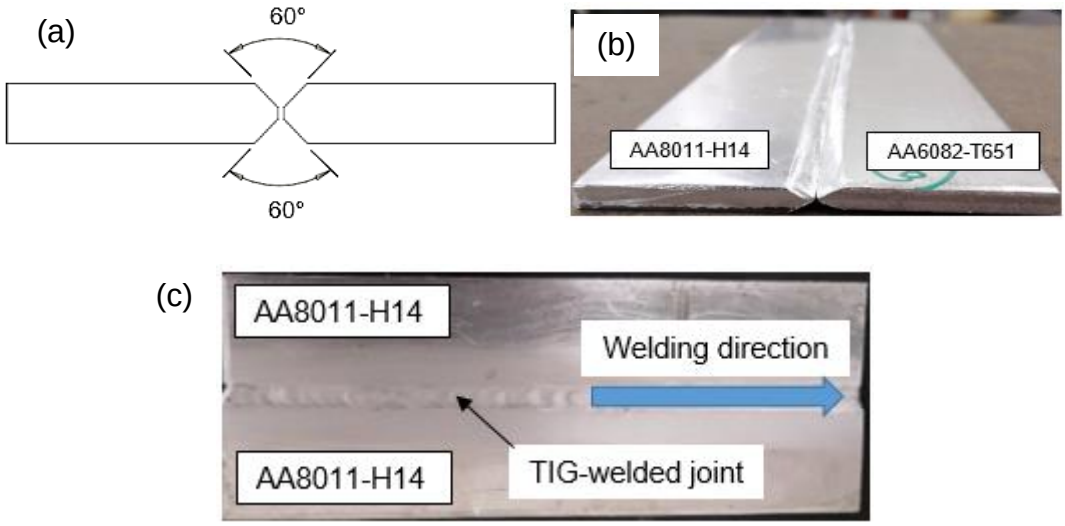

Figure 3.2.1: (a) Double V-shaped groove diagram; (b) plates configuration; (c) sample of a TIG-welded joint.

The ER4043 wire filler with a 2.4 mm diameter was used to fabricate the dissimilar joint. This filler was chosen based on previous studies wherein comparison with other fillers produced more sound results [174]. Table 3.2.1(a) shows the chemical composition of the wire filler. The welding parameters are presented in Table 3.2.1(b). Figure 3.2.1(c) shows a sample of a TIG-welded point formed. A total of five TIG-welded plate sets were produced. One set was kept for comparison while four sets were later friction stir processed under different conditions considering the material positioning.

Table 3.2.1(a): Wire filler chemical composition [175].

	Mg	Zn	Ti	Si	Fe	Cu	Al
ER4043	0.05	0.10	0.02	5.3	0.8	0.025	Bal

Table 3.2.1(b): TIG welding parameters.

Voltage (V)	Shielding gas	Current (Amps)	Gas flowrate (L/min)	welding speed (mm/min)
35	Argon	115	25	40

3.2.2 Friction stir welding

Figure 3.2.2(a) shows the FSW tool used in this study. The square pin with flute tool dimensions are presented in Table 3.2.2. The pin was made of high-speed steel. Friction stir welding was performed on the two dissimilar alloy plates. The respective tool was a fixed type due to the materials used having a uniform thickness. The tool pin was positioned in the centre of the two materials, with no offset distance used. A single-pass welding procedure fabricated the joints. No special treatment on the plate surfaces was carried out before welding. During the application of FSW, the two dissimilar aluminium alloy plates were clamped together tightly on the FSW fixture. The process parameters were predetermined using the Taguchi L9 method. The optimised process parameters are presented in Table 3.2.2. Material positioning was considered during the FSW process. Figure 3.2.2(b) presents the FSW with AA6082-T651 positioned on the retreating side of the tool and AA8011-H14 on the advancing side of the tool. Figure 3.2.2(c) shows FSW with AA6082-T651 positioned on the advancing side of the tool and AA8011-H14 positioned on the retreating side of the tool. The samples of the FSW plates are depicted in Figure 3.2.2(d-e). A total of six FSWed plate sets were produced. Two sets were retained for comparison while the four sets were later friction stir processed under different conditions taking the material positioning into consideration.

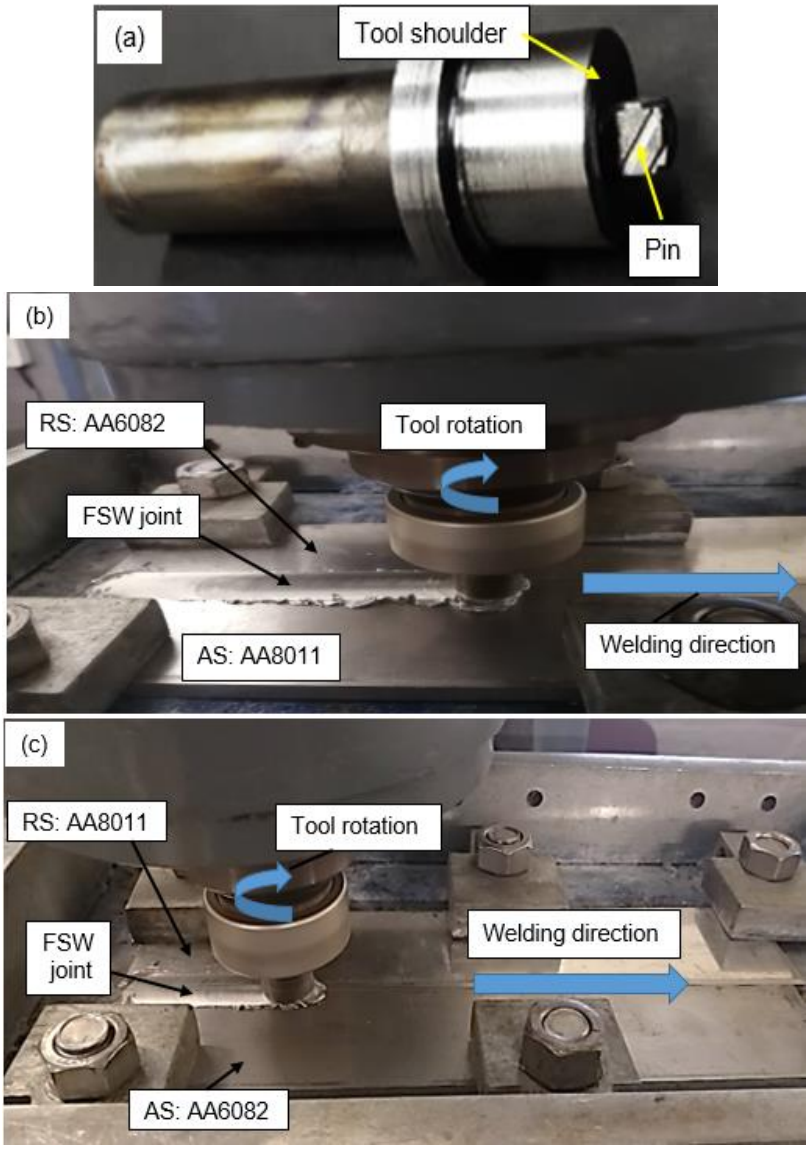

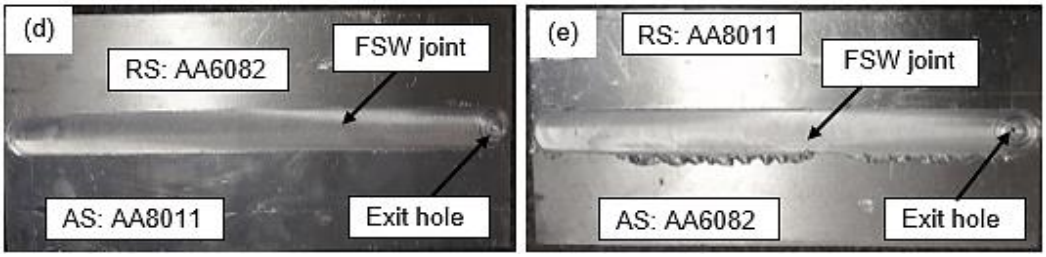

Figure 3.2.2: (a) FSW pin used; (b) FSW AA8011-AS; (c) FSW AA6082-AS; (d) FSW AA8011-AS joint; (e) FSW AA6082-AS joint.

Table 3.2.2: FSW/FSP welding parameters.

Parameter	Condition
Tool shoulder diameter	20 mm
Tool probe diameter	7 mm
Tool pin length	5.8 mm
Rotating speed	1200 rpm
Traverse speed	55 mm/min
Dwell time	20 s
Tool plunge depth	5.8 mm
Axial force	4 kN
Tool tilt	2°

3.2.3 Friction stir processing

Friction stir processing under normal conditions (NFSP) was performed on the friction stir welded dissimilar AA8011/AA6082 joints and on the TIG-welded dissimilar AA8011/AA6082 joints using the same machine as for FSW. The FSW parameters and tool were also used for FSP. Similar studies in which the same tool used for FSW was used for FSP were reported in the literature [176-178]. The FSW dissimilar joints produced with the AA6082 alloy on the advancing side were FSPed using the same material positioning. Similarly, the FSW dissimilar joints produced with AA8011 alloy on the advancing side were FSPed utilising the same material positioning. Figure 3.2.3(a-b) depict the setup scenarios for the FSP on the FSW dissimilar aluminium alloy joints. The NFSP-FSW dissimilar aluminium alloy joints are presented in Figure 3.2.3(c-d). A similar procedure was followed for the TIG-welded joints. The setup scenario for the FSP of the TIG-welded joints is depicted in Figure 3.2.3(e-f). The FSP-TIG-welded dissimilar aluminium alloy joints are illustrated in Figure 3.2.3(g-h).

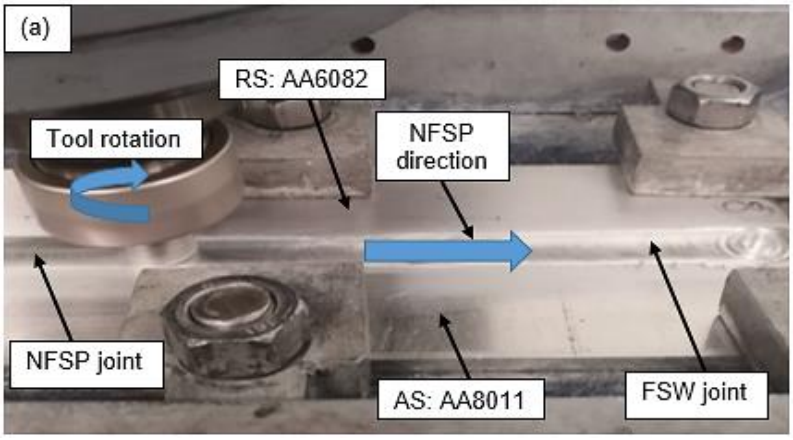

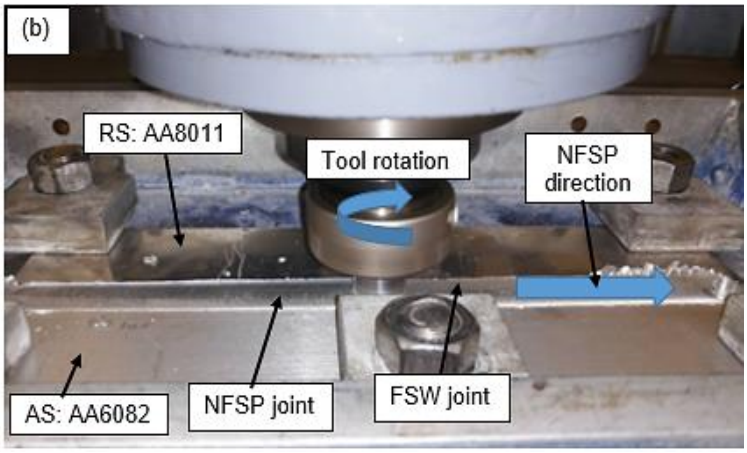
(b)
RS: AA8011
Tool rotation
NFSP direction
AS: AA6082
NFSP joint
FSW joint

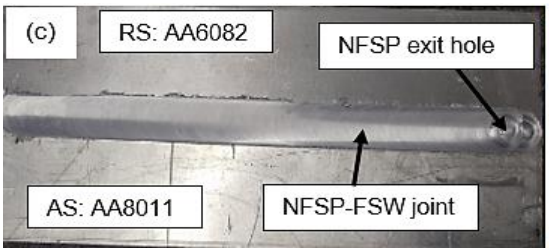
(c)
RS: AA6082
NFSP exit hole
AS: AA8011
NFSP-FSW joint

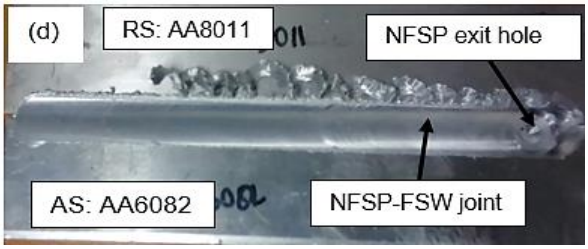
(d)
RS: AA8011
NFSP exit hole
AS: AA6082
NFSP-FSW joint

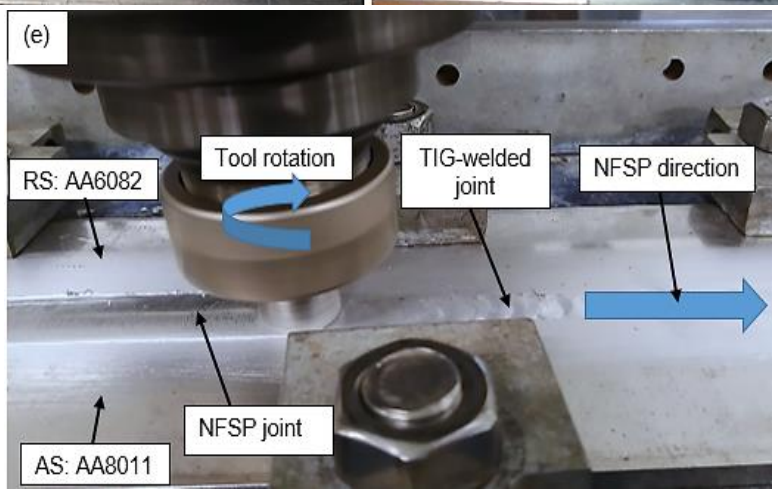
(e)
RS: AA6082
Tool rotation
TIG-welded joint
NFSP direction
NFSP joint
AS: AA8011

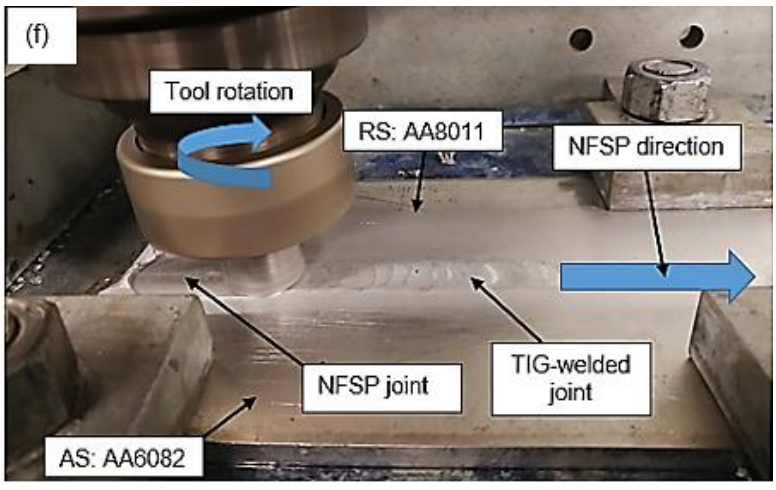
(f)
Tool rotation
RS: AA8011
NFSP direction
NFSP joint
TIG-welded joint
AS: AA6082

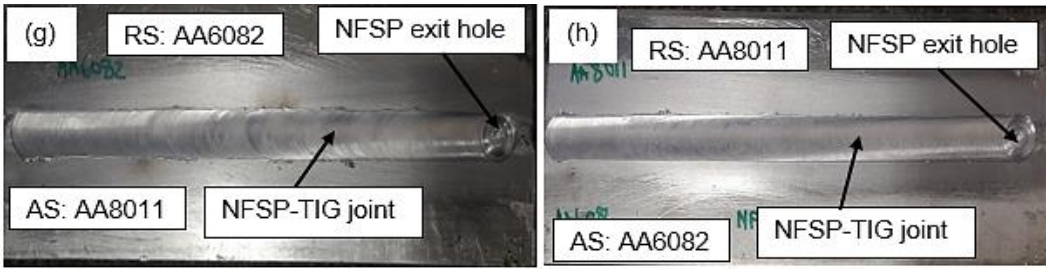

Figure 3.2.3: (a) NFSP of the FSW joint (AA8011-AS); (b) NFSP of the FSW joint (AA6082-AS); (c) NFSP-FSW joint (AA8011-AS); (d) NFSP-FSW joint (AA6082-AS); (e) NFSP of the TIG-welded joint (AA8011-AS); (f) NFSP of the TIG-welded joint (AA6082-AS); (g) NFSP-TIG joint (AA8011-AS); (h) NFSP-TIG joint (AA6082-AS).

3.2.4 Submerged friction stir processing

Submerged friction stir processing was performed on the friction stir welded and TIG-welded joints using the FSW machine. The submerged fluid was tap water at room temperature. The water inside the SFSP fixture was maintained at the head of 45 mm for the entire process. The parameters employed to perform the SFSP were the same as those used for NFSP, except the tool traverse speed was reduced to 40 mm/min and the tool rotation to 900 rpm. The changes were due to the pre-determination using the Taguchi method. The SFSP was executed taking into consideration the material positioning as previously explained for the NFSP process. Figure 3.2.4(a-b) shows the SFSP of the FSW joints. The produced SFSP-FSW dissimilar aluminium alloy joints are presented in Figure 3.2.4(c-d). The SFSP of the TIG-welded joints are depicted in Figure 3.2.4(e-f) and the produced SFSP-TIG dissimilar aluminium alloy joints are shown in Figure 3.2.4(g-h). A total of four SFSPed plates were produced, two for the SFSP-FSW and the other two for the SFSP-TIG dissimilar aluminium alloy joints.

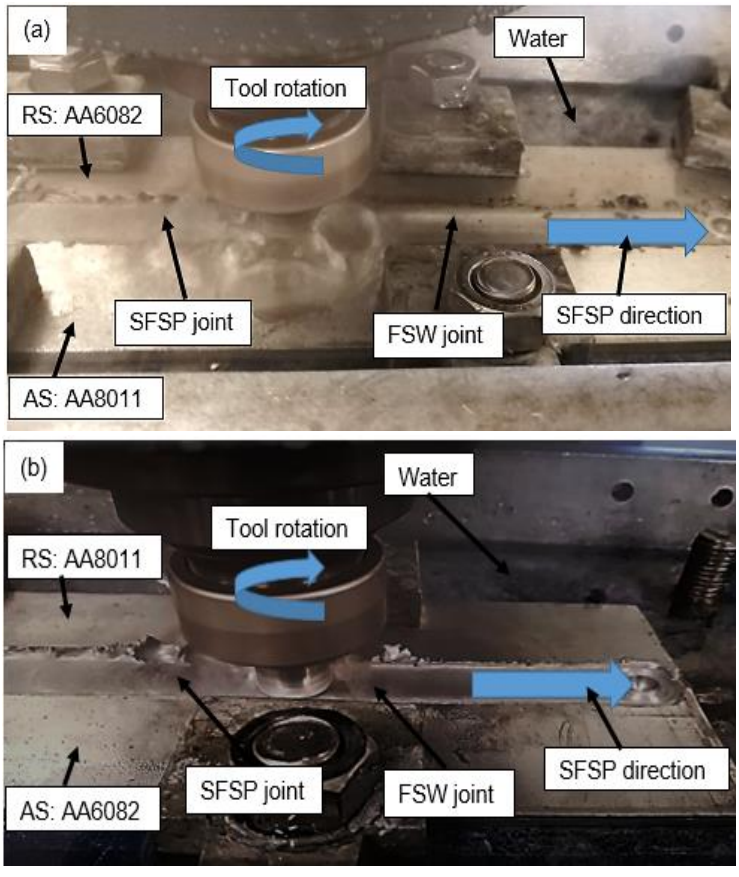

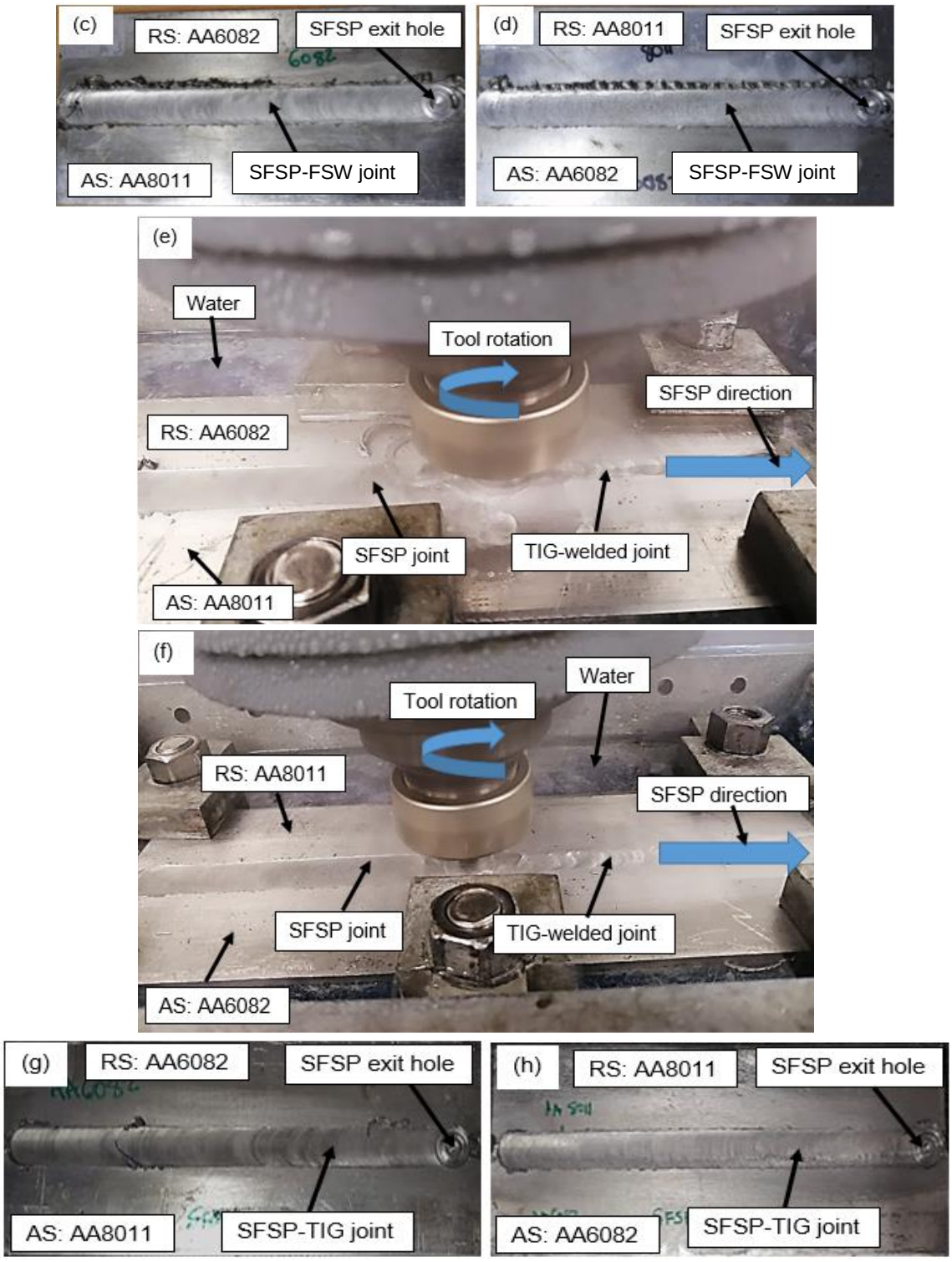

Figure 3.3.4: (a) SFSP of the FSW joint (AA8011 advancing); (b) SFSP of the FSW joint (AA6082 advancing); (c) SFSP-FSW joint (AA8011 advancing); (d) SFSP-FSW joint (AA6082 advancing); (e) SFSP of the TIG-welded joint (AA8011 advancing); (f) SFSP of the TIG-welded joint (AA6082 advancing); (g) SFSP-TIG joint (AA8011 advancing); (h) SFSP-TIG joint (AA6082 advancing).

3.3 Weldments analysis preparation

The equipment and techniques for analysing the weld joints obtained through the steps explained under section 3.2 are listed below:

- 5-Axis Waterjet;
- Struers Labopress-3 mounting press machine; and

- Struers LaboPol-5 polishing machine.

3.3.1 5-Axis Waterjet

Waterjet cutting is the recent cold cutting engineering method used for cutting objects, making use of energy at high speed, high density and ultra-high water pressure. Figure 3.3.1 demonstrated the Mach 3 7320b 5-Axis Waterjet cutting machine. During waterjet cutting, the high-pressure waterjet separates the work pieces from each other. However, an abrasive agent can also be used, depending on the application. The use of an abrasive agent for soft material is not required. There is no heat generation during the waterjet cutting, which therefore means no tempering of mechanical properties of the object or material [179]. Additionally, the end results consist of a high level of accuracy, stability and cleanliness. Waterjet cutting is suitable for hard materials and various soft materials like wood, plastics, rubber and aluminium. Applications of waterjet include cutting of roof materials, dashboards, aircraft fuselages and automobile bumpers. The produced welded plates were not polished or grinded prior and post waterjet to preserve the properties of the joints. It should be noted that the waterjet cutting of the specimens was out-sourced to Waterjet Cape Town.

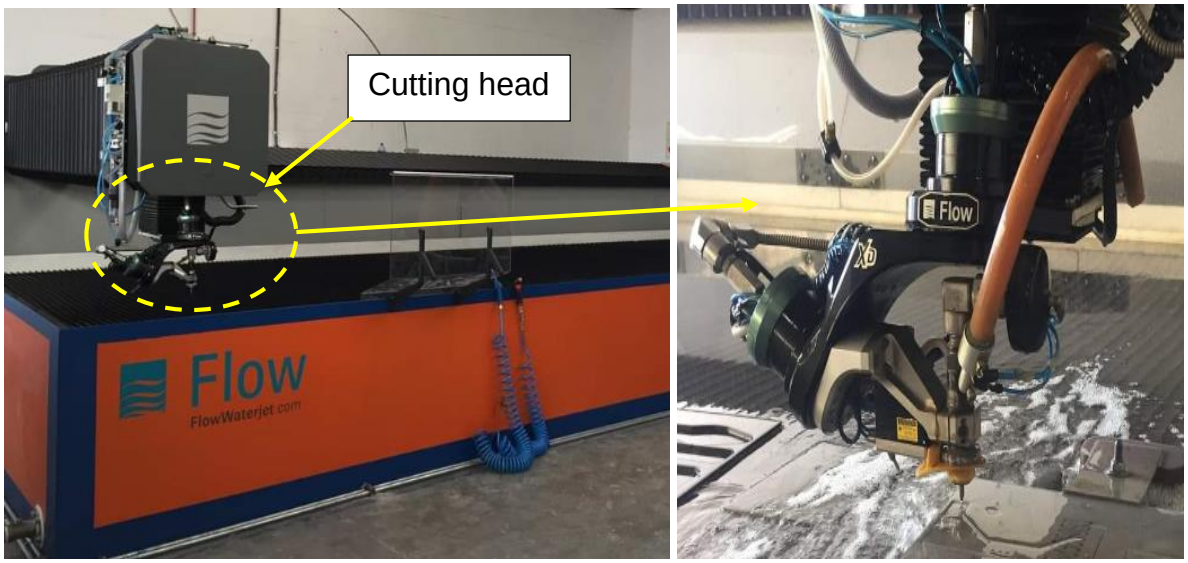

Figure 3.3.1: 5-Axis Waterjet cutting machine.

3.3.2 Struers Labopress-3 mounting press machine

Figure 3.3.2 shows a Struers Labopress-3 machine to mount a specimen in a hard epoxy resin. The mounting process works by positioning the specimen on the ram, then lowering the ram to a designated depth. The selected resin is then poured with a funnel on top of the specimen until the exposed inside cylinder depth is filled, followed by closing the ram with the lid. Once the lid is secured, the parameters such as force, heating time, temperature and cooling time are set. The process is executed automatically upon pressing the start button.

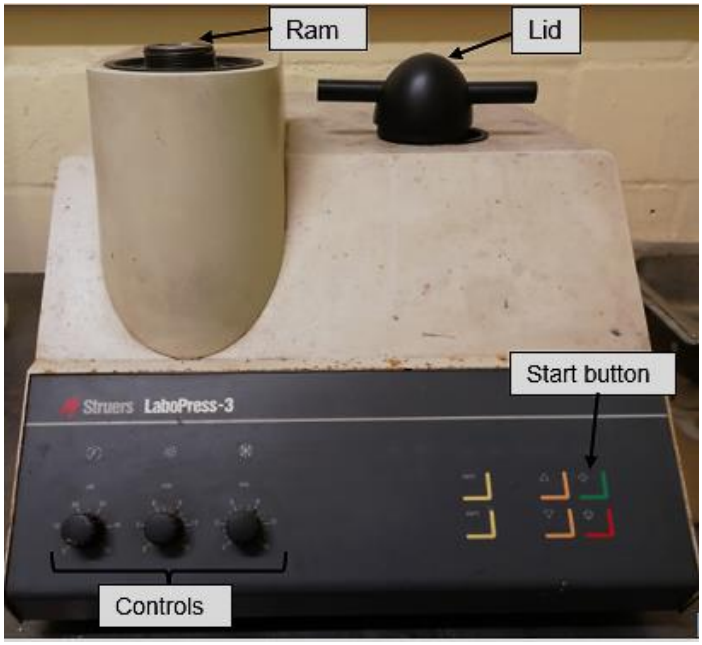

Figure 3.3.2: Mounting press machine.

3.3.3 Struers LaboPol-5 polishing machine

The Struers Labopol-5 depicted in Figure 3.3.3(a) is a polishing machine that grinds and polishes any kind of metals. The machine works by mounting a selected grinding or polishing disc onto the turntable, and then a suitable turntable rotational speed (ranging between 50-500 rpm) is chosen. The process resumes with the start button. During the process, to achieve a required surface finish, different discs, as shown in Figure 3.3.3(b), are utilised with suitable polishing agents, as shown in Figure 3.3.3(c), depending on the material being prepared. In the case of aluminium specimens, P230 and P1200 grit is used with normal tap water or distilled water for lubrication while the Aka-Moran, Aka-Daran and Aka-Napal disks are used with the blue Aka-Lube and the Aka-Chemal disc is used with water. For the final polishing step, ethanol is used to rinse the specimen prior to drying.

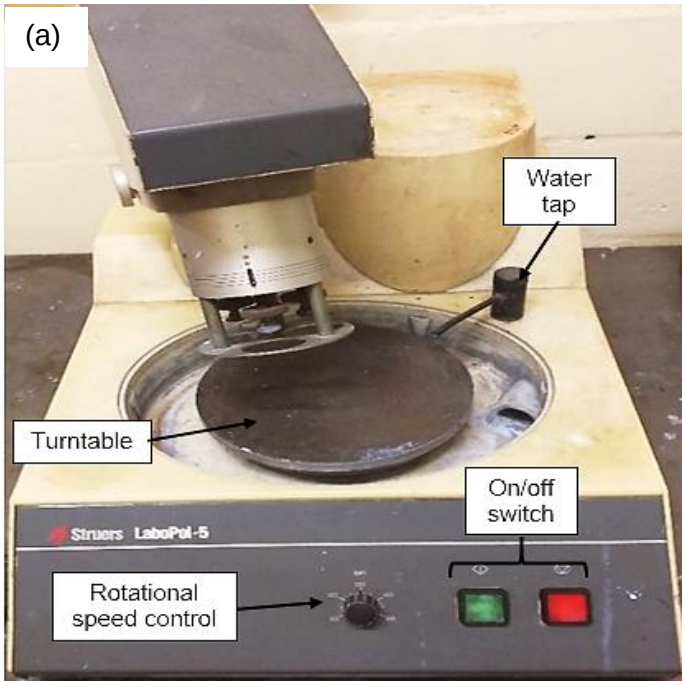

Figure 3.3.3: (a) Polishing machine; (b) polishing discs; (c) polishing agents.

3.4 Performance of specimen preparation

This section details the preparation of the specimens for all the tests conducted, namely tensile, bending, microstructural analysis, hardness, chemical analysis and X-ray diffraction analysis test.

3.4.1 Tensile test specimen preparation

The specimen design and geometry for the tensile specimen were abducted from the ASTM E8 standard. Figure 3.4.1 presents the dimensioned specimen drawing. SolidWorks design software was used to populate the drawing. The waterjet cutting machine was used to cut the specimens.

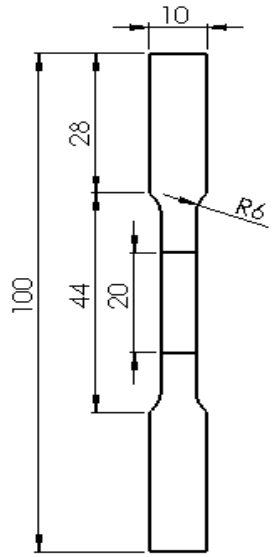

Figure 3.4.1: Tensile test specimen with dimensions in mm.

3.4.2 Bending test specimen preparations

The ASTM E290 standard was used for the specimen design and geometry. Figure 3.4.2 illustrates the SolidWorks populated dimensioned bending specimen. It should be noted that the specimen dimensions are in mm. The cutting of the bending was by the waterjet cutting machine.

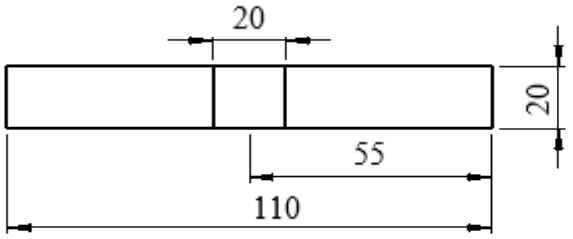

Figure 3.4.2: Bending test specimen with dimensions in mm.

3.4.3 Microstructural analysis specimen preparation

The microstructural analysis specimen (see Figure 3.4.3) was drawn using the SolidWorks design software. The designed specimens were cut using the waterjet cutting machine. The cut specimens were mounted in MultiFast phenolic hot mounting resin using Struers Labopress-3 machine at 150° mounting temperature. The mounted specimens were prepared for microstructural analysis using the Struers Labopol-5. The polishing preparation was as detailed in section 3.3.3. The specimens were removed from the etchant and immediately rinsed with water and methanol, followed by drying with a hot hairdryer. Two etching reagents were used – Weck's and modified Keller's reagents. Weck's reagent composition included 1 g of sodium hydroxide (NaOH), 4 g of potassium permanganate ($KMnO_4$) and 100 ml of distilled water. The modified Keller's reagent composition included 10 ml of nitric acid (HNO_3), 1.5 hydrochloric acid (Hcl), 1 ml of hydrofluoric acid (HF) and 87.5 ml of distilled water. The Weck's reagent was used as a pre-etch where the specimen was immersed for 13 seconds, then rinsed using distilled water and dried with methanol and hairdryer. The modified Keller's was applied after drying the Weck's etched specimen and immersed for 25 seconds. The same

was applied in all the microstructural analysis specimens. After the etching, the specimens then ready for computer analysis.

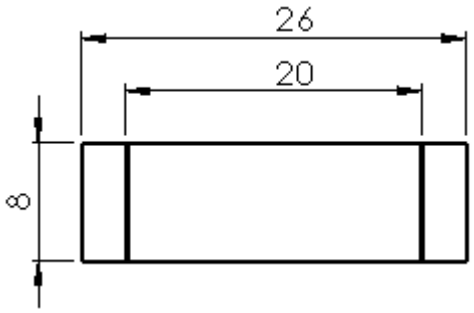

Figure 3.4.3: Microstructure test specimen with dimensions in mm**.**

3.4.4 Hardness test specimens

The specimen dimensions and geometry for microstructural analysis was also applied for hardness testing. Duplicates of the specimen (see Figure 3.4.3) were made, the second one set for hardness testing. The same preparation for the microstructural analysis specimens was also undergone for the hardness test specimens.

3.4.5 X-ray diffraction test specimens

Figure 3.4.6 presents the SolidWorks dimensioned drawing of the X-ray diffraction (XRD) specimen. The specimen geometry and design are based on the ASTM D5380. The waterjet cutting machine cut the XRD specimen.

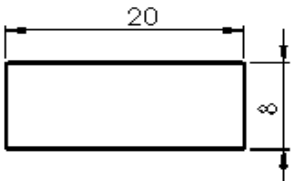

Figure 3.4.6: XRD specimen with dimensions in mm.

3.4.6 Chemical analysis specimens

The specimen dimensions and geometry used for the chemical analysis tests were the same as those of the XRD specimens (see Figure 3.4.6).

3.5 List of tests performed

Analysis was performed on the FSW, TIG-welded and friction stir processed joints under various conditions with the aim of creating a clear comparison. The tests performed were as follows:

- XRD tests
- Chemical analysis
- Microstructural analysis
- Bending tests
- Tensile tests
- Hardness tests
- SEM analysis

3.6 Mechanical tests

A different set of specimens were cut out from the TIG and FSW plates, as well as on the friction stir processed TIG and FSW plates. The prepared specimens were for tensile tests, bending tests, hardness tests, microstructural analysis, XRD and chemical analysis. All the specimens were extracted in three regions of the plate: the start, the middle and the end of the plate. A total of three specimens for each test were prepared. Figure 3.6 shows the specimen positioning sample where 'S' stands for start, 'M' stands for middle and 'E' stands for end.

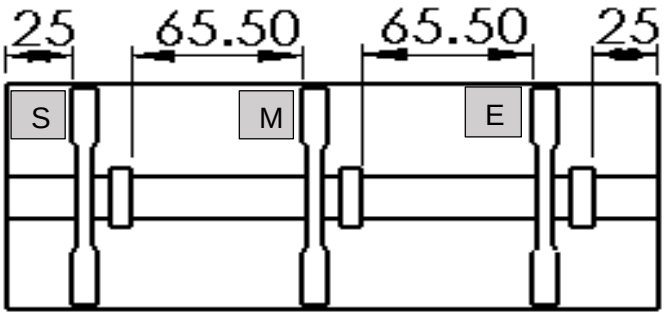

Figure 3.6: Specimen positioning sample.

3.6.1 Tensile tests

The uniaxial tensile testing was performed to analyse the tensile properties – ultimate tensile strength, yield strength, percentage elongation and the fracture strain – for all the welded and friction stir processed joints. Figure 3.6.1(a) shows the computer-operated Hounsfield 25K type tensile testing machine used for tensile testing. Flat clamping jaws were used to mount the tensile specimens (see Figure 3.6.1[b]). The dog bone-shaped specimens were utilised. The tensile test parameters are presented in Table 3.6.1. The ASTM E8 standard for tension testing of metallic materials was applied in this study for tensile testing. Table 3.6.1 presents the tensile test parameters.

Table 3.6.1: Tensile test parameters.

Speed (mm/min)	Extension range (mm)	Load range (kN)	Load cell (kN)
1	0-15	0-10	25

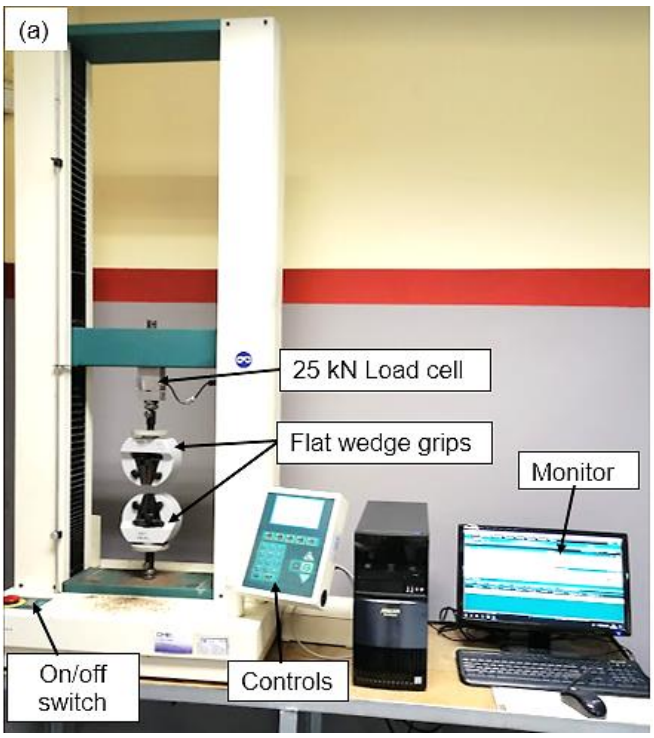

Figure 3.6.1(a): Hounsfield tensile test machine.

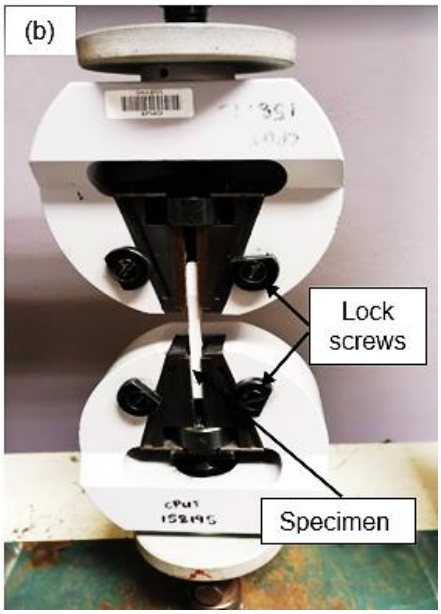

Figure 3.6.1(b): Tensile testing flat jaws.

Preceding installation of the specimens to the machine, specimen dimensions were measured and recorded (thickness and gauge length) to determine the engineering stress and engineering strain. The specimen was fit into the jaws for gripping. The screws were tightened to avoid slippage during the test. Horizon software logged the data – the applied tensile load and extension – which was later used to determine stress and strain. The yield strength, ultimate tensile strength, fracture strain and percentage elongation were determined. The graph of stress versus strain was generated.

The following formula was used to determine the ultimate tensile stress:

$$\sigma = \frac{F}{A} \quad (1)$$

Where σ is the ultimate tensile stress; F is the maximum force; and A is the cross-sectional area.

The equation to determine % elongation is:

$$\%E = \frac{Final\ Length - Original\ Length}{original\ Length} \times 100 \quad (2)$$

3.6.2 Bending tests

Bending testing is sometimes referred to as *flex* or *flexural testing.* This test was conducted to measure the flexural strength of all dissimilar aluminium alloy welded joints. A bending test was performed on the bending specimens using the Hounsfield testing machine with a 3-point bend fixture (illustrated in Figure 3.6.2[a]). The bending test parameters were the same as the those for tensile testing, and data was logged by the same procedure as for tensile testing.

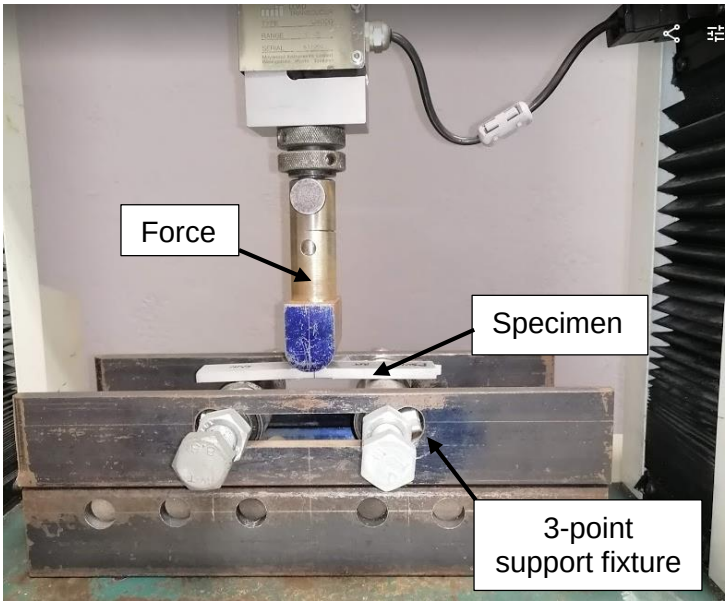

Figure 3.6.2(a): Bending test setup and apparatus.

The first step in performing the bending test was to measure the specimen to verify dimensions. The tests were performed one specimen at a time. The specimen was flat mounted against the rolling supports; the centre mark line aligned the specimen with the loading pin centre. The loading pin was then lowered until it was in contact with the specimen's top surface. The ASTM E290 standard embedded on the Horizon software program was selected, giving a screen where the specimen dimensions were entered. Thereafter the machine was zeroed before the commencement of the test. The test was run until the specimen broke or fractured. The data was logged automatically from the beginning until the failure of the specimen.

The formula used to determine the maximum stress was as follows:

$$\sigma = \frac{3FL}{2bd^2} \quad (4)$$

Where F is the force; b is the width of the specimen; L is the length; and d is the thickness. Refer to Figure 3.6.2(b) for the schematic diagram for the bending test.

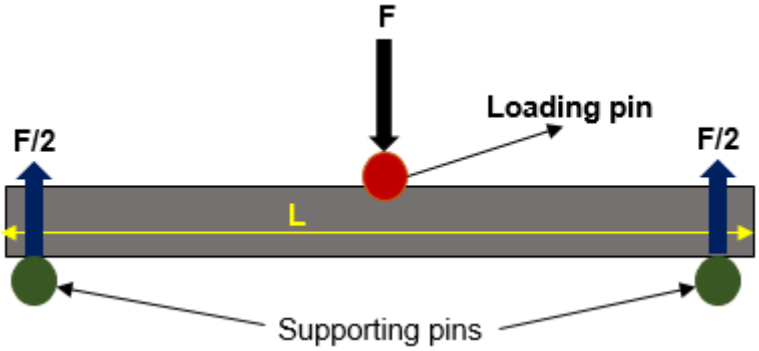

Figure 3.6.2(b): Schematic diagram of a bending test.

3.6.3 Hardness tests

The hardness tests to determine the Vicker's hardness of the produced joints were performed using the InnovaTest Falcon 500 hardness testing machine (see Figure 3.6.3). The hardness testing was executed following the ASTM E384-11 standard. The 10× and the 20× objectives were used for specimen focusing during setup. The load of 0.5 kg and an interval of 1 mm were applied from the centre of the specimen to either side (retreating and advancing). In performing the hardness test, the first step was to open the falcon IMPRESSIONS software programme on the screen, followed by positioning the specimen at the centre of the machine bed. Then was the use of the objectives to focus, then the type of pattern in this study case (a line pattern) was used, then the number of points (indents) in each line, the distance between the points and the distance between the lines were all set. The autofocus button was pressed, then the software program took a snap of the specimens automatically and the process resumed once the start button was selected. The obtained Vicker's hardness data was populated into a PDF document at the end, was saved directly to the memory stick and desktop folder. The specimen snapshots were later used for macrostructural analysis purposes.

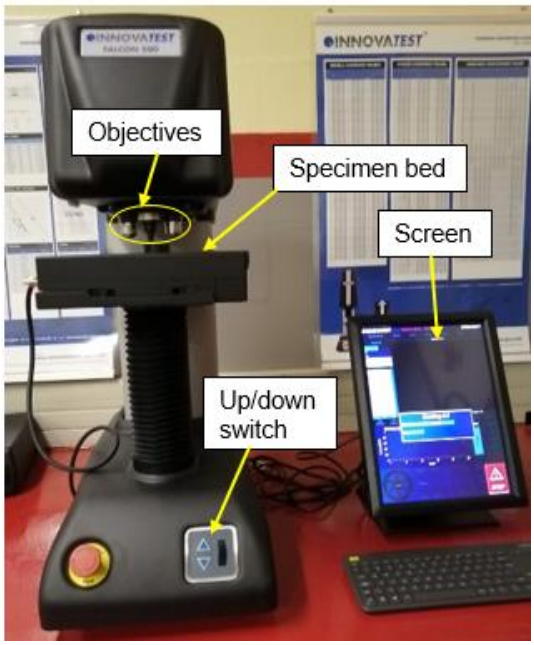

Figure 3.6.3: Hardness test machine.

3.6.4 Microstructural analysis

Microstructure analysis was performed to analyse the grain sizes of the produced weld joints. The Motic AE2000 metallurgical microscope (see Figure 3.6.4) allowed for obtaining the microstructural images for analysis. The process of obtaining the desired microstructure grain images was initiated by opening the Moticam software after the specimen was positioned on the specimen bed. The specimen was then focused using the zoom in and out control switch; then the scale on the software was set to 100 µm; then the objective indicator or stamp was set so that it was visible on the image for further analysis purposes. The selection of the preferred image was then made from the 5× which was used for larger imaging showing different microstructural zones desired; 10×, 20×, 50× and 100× were also used. It should be noted that the bigger the objective size, the more it gives zoomed-in imaging. Once the desired images were obtained, they were collected on a memory stick from the desktop folder that the software sends to as each image was taken. The ASTM E112-13 standard for linear intercept method through the use of ImageJ software then determined the grain sizes and grain distribution curves.

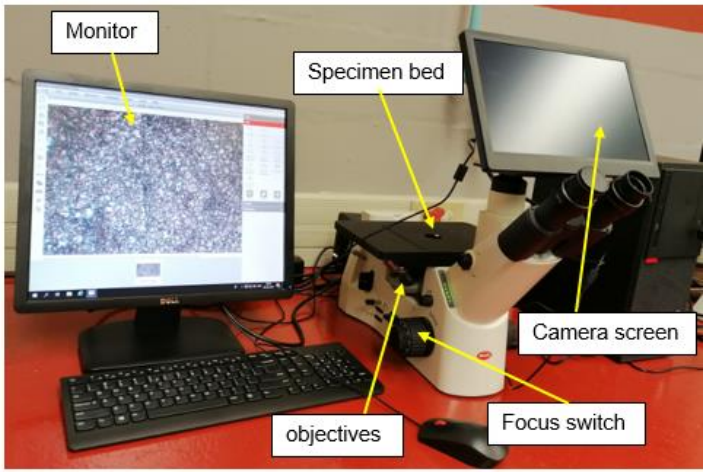

Figure 3.6.4: Microstructure apparatus.

3.6.5 XRD analysis

The XRD analysis was outsourced to iThemba Laboratory Solutions. During the XRD analysis, measurements were performed using a multi-purpose X-ray diffractometer D8-Advance from Bruker, operated in a continuous θ-θ scan in locked coupled mode with Cu-K_α radiation. During the analysis, the sample was mounted in the centre of the sample holder on a glass slide and levelled up to the correct height. The measurements ran within a range in 2θ defined by the user with a typical step size of 0.034°. A position-sensitive detector, Lyn-Eye, was used to record diffraction data at a typical speed of 0.5 sec/step, equivalent to an effective time of 92 sec/step for a scintillation counter. The data was background subtracted so that phase analysis was carried out for the diffraction patterns with zero background after the selection of a set of possible elements from the periodic table. Phases were identified from the match of the calculated peaks with the measured ones until all phases were identified within the limits of the resolution of the results.

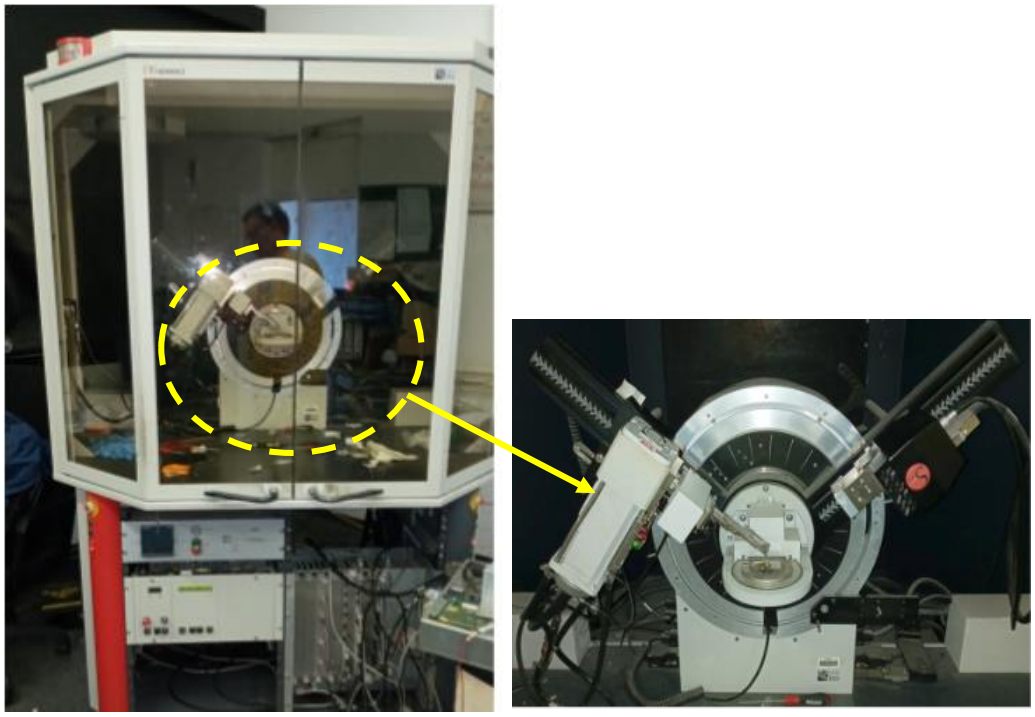

Figure 3.6.5: X-ray diffractometer D8-Advance machine.

3.6.6 Chemical analysis

Chemical analysis was undertaken with the chemical composition of the joints produced in the study so as to identify the phase on the XRD analysis. Figure 3.6.6 shows the Belec Compact Spectrometer HLC machine for detecting the chemical composition of the specimens produced. Before the chemical measuring process, the 99.99 high purity Argon gas was opened and then the machine switched on. The specimen was positioned on a flat laboratory table. The process continued by switching on the spark button; the machine screen display was also switched on, and then the Belec WIN 21 software situated on the desktop of the machine built-in computer was switched on. Once the software was opened, the aluminium test option was chosen and the correct description of the specimen being tested was inserted. The process was then ready to be executed, which occurred by pressing the face of the Belec probe against the specimen, applying adequate pressure to ensure no air was penetrating between the specimen and the probe. Then the start button on the probe was pushed, the probe sparked on the workpiece for a few seconds. The probe was kept in position until the screen flashed yellow indicating the measurement was completed. The yellow flashing was accompanied by the display of results in a table form, as can be seen in Figure 3.6.6. The projected table of results was saved onto the memory drive.

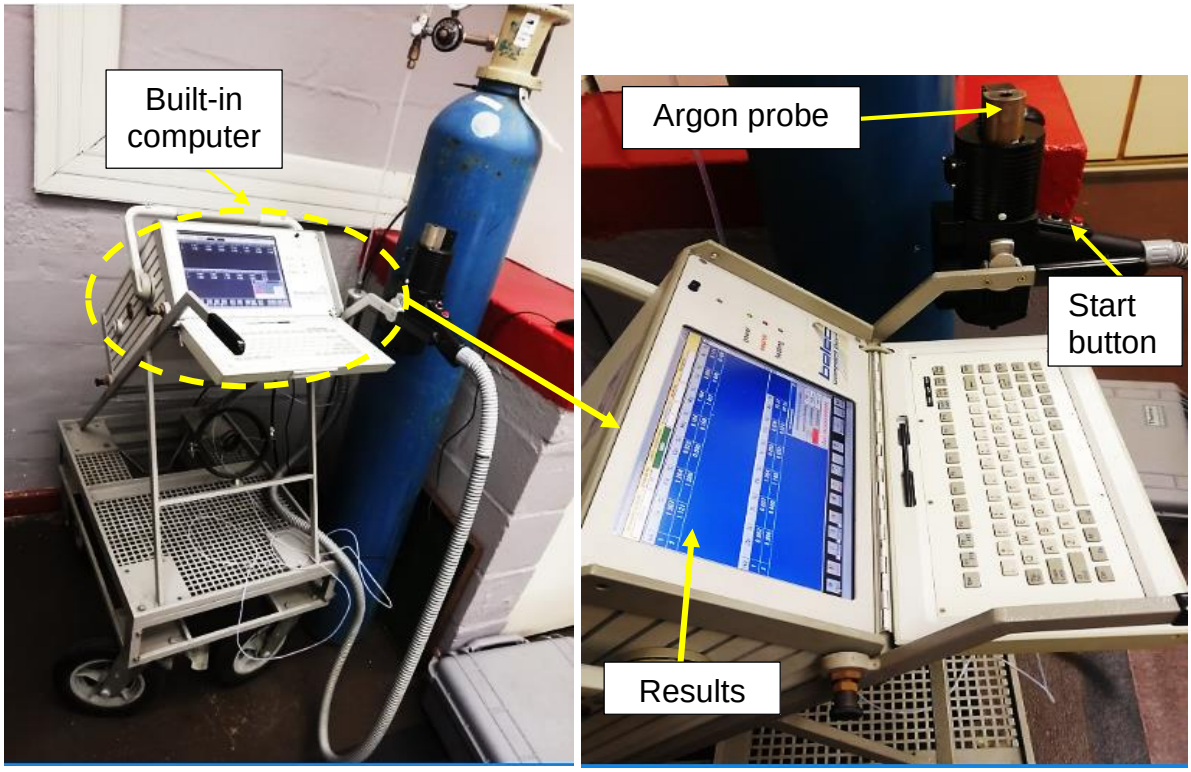

Figure 3.6.6: Belec compact spectrometer machine.

CHAPTER FOUR

RESULTS AND DISCUSSION

This chapter presents the results and discussions obtained from the tests conducted. The data obtained from the NFSP-TIG dissimilar aluminium alloy joints is studied comparatively to the SFSP-SFSP ones. Likewise, the NFSP-FSWed dissimilar joints are compared to the SFSP-FSWed dissimilar joints. The unprocessed FSW and TIG-welded data is also provided for better understanding and clarity.

4.1 FSP of TIG-welded points

This section presents the detailed results and discussions of the TIG-welded, NFSP-TIG-welded joints and SFSP-TIG-welded joints. It should be noted that the AA6082-AS refers to the AA6082-AA8011 joint and the AA8011-AS refers to the AA8011-AA6082 joint.

4.1.1 X-ray diffraction analysis and chemical composition of the joints

X-ray diffraction analysis was performed to analyse the phases formed during welding and the friction stir processing of the joints. To detect new phases formed, the base materials AA6082 and AA8011 (presented in Figure 4.1.1 [a] and [b] respectively) were examined for reference purposes. The red lines in all the patterns represent the aluminium phase. The detected phases for AA6082 included the $Al_9Fe_{0.7}Mn_{2.3}Si$ and Mg_2Si. The identified phases correlate with the findings reported in the literature [180-181]. The AA6082 alloy is known for being precipitate strengthened. The precipitate referred to is the Mg_2Si sometimes referred to as the β particles. These particles are commonly acknowledged as sensitive to high temperatures exceeding 200°C; the exposure beyond such temperatures weakens the properties of the alloy [183]. The $Mn_{1.2}Fe$ and Al_8Fe_2Si were identified on the AA8011 alloy XRD patterns. The Al_8Fe_2Si, also known as α particles of the said alloy, are responsible for the good ductility of the alloy [184].

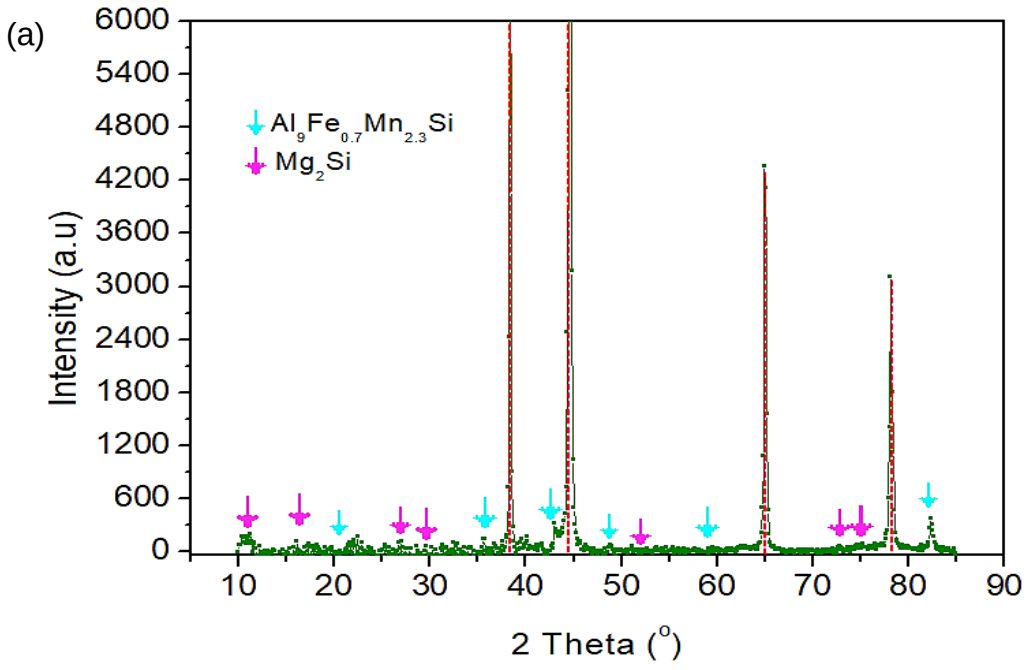

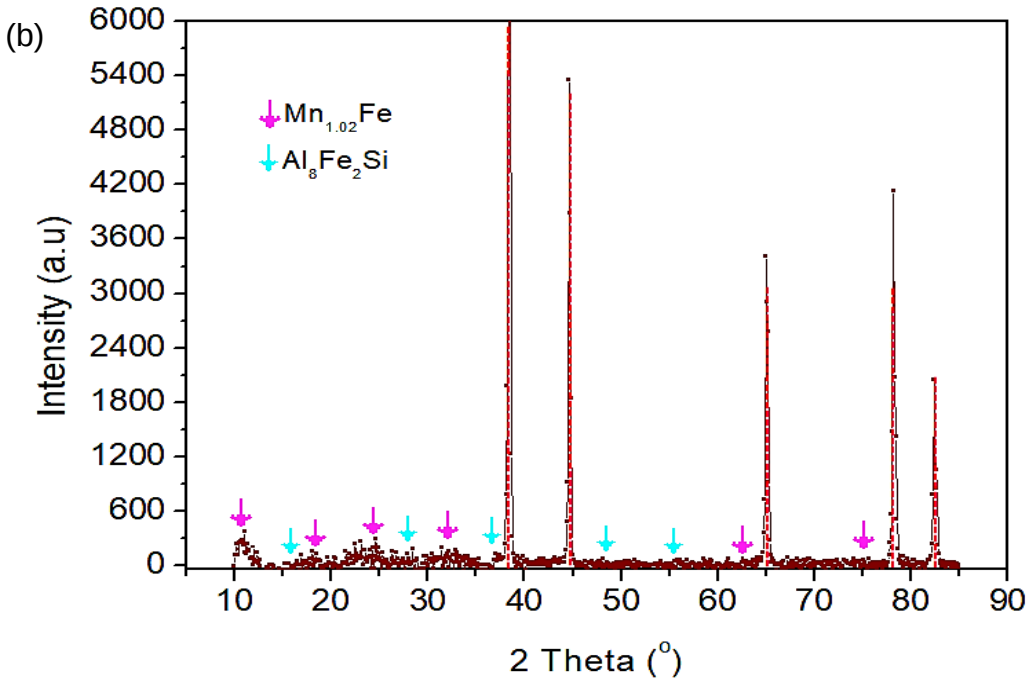

Figure 4.1.1: Base materials XRD patterns: (a) AA6082; (b) AA8011.

Figure 4.1.1(c) to (g) shows the XRD patterns of the TIG-welded and friction stir processed TIG-welded dissimilar joints AA6082-AS and AA8011-AS, with Table 4.1.1 showing the respective chemical composition of the joints. The TIG-welded XRD patterns shown in Figure 4.1.1(c) detected three phases besides aluminium: the $Mg_{2.7}Fe$, Mg_2Si and Al_9Mn_3Si. The NFSP-TIG and SFSP-TIG joints also detected similar phases. However, the TIG-welded joints consisted of exceptionally high silicon (Si) content, a behaviour resulting from the use of the ER4043 filler wire during the welding of the joint which contains very high silicon content, increasing the fluidity of the joint [185-186]. While several phases were also identified, the significance of their presence was determined as less significant than those discussed.

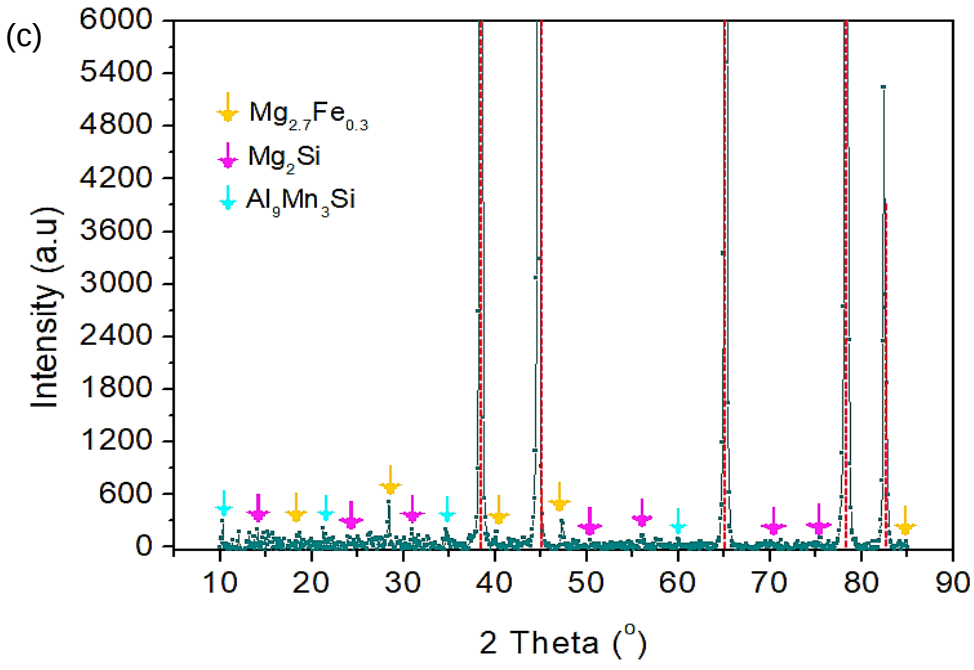

(d)

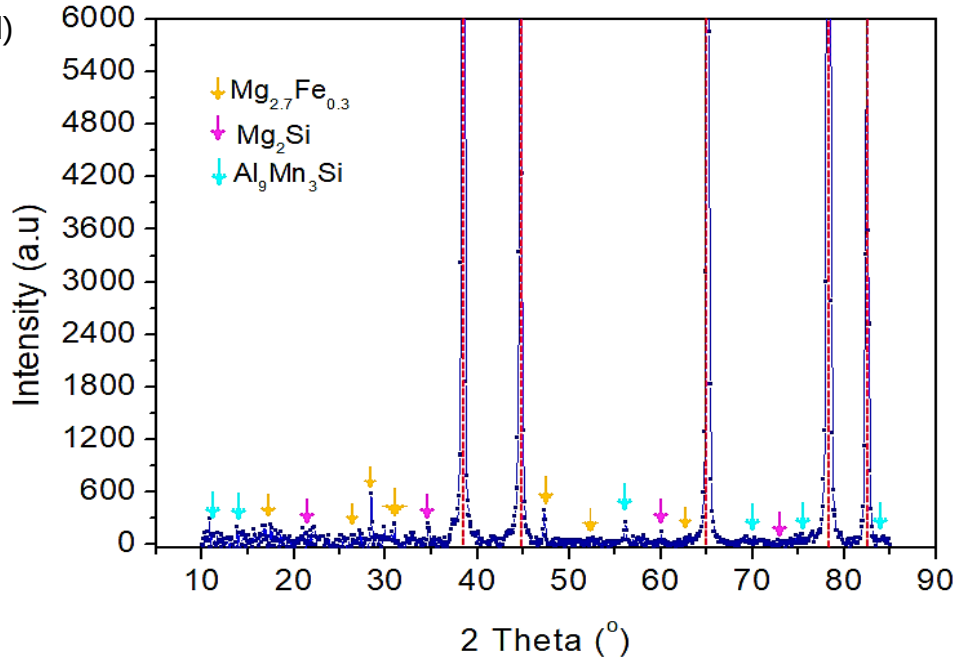
Mg2.7Fe0.3
Mg2Si
Al9Mn3Si
Intensity (a.u)
2 Theta (°)

(e)

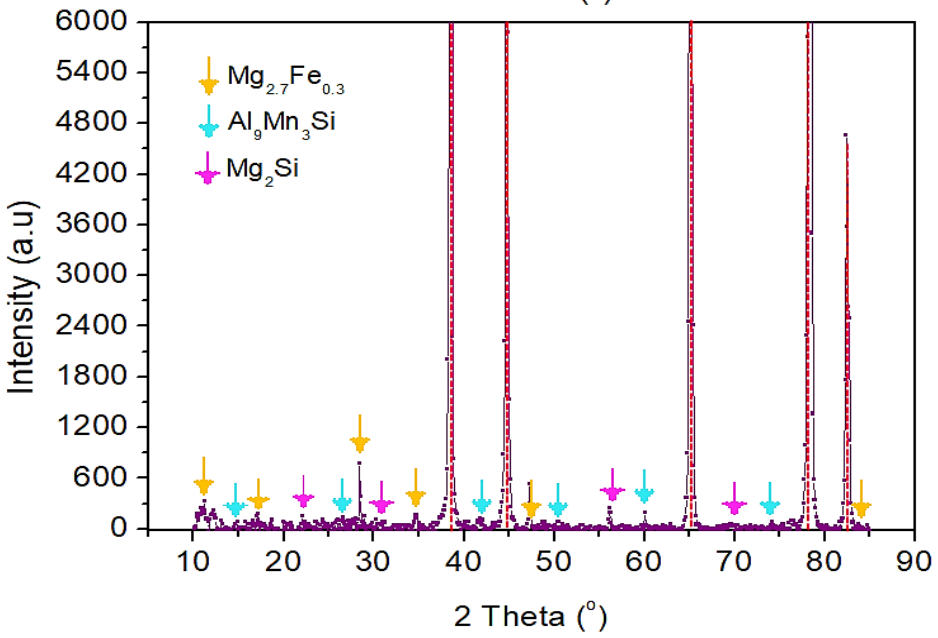
Mg2.7Fe0.3
Al9Mn3Si
Mg2Si
Intensity (a.u)
2 Theta (°)

(f)

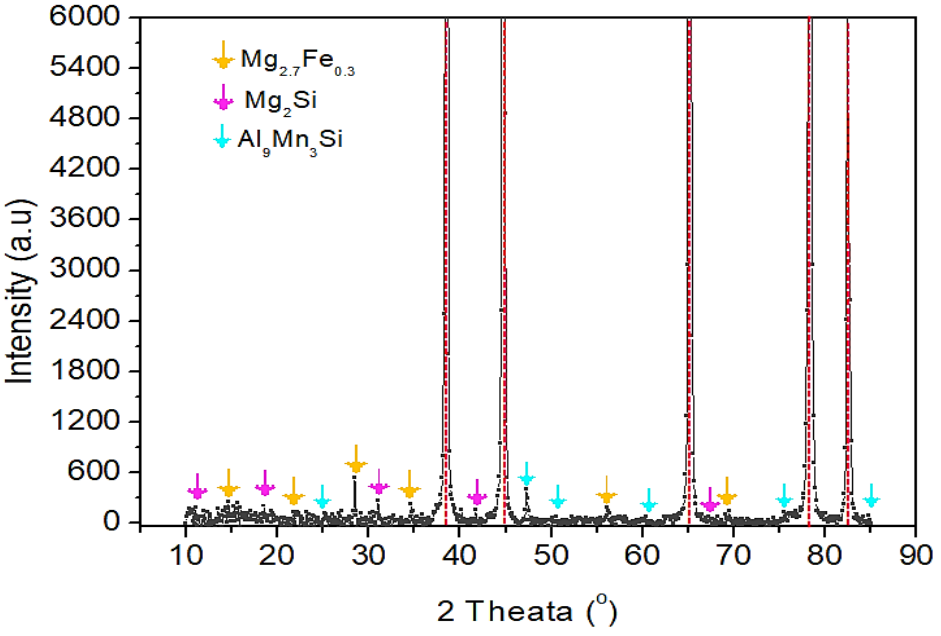
Mg2.7Fe0.3
Mg2Si
Al9Mn3Si
Intensity (a.u)
2 Theata (°)

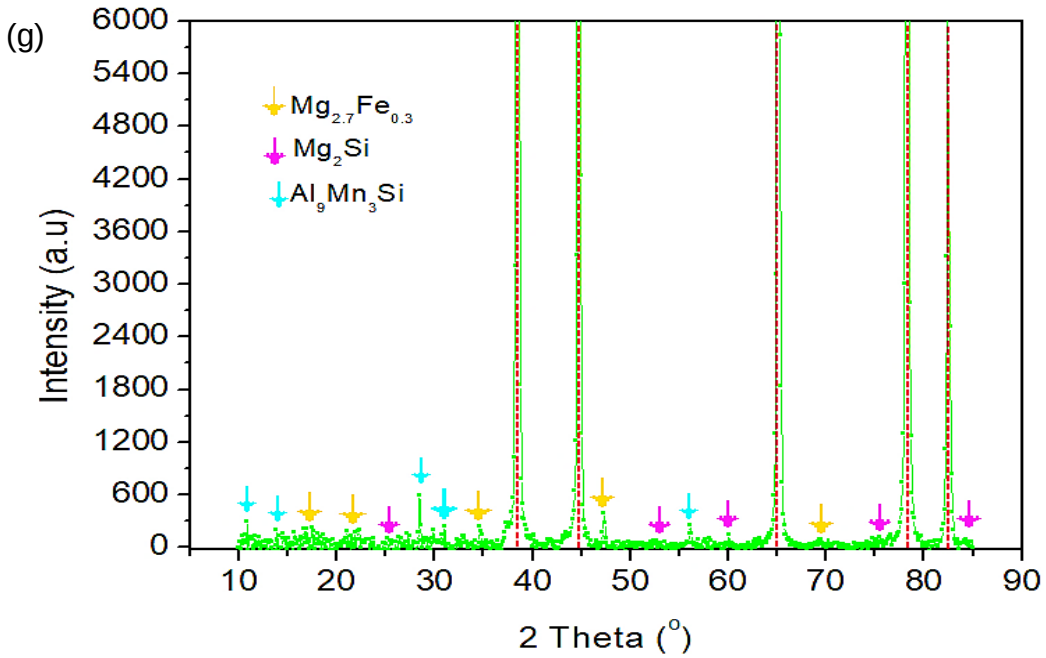

Figure 4.1.1: (c) TIG; (d) NFSP-TIG AA6082-AS joint; (e) NFSP-TIG AA8011-AS joint; (f) SFSP-TIG AA6082-AS joint; (g) SFSP-TIG AA8011-AS joint.

Table 4.1.1: Chemical composition of joints (Wt%).

Joint type	Si	Fe	Cu	Mn	Mg	Ni	Zn	Ti	Pb	Al
TIG	1.891	0.103	0.004	0.032	0.909	0.012	0.717	0.003	0.013	Bal
NFSP-TIG AA6082-AS	0.502	1.138	0.080	0.150	1.375	0.015	0.806	0.030	0.040	Bal
NFSP-TIG AA8011-AS	0.345	1.439	0.030	0.511	1.315	0.014	0.605	0.040	0.043	Bal
SFSP-TIG AA6082-AS	0.319	1.129	0.029	0.165	1.290	0.011	0.863	0.039	0.058	Bal
SFSP-TIG AA8011-AS	0.286	1.257	0.036	0.204	1.223	0.098	0.987	0.047	0.080	Bal

4.1.2 Macrostructural analysis

Figure 4.1.2 demonstrates the macrographs of the TIG-welded joints, NFSP-TIG with AA6082 positioned on the advancing side joints and NFSP-TIG with AA8011 positioned on the advancing side joints. There were no visible defects noted in the macrographs of the TIG-welded joints, as presented in Figure 4.1.2(a-c). However, tunnel defects marked by a blue circle were noted in the NFSP-TIG with AA6082 positioned on the advancing side macrographs (Figure 4.1.2[a, b]) and on the NFSP-TIG with AA8011 positioned on the advancing side (Figure 4.1.2[g]). The formation of the tunnel defects resulted from the material flow and insufficient heat experienced at the beginning of the FSP of the joint [187-188]. During the processing of the dissimilar alloys, the difference in the alloy melting points resulted in the AA8011 alloy, the weaker strength alloy, melting and softening quicker than the AA6082, the higher strength alloy. That resulted in what is known as rapid heat dissipation in the immediate deformation zone forming cold, hard welds [189-190]. The SFSP-TIG with AA6082 positioned on the advancing side macrographs (Figure 4.1.2[j, k]) showed decreasing tunnel defects (Figure 4.1.2[l]) or showing no defects present. Small tunnel defects were also noted (Figure 4.1.2[m-o]). The red marking represents microstructural zones where 1 is the base metal, 2 is the heat-affected zone, 3 is the thermos-mechanically affected zone and 4 is the nugget zone.

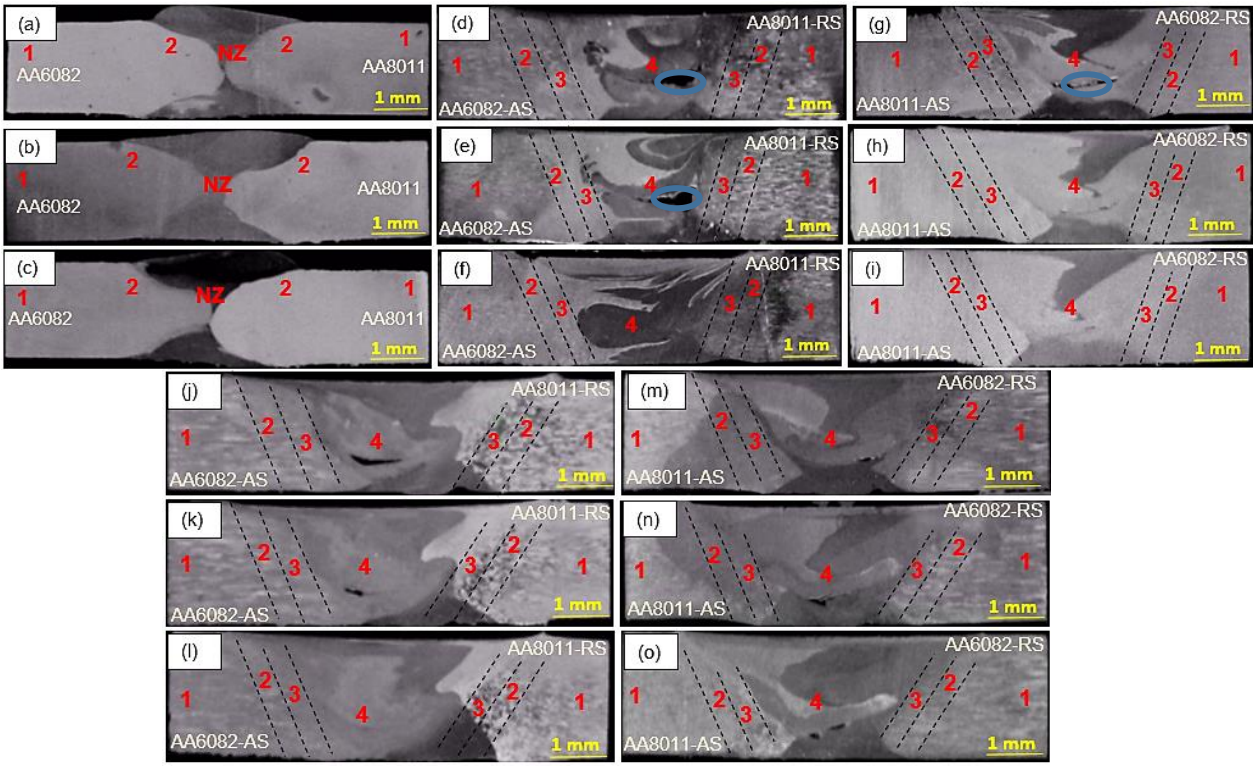

Figure 4.1.2: Macrographs: TIG-welded joints (a) start (b) middle (c) end; NFSP-TIG AA6082-AS joints (d) start (e) middle (f) end; NFSP-TIG AA8011-AS joints (g) start (h) middle (i) end; SFSP-TIG AA6082-AS joints (j) start (k) middle (l) end; SFSP-TIG AA8011-AS joints (m) start (n) middle (o) end.

4.1.3 Microstructural analysis

Figure 4.1.3 presents the optical micrographs of the base materials, TIG-welded joints and friction stir processed joints under different conditions. Figure 4.1.3(a) and (b) shows the AA6082 and AA8011 base material grain structures, respectively. The elongated grains with a mean grain size of 97.2 µm were noted on the AA6082 micrograph. Meanwhile, the AA8011 base material showed an elongated grain structure with a mean grain size of 80.09 µm. The distribution of the dark magnesium silicon (Mg_2Si) intermetallic particles were spotted on the AA6082 base material. Similar observations were noted on the AA6082 base material in the literature [191]. Figure 4.1.3(c-k) shows the micrograph with three different zones of the TIG-welded joints at different specimen location and positioning. The three distinctive regions present were the heat-affected zone (HAZ), partially melted zone (PMZ) and the fusion zone (FZ). The HAZ regions revealed a granular epitaxial dendritic grain closer to the weld interface. Similarly, Gou et al. [192] affirmed that the HAZ grain structure consists of large non-homogeneous microstructures. The non-homogeneity of the grains is a result of the weld thermal cycle [193-194]. The HAZ is popular as a common region where failure is most likely to occur during tensile loading, because of the softening phenomenon that it experiences, rendering it the weakest position in the weld joint [183]. Succeeding the HAZ is the PMZ region depicted in Figure 4.1.3(c,e,f,h,i,k), located between the HAZ and the FZ region and consisting of coarse recrystallized grains formed by the partial melting of the grain boundaries [195-196]. The PMZ region harbours weak mechanical properties due to the parent hardened precipitates experiencing over-ageing heat treatment causing a phase formation [197]. The FZ regions showed both epitaxial growth and columnar grain structure. The epitaxial nucleation in the FZ region controls the microstructural evolution [196, 198]. The FZ, compared to the other zones, had coaxial, fine and homogeneously distributed grains. The weld centre regions illustrated in

Figure 4.1.3(d,g,j) revealed a few weld defects, including cavity and large pores. The large pores were also noted in Figure 4.1.3(c,h). The presence of such defects contributes towards the weakness of the joint resulting in lower mechanical properties. According to Mathers [99], the formation of pores in the weld is a typical condition in fusion welds which rises from the TIG welding wire, shielding gas and materials used.

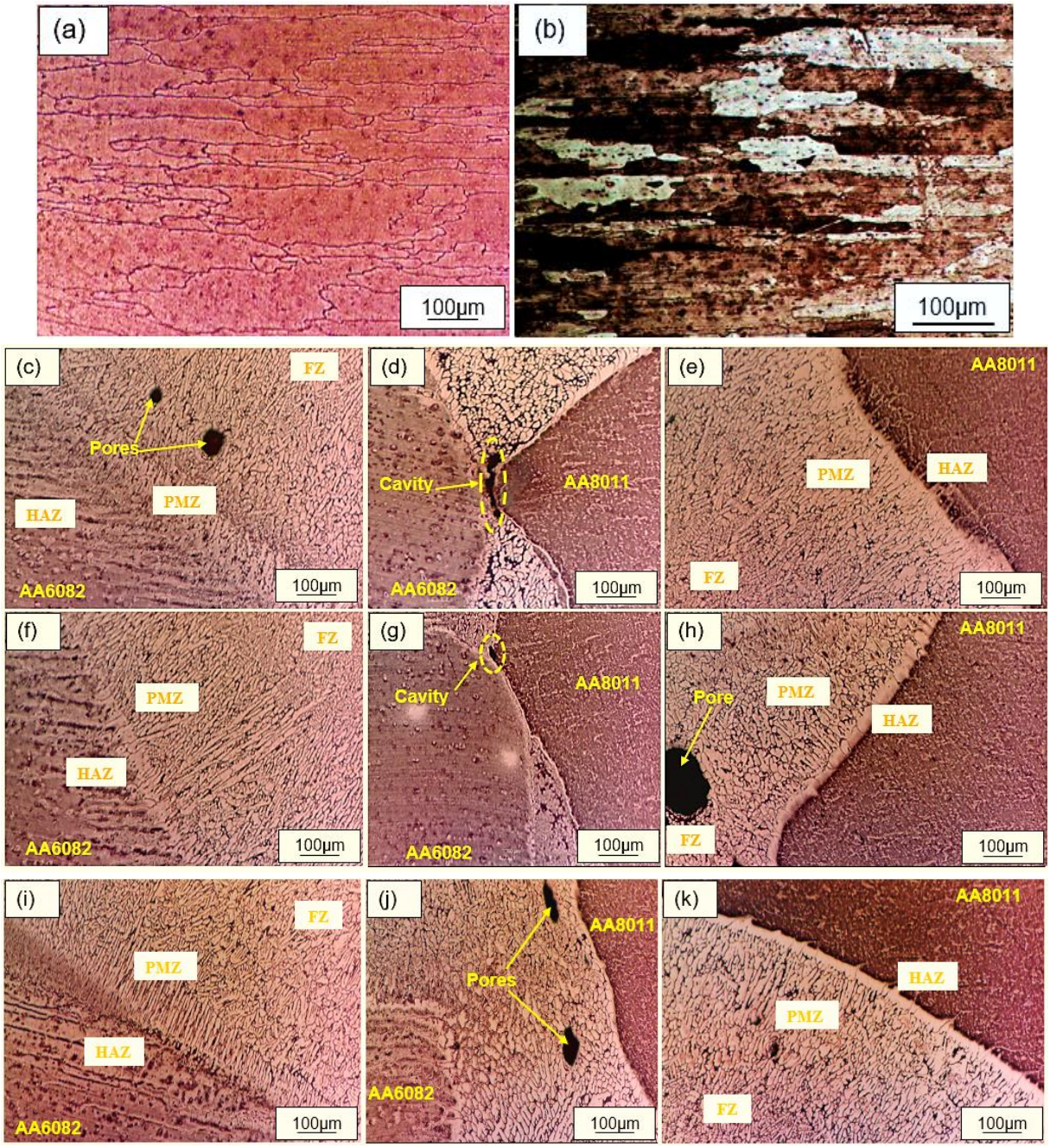

Figure 4.1.3: Optical micrographs: (a) base material AA6082; (b) base material AA8011, TIG-welded joints, start; (c) HAZ, PMZ and FZ on the AA6082 side; (d) centre of the weld; (e) HAZ, PMZ and FZ on the AA8011 side, middle; (f) HAZ, PMZ and FZ on the AA6082 side; (g) centre of the weld; (h) HAZ, PMZ and FZ on the AA8011 side, end; (i) HAZ, PMZ and FZ on the AA6082 side; (j) centre of the weld; (k) HAZ, PMZ and FZ on the AA8011 side.

Figures 4.1.3.1 and 4.1.3.2 present the NFSP-TIG joint micrographs. The micrographs showed three different microstructural zones: namely HAZ, thermo-mechanical affected zone (TMAZ) and nugget zone (NZ). The fusion zones of the TIG-welded joint coarse grain modification

process occurred in the HAZ and TMAZ regions irrespective of the material positioning. The HAZ behaviour is similar to that of the TIG-welded joints while in the TMAZ regions, for all the NFSP-TIG joints the material experienced a plastic deformation as a result of the heat during the stirring process that induced microstructural changes [200-202]. The NZ, regardless of specimen positioning, showed fine equiaxed recrystallized grains. The maximum plastic deformation that occurred during the FSP of the joint was determined as the reason behind the obtained grain structure [201]. After the FSP of the TIG-welded joints, the porosity noted on the TIG-welded microstructure was eliminated.

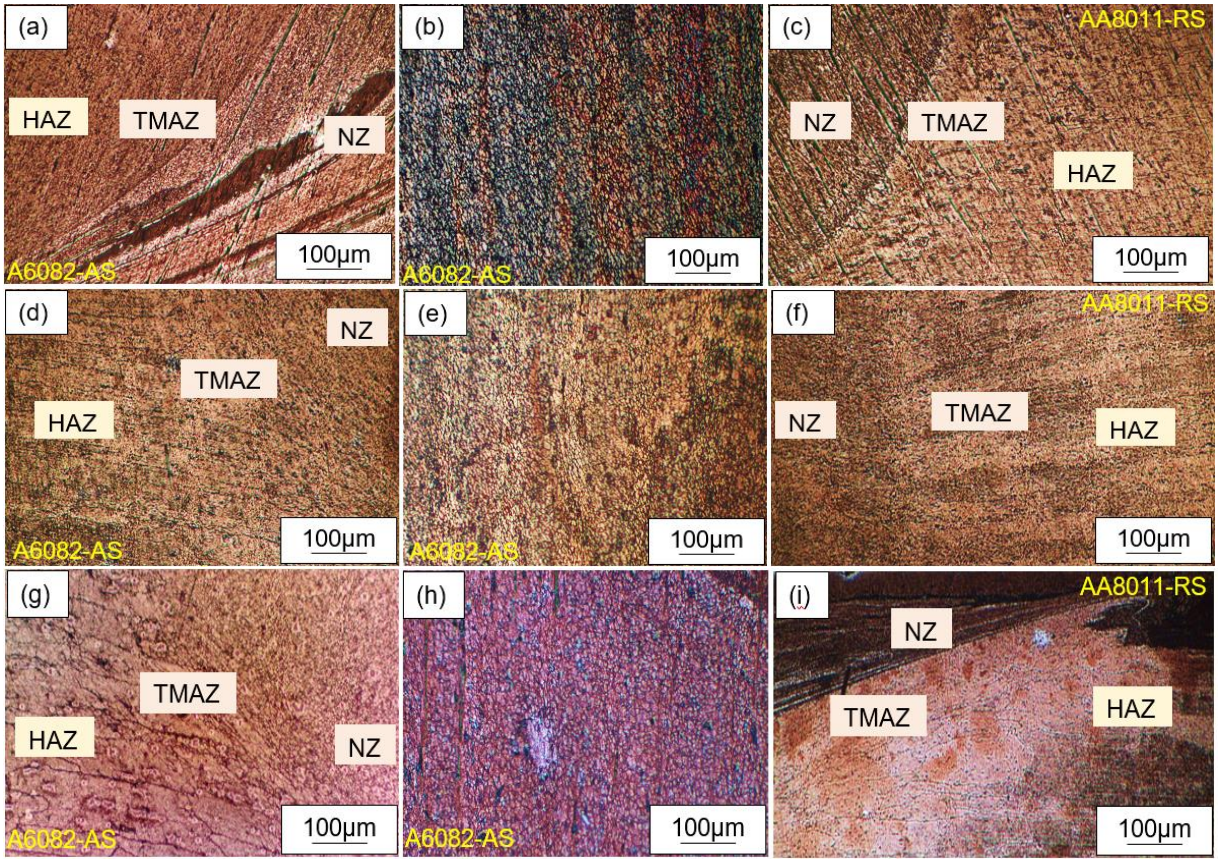

Figure 4.1.3.1: NFSP-TIG AA6082-AS joints optical micrographs, start; (a) advancing side; (b) nugget zone; (c) retreating side, middle; (d) advancing side; (e) nugget zone; (f) retreating side, end; (g) advancing side; (h) nugget zone; (i) retreating side.

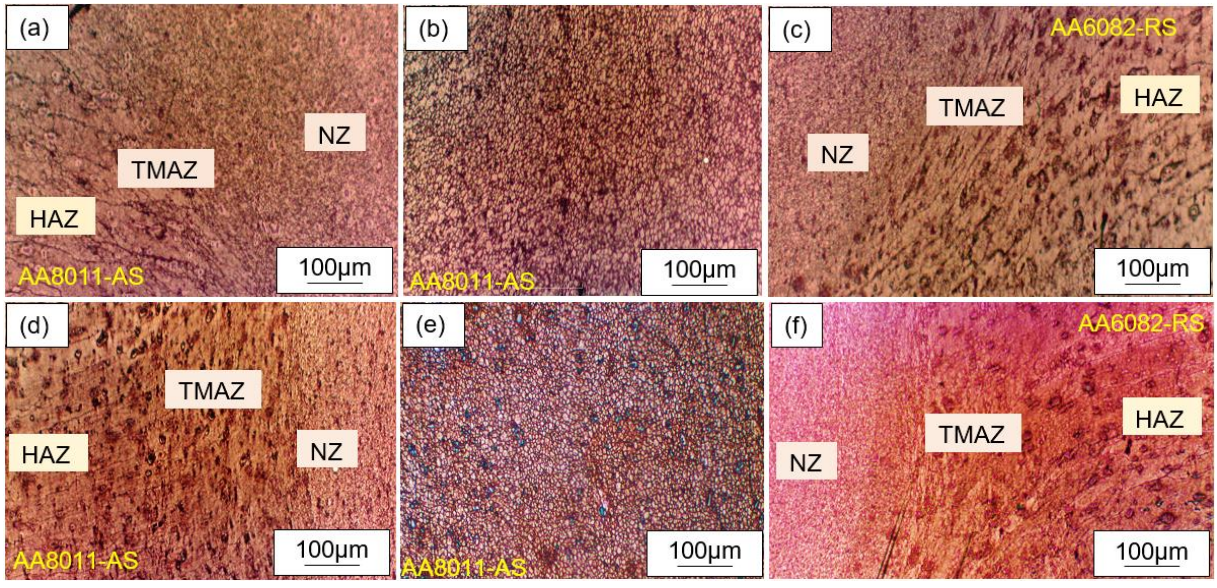

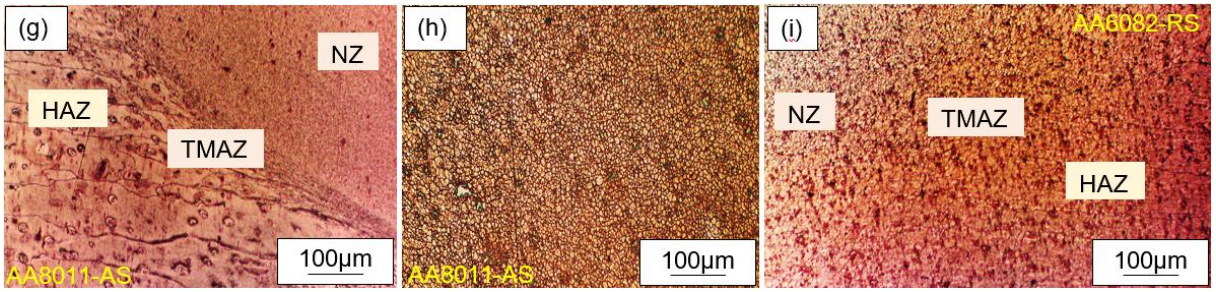

Figure 4.1.3.2: NFP-TIG AA8011-AS joints optical micrographs: start; (a) advancing side; (b) nugget zone; (c) retreating side; middle; (d) advancing side; (e) nugget zone; (f) retreating side; end: (g) advancing side; (h) nugget zone; (i) retreating side.

Figures 4.1.3.3 and 4.1.3.4 illustrate the optical micrographs of the SFSP-TIG-welded joints. Similar observations on the NFSP-TIG joints were also noted on the SFSP-TIG joints. However, due to rapid cooling of the weld joints, the NZ had a finer grain structure than under normal conditions. This phenomenon is due to NFSP experiencing higher peak temperature resulting in the process taking longer for the weld to cool down to room temperature [203]. This encourages grain growth, which thereby affects the weld properties negatively compared to SFSP [204], whereas during SFSP, the weld experienced lower peak temperature due to rapid cooling rate which substantially improves the weld properties [205].

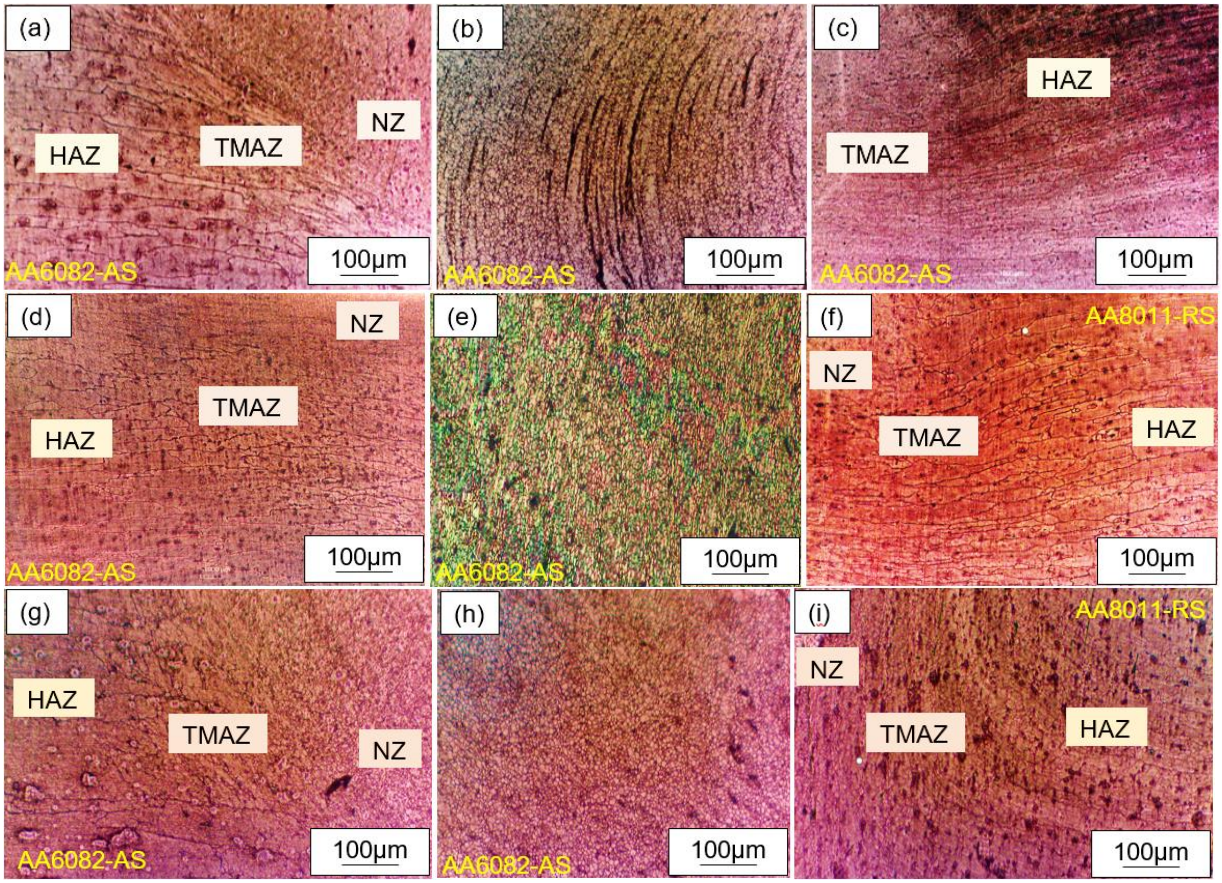

Figure 4.1.3.3: SFSP-TIG AA6082-AS joints optical micrographs: start: (a) advancing side; (b) nugget zone; (c) retreating side; middle: (d) advancing side; (e) nugget zone; (f) retreating side; end: (g) advancing side; (h) nugget zone; (i) retreating side.

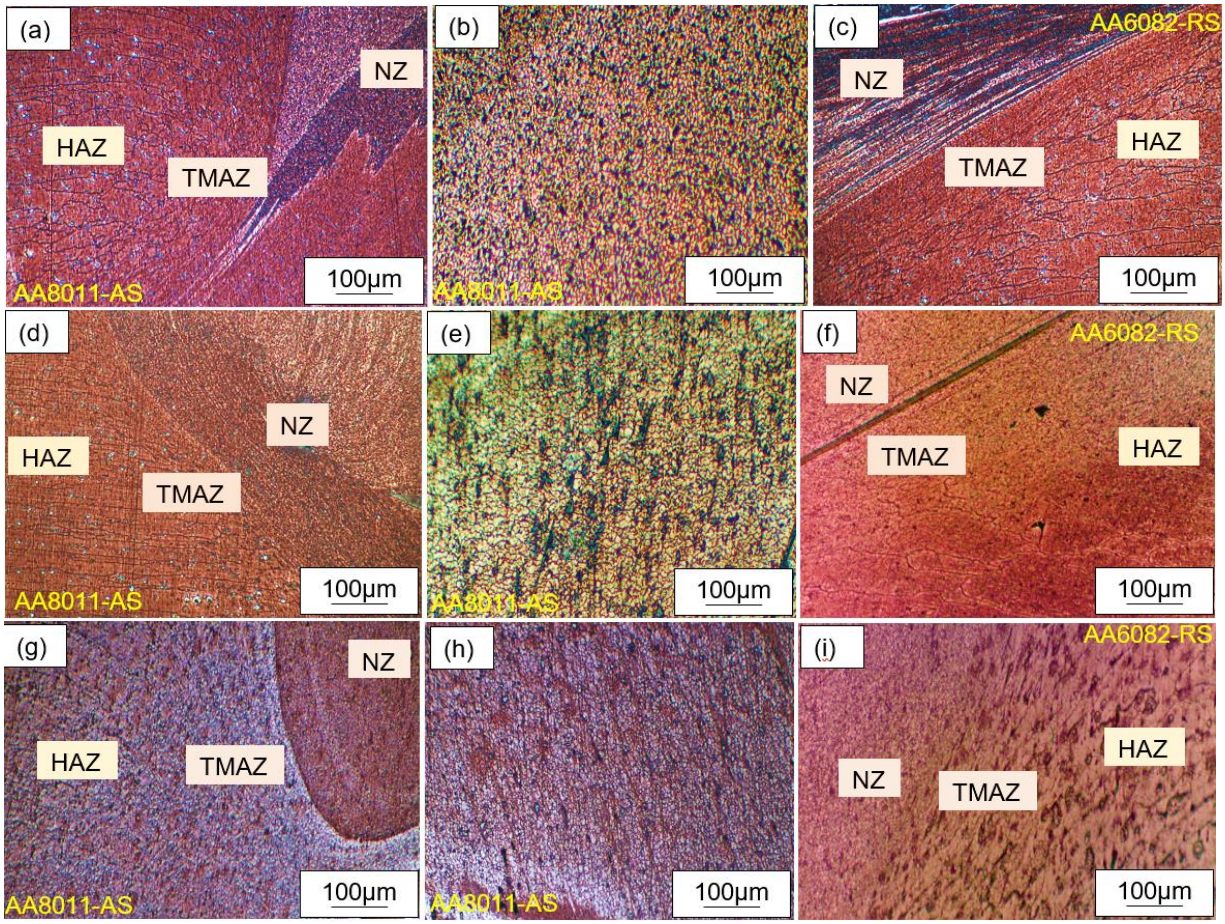

Figure 4.1.3.4: SFSP- TIG AA8011-AS joints optical micrographs: start: (a) advancing side; (b) nugget zone; (c) retreating side; middle: (d) advancing side; (e) nugget zone; (f) retreating side; end: (g) advancing side; (h) nugget zone; (i) retreating side.

Figure 4.1.3.5 presents the NZ optical micrographs for the TIG-welded, NFSP-TIG and SFSP-TIG joints. The measured grain sizes and standard deviation for the figure are tabulated in Table 4.1.3 with the grain distribution graphs presented in Figure 4.1.3.6. The TIG-welded joints had a mean grain size range of 30.8 µm to 33.19 µm with a standard deviation of 11.108 µm to11.661 µm. The mean grain size had a range of 9.762 µm to 11.472 µm for the NFSP-TIG joints with AA6082 positioned on the advancing side, with a standard deviation range of 3.128 µm to 3.919 µm. The NFSP-TIG joints with AA8011 positioned on the advancing side of the tool had a mean grain size range of 11.699 µm to 12.757 µm and standard deviation range of 3.397 µm to 4.698 µm. The SFSP-TIG joints with AA6082 positioned on the advancing side of the tool had a mean grain size range of 3.848 µm to 5.067 µm, with a standard deviation range of 1.544 µm to 1.898 µm. And finally, the SFSP-TIG joints with AA8011 positioned on the advancing side of the tool had a mean grain size range of 4.781 µm to 5.805 µm with a standard deviation range of 1.711 µm to 2.072 µm.

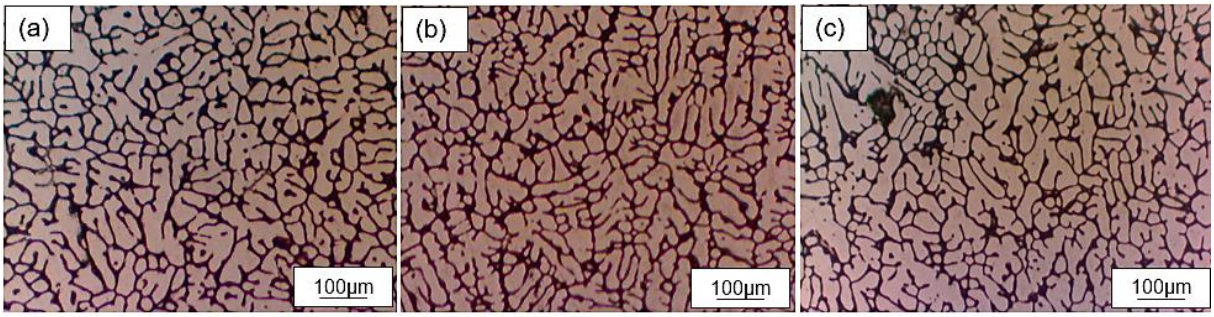

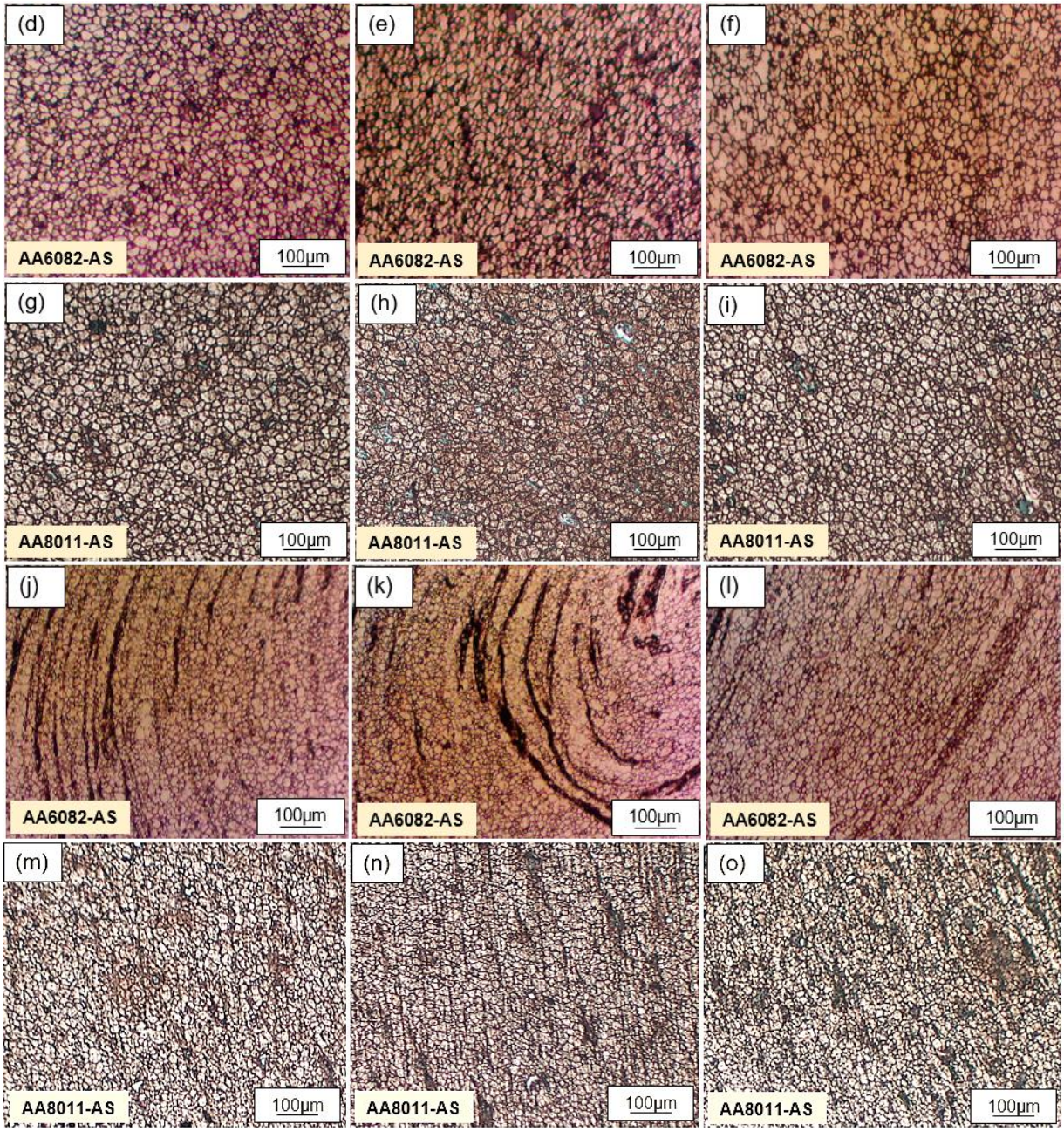

Figure 4.1.3.5: Optical micrographs at objective 20×, TIG-welded joints: (a) start (b) middle (c) end; NFSP-TIG AA6082-AS joints: (d) start (e) middle (f) end; NFSP-TIG AA8011-AS joints: (g) start (h) middle (i) end; SFSP-TIG AA6082-AS joints: (j) start (k) middle (l) end; SFSP-TIG AA68011-AS joints: (m) start (n) middle (o) end.

The obtained grain sizes suggest that the TIG-welded joint microstructure was greatly improved post-NFSP and SFSP. This improvement is owed to the stirring, plastic deformation and dynamic recrystallization caused by the frictional heat experienced during the processing [206-208]. Comparing the NFSP-TIG to the SFSP-TIG grain sizes (see Figure 4.1.3.7), the SFSP-TIG grain size showed a significant refinement of 41.37% when looking at the joints where AA6082 was on the advancing side, and 43.86% when AA8011 on the advancing side of the tool. This behaviour was caused by the water-cooling method which reduced the processing duration at lower temperatures compared to NFSP, eliminating the occurrence of grain growth [48, 73, 209]. Regardless of the FSP condition, the grain size of the joints where AA6082 (the higher strength alloy) was positioned on the advancing side of the tool showed higher grain refinement compared to when AA8011 (the lower strength alloy) was positioned on the same. Similar findings were reported in the literature [108, 210-211]. Lee et al. [96]

advocated that the temperature gradient and strain rate are basically dictated by the material positioning, greatly influencing the microstructural grain sizes. The application of FSP also reduced standard deviation, with the SFSP-TIG having a more reduced value to 1.711 µm. The standard deviation gives a clear variability of data points. As far as the specimen positioning is concerned, the TIG-welded specimens showed no particular trend. The NFSP-TIG and the SFSP-TIG specimens extracted towards the end of the processed joint showed finer grain sizes than those extracted at the beginning of the joint. This behaviour was associated with the heat input experienced at the different locations, as the tool traversed along with the joint [107, 142, 173].

Table 4.1.3: Grain sizes and standard deviations for the NZ.

Joint	Mean grain size (µm)	Minimum grain size (µm)	Maximum grain size (µm)	Standard deviation (µm)
TIG S	31.285	13.672	56.375	11.227
TIG M	30.801	14.305	55.051	11.661
TIG E	33.190	18.111	59.081	11.109
AA6082-AS				
NFSP-TIG S	11.472	4.938	16.791	3.128
NFSP-TIG M	10.981	5.174	22.42	3.919
NFSP-TIG E	9.763	5.521	21.095	3.574
AA8011-AS				
NFSP-TIG S	12.757	5.453	21.441	3.397
NFSP-TIG M	12.641	4.622	22.932	3.691
NFSP-TIG E	11.699	5.59	27.042	4.698
AA6082-AS				
SFSP-TIG S	4.407	2.75	8.953	1.545
SFSP-TIG M	5.067	1.997	9.053	1.653
SFSP-TIG E	3.848	1.001	9.227	1.898
AA8011-AS				
SFSP-TIG S	5.805	2.216	11.924	2.006
SFSP-TIG M	5.688	2.503	11.105	2.072
SFSP-TIG E	4.781	1.863	9.664	1.711

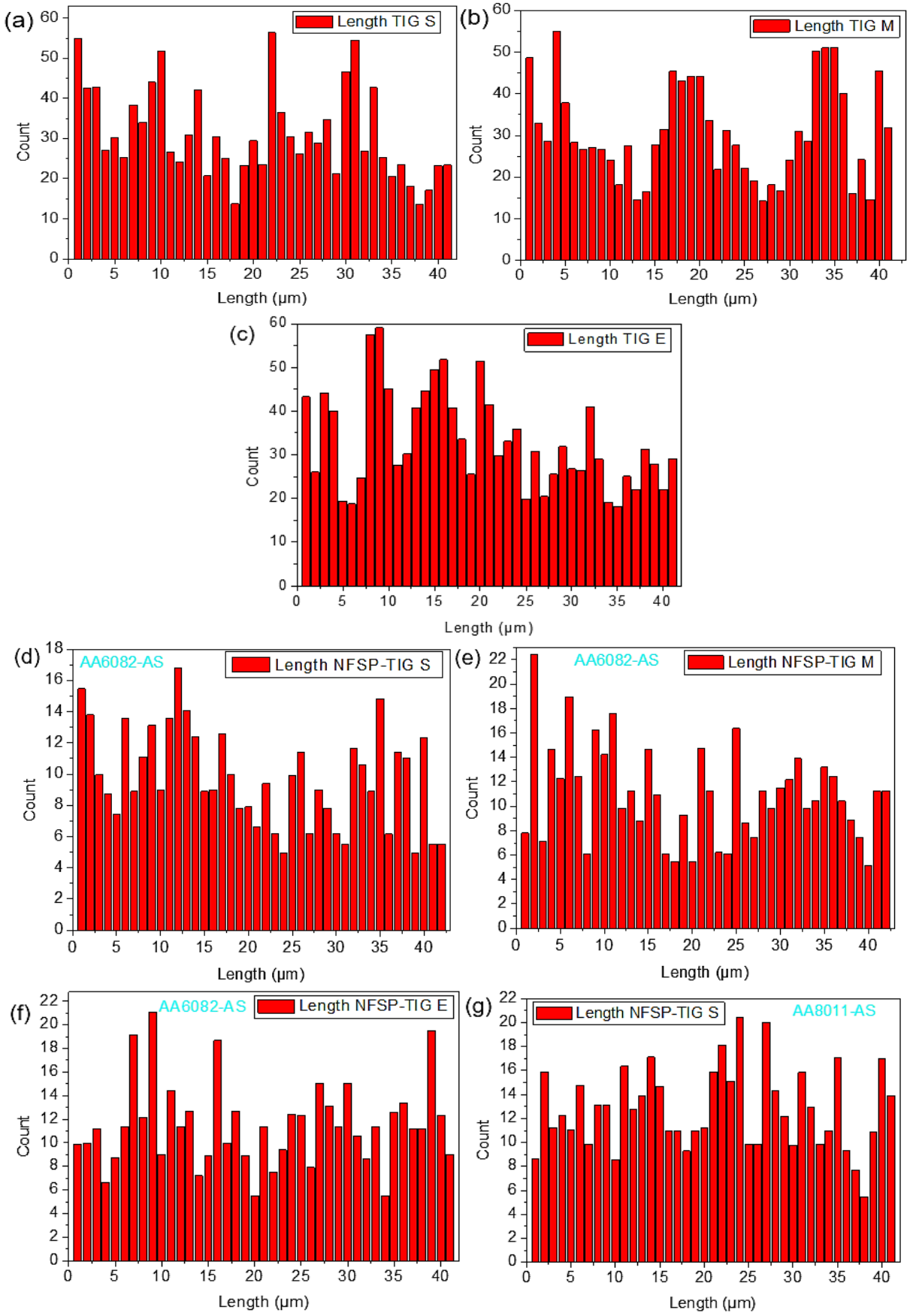
(a)
Length TIG S
Count
Length (μm)
(b)
Length TIG M
Count
Length (μm)
(c)
Length TIG E
Count
Length (μm)
(d)
AA6082-AS
Length NFSP-TIG S
Count
Length (μm)
(e)
AA6082-AS
Length NFSP-TIG M
Count
Length (μm)
(f)
AA6082-AS
Length NFSP-TIG E
Count
Length (μm)
(g)
Length NFSP-TIG S
AA8011-AS
Count
Length (μm)

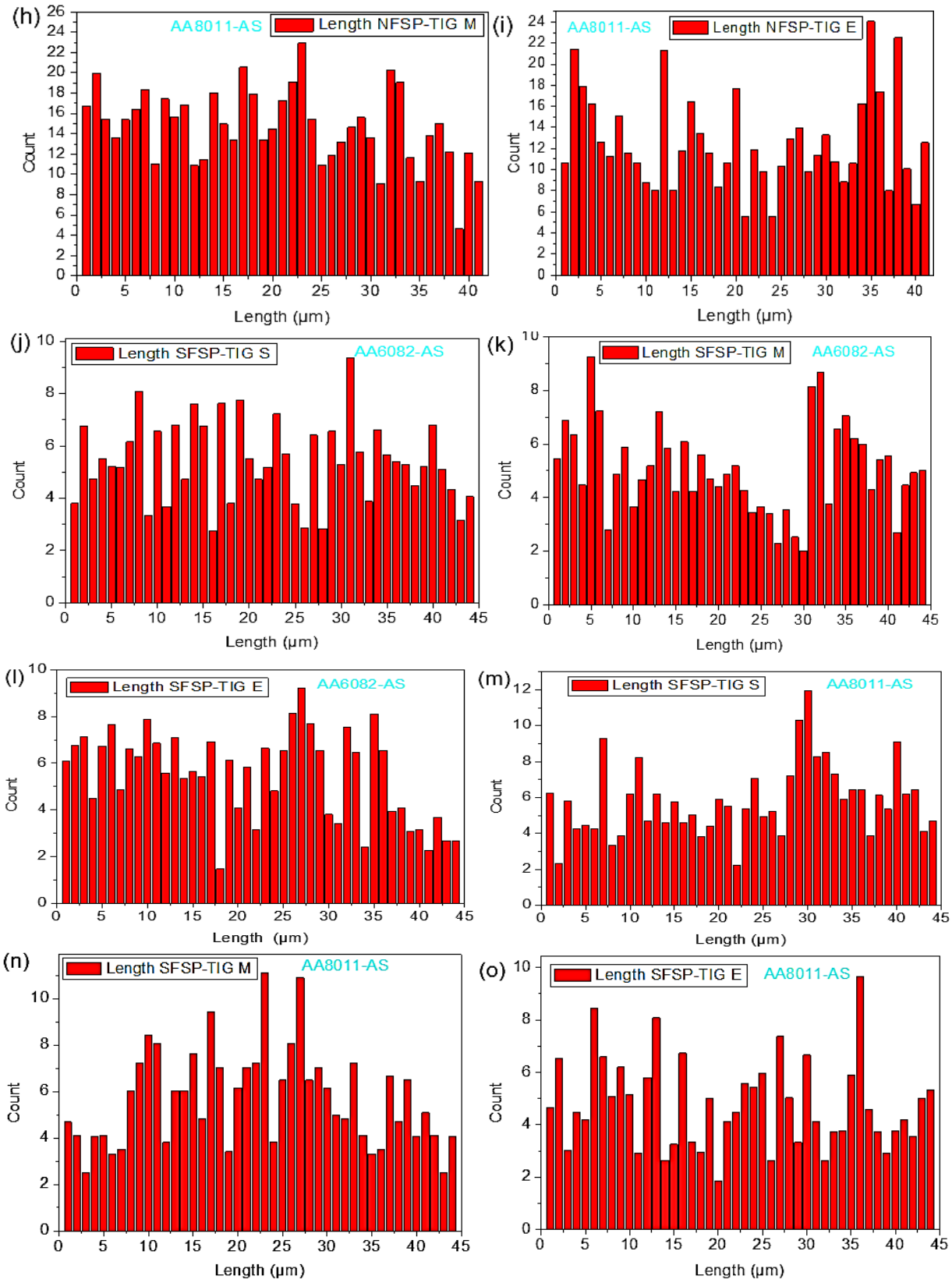

Figure 4.1.3.6: Grain distribution graphs: TIG-welded joints: (a) start(b) middle; (c) end; NFSP-TIG AA6082-AS joints: (d) start (e) middle (f) end; NFSP-TIG AA8011-AS joints: (g) start (h) middle (i) end; SFSP-TIG AA6082-AS joints: (j) start (k) middle (l) end; SFSP-TIG AA68011-AS joints: (m) start (n) middle (o) end.

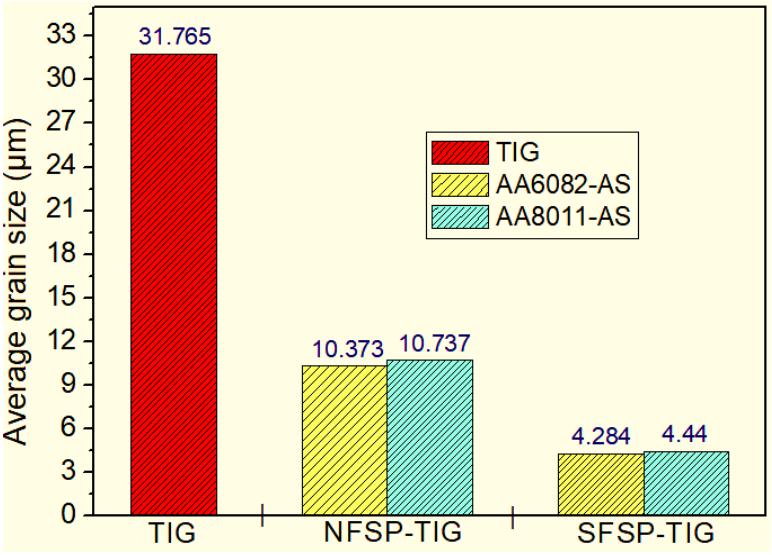

Figure 4.1.3.7: Average grain sizes of the joints.

4.1.4 Flexure tests

Figure 4.1.4 shows the post-flexure test specimens. In all specimens, regardless of the type of the weld, all flexed towards the AA8011 side which is the weaker strength alloy. This behaviour suggested that the TIG-welded and friction stir processed joints, regardless of the conditions, had a stronger joint strength compared to the AA8011 base material. Similar findings were reported in the literature [107,213]. No visible cracks were noted on the post specimens. Figure 4.1.4.1 illustrates the flexural strength and strain curves for the TIG-welded and friction stir processed joints. The TIG-welded face bending presented in Figure 4.1.4.1(a) revealed an ultimate flexural strength (UFS) range of 109.25 MPa at a strain rate of 0.366 to 166.315 MPa at a strain rate of 0. 288. The obtained UFS are a result of the grain structure arrangement at the respective specimen positions. A maximum flexural strain of 0.464 was noted on the specimen extracted at the start of the joint and the lowest (0.0.443) at the specimen extracted at the middle of the joint. The flexural strength and strain for the TIG-welded root specimens (see Figure 4.1.4.1[b]) showed a UFS range of 119.063 MPa to 198.813 MPa at a flexural strain of 0.282 and 0.276, respectively. A maximum flexural strain of 0.466 was noted on the specimen extracted at the middle of the joint and the lowest (0.433) at the specimen extracted at the start of the joint. The maximum UFS was observed on the root of the TIG-welded rather than on the face. This kind of behaviour was also reported in the literature [140].

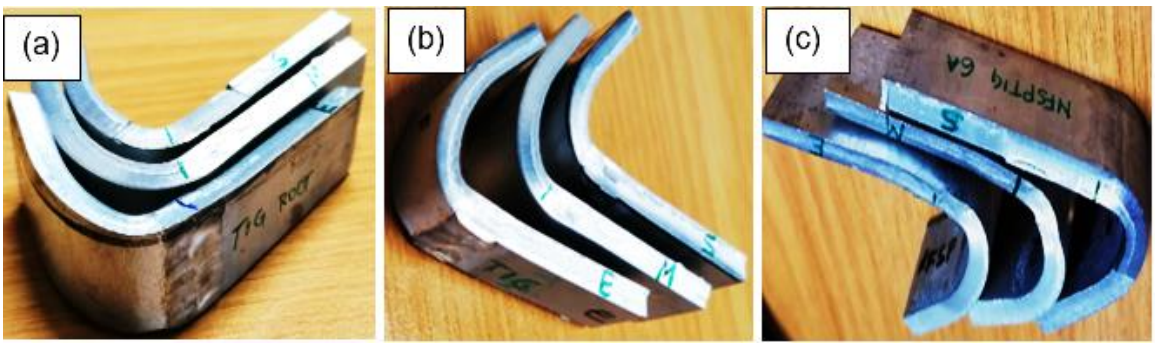

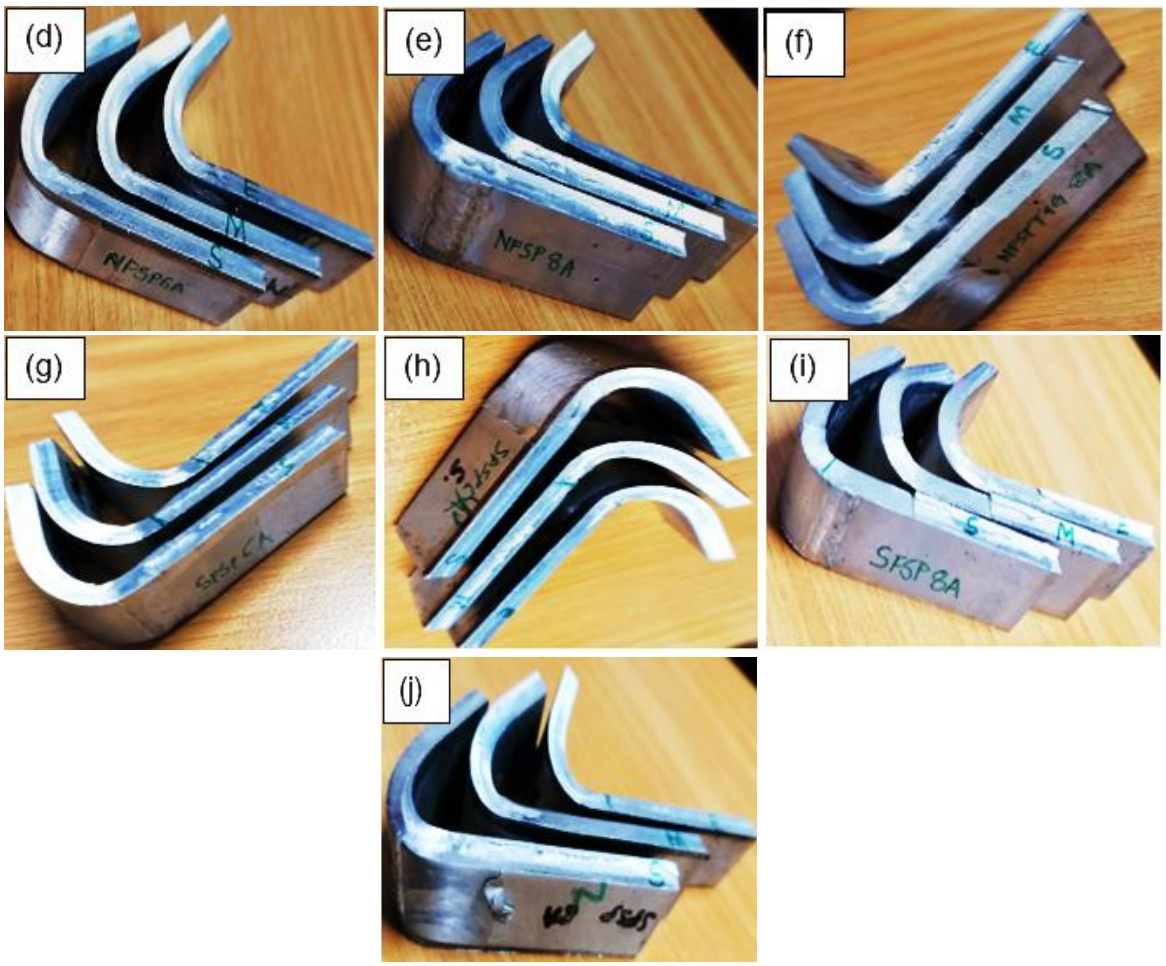

Figure 4.1.4: Post-flexural test specimens: (a) TIG-welded (face); (b) TIG-welded (root); (c) NFSP-TIG AA6082-AS (face); (d) NFSP-TIG AA6082-AS (root); (e) NFSP-TIG AA8011-AS (face); (f) NFSP-TIG AA8011-AS (root); (g) SFSP-TIG AA6082-AS (face); (h) SFSP-TIG AA6082-AS (root); (i) SFSP-TIG AA8011-AS (face); (j) SFSP-TIG AA8011-AS (root).

Figure 4.1.4.1(c-f) shows the flexural strength and strain curves for the NFSP-TIG specimens. The NFSP-TIG (face) with AA6082 positioned on the advancing side (see Figure 4.1.4.1[c]) showed a UFS range of 148.125 MPa to 260.25 MPa at a flexural strain of 0.12 and 0.31, respectively. A maximum flexural strain of 0.432 was noted on the specimen extracted at the start of the weld, and the lowest (0.421) on the specimen extracted at the middle of the joint. The root of the same NFSP-TIG joint (see Figure 4.1.4.1[d]) showed a UFS range of 120 MPa to 151.188 MPa at a flexural strain of 0.13 and 0.148, respectively. A maximum and minimum flexural strain of 0.423 and 0.448 of the joint, respectively, was obtained. The maximum UFS was noted on the face specimens compared to the root specimens of the NFSP-TIG with AA6082 positioned on the advancing side. Similar behaviour was noted on the NFSP-TIG specimens with AA8011 positioned on the advancing side. This kind of behaviour was noted in several studies, including Sorger et al. [213] and Takhakh [214]. The UFS range of the NFSP-TIG specimens with AA8011 positioned on the advancing side (see Figure 4.1.4.1[e]) for the face joint was 201 MPa at a flexural strain of 0.168 to 257.43 MPa at a flexural strain of 0.2. A maximum flexural strain of 0.448 and the minimum flexural strain of 0.398 were noted at the specimens extracted at the end and middle of the joint, respectively. The UFS range for the root joints (see Figure 4.1.4.1[f]) was 165.936 MPa and 225.36 MPa at a flexural strain of 0.217 and 0.152, respectively. The maximum flexural strain of 0.378 and minimum of 0.345 were noted on the specimens extracted from the start and middle of the processed joint.

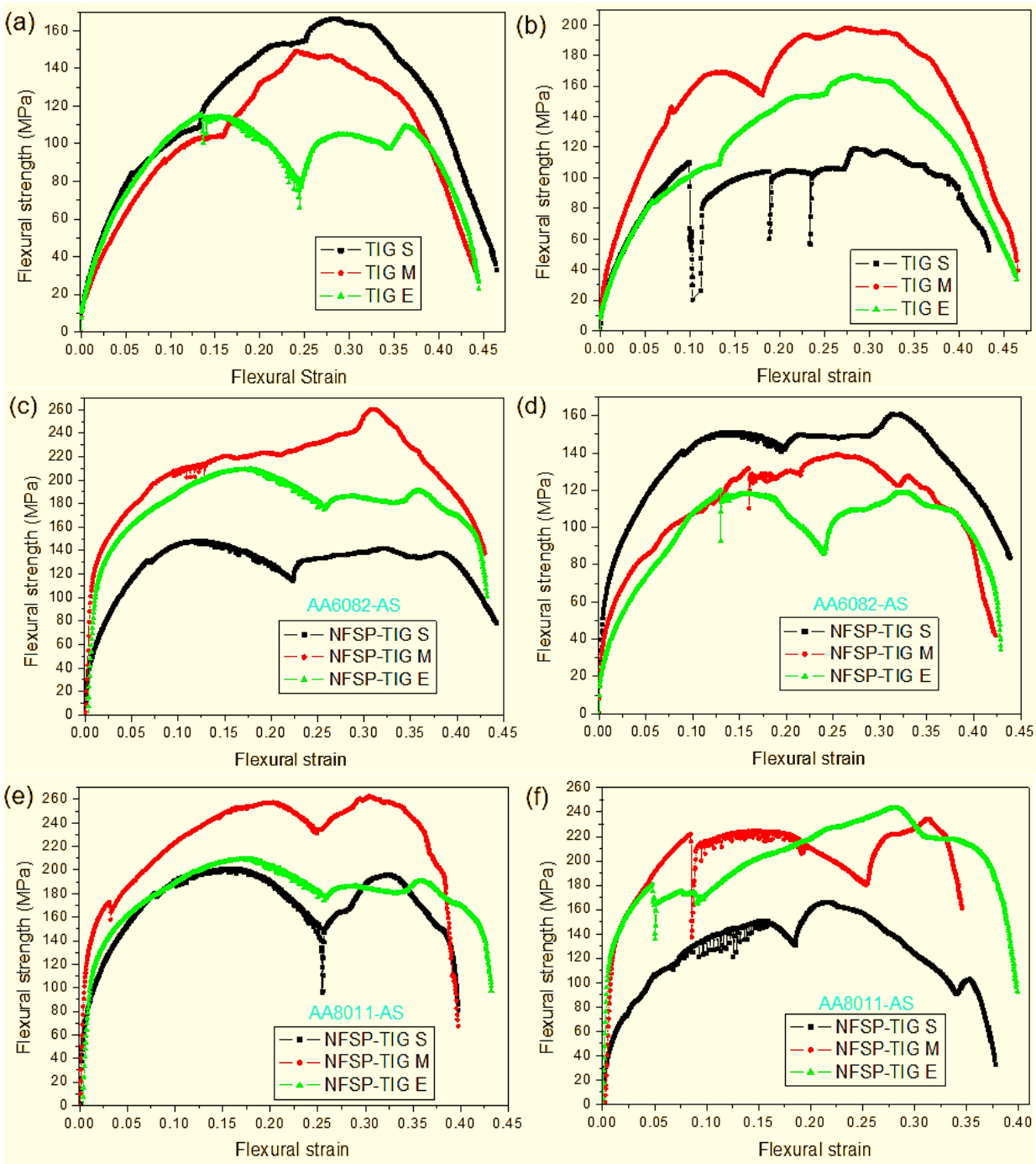

Figure 4.1.4.1: Flexural strength – strain curves: (a) TIG-welded (face); (b) TIG-welded (root); (c) NFSP-TIG AA6082-AS (face); (d) NFSP-TIG AA6082-AS (root); (e) NFSP-TIG AA8011-AS (face); (f) NFSP-TIG AA8011-AS (root).

Figure 4.1.4.1(g-j) shows the flexural strength and strain curves for the SFSP-TIG joints for different material positioning. The curves for SFSP-TIG (face) joint with AA6082 on the advancing side are presented in Figure 4.1.4.1(g). The UFS ranged from 160 MPa to 300 MPa at flexural strains of 0.087 and 0.233, respectively. The 160 MPa is due to the start position having what is known as 'cold welds', where the harder alloy was not fully melted [189-190]. This led to the joint having cavity. This behaviour correlates to the macrostructure obtained. The maximum flexural strain of 0.409 and a minimum of 0.397 were obtained on the start and end specimen positioning. The root curves of the same joint (see Figure 4.1.4.1[h]) were determined to have a UFS range of 136.25 MPa to 211.375 MPa with a corresponding flexural strain of 0.233 and 0.403, respectively. The maximum flexural strain was obtained from the

specimen extracted at the end of the joint and the minimum from the specimen extracted at the start of the joint. Figure 4.1.4.1(i) represents the SFSP-TIG joints with AA8011 on the advancing side (face) with a UFS range of 183.375 MPa to 243.375 MPa at the respective flexural strain of 0.256 and 0.334. The maximum flexural strain of 0.427 and a minimum of 0.423 were obtained. Figure 4.1.4.1(j) shows the SFSP-TIG joints with AA8011 (root) on the advancing side with a UFS range of 86.185 MPa to 202.25 MPa at a flexural strain of 0.163 and 0.299, respectively. There was no particular trend as far as the specimen positioning for the UFS. A minimum flexural strain of 0.214 and a maximum of 0.418 were noted.

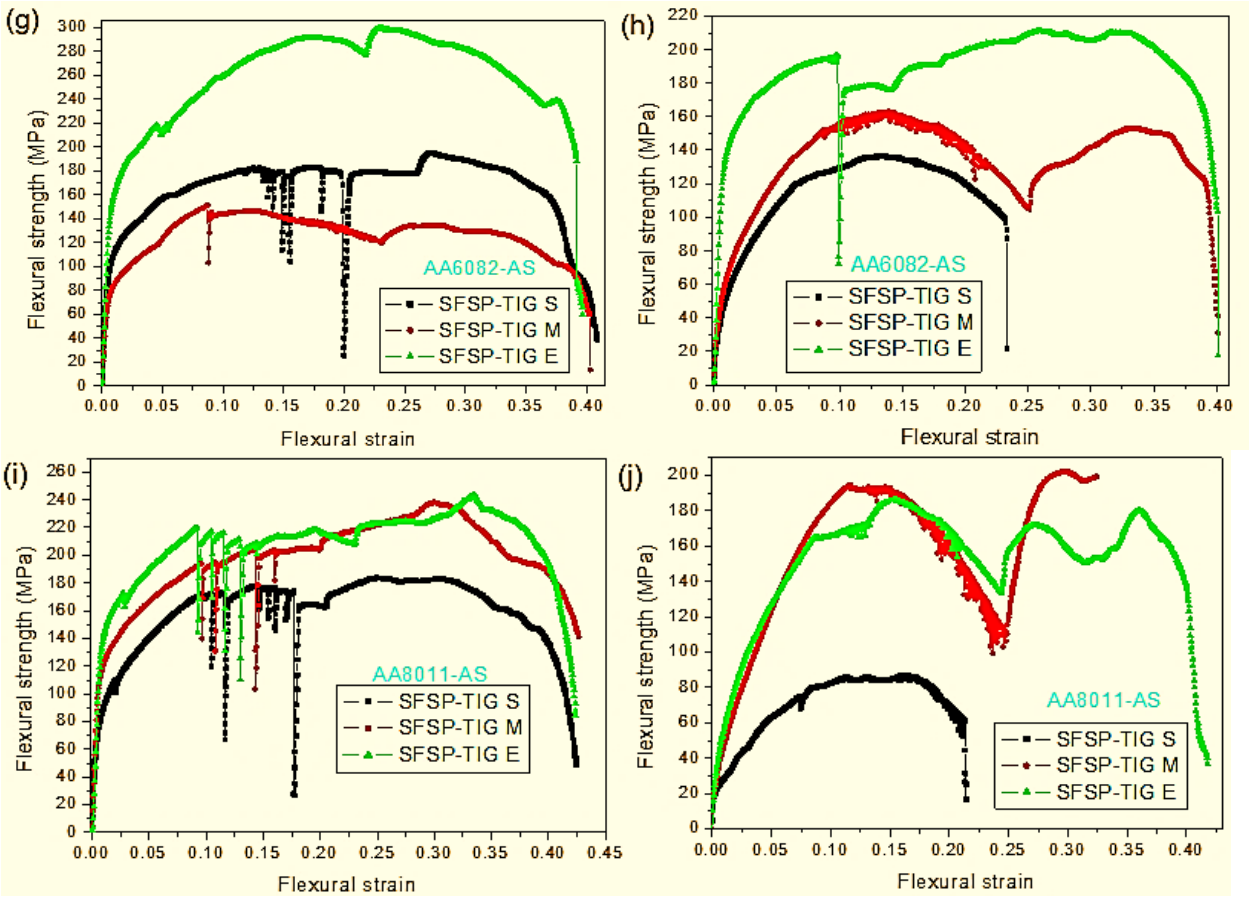

Figure 4.1.4.1: Flexural strength – strain curves: (g) SFSP-TIG AA6082-AS (face); (h) SFSP-TIG AA6082-AS (root); (i) SFSP-TIG AA8011-AS (face); (j) SFSP-TIG AA8011-AS (root).

Figure 4.1.4.2 depicts the UFS and maximum flexural strain (MFS) obtained on each joint configuration as discussed. The maximum UFS was obtained on the SFSP-TIG with AA6082-AS (face) while the maximum UFS OF for the specimens subjected to root bending was noted on the NFSP-TIG AA8011-AS joint. Furthermore, it was observed that the TIG-welded joints, regardless of face or root urface, showed a higher strain rate (%) than the NFSP-TIG and SFSP-TIG joints. However, comparing the NFSP-TIG to the SFSP-TIG, the NFSP-TIG showed a higher strain rate. This suggests that when the MFS increases, the UFS, which is the ductility, decreases and vice versa. Similar behaviour was reported in the literature [215].

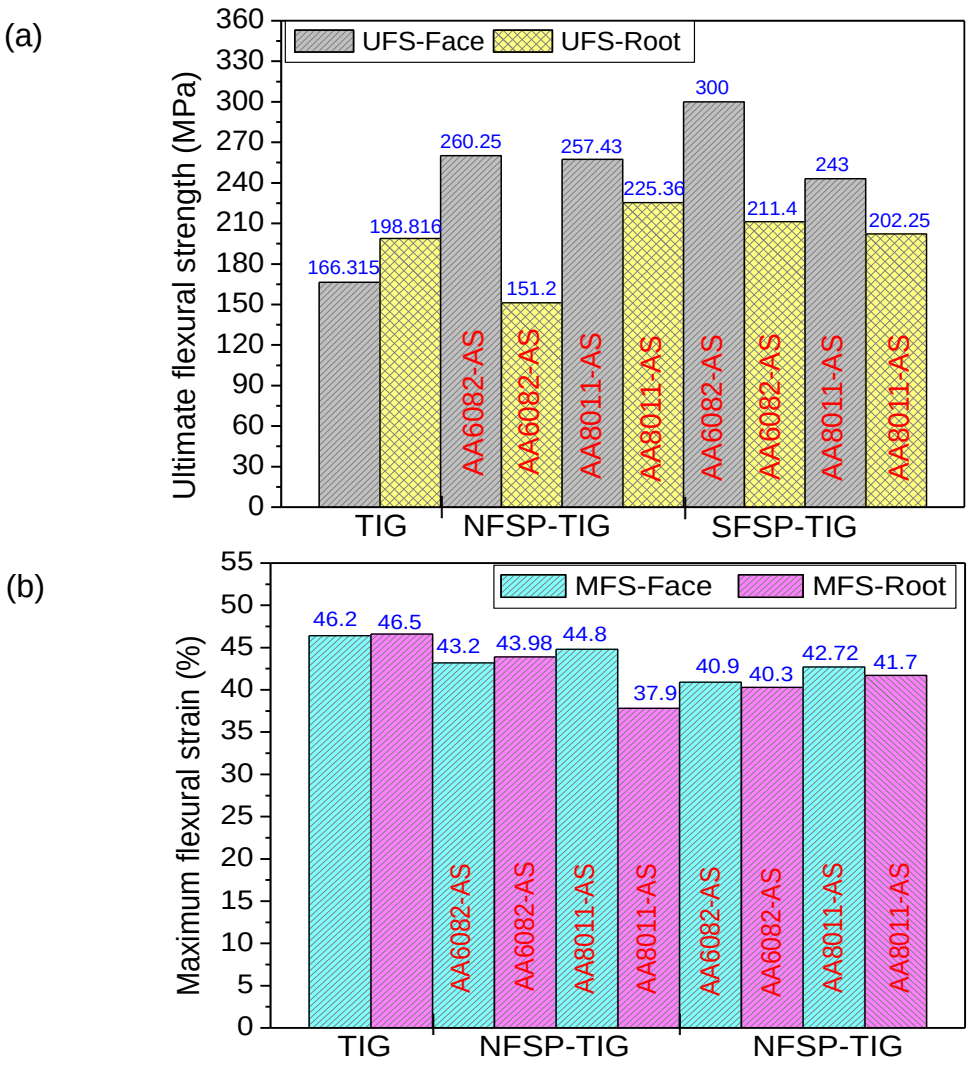

Figure 4.1.4.2: Bar charts: (a) ultimate flexural strength (MPa); (b) maximum flexural strain.

4.1.5 Tensile tests

Figure 4.1.5.1 illustrates the post-tensile specimens of the TIG-welded, NFSP-TIG and SFSP-TIG joints. The TIG-welded specimens fractured on the HAZ of the AA8011 side. This behaviour confirms that the HAZ consists of the weakest strength compared to that of the fusion zone and the AA6082 side of the specimen [216-217]. Additionally, there is no strain in the thermal cycles experienced by the HAZ [218]. This phenomenon is quite common with the joining of dissimilar materials. Of the NFSP-TIG AA6082-AS specimens, all the specimens fractured on the NZ, confirming that the NZ had a lower strength than the AA6082 and AA8011 material due to the presence of tunnel defects previously observed on the macrostructural analysis. Similar behaviour was noted on the NFSP-TIG AA8011-AS (middle and end specimens), SFSP-TIG AA6082-AS (start specimen) and the SFSP-TIG specimens. The NFSP-TIG AA8011-AS specimens extracted from the start of the weld fractured at the HAZ of the AA8011 because the region had lower mechanical properties than the NZ and the AA6082 BM [216]. Similarly, the SFSP-TIG AA6082-AS middle and end specimens also fractured on the HAZ.

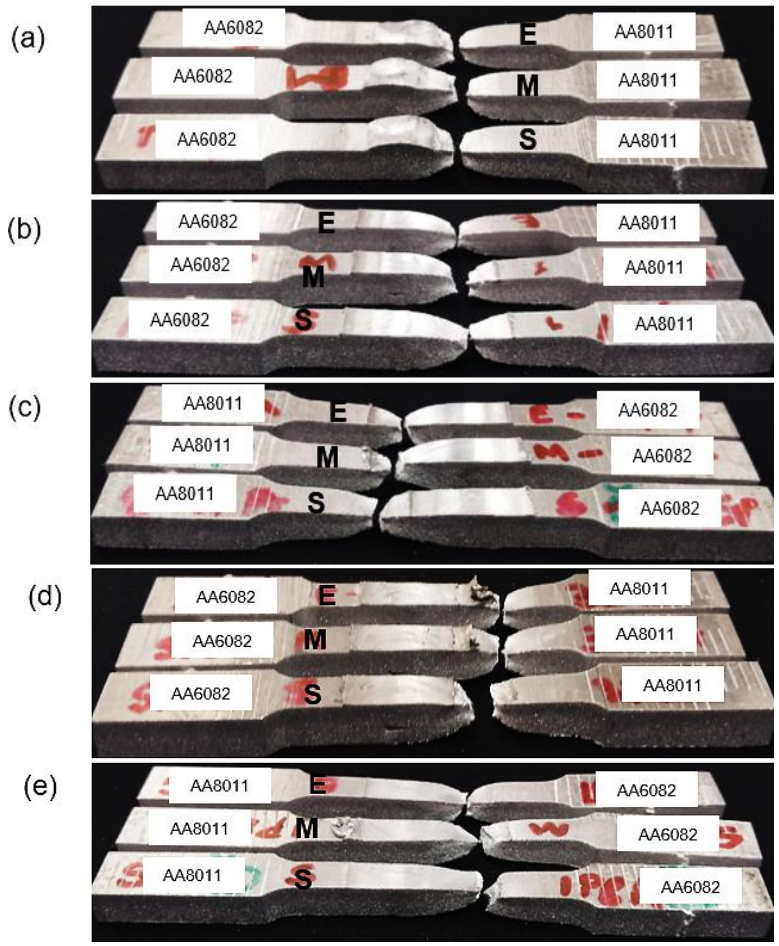

Figure 4.1.5.1: Post-tensile specimens: (a) TIG-welded; (b) NFSP-TIG AA6082-AS; (c) NFSP-TIG AA8011-AS; (d) SFSP-TIG AA6082-AS; (e) SFSP-TIG AA8011-AS.

Figure 4.1.5.2 presents the tensile stress-strain curves of the TIG-welded and FSPed joints. Table 4.1.5 shows the tensile properties concerning Figure 4.1.5.2. The TIG-welded joint had a maximum UTS of 85.42 MPa at a corresponding tensile strain rate of 13.781% and a maximum yield strength of 68.336 MPa. The minimum UTS and yield strength were at 80.277 MPa at a corresponding tensile strain rate of 11.588% and yield strength of 64.222 MPa. The minimum and maximum tensile strain rates at the fracture point of the TIG-welded joint were 21.885% and 23.889%, respectively. The NFSP-TIG AA6082-AS joints had a maximum UTS of 88.53 MPa at a corresponding tensile strain rate of 15.49% with a maximum yield strength of 70.824 MPa. The minimum UTS of the said joints were 86.958 MPa at a corresponding tensile strain rate of 14.96% and yield strength of 69.566 MPa. The maximum and minimum tensile strain rates at the fracture point were 27.251% and 27.666%, respectively. The NFSP-TIG AA8011-AS showed a maximum UTS of 89.777 MPa at a tensile strain rate of 15.61%, with a yield strength of 71.822 MPa. The minimum UTS of 85.777 MPa at a tensile strain of 13.86% with a yield strength of 68.622 MPa were noted. The minimum and maximum tensile strain rates of 25.166% and 27.994% were obtained. The application of the NFSP technique increased both the tensile strength and tensile strain. This behaviour was associated with the stirring and dynamic recrystallization of the joints that resulted in the notable grain refinement which is acknowledged as having a positive impact on joint tensile properties [218-219].

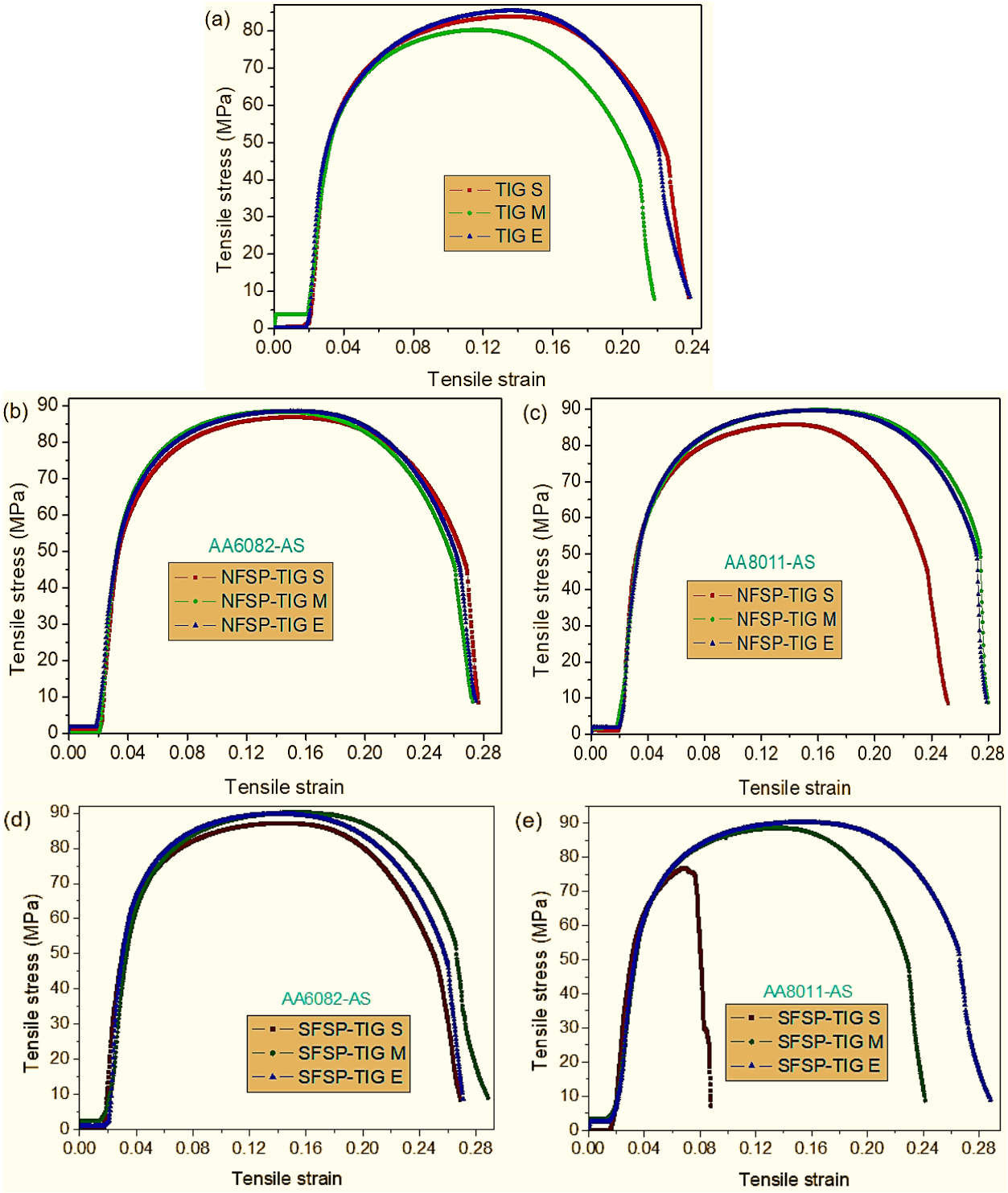

Figure 4.1.5.2: Tensile stress-strain curves: (a) TIG-welded; (b) NFSP-TIG AA6082-AS; (c) NFSP-TIG AA8011-AS; (d) SFSP-TIG AA6082-AS; (e) SFSP-TIG AA8011-AS.

The maximum UTS for the SFSP-TIG AA6082-AS joints was 90.222 MPa at a corresponding tensile strain rate of 13.75% and a yield strength of 71.778 MPa. The minimum UTS was 87.148 MPa at a tensile strain rate of 14.32% and yield strength of 69.719 MPa. The minimum and maximum tensile strain rates at the breakpoint were 24.131% and 27.099%, respectively. Additionally, the SFSP-TIG AA8011-AS had a maximum UTS of 90.25 MPa at a tensile strain rate of 15.36% and yield strength of 72.2 MPa. A minimum UTS was 76.944 MPa at a corresponding tensile strain rate of 6.92% and a yield strength of 61.555 MPa. The said joints had a minimum and maximum tensile strain rate (breakpoint) of 25.437% and 28.829%. The

tensile strength and tensile strain were significantly improved post-SFSP regardless of material positioning. This behaviour was in agreement with the microstructural grain sizes of the same joints which, showing remarkable refinement, plays a vital role in the strengthening of the material properties [220]. Moreover, this behaviour was in agreement with the Orowam hardening mechanism: the refinement of grain sizes reduces the presence of cracks within the joints, making the joint impossible to crack at lower stress, and thereby increasing the tensile strength of the SFSPed joints [221]. Furthermore, rapid cooling also played a crucial role in the improvement of the tensile properties by decreasing the chances of abnormal grain growth which is a common phenomenon when joints experience excessive heat which affects the joint properties negatively [222].

Table 4.1.5: Tensile properties of the joints.

Joint	Ultimate tensile stress (MPa)	Strain rate (%)	Yield strength (MPa) @ 0.2% offset	Fracture location
TIG S	83.833	23.790	67.076	HAZ
TIG M	80.277	21.885	64.222	HAZ
TIG E	85.42	23.889	68.336	HAZ
AA6082-AS				
NFSP-TIG S	86.958	27.666	69.566	NZ
NFSP-TIG M	88.472	27.251	70.778	NZ
NFSP-TIG E	88.53	27.489	70.824	NZ
AA8011-AS				
NFSP-TIG S	85.777	25.166	68.622	HAZ
NFSP-TIG M	89.777	27.994	71.822	NZ
NFSP-TIG E	89.588	27.886	71.670	NZ
AA6082-AS				
SFSP-TIG S	87.148	26.880	69.718	NZ
SFSP-TIG M	88.528	24.131	70.899	HAZ
SFSP-TIG E	90.222	27.099	71.778	HAZ
AA8011-AS				
SFSP-TIG S	76.944	8.769	61.555	NZ
SFSP-TIG M	88.578	27.489	70.863	NZ
SFSP-TIG E	90.250	28.829	72.201	NZ

With regards to specimen positioning, there was no particular order observed for the TIG-welded. However, for both NFSP-TIG and SFSP-TIG, the specimens extracted from the start of the joint possessed minimal tensile properties compared to those from the middle and towards the end of the joint. This behaviour is typically influenced by the mixing of material: at the beginning of the joint, the two materials reach melting points at different temperatures, with the AA6082 taking longer to melt completely, resulting in what is known as cold welds [217]. These cold welds render the beginning of the joint the weakest position and influence the joint properties negatively. Similar findings were identified in literature [108, 142, 172, 180]. Figure 4.1.5.3 depicts the average tensile properties of the TIG-welded and FSPed joints. The figure makes evident that both NFSP-TIG and SFSP-TIG joints were improved more than those of the TIG-welded joints. However, the most tensile properties were noted on the SFSP-TIG joints. Concerning material positioning on the NFSP-TIG, the AA6082-AS joint had a slightly higher strain rate than the AA8011-AS. However, the AA8011-AS had a higher tensile strength than the AA6082-AS. Additionally, the SFSP-TIG AA6082-AS joints showed both higher strain

rate and tensile strength than the AA8011-AS. The findings correlated with studies in literature [172-173].

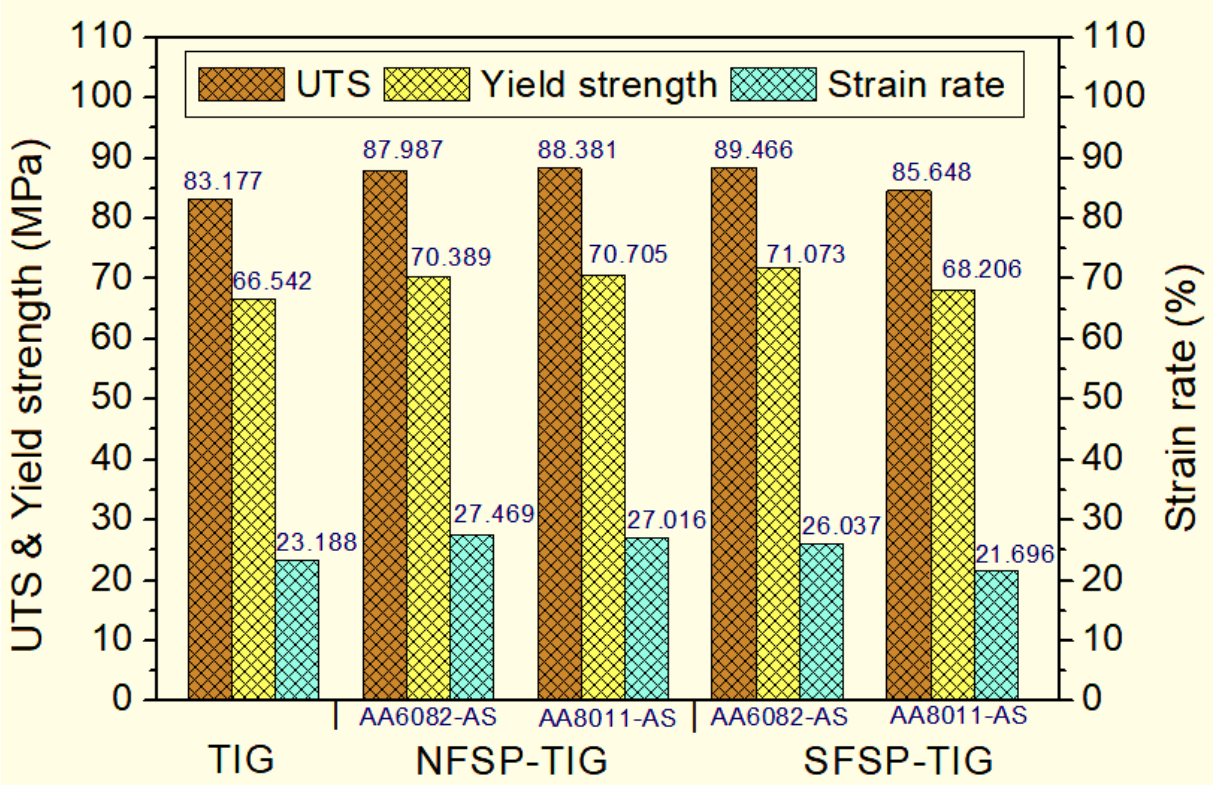

Figure 4.1.5.3: Average tensile properties of the TIG-welded, NFSP-TIG and SFSP-TIG joints.

4.1.6 Fracture surface analysis

The fracture surface morphology of the TIG-welded, NFSP-TIG and SFSP-TIG joints, presented in Figure 4.1.6, all showed a ductile failure mechanism. The ductility of the joints was manifested by the failure characteristics like the microvoids, dimples interfaced by the cleavage facets, dimples tore ridges and grain boundaries [141, 190, 206]. A sample of the ductile characteristics were marked on the figure: the yellowish circle represents large voids; the red arrow represents cleavage facets; the navy arrow for the tore ridges; and blue arrows for the microvoids. Figure 4.1.6(a, b, c, g, k, l) reveal similar morphologies, substantiated by the location of the fracture which was similar (HAZ). The morphology for Figure 4.1.6(m) shows a few dimples at the far end of the flat facets, representing a rather brittle mode that resulted in a rapid failure of the specimen. This behaviour correlates with the tensile stress and strain curves in Figure 4.5.1.2(e). As evident, the tensile strain confirmed the rapid failure.

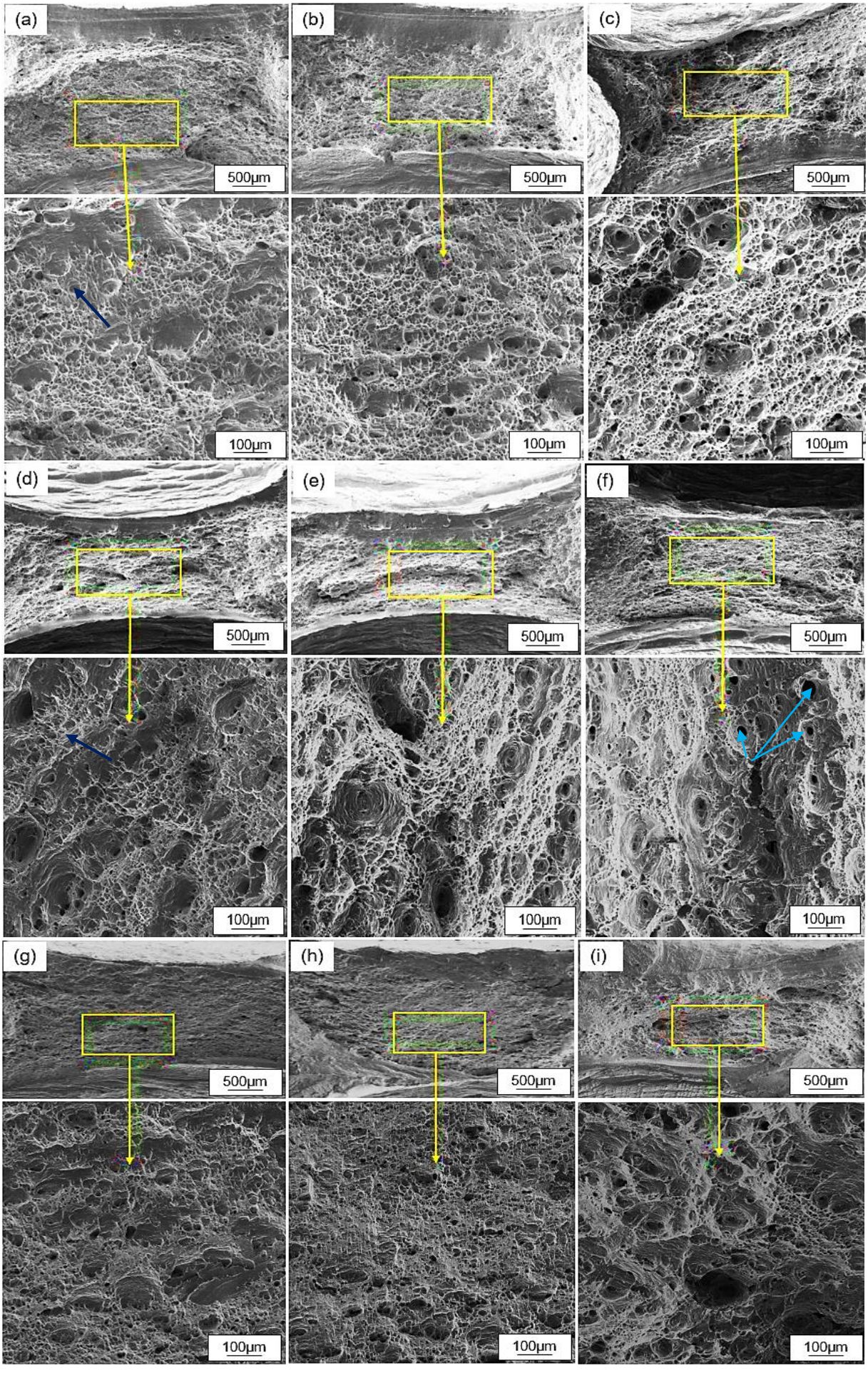
(a)
500μm
100μm
(b)
500μm
100μm
(c)
500μm
100μm
(d)
500μm
100μm
(e)
500μm
100μm
(f)
500μm
100μm
(g)
500μm
100μm
(h)
500μm
100μm
(i)
500μm
100μm

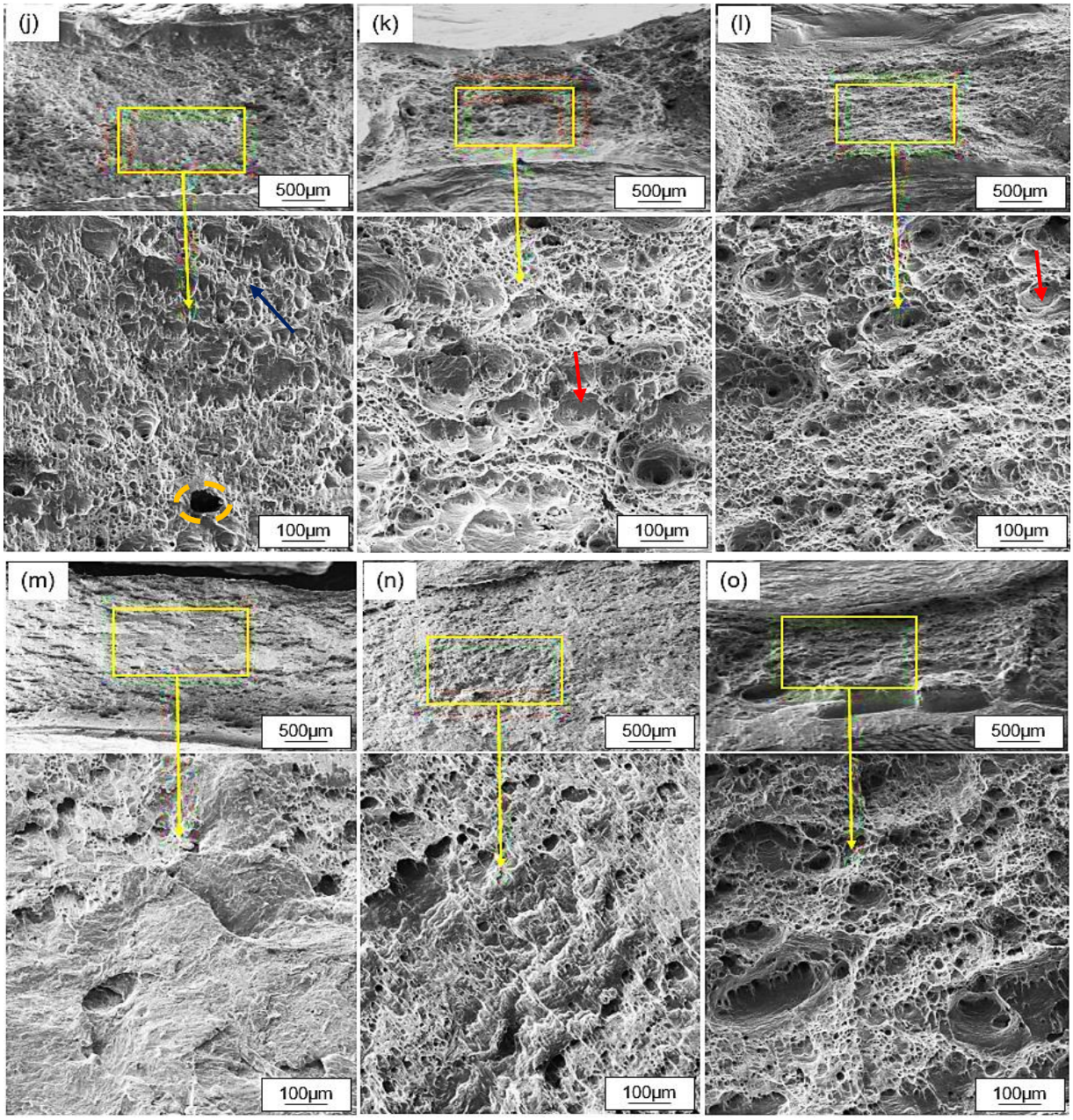

Figure 4.1.3.3: Fracture surface morphologies, TIG-welded joints: (a) start (b) middle (c) end; NFSP-TIG AA6082-AS joints: (d) start (e) middle (f) end; NFSP-TIG AA8011-AS joints: (g) start (h) middle (i) end; SFSP-TIG AA6082-AS joints: (j) start (k) middle (l) end; SFSP-TIG AA68011-AS joints: (m) start (n) middle (o) end.

4.1.7 Hardness tests

The Vickers hardness profiles for the TIG-welded, NFSP-TIG and SFSP-TIG joints are depicted in Figure 4.1.7.1. The corresponding NZ hardness bar charts are illustrated in Figure 4.1.7.2. The TIG-welded joints possessed a hardness range of 57 HV to 60 HV with an average of 58.5 HV. The NFSP-TIG AA6082-AS hardness ranged between 58 HV to 63 HV with an average of 60.5 HV, and the NFSP-TIG AA8011-AS was between 59 HV to 64 HV with a range of 61.5. The SFSP-TIG hardness range obtained for the AA6082-AS was 60 HV to 66 HV with an average of 63 HV and for the AA8011-AS was 67 HV to 70 HV with an average of 69 HV. The NZ hardness obtained in all the joints was lower than the AA6082 alloy but higher than the AA8011 alloy. This behaviour was related to the AA6082 alloy being a precipitate tempered alloy which is very sensitive to elevated temperatures [223-225]. These precipitates are

referred to as β' or MgSi precipitates. Sameer and Birru [208] specified that precipitates result in the drop of mechanical properties at temperatures above 200°C. However, the extent of the weakening of the properties depends not only on temperature but also on the time of exposure [226]. Comparing the SFSP-TIG and the NFSP-TIG NZ hardness of the joints, it is undeniable that the operating mediums yielded different results on the hardness, a conclusion that correlates with the study by Rakhmonov et al. [226] as explained previously. Additionally, the low temperature of the water hindered the rate of precipitate dissolution and grain growth [227].

The hardness in all the AA6082-AS joints showed a decline from the AA6082 alloy to the HAZ, rising to the TMAZ and NZ. However, past the NZ, they decline to the hardness of the AA8011. Furthermore, in the AA8011-AS joints, the hardness decreases after the AA8011 alloy to the HAZ, rises to the NZ and continues to rise to the hardness of the AAA6082 alloy. This phenomenon was governed by the variation in the grain sizes at the respective zones [217]. The hardness behaviour on the HAZ and TMAZ supports the belief that the said regions are the lowest hardness distribution regions (LHDR) [228]. As far as specimen positioning is concerned, there was no particular trend noted. However, with regards to the material positioning of the FSPed joints, the maximum NZ hardness was obtained when the AA8011 alloy was positioned on the advancing side.

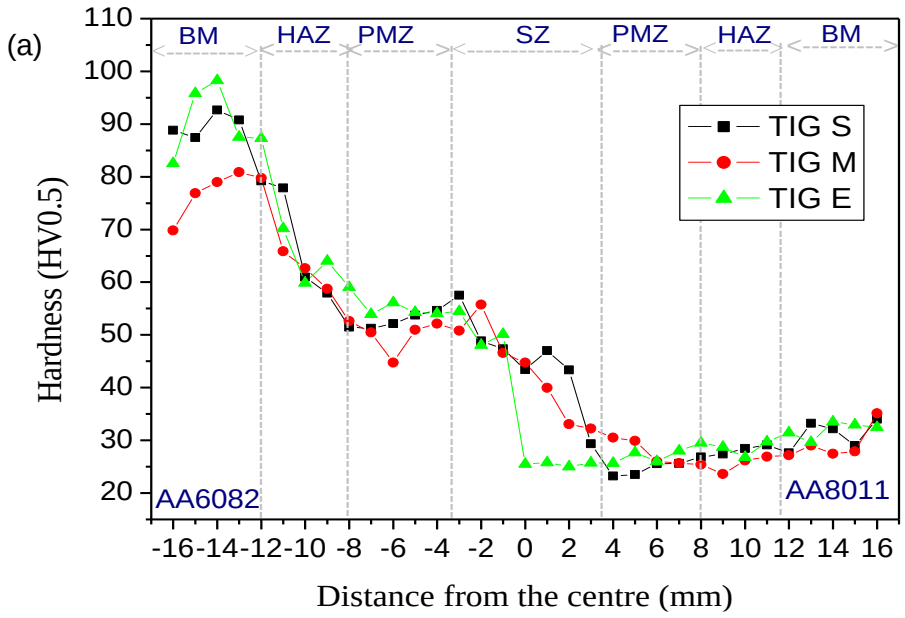

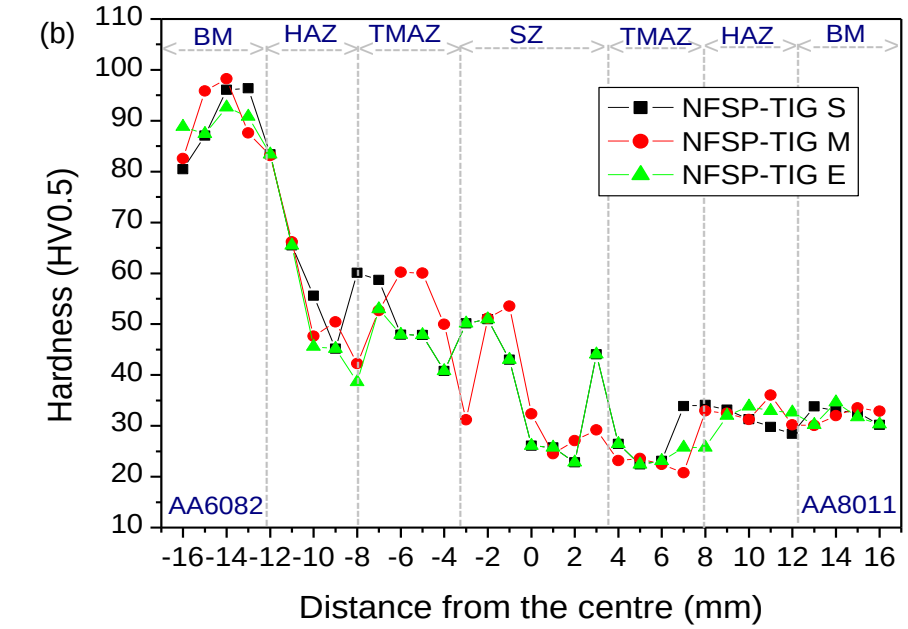
(b)
BM
HAZ
TMAZ
SZ
TMAZ
HAZ
BM
NFSP-TIG S
NFSP-TIG M
NFSP-TIG E
Hardness (HV0.5)
AA6082
AA8011
Distance from the centre (mm)

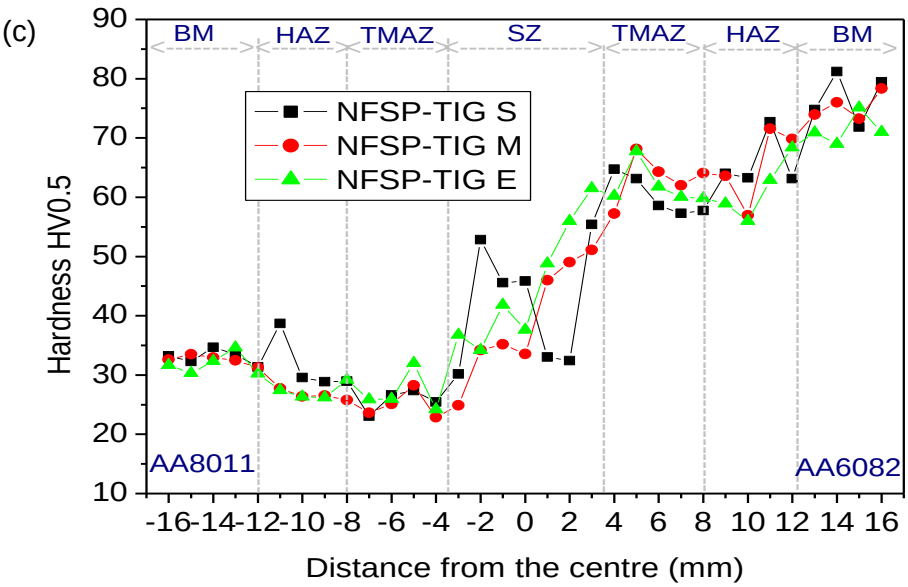
(c)
BM
HAZ
TMAZ
SZ
TMAZ
HAZ
BM
NFSP-TIG S
NFSP-TIG M
NFSP-TIG E
Hardness HV0.5
AA8011
AA6082
Distance from the centre (mm)

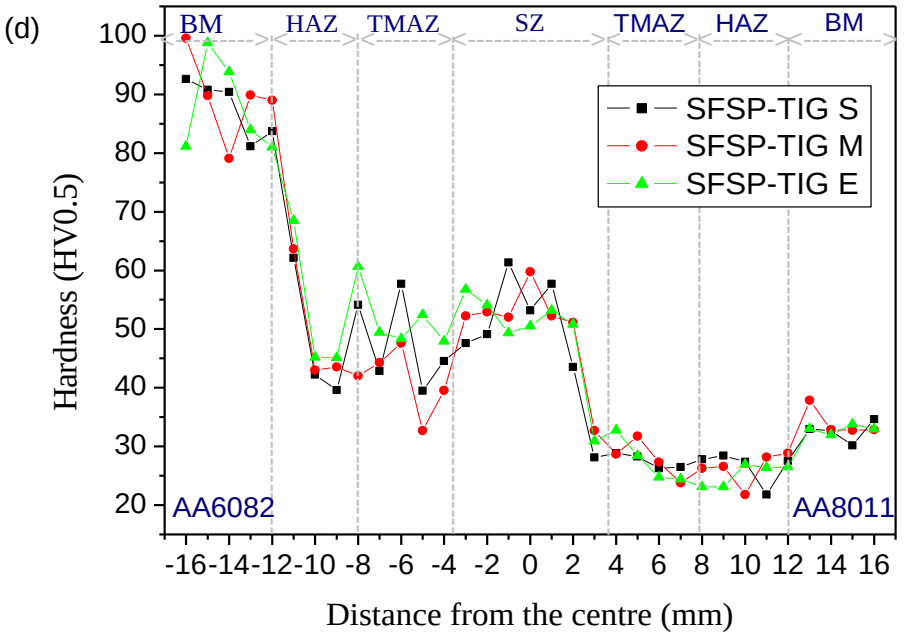
(d)
BM
HAZ
TMAZ
SZ
TMAZ
HAZ
BM
SFSP-TIG S
SFSP-TIG M
SFSP-TIG E
Hardness (HV0.5)
AA6082
AA8011
Distance from the centre (mm)

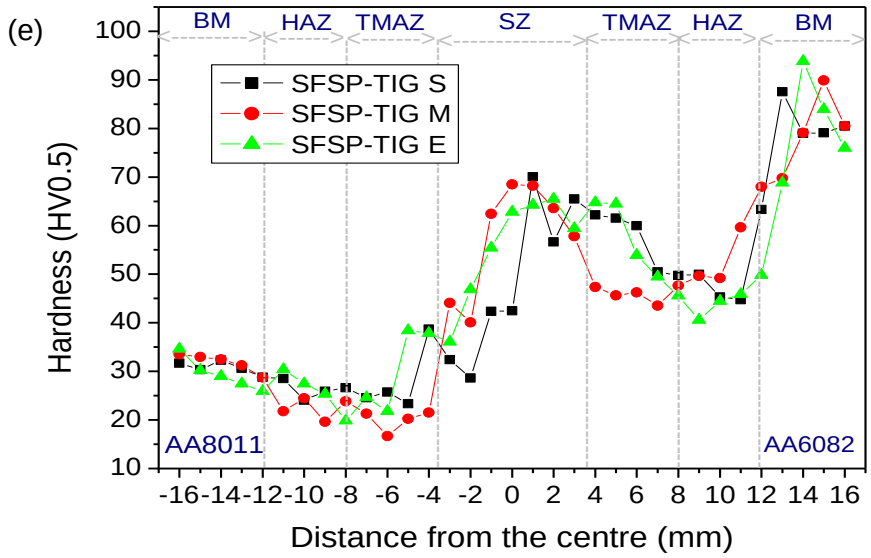

Figure 4.1.7.1: Hardness profiles: (a) TIG-welded; (b) NFSP-TIG AA6082-AS; (c) NFSP-TIG AA8011-AS; (d) SFSP-TIG AA6082-AS; (e) SFSP-TIG AA8011-AS.

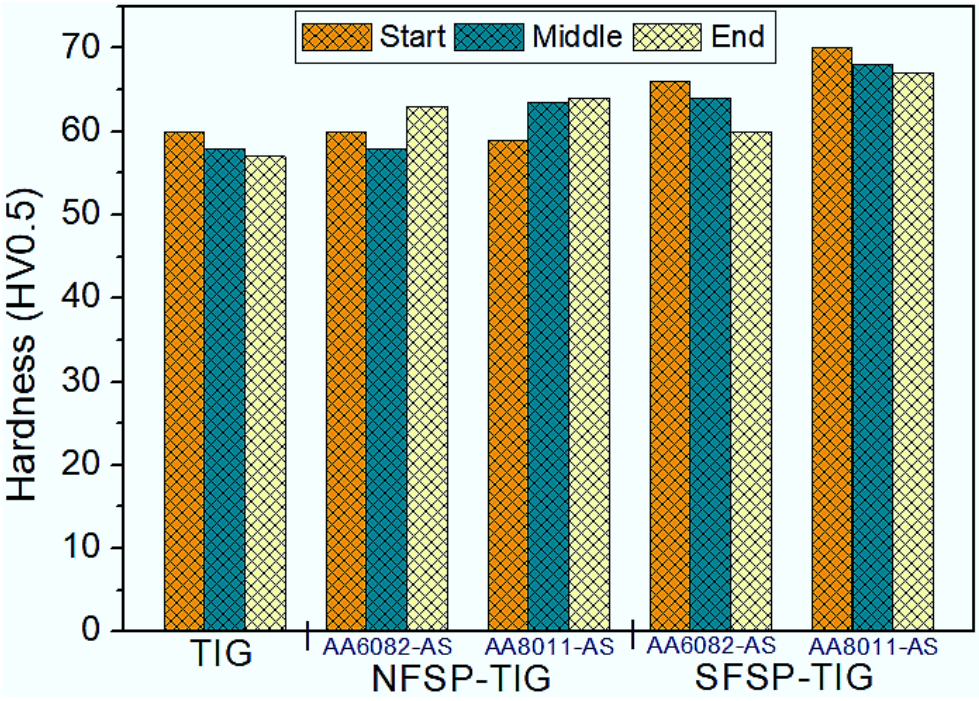

Figure 4.1.7.2: Nugget zone hardness bar charts of the TIG-welded, SFSP-TIG and NFSP-TIG.

4.2 FSP of FSWed joints

4.2.1 X-ray diffraction analysis and chemical composition of the joints

XRD patterns for the FSWed, NFSP-FSWed and SFSP-FSWed are shown in Figure 4.2.1. and respective chemical compositions in Table 4.2.1. All the joint patterns showed one dominant phase present – aluminium (α-Al) – identified by the red dotted lines. Examining the obtained diffraction patterns, it was noted that the patterns had similar phases. The phases obtained were the Mg_2Si, $Mg_{2.7}Fe$ and the Al_7Mn_4Fe. The Mg_2Si particles are very significant for the strengthening or the joint properties as previously discussed in section 4.1.1 [183].

(a)

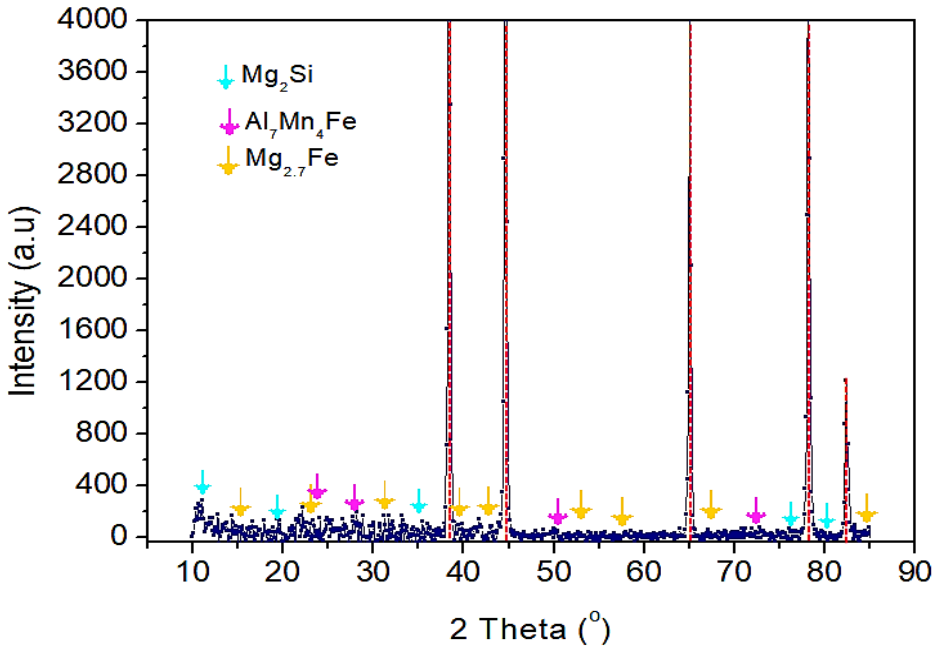
Mg2Si
Al7Mn4Fe
Mg2.7Fe
Intensity (a.u)
2 Theta (°)

(b)

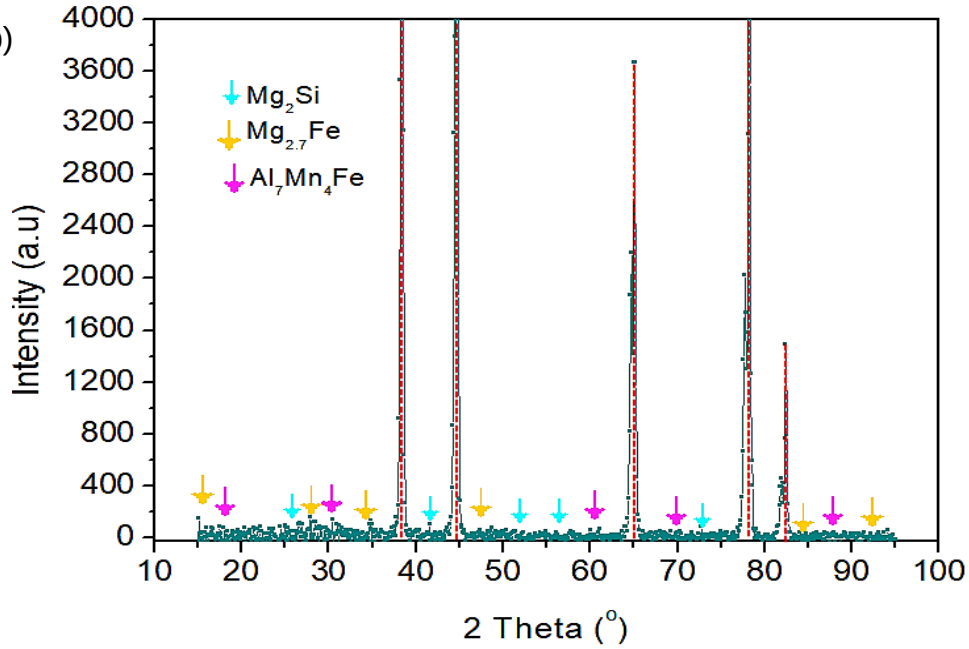
Mg2Si
Mg2.7Fe
Al7Mn4Fe
Intensity (a.u)
2 Theta (°)

(c)

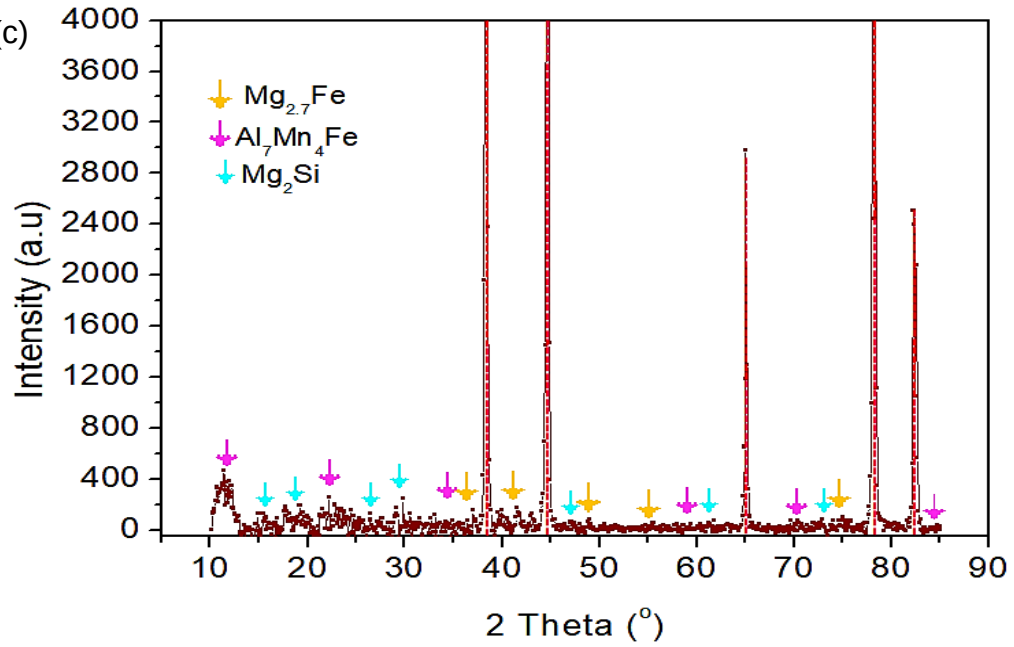
Mg2.7Fe
Al7Mn4Fe
Mg2Si
Intensity (a.u)
2 Theta (°)

(d)

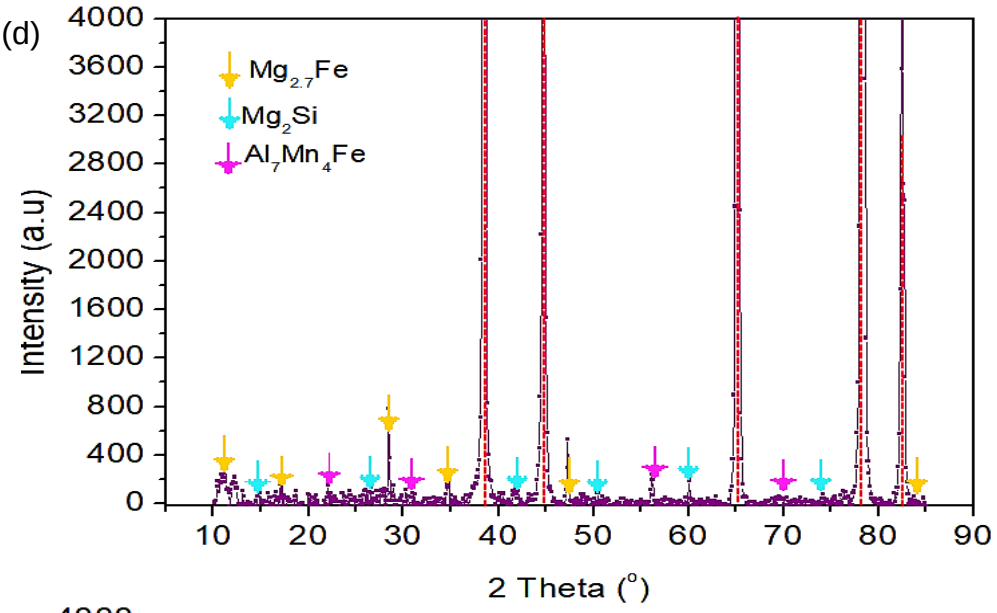
Mg2.7Fe
Mg2Si
Al7Mn4Fe
Intensity (a.u)
2 Theta (°)

(e)

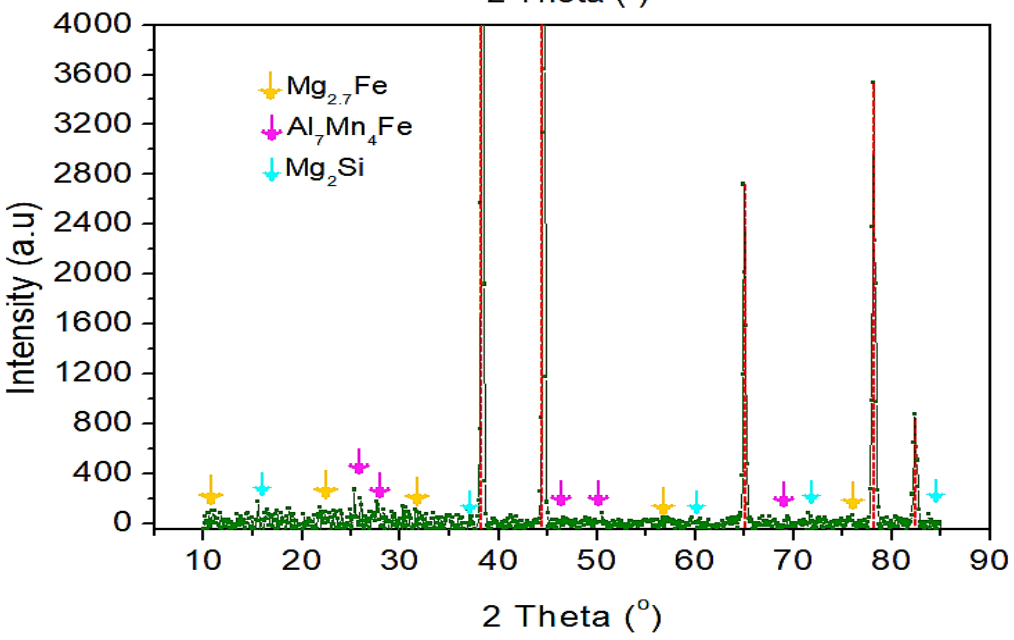
Mg2.7Fe
Al7Mn4Fe
Mg2Si
Intensity (a.u)
2 Theta (°)

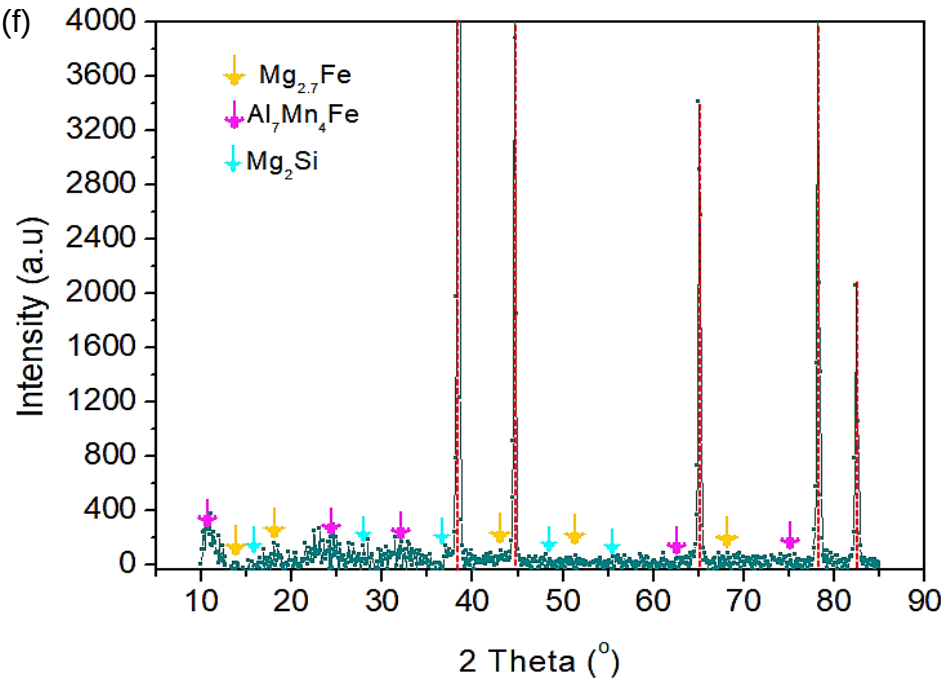

Figure 4.2.1: X-ray diffraction patterns collected from the top surface: (a) FSW AA6082-AS; (b) FSW AA8011-AS; (c) NFSP-FSW AA6082-AS; (d) NFSP-FSW AA8011-AS; (e) SFSP-FSW AA6082-AS; (f) SFSP-FSW AA8011-AS.

Table 4.2.1: Chemical composition of joints (Wt%).

Joint type	Si	Fe	Cu	Mn	Mg	Ni	Zn	Ti	Pb	Al
FSW AA6082-AS	0.452	1.362	0.044	0.170	1.175	0.112	0.613	0.038	0.013	Bal
FSW AA8011-AS	0.538	1.310	0.005	0.505	1.128	0.109	0.967	0.040	0.027	Bal
NFSP-FSW AA6082-AS	0.421	1.164	0.061	0.162	1.072	0.113	0.830	0.032	0.045	Bal
NFSP-FSW AA8011-AS	0.474	1.349	0.050	0.154	1.165	0.122	1.047	0.035	0.030	Bal
SFSP-FSW AA6082-AS	0.336	1.206	0.033	0.177	1.019	0.137	0.754	0.041	0.058	Bal
SFSP-FSW AA8011-AS	0.417	1.098	0.078	0.161	1.159	0.102	0.857	0.034	0.080	Bal

4.2.2 Macrostructural analysis

The macrographs for the FSW, NFSP-FSW and SFSP-FSW joints are illustrated in Figure 4.2.2. The FSW joints for both AA6082-AS and AA8011-AS showed micrographs with pores and tunnel defects (see Figure 4.2.2[a-f]). Similarly, Figure 4.2.2(g,h,j,k) for the NFSP-FSW joints showed macrographs with tunnel defects, and Figure 4.2.2(m) for the SFSP-FSW joints. Regardless of the joint configuration, tunnel defects are common when joining dissimilar materials. This kind of defect is associated with insufficient heat input and inadequate consolidation of material at the joint [188, 229]. Additionally, the tool may have traversed ahead before enough material was deposited behind, thereby creating a void. The created void then manifests itself as a tunnelling defect which results in the degradation of mechanical properties [230]. Figure 4.2.2(i,l,) of the NFSP-FSW joints and Figure 4.2.2(n-r) of the SFSP-FSW joints showed macrographs with no defects. This, therefore, means there was sufficient heat input formed by the plastic deformation and frictional energy during FSP [231-232]. Single oval-shaped stir bands were noted on the FSW joints structures. These oval-shaped nugget bands are primarily referred to as onion ring structures [233-234]. The NFSP-FSW and the SFSP-FSW joints showed a double onion ring structure due to the re-stirring and repeated plastic deformation of the joints. The onion rings were a result of the maximum deformation of the

AA6082/AA8011 alloys and dynamic recrystallization of the joints resulting in a homogeneous equiaxed grain structure [149,235-236].

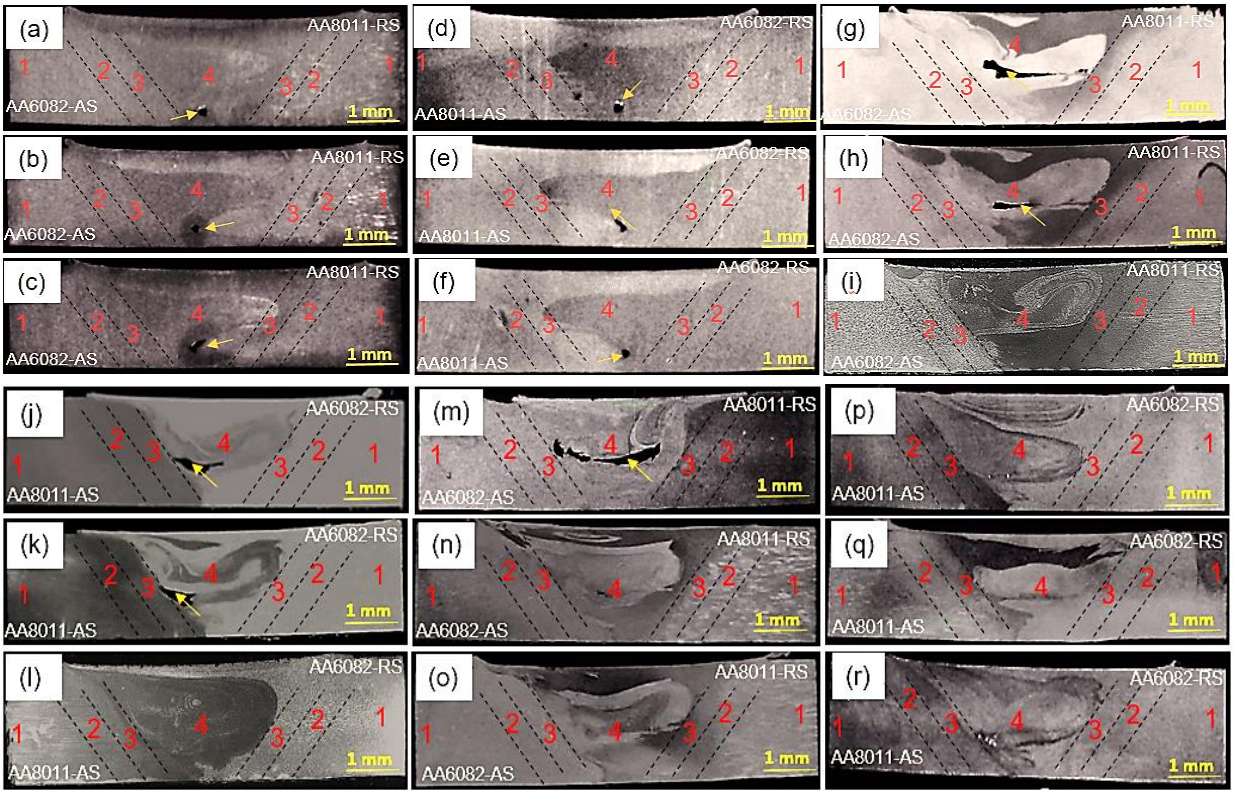

Figure 4.2.2: Macrographs: FSWed joints AA6082-AS: (a) start (b) middle (c) end; FSWed joints AA68011-AS: (d) start (e) middle (f) end; NFSP-FSW AA6082-AS joints: (g) start (h) middle (i) end; NFSP-FSW AA8011-AS joints: (j) start (k) middle (l) end; SFSP-FSW AA6082-AS joints: (m) start (n) middle (o) end; SFSP-FSW AA68011-AS joints: (p) start (q) middle (r) end.

4.2.3 Microstructural analysis

Figures 4.2.3.1 and 4.2.3.2 depict micrographs for the FSW joints at AA6082-AS and AA8011-AS. respectively. Three microstructural zones – namely HAZ, TMAZ and NZ – were noted on these figures. The different flow of the materials was noted in the nugget zones, in the form of different colours mixing the light brown and the dark brown. The light brown represents the AA8011 alloy while the dark brown represents the AA6082 alloy. This indicates that the FSWed joints, regardless of material positioning, underwent plastic deformation and dynamic recrystallization resulting in fine equiaxed grain structures [200-201]. This behaviour is noted by the oval flow pattern as visible on the nugget zones. A kissing bond was highlighted in Figure 4.3.2(h) by a red arrow: this type of defect results from inadequate pressure and insufficient stirring of the materials, thus instigating inefficient material deformation in the joint [230]. However, the kissing bond can also be a result of the oxide layer present on the base materials, when not removed properly prior to FSW, which can lead to improper bonding and manifest itself as a kissing bond [237]. The kissing bond is usually found at the interface of the materials [234].

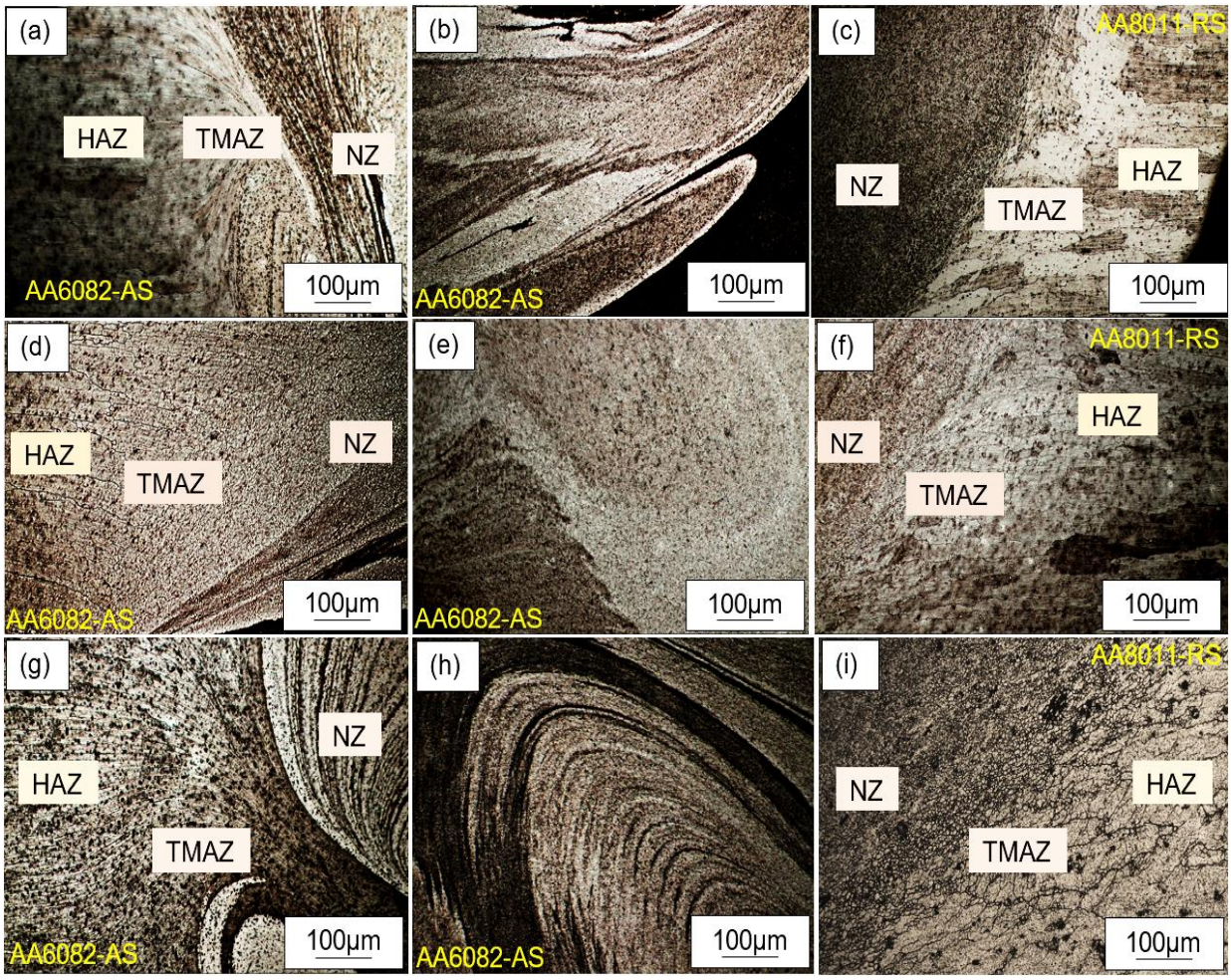

Figure 4.2.3.1: FSW joints optical micrographs at objective 5×, AA6082-AS: start: (a) advancing side (b) NZ (c) retreating side; middle: (d) advancing side (e) NZ (f) retreating side; end: (g) advancing side (h) NZ (i) retreating side.

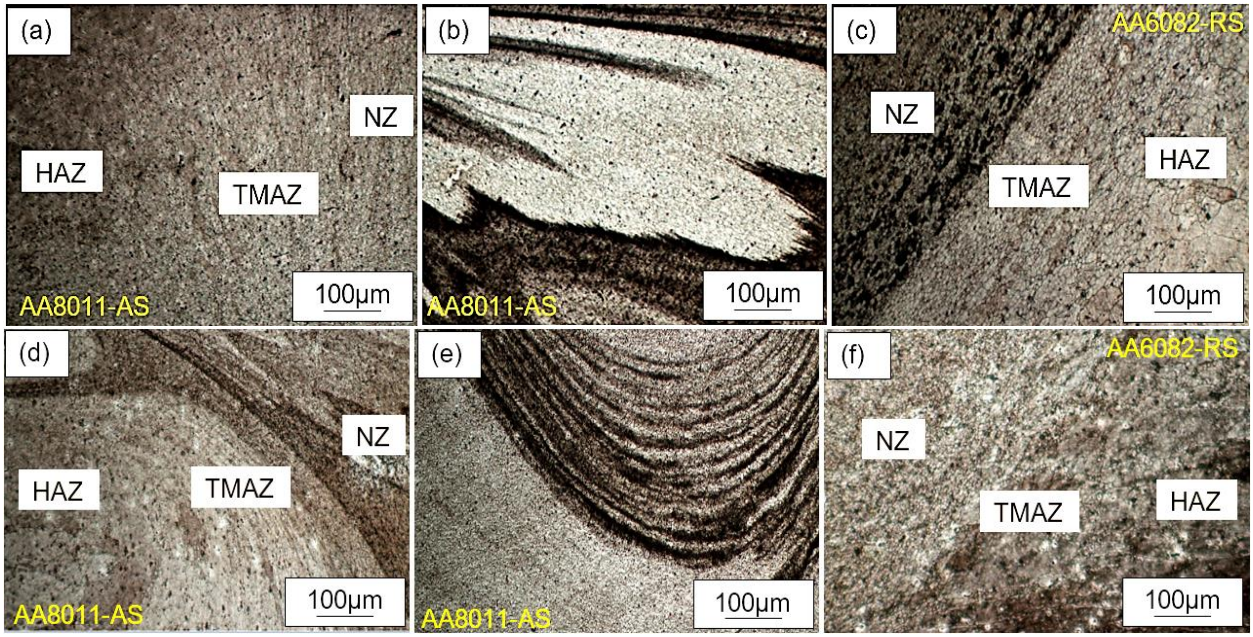

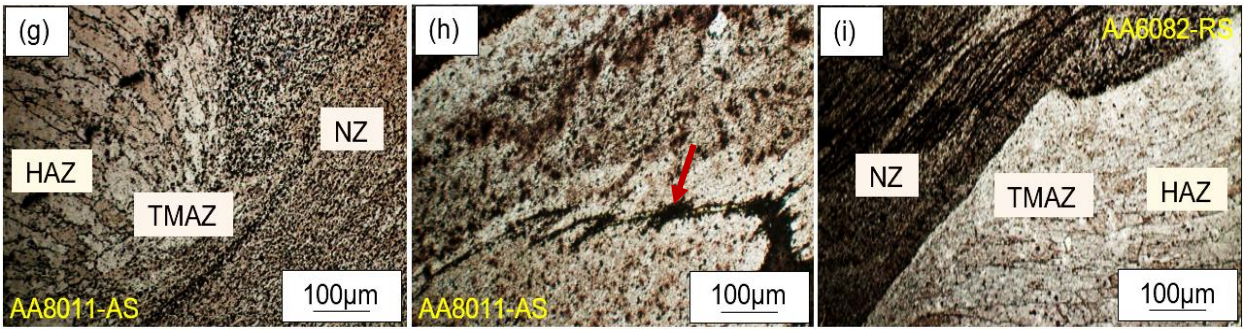

Figure 4.2.3.2: FSW joints optical micrographs, AA8011-AS: start: (a) advancing side (b) NZ (c) retreating side; middle (d) advancing side (e) NZ (f) retreating side; end: (g) advancing side (h) NZ (i) retreating side.

The NFSP-FSW optical micrographs are illustrated in Figures 4.2.3.3 and 4.2.3.4. The three previously mentioned microstructural zones were noted from the figures. Similar observations were also noted on the SFSP-FSW joints in Figures 4.2.3.5 and 4.2.3.6. The FSPed joints regardless of the conditions showed more homogenous grain structures, compared to that of the FSW joints. There were no defects noted on the micrographs of the NFSP-FSW and SFSP-FSW joints. The FSP application through the double stirring and repeated maximum plastic deformation resulted in a recrystallized microstructural zones, resulting in the repairing of the defects previously noted on the FSW joints [239].

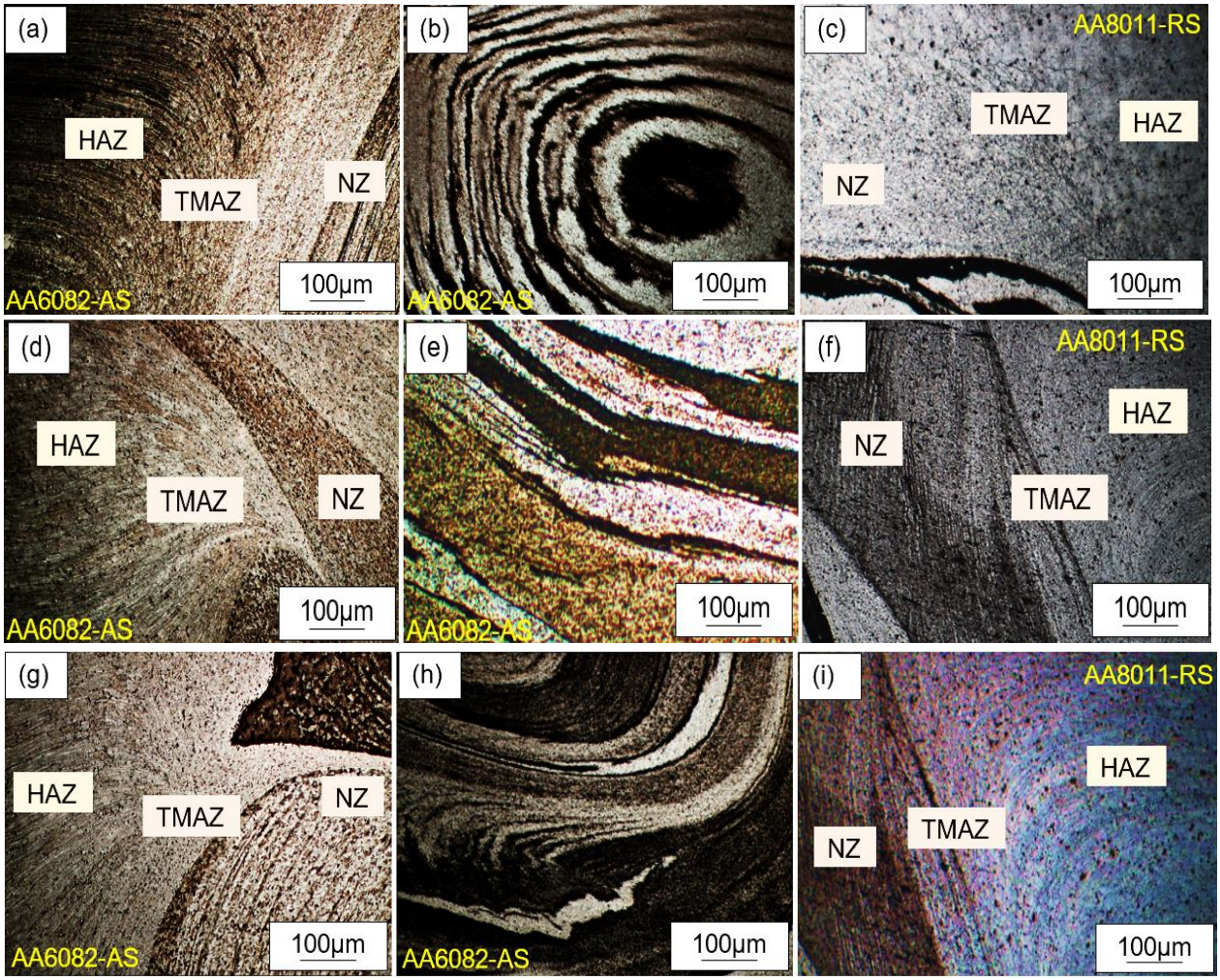

Figure 4.2.3.3: NFSP-FSW joints optical micrographs, AA6082-AS: start: (a) advancing side (b) NZ (c) retreating side; middle: (d) advancing side (e) NZ (f) retreating side; end: (g) advancing side (h) NZ (i) retreating side.

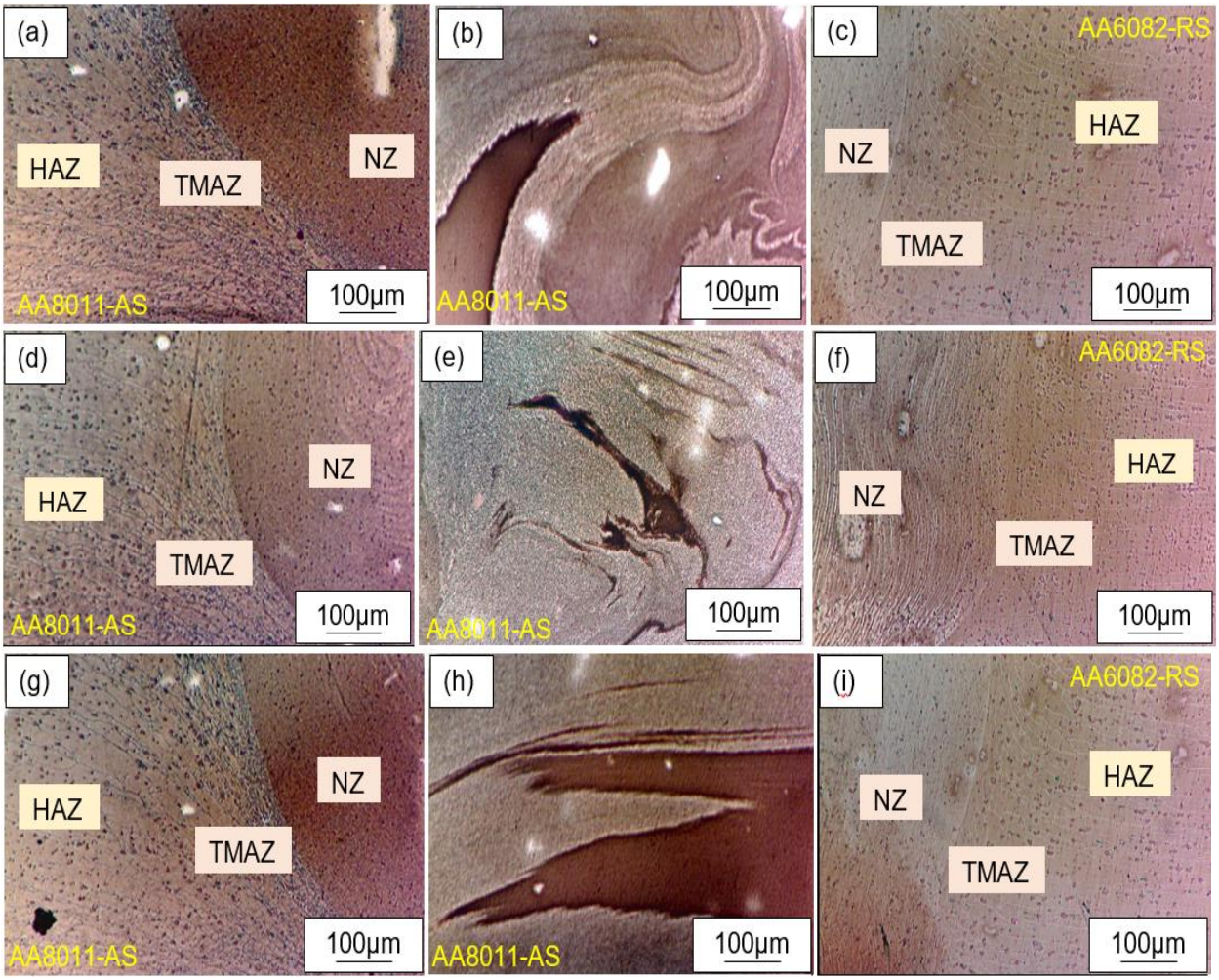

Figure 4.2.3.4: NFSP-FSW joints optical micrographs, AA6082-AS: start: (a) advancing side (b) NZ (c) retreating side; middle: (d) advancing side (e) NZ (f) retreating side; end: (g) advancing side (h) NZ (i) retreating side.

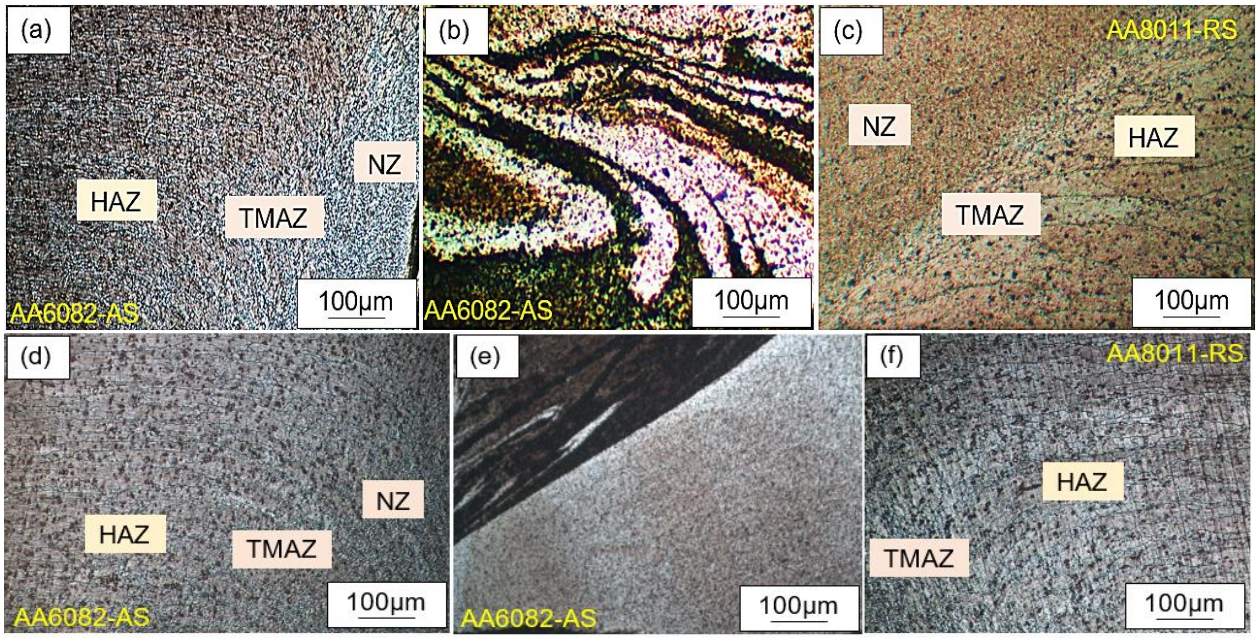

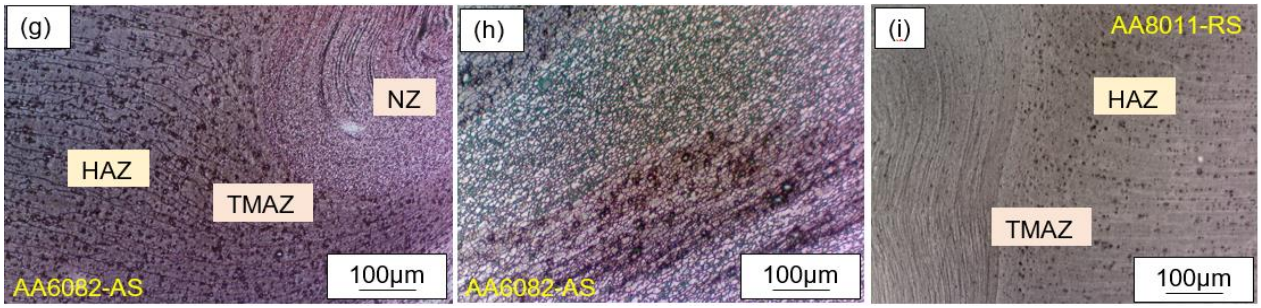

Figure 4.2.3.5: SFSP-FSW joints optical micrographs, AA8011-AS: start: (a) advancing side (b) NZ (c) retreating side; middle (d) advancing side (e) NZ (f) retreating side; end (g) advancing side (h) NZ (i) retreating side.

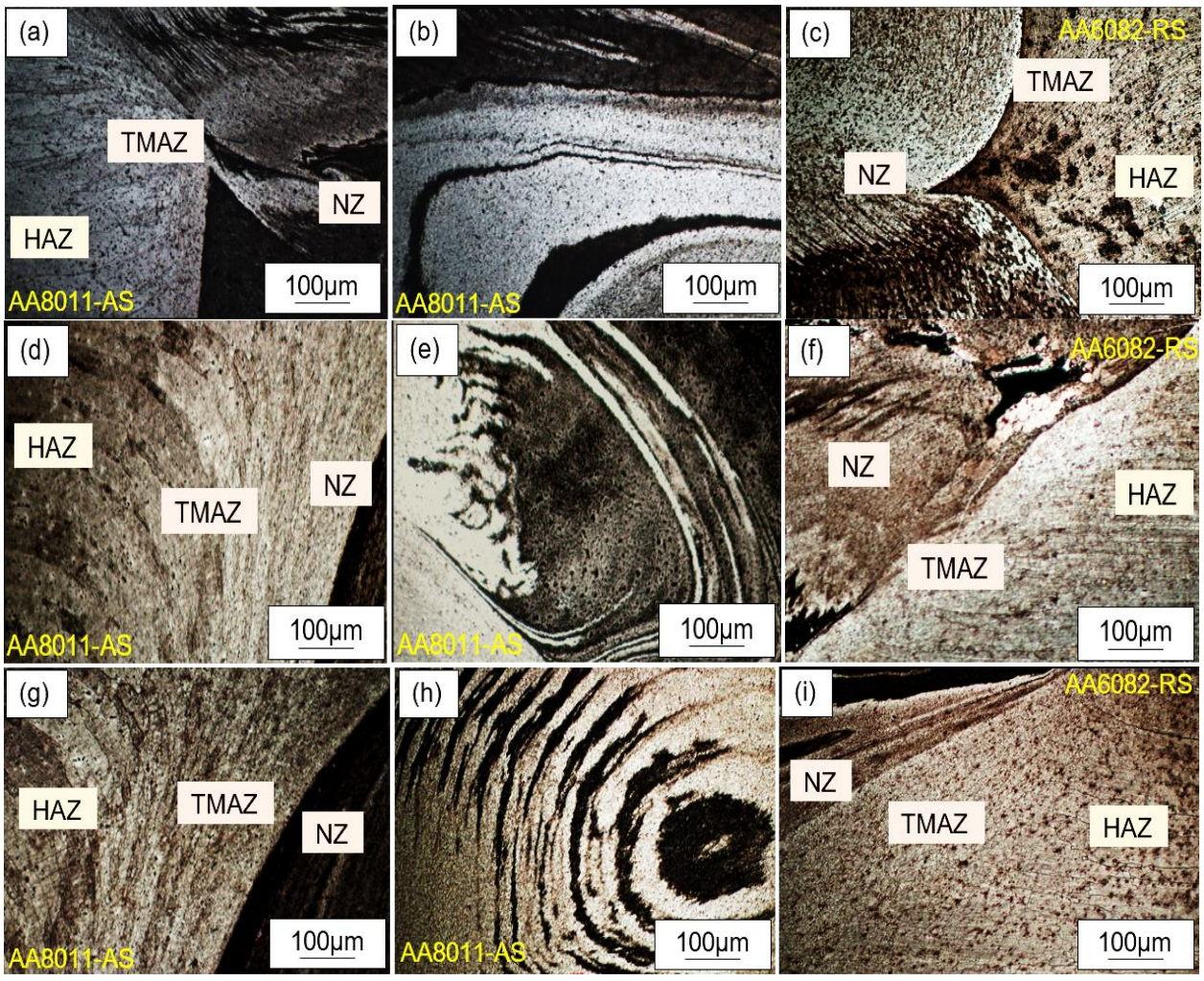

Figure 4.2.3.6: SFSP-FSW joints optical micrographs, AA8011-AS start: (a) advancing side (b) NZ (c) retreating side; middle: (d) advancing side (e) NZ (f) retreating side; end: (g) advancing side (h) NZ (i) retreating side.

Figure 4.2.3.7 presents the NZ optical micrographs for the FSW-welded, NFSP-FSW and SFSP-FSW joints. Table 4.2.3 shows the measured grain sizes and standard deviation of the optical micrographs of the NZ with the grain distribution charts presented in Figure 4.2.3.8. The mean grain size of the FSWed AA6082-AS was 22.470 µm to 23.976 µm with a standard deviation range of 6.521 µm to 7.770 µm. The FSWed AA8011-AS joints had a mean grain size range of 23.720 µm to 24.249 µm with a standard deviation range of 6.854 µm to 9.946 µm. The NFSP- FSW AA6082-AS mean grain size range was 11.250 µm to 13.460 µm and a

standard deviation of 3.686 µm to 4.535 µm. The mean grain size range for the NFSP-FSW AA8011-AS was 12.453 µm to 14.171 µm and a standard deviation of 3.919 µm to 4.982 µm. The SFSP-FSW AA6082-AS joints had a mean grain size range of 4.966 µm to 6.688 µm, with a standard deviation range of 1.795 µm to 2.662 µm. A mean grain size range of 5.824 µm to 6.760 µm with a standard deviation range of 1.923 µm to 2.471 µm was obtained for the SFSP-FSW AA8011-AS joints.

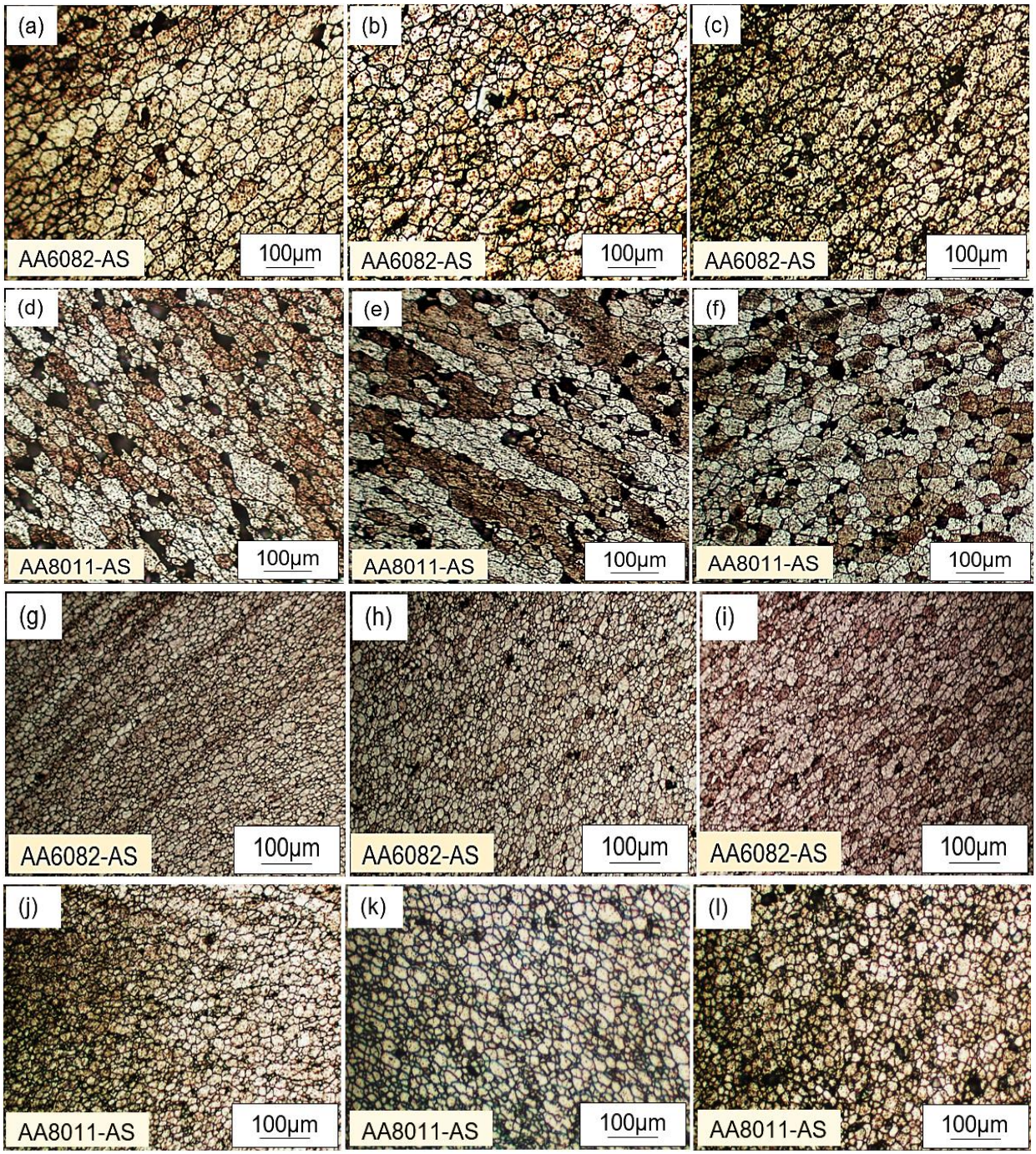

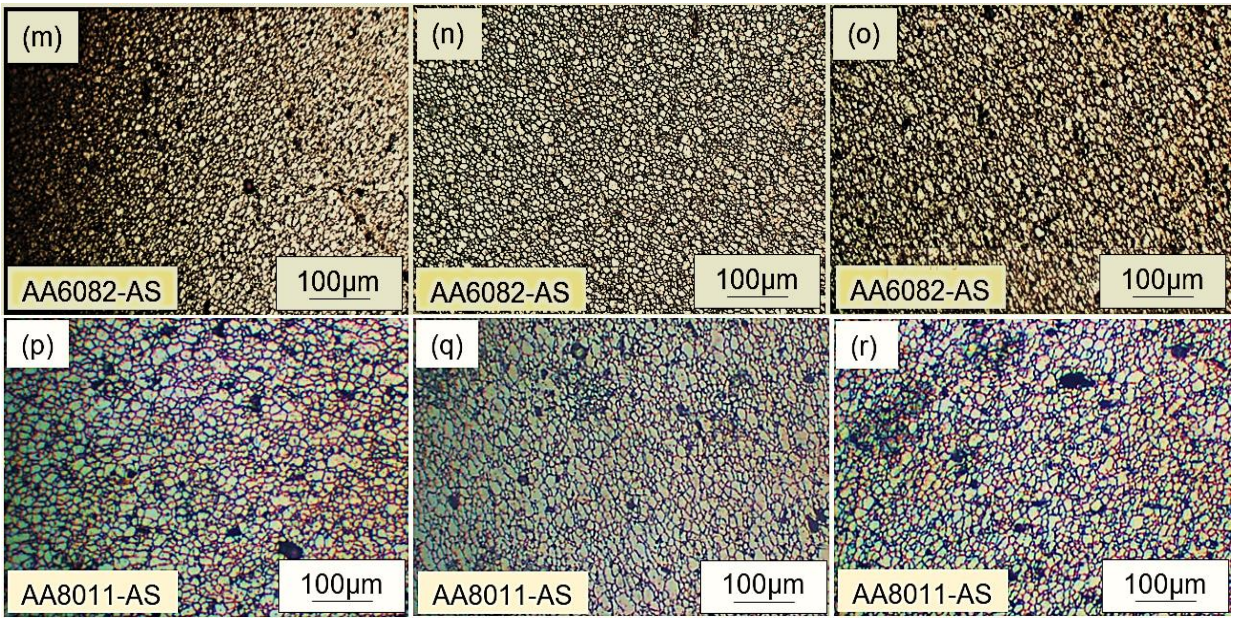

Figure 4.2.3.7: Optical micrographs at objective 20×, FSW AA6082-AS joints: (a) start (b) middle (c) end; FSW AA8011-AS joints: (d) start (e) middle (f) end; NFSP-FSW AA6082-AS joints: (g) start (h) middle (i) end; NFSP-FSW AA8011-AS joints: (j) start (k) middle (l) end; SFSP-FSW AA6082-AS joints: (m) start (n) middle (o) end; SFSP-FSW AA68011-AS joints: (p) start (q) middle (r) end.

The obtained grain distribution of the FSW showed uniformity with a partly homogeneous grain structure (see Table 4.2.3). The mean grain sizes prove that the application of both NFSP and SFSP improved the microstructure of the FSWed joint. The stirring of the materials and plastic deformation that occurred during the FSP of the FSWed joints were determined as responsible for the recrystallized grain structures [207-208]. The application of FSP was noted to also decrease in the standard deviation of the joints. This behaviour means that the FSPed joints had fewer measurement deviations in the grain sizes [173]. Similar findings were reported in the literature [149]. As far as specimen positioning is concerned, there was no particular trend found on any joints produced.

Table 4.2.3: Grain sizes and standard deviations for the NZ.

Joint	Mean grain size (µm)	Minimum grain size (µm)	Maximum grain size (µm)	Standard deviation (µm)
AA6082-AS				
FSW E	23.297	11.779	39.791	6.521
FSW M	22.470	8.724	45.296	9.014
FSW E	23.976	7.070	41.736	7.770
AA8011-AS				
FSW S	23.720	9.980	45.186	9.946
FSW M	24.249	10.118	46.825	9.753
FSW E	24.049	8.957	40.470	6.854
AA6082-AS				
NFSP-FSW S	11.250	3.342	19.738	3.948
NFSP-FSW M	13.460	7.057	25.143	3.686
NFSP-FSW E	12.716	4.236	23.786	4.535
AA8011-AS				
NFSP-FSW S	14.171	4.003	27.384	4.671
NFSP-FSW M	14.075	5.219	22.644	3.919
NFSP-FSW E	12.453	4.564	25.973	4.982

AA6082-AS				
SFSP-FSW S	5.180	1.738	9.214	1.795
SFSP-FSW M	4.966	1.218	9.82	2.170
SFSP-FSW E	6.688	1.910	10.15	2.662
AA8011-AS				
SFSP-FSW S	6.760	1.658	10.735	1.923
SFSP-FSW M	6.378	1.746	12.345	2.449
SFSP-FSW E	5.824	1.325	10.019	2.471

Figure 4.2.3.9 depicts the average grain sizes of the FSWed, NFSP-FSW and SFSP-FSW joints. Comparing the average grain sizes for NFSP-FSW to the SFSP-FSW joints, the SFSP-FSW AA6082-AS showed a much-refined grain size of about 44.978% and 38.156% for the SFSP-FSW AA8011-AS joints. The grain refinement was owed to the dynamic recrystallization whereby the maximum plastic deformation and thermal softening occurred in the nugget zone [102, 239]. Additionally, the SFSP had higher grain refinement due to the rapid cooling resulting in low temperatures, which prevents possible grain growth and lowers the duration of the processing [84, 156, 240]. Regardless of the FSP condition, the grain sizes of the AA6082-AS joints showed higher grain refinement than the AA8011-AS ones, a behaviour due to placing higher strength alloy on the AS which resulted in stirring, proper material flow and adequate heat input [91, 241]. Similar findings were reported in the literature [108, 210-211].

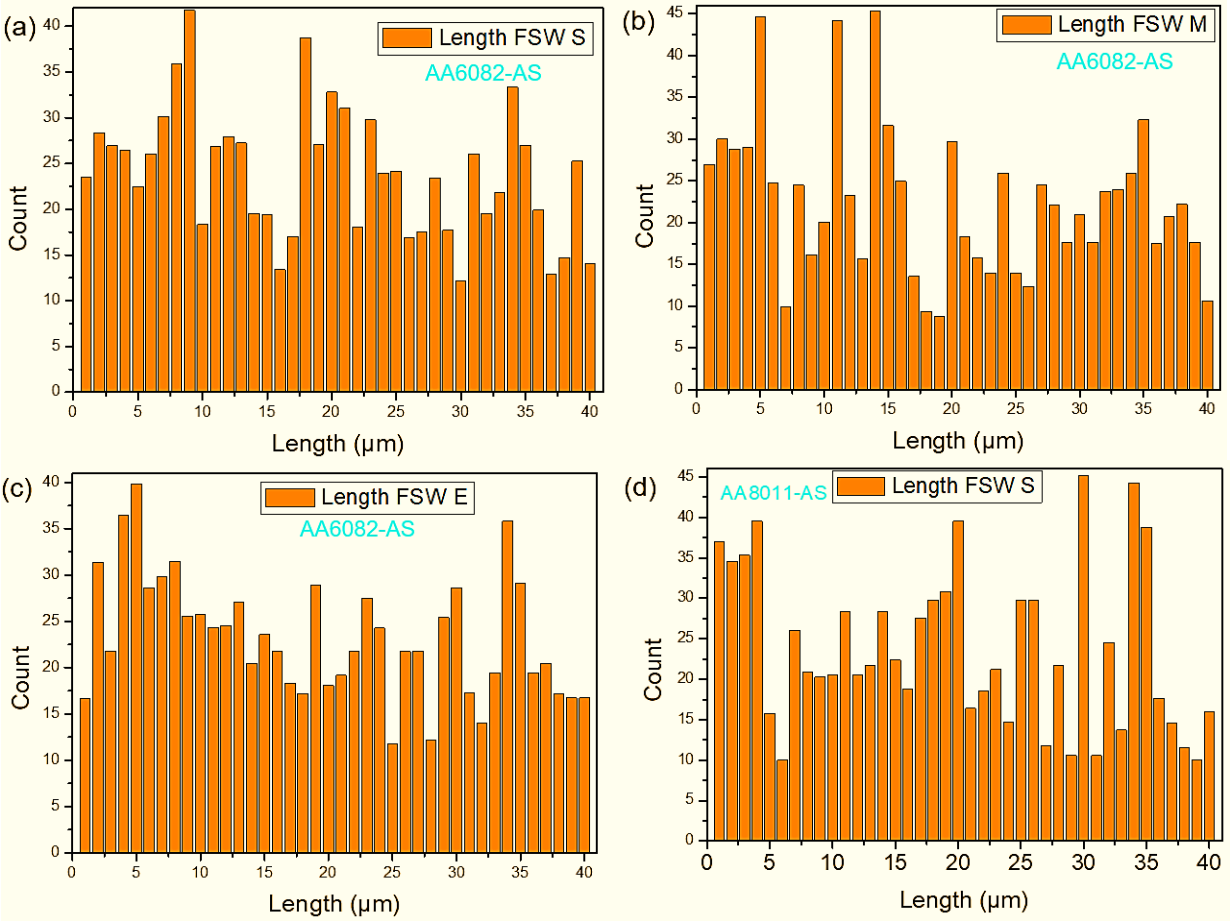

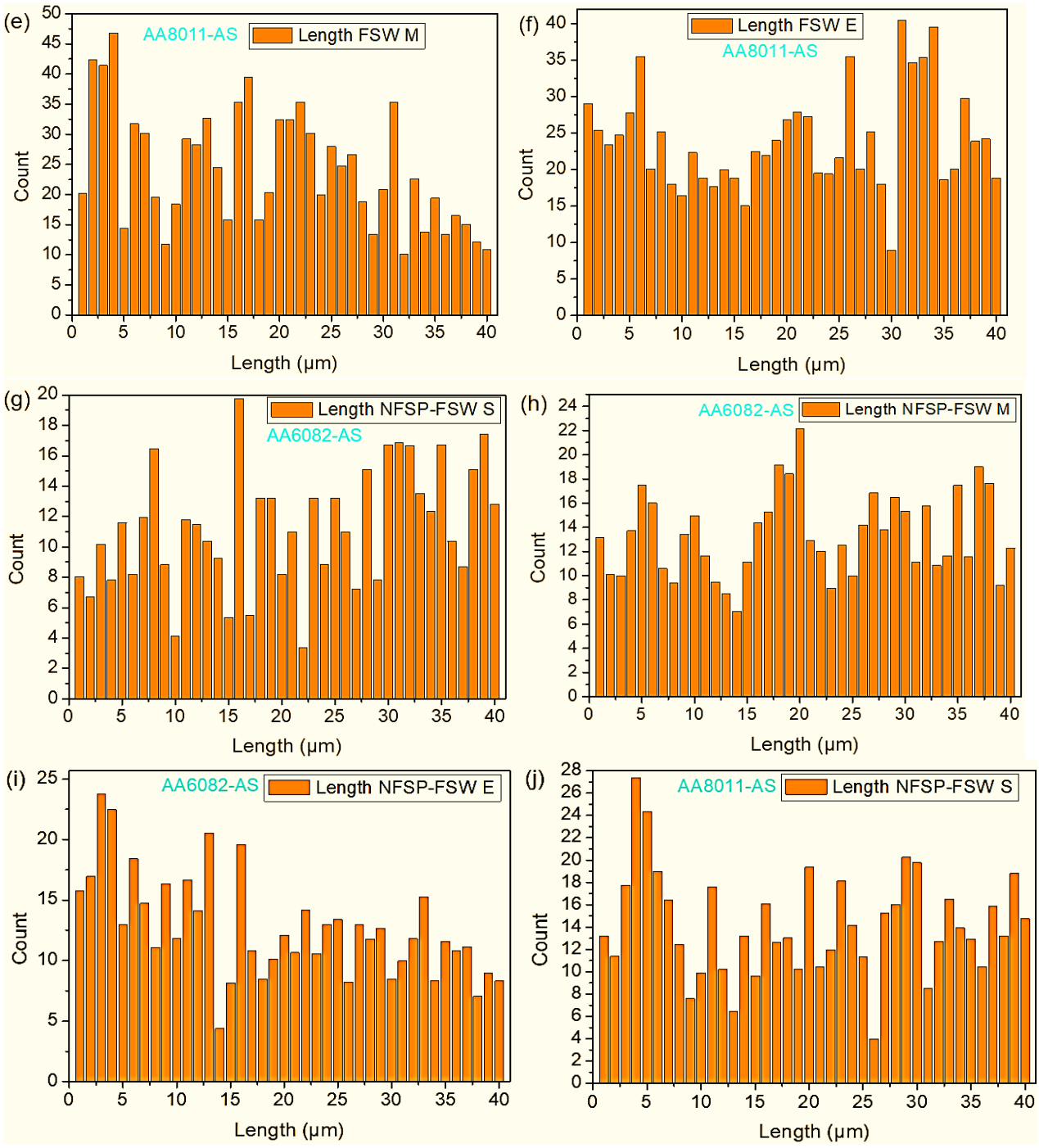
(e)
AA8011-AS
Length FSW M
Count
Length (μm)
(f)
Length FSW E
AA8011-AS
Count
Length (μm)
(g)
Length NFSP-FSW S
AA6082-AS
Count
Length (μm)
(h)
AA6082-AS
Length NFSP-FSW M
Count
Length (μm)
(i)
AA6082-AS
Length NFSP-FSW E
Count
Length (μm)
(j)
AA8011-AS
Length NFSP-FSW S
Count
Length (μm)

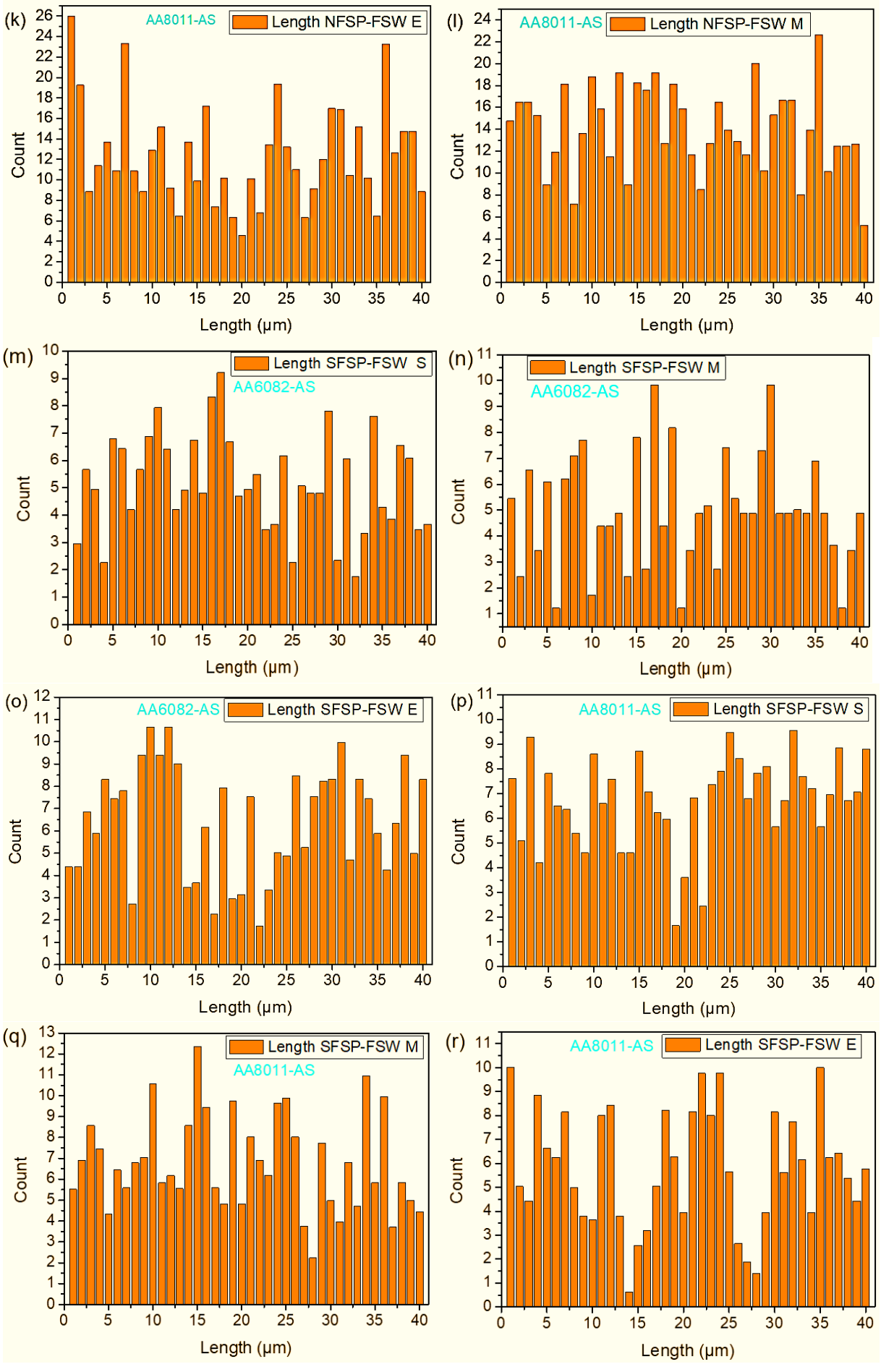
(k)
AA8011-AS
Length NFSP-FSW E
Count
Length (μm)
(l)
AA8011-AS
Length NFSP-FSW M
Count
Length (μm)
(m)
Length SFSP-FSW S
AA6082-AS
Count
Length (μm)
(n)
Length SFSP-FSW M
AA6082-AS
Count
Length (μm)
(o)
AA6082-AS
Length SFSP-FSW E
Count
Length (μm)
(p)
AA8011-AS
Length SFSP-FSW S
Count
Length (μm)
(q)
Length SFSP-FSW M
AA8011-AS
Count
Length (μm)
(r)
AA8011-AS
Length SFSP-FSW E
Count
Length (μm)

Figure 4.2.3.8: Grain distribution graphs: FSW AA6082-AS joints: (a) start (b) middle (c) end; FSW AA8011-AS joints: (d) start (e) middle (f) end; NFSP-FSW AA6082-AS joints: (g) start (h) middle (i) end; NFSP-FSW AA8011-AS joints: (j) start (k) middle (l) end; SFSP-FSW AA6082-AS joints: (m) start (n) middle (o) end; SFSP-FSW AA68011-AS joints: (p) start (q) middle (r) end.

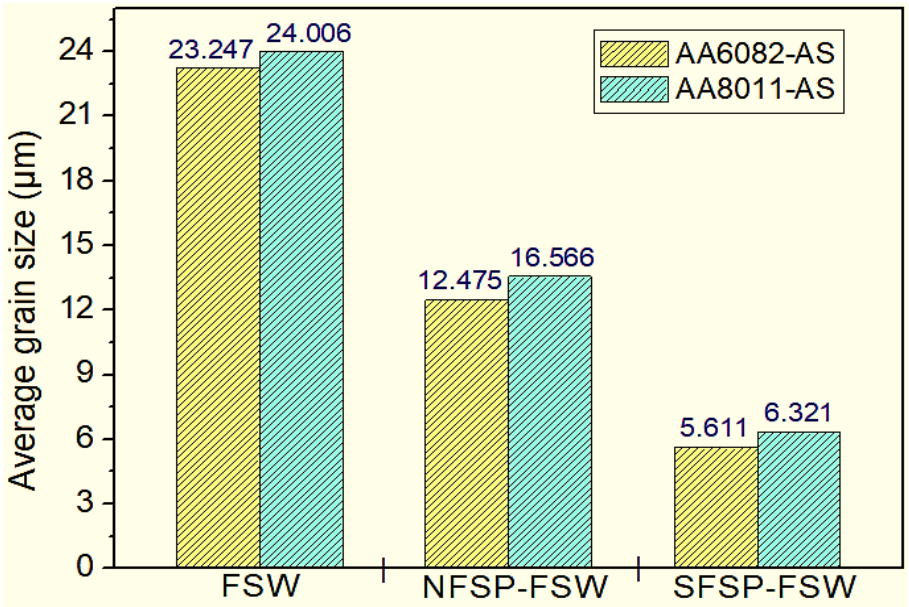

Figure 4.2.3.9: Average grain sizes of the nugget zones of the FSWed, NFSP-FSW and SFSP-FSW joints.

4.2.4 Flexure tests

Post-flexure test specimens are presented in Figure 4.2.4.1. The FSW AA6082-AS specimens, both root and face tested, showed no visible cracks; likewise, the FSW AA8011-AS root specimens also showed no cracks. However, the FSW AA8011-AS face specimens all showed cracks at the centre of the nugget zone. The NFSP-FSW showed no visible cracks regardless of material positioning except for the specimen extracted from the start of the joint on the NFSP-FSW AA6082-AS (face) and the specimen extracted from the middle of the NFSP-FSW AA8011-AS (face). The SFSP-FSW AA6082-AS (face) specimen extracted from the start fractured shortly after the test was initiated; hence, there was not much demonstrable flexing. The rest of the specimen did not show any visible cracking for both face and root flexing. The SFSP-FSW AA8011-AS (face) specimens extracted from the start and middle of the joint showed cracks on the centre of the joint, which is the centre of the nugget zone. However, the specimen extracted towards the end of the joint showed no cracks as well as the specimens subjected to root flexing. The cracks of all the specimens noted were all in the centre of the joints, suggesting that the cracks were initiated by defects present at the respective joints which were previously noted on the macrostructure of the same joints. The specimens all bent on the HAZ of the AA8011 alloy regardless of the joint configuration. This behaviour suggests that the joint strength was stronger than that of the weakest alloy AA8011 [140]. Similar findings were noted in the literature [107, 213].

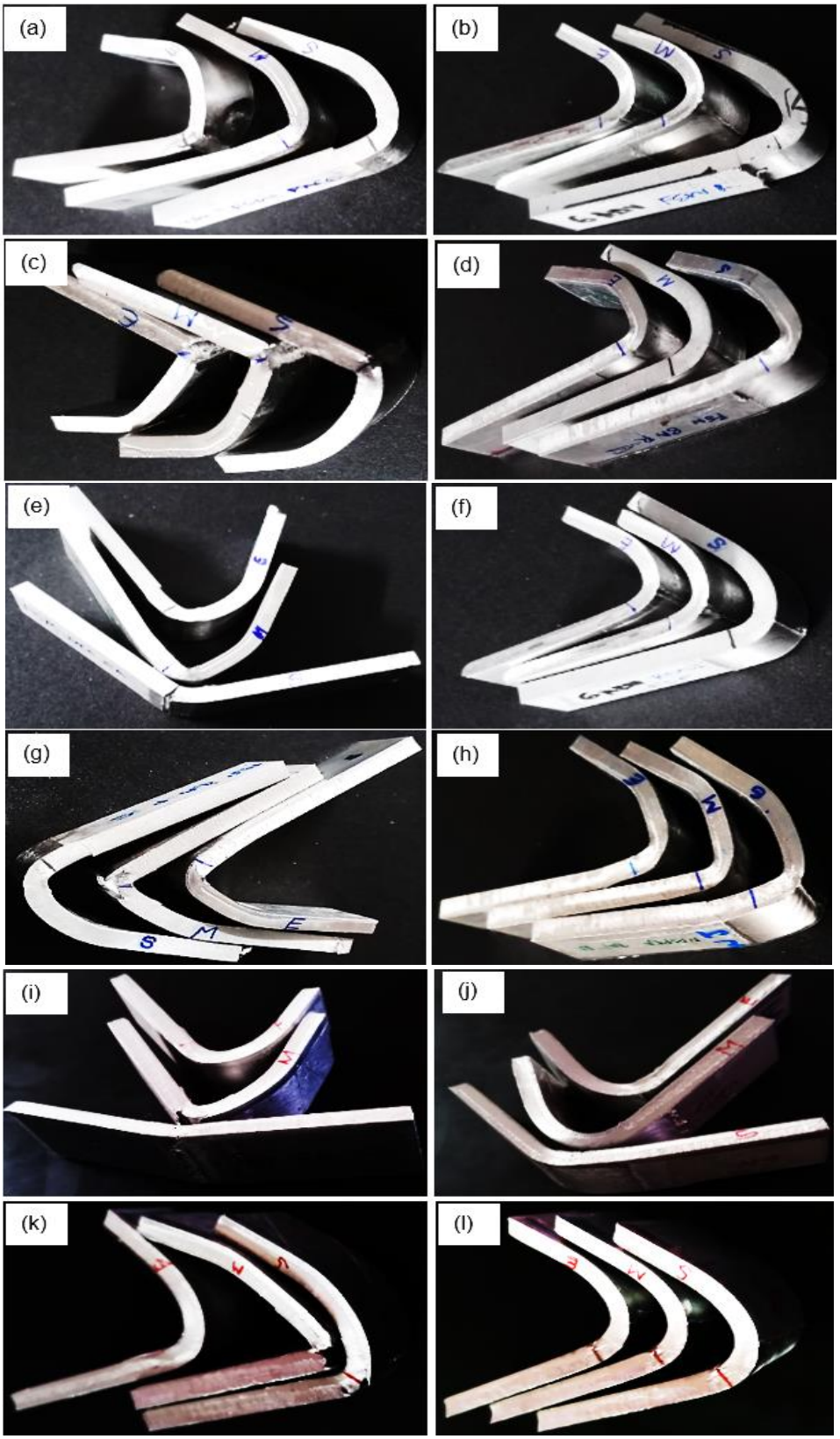

Figure 4.2.4.1: Flexural strength – strain curves: (a) FSW AA6082-AS (face); (b) FSW AA6082-AS (root); (c) FSW AA8011-AS (face); (d) FSW AA8011-AS (root); (e) NFSP-FSW AA6082-AS (face); (f) NFSP-FSW AA6082-AS (root); (g) NFSP-FSW AA8011-AS (face); (h) NFSP-FSW AA8011-AS (root); (i) SFSP-FSW AA6082-AS (face); (j) SFSP-FSW AA6082-AS (root); (k) SFSP-FSW AA8011-AS (face); (l) SFSP-FSW AA8011-AS (root).

Figure 4.2.4.2 (a-d) depicts the flexural strength and strain curves for the FSW joints. The FSW AA6082-AS (face) joints showed a UFS range of 175.375 MPa to 281.675 MPa at a flexural strain rate of 37.88% and 33.111%, respectively. The FSW AA6082-AS (root) had a UFS range of 144 MPa to 282.375 Mpa at respective strain rates of 22% and 34%. The minimum and maximum flexural strain rates obtained at fracture point for the FSW AA6082-AS (face) were 42.556% and 46%, respectively. The FSW AA6082-AS (root) had a minimum flexural strain rate of 41.783% and the maximum was 44.58%. The FSW AA8011-AS (face) UFS range was from 148.125 MPa to 260.25 MPa at strain rates of 11.2% and 27.88%, respectively, with a UFS range of 120 MPa to 151.189 MPa at a respective strain rate of 11.7% and 14.823. The minimum and maximum flexural strain rates obtained at fracture point for the FSW AA8011-AS (face) were 38.7% and 43.88%, respectively. The FSW AA8011-AS (root) had a minimum flexural strain rate of 38.1% and maximum of 43.88%. There was a minimal difference between the face and the root results for the FSW AA6082-AS joints. However, the FSW AA8011-AS joint results showed that the face results were sounder than the root results. This behaviour was noted only for the flexural strength, as the flexural strain, in contrast, showed a minimal difference.

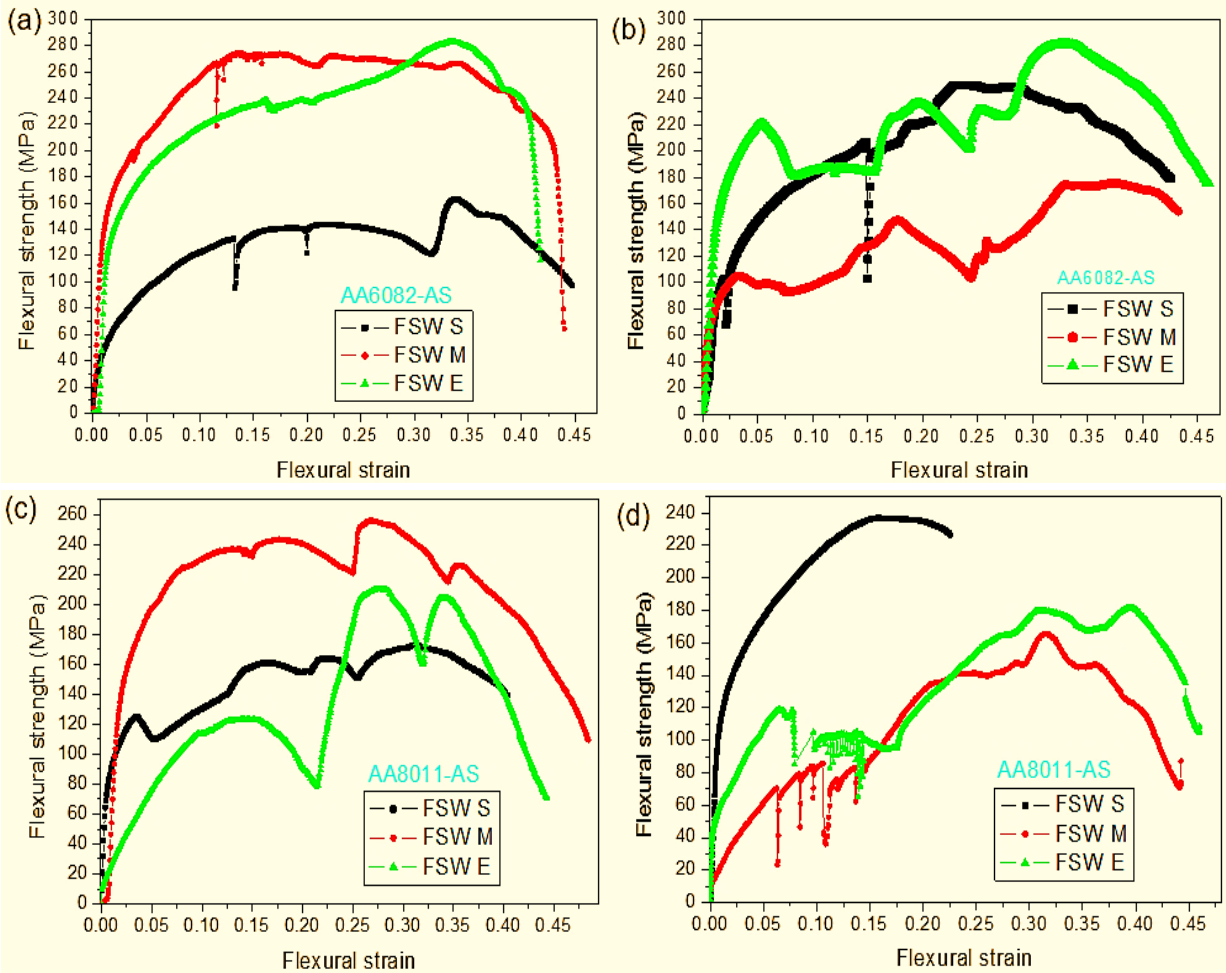

Figure 4.2.4.2: Flexural strength – strain curves: (a) FSW AA6082-AS (face); (b) FSW AA6082-AS (root); (c) FSW AA8011-AS (face); (d) FSW AA8011-AS (root).

Figure 4.2.4.2(e-h) shows the flexural strength and strain curves for the NFSP-FSW specimens. The NFSP-FSW AA6082-AS (face) depicted in Figure 4.2.4.2(e) showed a UFS range of 120.375 MPa to 327.563 MPa at a flexural strain rate of 18.889% and 35.111%, respectively. A maximum flexural strain rate of 44.778% was noted on the specimen extracted at the middle of the weld and the lowest (18.889%) on the specimen extracted at the start of

the joint. The root of the same NFSP-FSW AA6082-AS joint presented in Figure 4.2.4.2(f) showed a UFS range of 149.625 MPa to 307.125 MPa at a flexural strain rate of 18.333% and 18.778%, respectively. A maximum and minimum flexural strain rate of 43.556% and 42% of the joint, respectively, were obtained. The maximum UFS was noted on the face specimens compared to the root specimens of the NFSP-FSW AA6082-AS. This kind of behaviour was indicated in several studies, including Sorger et al. [213] and Takhakh [214]. The UFS range of the NFSP-FSW AA8011-AS specimens (see Figure 4.2.4.2[g]) for the face joint was 185.25 MPa at a flexural strain rate of 30.778% to 314.063 MPa at a flexural strain rate of 30.778%. A maximum flexural strain rate of 46.889% and the lowest flexural strain rate of 40% were noted for the specimens extracted at the middle and end of the joint, respectively. The UFS range for the root NFSP-FSW AA8011-AS joints (see Figure 4.2.4.2[h]) was 183.375 MPa and 205.688 MPa at a flexural strain rate of 31.333% and 15.111%, respectively. The maximum flexural strain rate of 46.222% and minimum of 22.111% were noted on the specimens extracted from the end and middle of the processed joint.

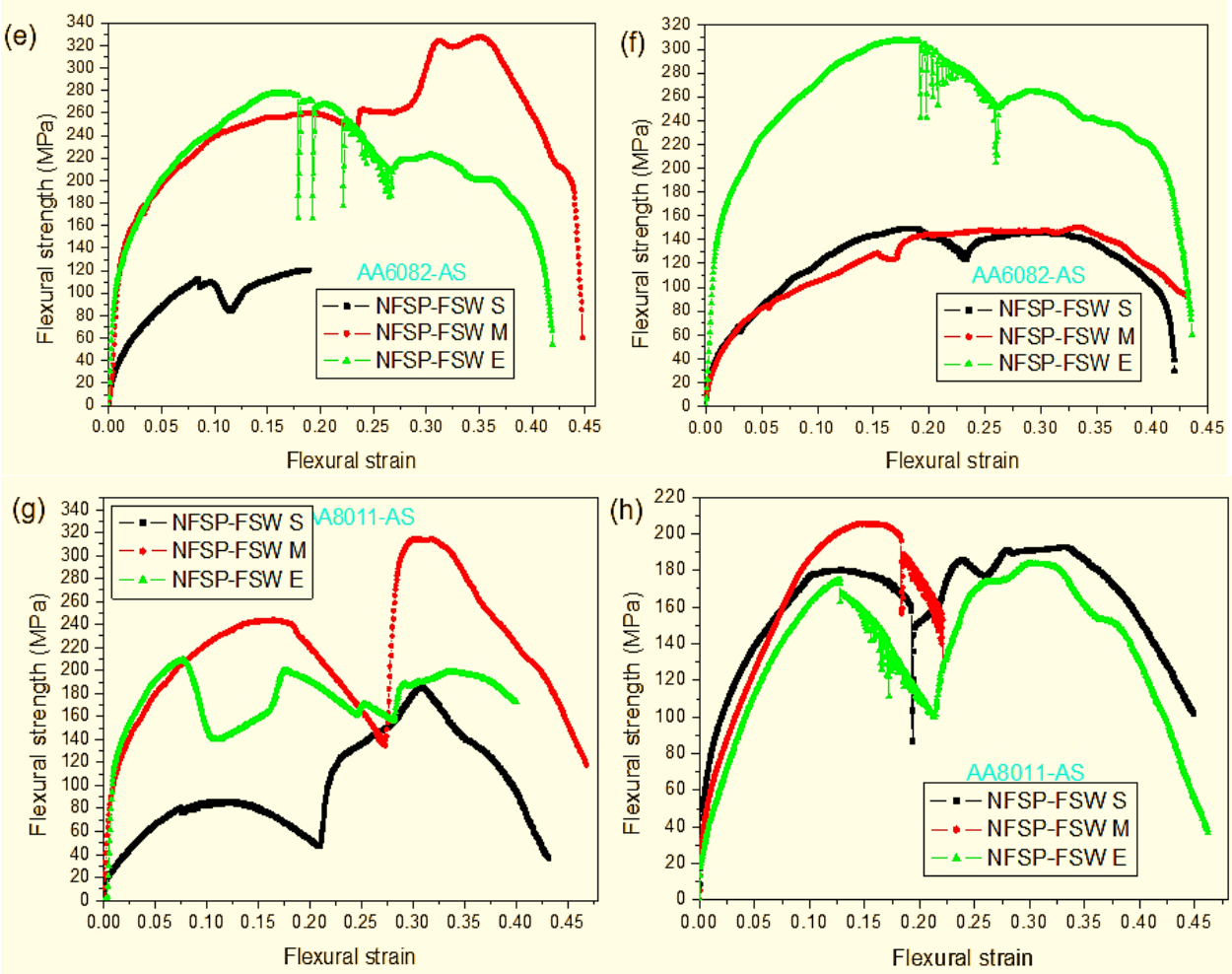

Figure 4.2.4.2: Flexural strength – strain curves: (e) NFSP-FSW AA6082-AS (face); (f) NFSP-FSW AA6082-AS (root); (g) NFSP-FSW AA8011-AS (face); (h) NFSP-FSW AA8011-AS (root).

The SFSP-FSW flexural strength and strain curves for different joint configurations are depicted in Figure 4.2.4.2(i-l). The curves for SFSP-FSW AA6082-AS (face) joints are presented in Figure 4.2.4.2(i). The UFS range was found to be 69 MPa to 141.875 MPa at a flexural strain rate of 24.55% and 23.44%, respectively. The 69 MPa was due to the start position having what is known as cold welds, where the harder alloy was not fully melted [189-190]. This, therefore, led to the joint having a cavity defect. This behaviour correlates to the

macrostructure obtained. The maximum flexural strain rate of 49.220% and minimum of 31.44% were obtained on the start and middle specimen positioning. The root curves of the same joint (see Figure 4.2.4.2[j]) have a UFS range of 141.75 MPa to 171.56 MPa with corresponding flexural strain rates of 23.89% and 11%, respectively. The maximum flexural strain of 42.221% was obtained from the specimen extracted at the end of the joint and the minimum (12.44%) from the specimen extracted at the start of the joint. Figure 4.2.4.2(k) represents the SFSP-FSW AA8011-AS (face) with a UFS range of 95 MPa to 270.975 MPa at the respective flexural strain rate of 19.25% and 35.78%. The maximum flexural strain rates of 61.55% and a minimum of 42.22% were obtained. Figure 4.2.4.2(l) shows the SFSP-TIG AA8011-AS (root) with a UFS range of 139.44 MPa to 262.75 MPa at a flexural strain of 13.87% and 34.33%, respectively. A minimum flexural strain of 14.67% and a maximum of 58.78% were noted. There was no particular identifiable trend in regards to specimen positioning for the UFS and flexural strain.

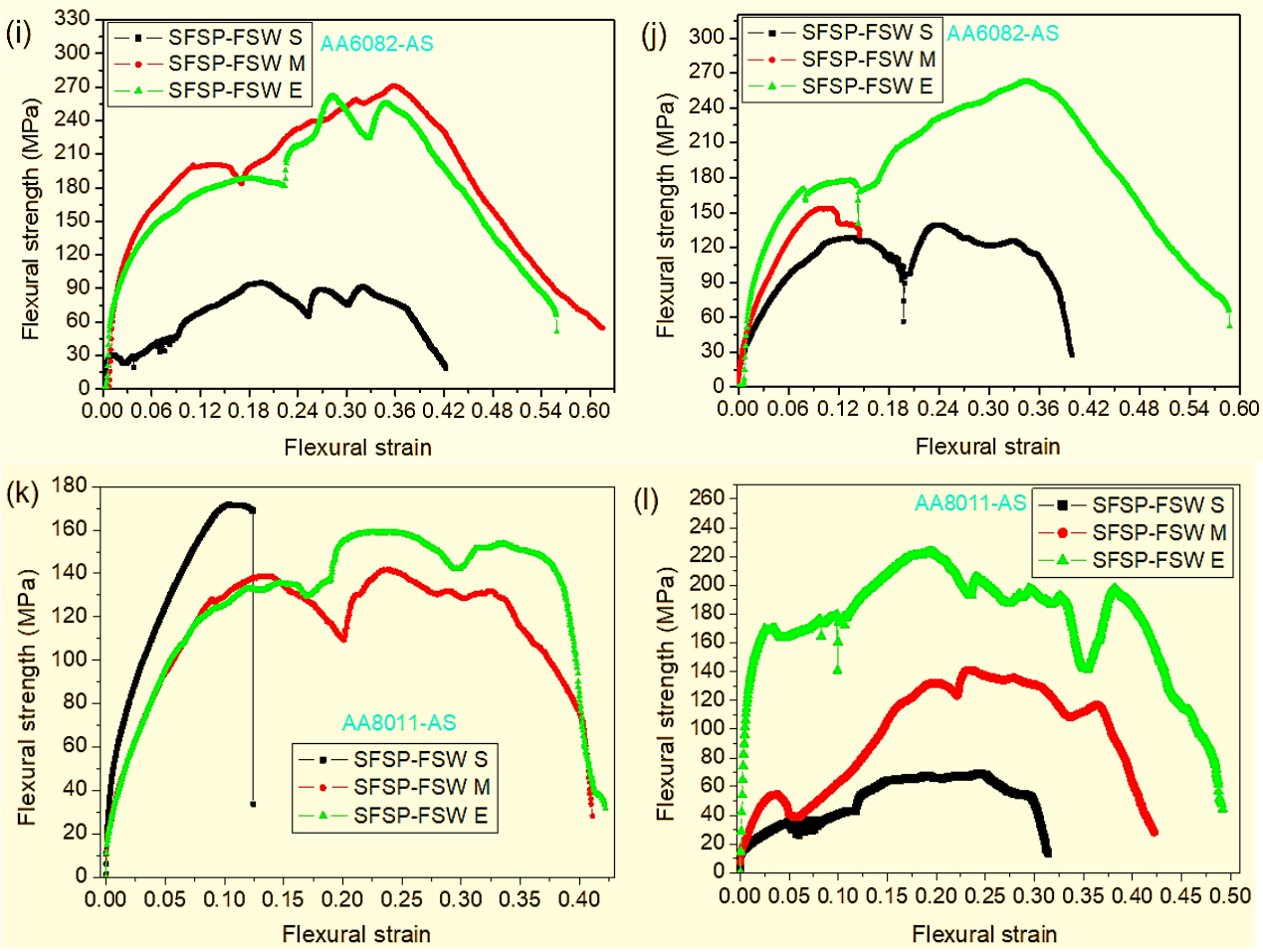

Figure 4.2.4.2: Flexural strength – strain curves: (i) SFSP-FSW AA6082-AS (face); (j) SFSP-FSW AA6082-AS (root); (k) SFSP-FSW AA8011-AS (face); (l) SFSP-FSW AA8011-AS (root).

Figure 4.2.4.3 depicts the UFS and maximum flexural strain (MFS) obtained on each joint configuration as discussed. The UFS charts revealed that the maximum UFS was obtained on the NFSP-FSW AA6082-AS (face) and the maximum UFS for the specimens subjected to root bending was also noted on the same joint. A difference of 20.6 MPa was obtained between the maximum UFS face and the maximum UFS root. Furthermore, it was observed that the SFSP-FSW joints, regardless of face or root surface, showed a higher maximum flexural strain rate than the NFSP-FSW and FSW joints. There was a 2.8% difference between the MFS root

and MFS face. The results suggest that when the UFS increases, the MFS (which is the ductility) decreases and vice versa. Similar behaviour was reported in the literature [140, 215].

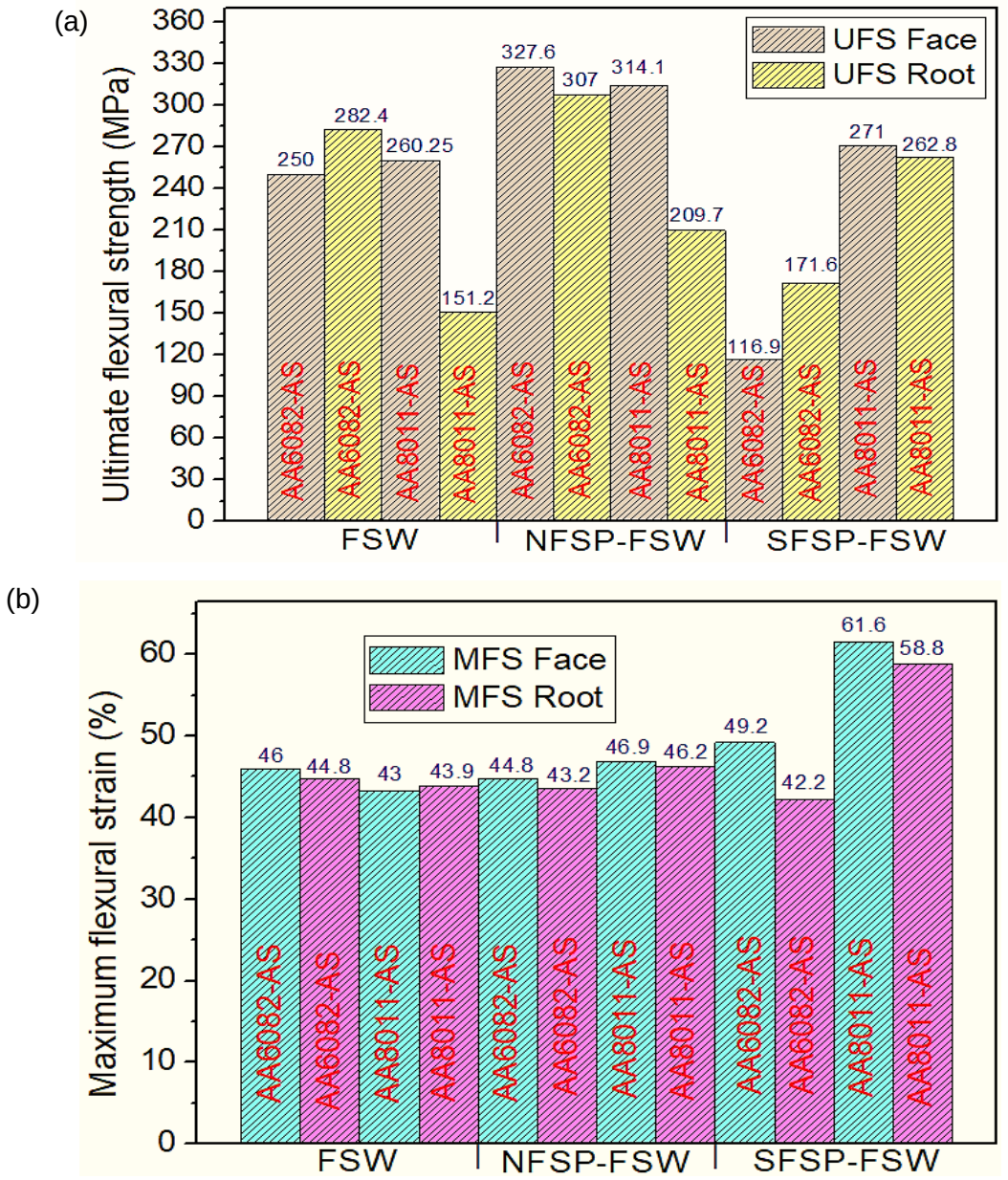

Figure 4.2.4.3: Bar charts: (a) ultimate flexural strength; (b) maximum flexural strain.

4.2.5 Tensile tests

Figure 4.2.5.1 illustrates the post-tensile specimens of the FSWed, NFSP-FSW and SFSP-FSW joints. The FSWed AA6082-AS specimens extracted from the middle and start of the joint fractured on the HAZ of the AA8011 side, while the one extracted from the start fractured at the nugget zone. The FSW AA8011-AS specimens extracted at the start and end of the joint failed at the nugget zone, while the one extracted at the middle of the joint failed at the HAZ of the AA8011 alloy. This behaviour confirms that the HAZ consisted of the weakest strength compared to that of the fusion zone and the AA6082 side of the specimen [216-217]. This phenomenon is common with the joining of dissimilar materials. All the NFSP-FSW AA6082-AS specimens fractured on the HAZ, suggesting that the NZ tensile strength was stronger than

that of the AA8011 alloy [90,242]. However, the NFSP-FSW AA8011-AS post-tensile specimens all failed at the NZ of the joints. This behaviour was due to the presence of tunnel defects at the NZ as previously mentioned in the macrostructural analysis, rendering the NZ the weakest position compared to the HAZ of the weakest alloy. Similar behaviour was noted on the SFSP-FSW AA8011-AS. Conversely, SFSP-FSW AA6082-AS (start specimen) failed at the NZ due to the tunnel defect that was present prior to tensile testing. However, the middle and end specimens failed at the HAZ of the weaker alloy. The behaviour is expected as it is popular for inhabiting minimum hardness compared to other positions of the specimen [243-244].

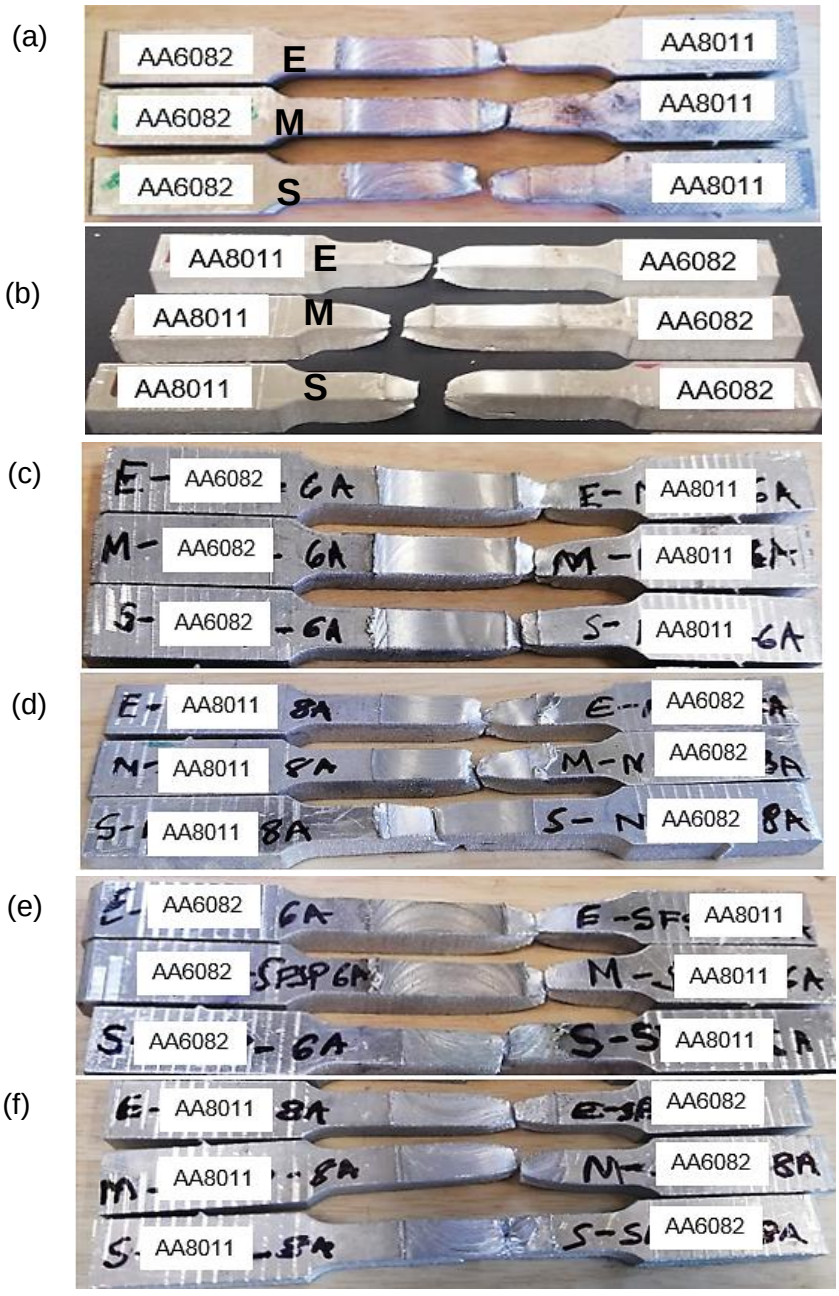

Figure 4.2.5.1: Post-tensile specimens: (a) FSWed joints AA6082-AS; (b) FSWed joints AA68011-AS; (c) NFSP-FSW joints AA6082-AS; (d) NFSP-FSW AA8011-AS; (e) SFSP-FSW AA6082-AS; (f) SFSP-FSW AA8011-AS joints.

Figure 4.2.5.2 presents the tensile stress-strain curves of the FSWed and FSPed joints. Table 4.2.5 shows the tensile properties regarding Figure 4.2.5.2. The FSWed AA6082-AS joint had a maximum UTS of 84.444 MPa at a corresponding tensile strain rate of 12.41% and a

maximum yield strength of 67.555 MPa. The minimum UTS and yield strength were at 76.944 MPa at a corresponding tensile strain rate of 6.944% and yield strength of 61.555 MPa. The minimum and maximum tensile strain rates at the fracture point of the FSWed joint were 8.769% and 23.03%, respectively. The FSWed A8011-AS joint had a maximum UTS of 77.444 MPa at a corresponding tensile strain rate of 5.71% and a maximum yield strength of 61.955 MPa. The minimum UTS and yield strength were found to be 71.338 MPa at a corresponding tensile strain rate of 10.382% and yield strength of 57.070 MPa. The minimum and maximum tensile strain rates at the fracture point of the FSWed joint were 7.68% and 16.13%, respectively. The NFSP-FSW AA6082-AS joints had a minimum UTS of 85.611 MPa at a corresponding tensile strain rate of 11.680% with a maximum yield strength of 69.845 MPa. The maximum UTS of the said joints was 89.611 MPa at a corresponding tensile strain rate of 12.655% and yield strength of 71.289 MPa. The maximum and minimum tensile strain rates at the fracture point were 24.609% and 20.620%, respectively. The NFSP-FSW AA8011-AS joints showed a maximum UTS of 87.556 MPa at a tensile strain rate of 12.860%, with a yield strength of 70.004 MPa. The minimum UTS of 87.111 MPa at a tensile strain of 12.921% with a yield strength of 69.689 MPa were noted. The minimum and maximum tensile strain rates of 14.251% and 21.652% were obtained at the joint breakpoints. The application of the NFSP technique increased both the tensile strength and tensile strain. This behaviour was associated with the stirring and dynamic recrystallization of the joints that resulted in the notable grain refinement, known for positively impacting joint tensile properties [218-219].

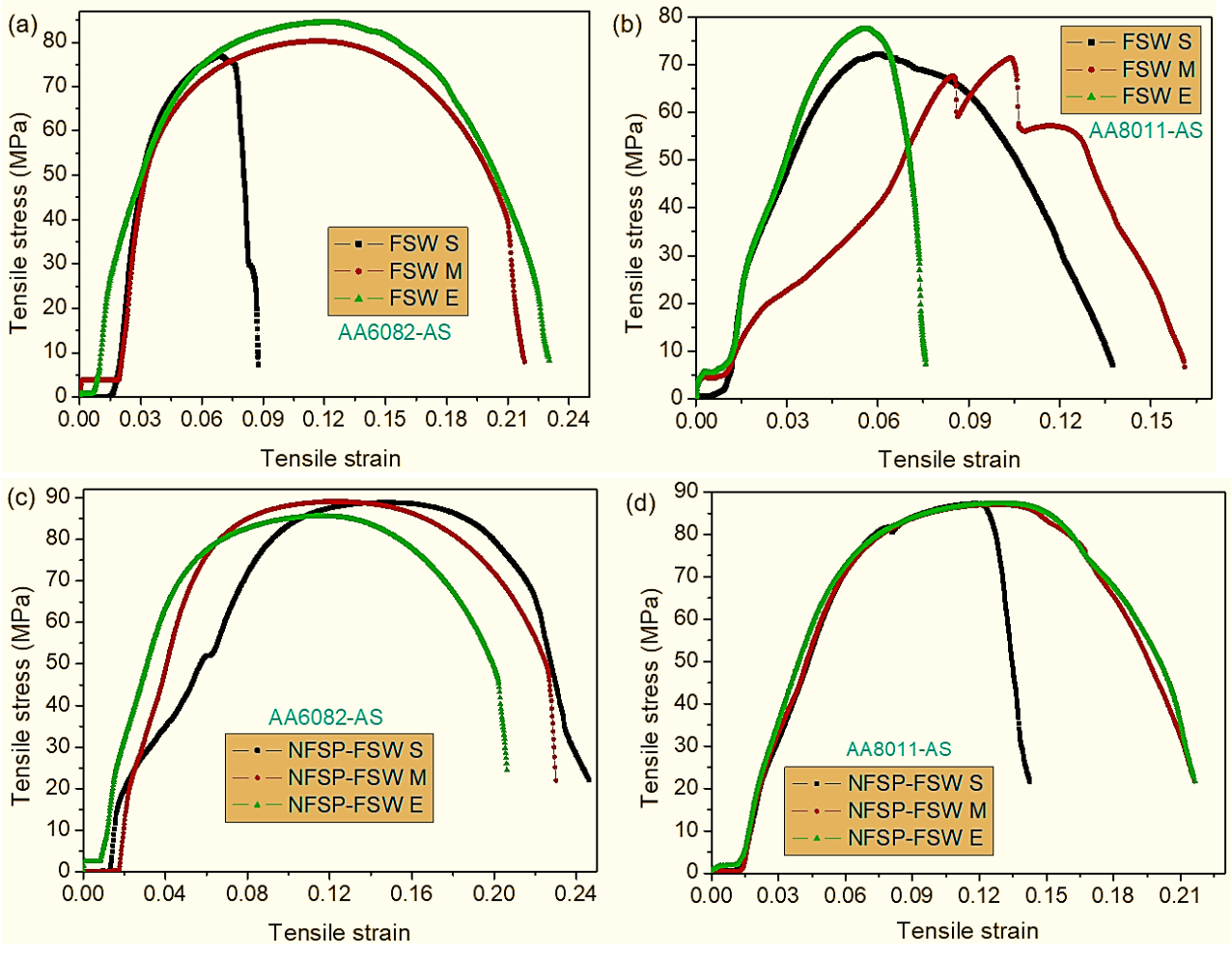

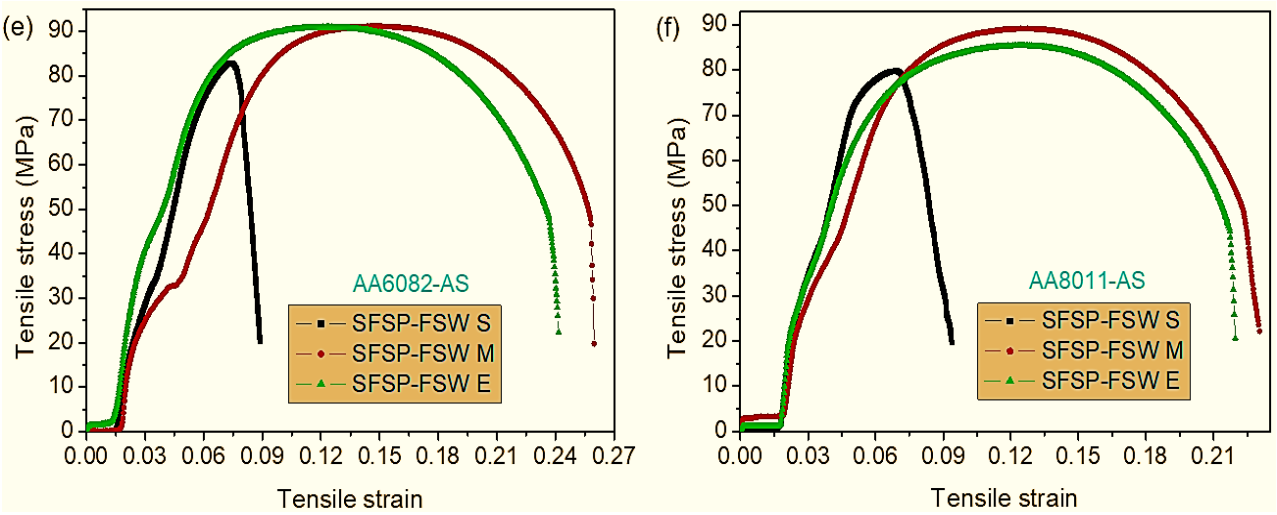

Figure 4.2.5.2: Tensile stress-strain curves: (a) FSWed joints AA6082-AS; (b) FSWed joints AA68011- AS; (c) NFSP-FSW AA6082-AS joints; (d) NFSP-FSW AA8011-AS joints; (e) SFSP-FSW AA6082-AS joints; (f) SFSP-FSW AA68011-AS joints.

The maximum UTS for the SFSP-FSW AA6082-AS joints was 92.511 MPa at a corresponding tensile strain rate of 15.095% and a yield strength of 74.009 MPa. The minimum UTS was 83.833 MPa at a tensile strain rate of 7.381% and yield strength of 67.066 MPa. The minimum and maximum tensile strain rates at the breakpoint were 8.888% and 25.978%, respectively. Additionally, the SFSP-FSW AA8011-AS had a maximum UTS of 90.011 MPa at a tensile strain rate of 13.50% and yield strength of 71.288 MPa. The minimum UTS was 80.25 MPa at a corresponding tensile strain rate of 6.959% and a yield strength of 63.778 MPa. The said joints had a minimum and maximum tensile strain rate (at breakpoint) of 9.389% and 23.045%. The tensile strength and tensile strain were significantly improved post-SFSP regardless of material positioning. This behaviour was in agreement with the microstructural grain sizes of the same joints which showed remarkable refinement, which has a vital role in the strengthening of the material properties [220]. Additionally, this behaviour was in agreement with the Orowam hardening mechanism: the refinement of grains sizes reduces the presence of cracks within the joints, making the joint impossible to crack at lower stress, thereby increasing the tensile strength of the SFSPed joints [221]. Additionally, rapid cooling also played a crucial role in the improvement of the tensile properties by decreasing the chances of abnormal grain growth, a very common phenomenon when the joints experience excessive heat which affects the joint properties negatively [222].

Table 4.2.5: Tensile properties of the joints.

Joint	Ultimate tensile strength (MPa)	Yield strength (MPa) @ 0.2% offset	Strain rate (%)	Fracture location
AA6082-AS				
FSW S	76.944	61.555	8.769	NZ
FSW M	80.278	64.222	21.828	HAZ
FSW E	84.444	67.555	23.035	HAZ
AA8011-AS				
FSW S	72.167	57.733	13.753	HAZ
FSW M	71.338	57.070	16.138	NZ
FSW E	77.444	61.955	7.682	HAZ

AA6082-AS				
NFSP-FSW S	88.944	71.155	24.609	NZ
NFSP-FSW M	89.611	71.289	23.091	HAZ
NFSP-FSW E	85.611	68.489	20.620	HAZ
AA8011-AS				
NFSP-FSW S	87.306	69.845	14.251	NZ
NFSP-FSW M	87.111	69.689	21.610	NZ
NFSP-FSW E	87.556	70.004	21.652	NZ
AA6082-AS				
SFSP-FSW S	83.833	67.066	8.888	NZ
SFSP-FSW M	92.511	74.009	25.978	HAZ
SFSP-FSW E	91.778	73.422	24.164	HAZ
AA8011-AS				
SFSP-FSW S	80.25	63.778	9.389	NZ
SFSP-FSW M	90.011	71.288	23.045	NZ
SFSP-FSW E	86.333	68.266	21.960	NZ

With regards to specimen positioning, there was no particular order observed for all the specimens. However, no maximum tensile properties were obtained at the specimens extracted from the start of the joint. This behaviour is mostly influenced by the mixing of the material which at the beginning of the joint, the two materials reach melting points at different temperatures, with the AA6082 taking longer to completely melt resulting in what is known as cold welds [217]. These cold welds make the beginning of the joint the weakest position and influence the joint properties negatively. Similar findings were identified in literature [108, 142, 172, 180]. Comparing the NFSP-FSW to the SFSP-FSW, the SFSP-FSW had more improved UTS, yield strength and ductility. However, only the specimens extracted at the start of the SFSPed joints showed minimal tensile properties due to the defects which were previously noted on the macrostructural analysis. Figure 4.2.5.3 depicts the average tensile properties of the FSWed and FSPed joints. The figure makes evident that both NFSP-FSW and SFSP-FSW joints were improved compared to those of the FSWed joints. However, the most improved tensile and yield strengths were noted on the SFSP-FSW joints, while the improved average ductility was noted on the NFSP-FSW joints. This behaviour was due to the SFSP having a higher cooling rate than the NFSPed joints. Concerning material positioning, all the joints, regardless of configuration the AA6082-AS joint, had higher tensile properties than the AA8011-AS joints. The findings obtained were in correlation with those found in the literature [173, 245].

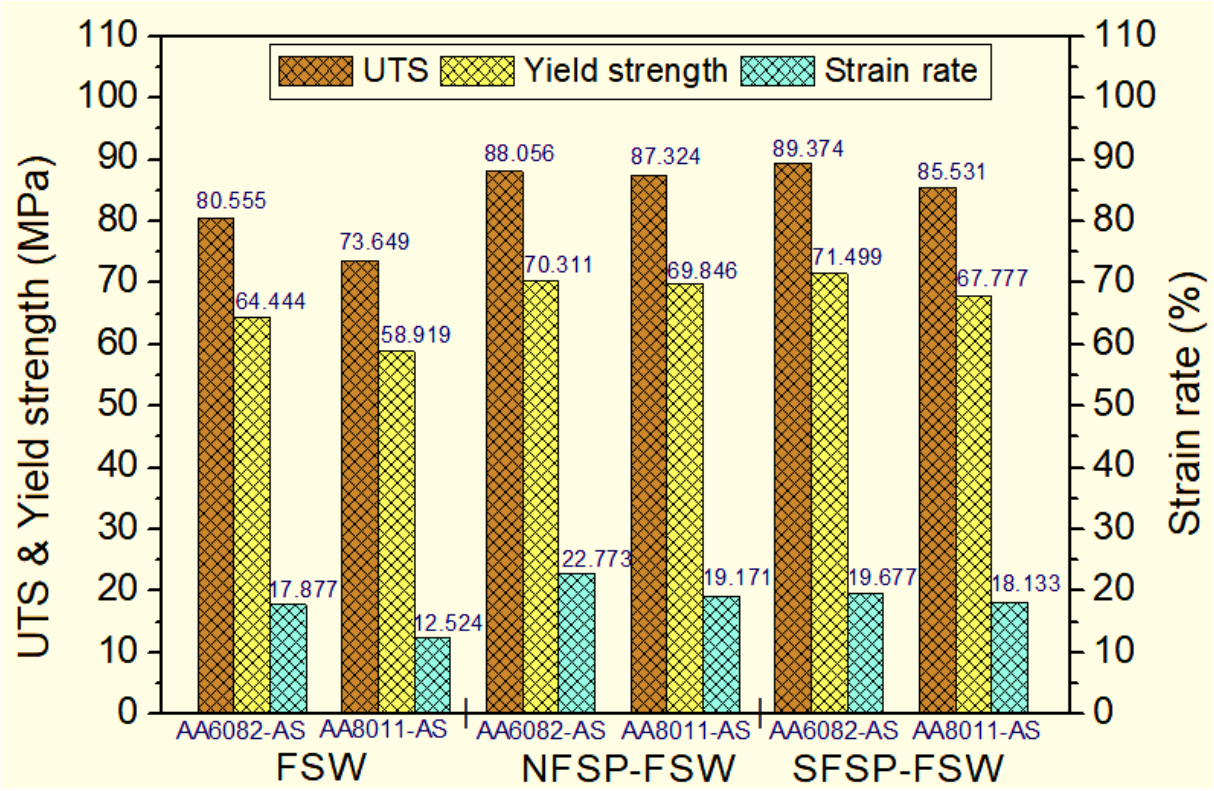

Figure 4.2.5.3: Average tensile properties of the FSWed, NFSP-FSW and SFSP-FSW joints.

4.2.6 Fracture surface analysis

Figure 4.2.6 shows the fracture surface morphology of the FSWed, NFSP-FSW and SFSP-FSW joints. The fractured surfaces all displayed a dominant ductile failure mechanism. The ductility of the joints was manifested by the failure characteristics like the microvoids, dimples interfaced by the transgranular cleavage facets, dimples of various sizes and grain boundaries [141,190, 206]. On the figure, samples of the ductile characteristics were marked, with the yellow arrow for inclusion particles, the red arrow representing the transgranular cleavage facets, the red circle for micro dimples and the blue arrow for microvoids.

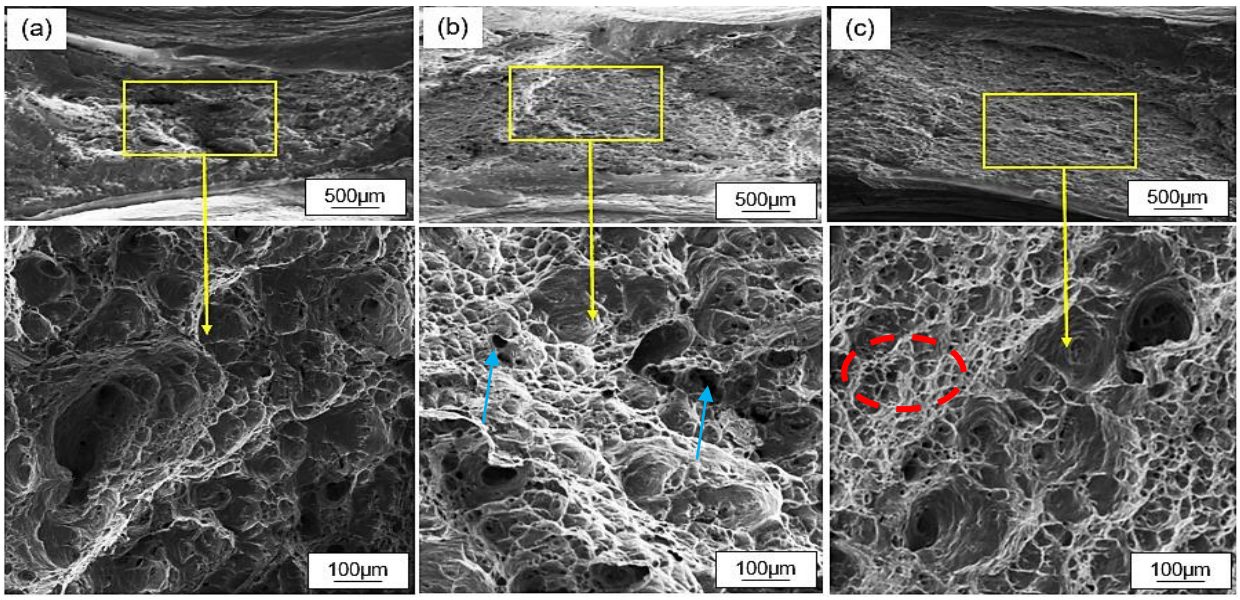

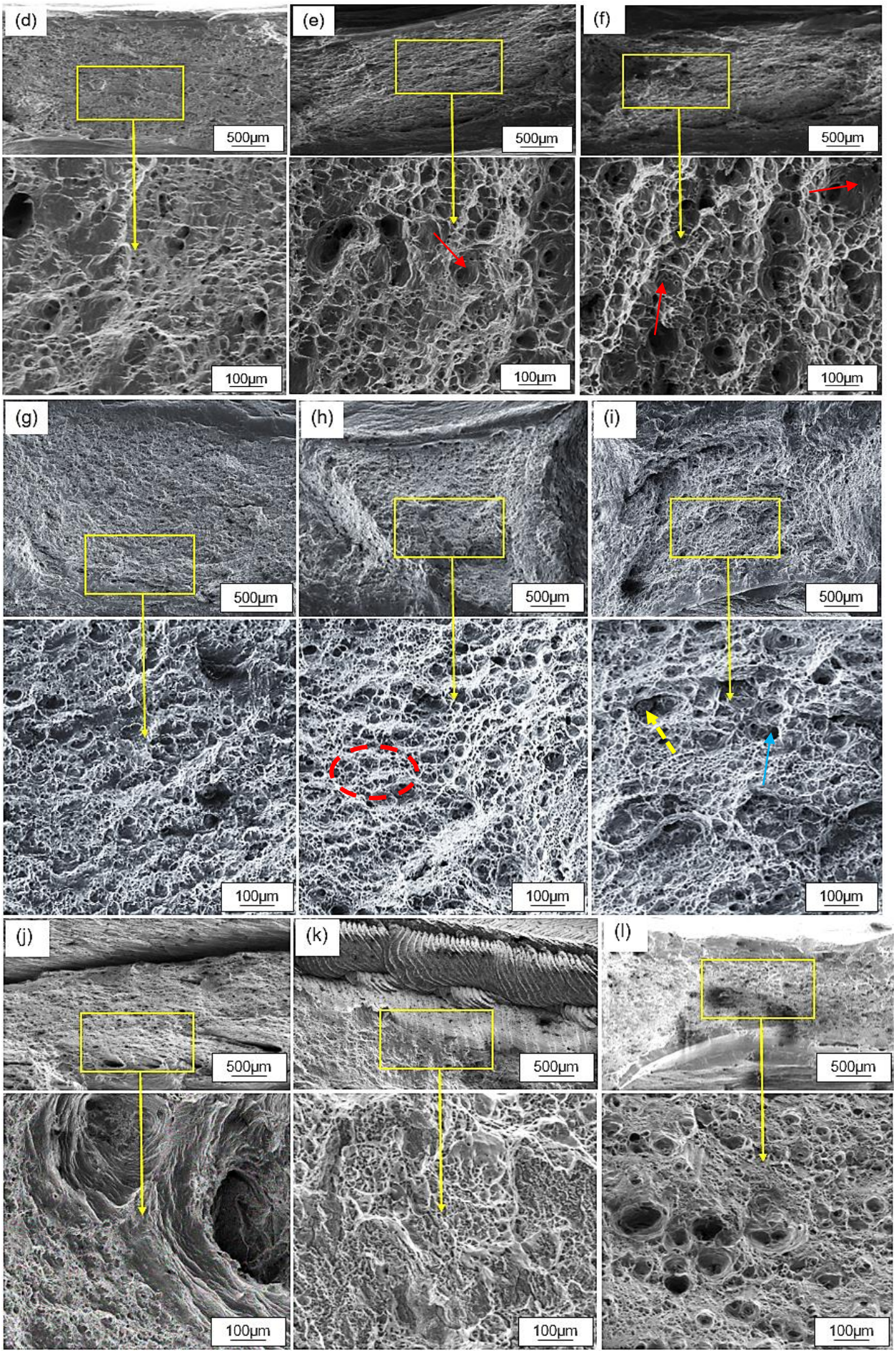
(d)
500μm
100μm
(e)
500μm
100μm
(f)
500μm
100μm
(g)
500μm
100μm
(h)
500μm
100μm
(i)
500μm
100μm
(j)
500μm
100μm
(k)
500μm
100μm
(l)
500μm
100μm

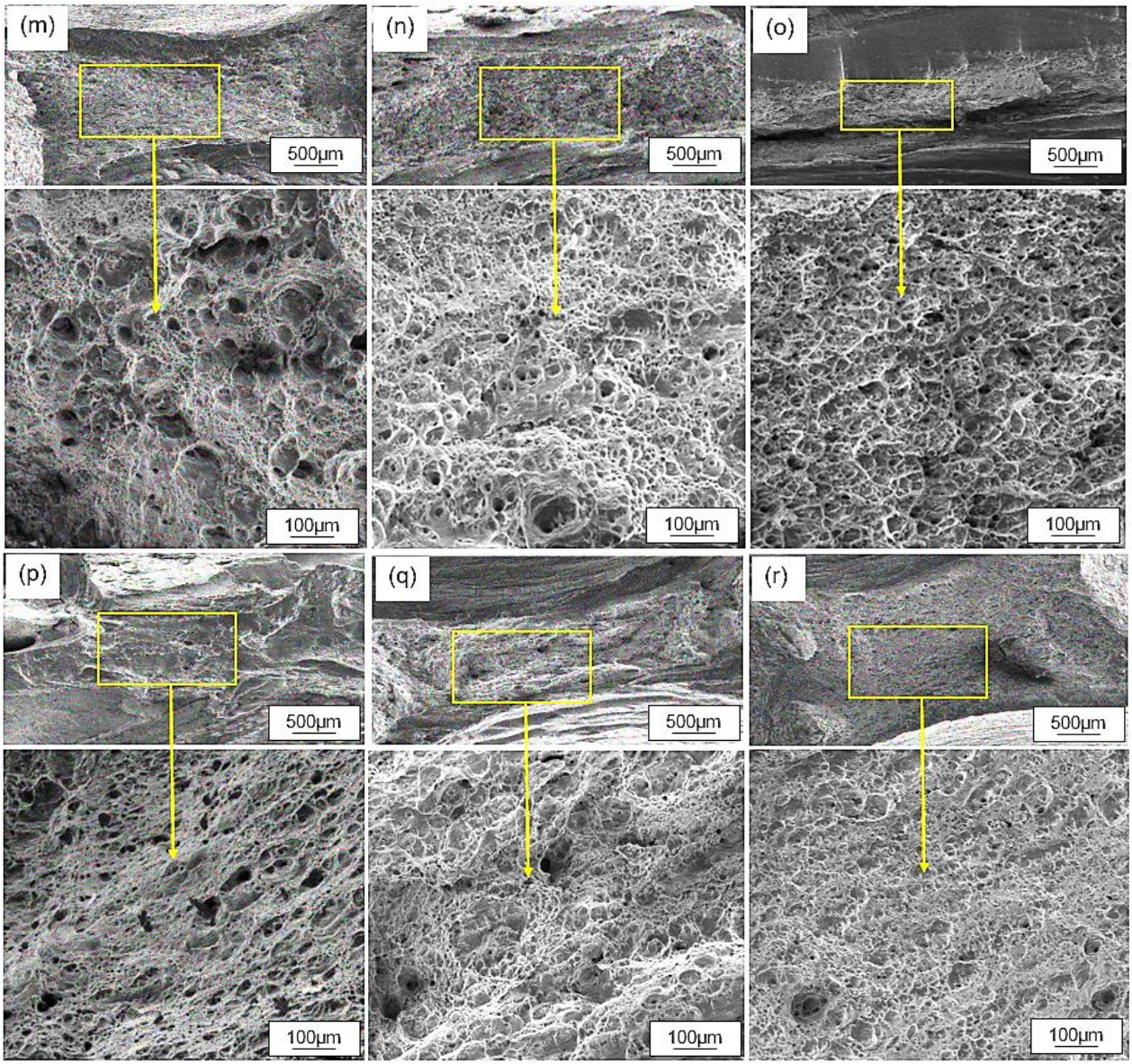

Figure 4.2.6: Fracture surface morphologies: FSWed joints AA6082-AS: (a) start (b) middle (c) end; FSWed joints AA68011-AS: (d) start (e) middle (f) end; NFSP-FSW AA6082-AS joints: (g) start (h) middle (i) end; NFSP-FSW AA8011-AS joints: (j) start (k) middle (l) end; SFSP-FSW AA6082-AS joints: (m) start (n) middle (o) end; SFSP-FSW AA68011-AS joints: (p) start (q) middle (r) end.

4.2.7 Hardness tests

Figure 4.2.7.1 illustrates the FSWed, NFSP-FSW and SFSP-FSW nugget zone hardness profiles with respect to material positioning, with Figure 4.2.7.2 depicting the summarised hardness values of the same. The FSW AA6082-AS hardness was in the range of 49 HV to 53 HV, with an average of 48 HV, while the AA8011-AS had a range of 46 HV to 49 HV with an average of 47 HV. The NFSP-FSW AA6082-AS had a hardness range of 52 HV to 53 HV with an average of 53 HV, whereas the AA8011-AS joint had a 47 HV to 56 HV range with an average of 52. The increase in the NFSP-FSW hardness was substantiated as caused by the improved dynamic recrystallization of the joints which resulted in the complete solution forming new precipitation in the nugget zone [241]. The hardness range of the SFSP-FSW AA6082-AS joint was 51 HV to 67 HV with an average of 61 HV, while the AA8011-AS joint had a hardness range of 48 HV to 63 HV with an average of 55 HV. The submerged conditions hardness behaviour was a result of grain size refinement and strain hardening of the low-

density dislocations [164, 246-248]. The SFSP-FSW joints had more increased hardness, unlike the NFSP-FSW which experienced a higher rapid cooling that inhibited the formation of coarsened microstructural grains [97, 227, 249]. The AA6082-AS joints, regardless of the joint configuration, showed a decline in the hardness of the advancing AA6082 alloy to that on the retreating side. Nevertheless, the degree of decline differed in all joints based on the conditions experienced. The inverse was observed on the AA8011-AS joints. Similar findings were reported in the literature [108, 173, 205]. In as much as the application of FSP improved the nugget zone hardness compared to the FSW ones, the obtained hardness was still lower than that of the AA6082 alloy but higher than that of the AA8011 alloy. The reason behind this behaviour was that the nugget zone was filled with both the AA8011 and the AA6082, not solely the AA6082, forming a new solution as previously indicated in the XRD analysis. Moreover, the nugget zone goes through frictional heat which differs depending on the method; hence the NFSP-FSW was lower than the SFSP one. It is accepted that the AA6082 alloy is a precipitate hardened alloy, rendering it extremely sensitive to temperatures above 200°C [208, 250-251].

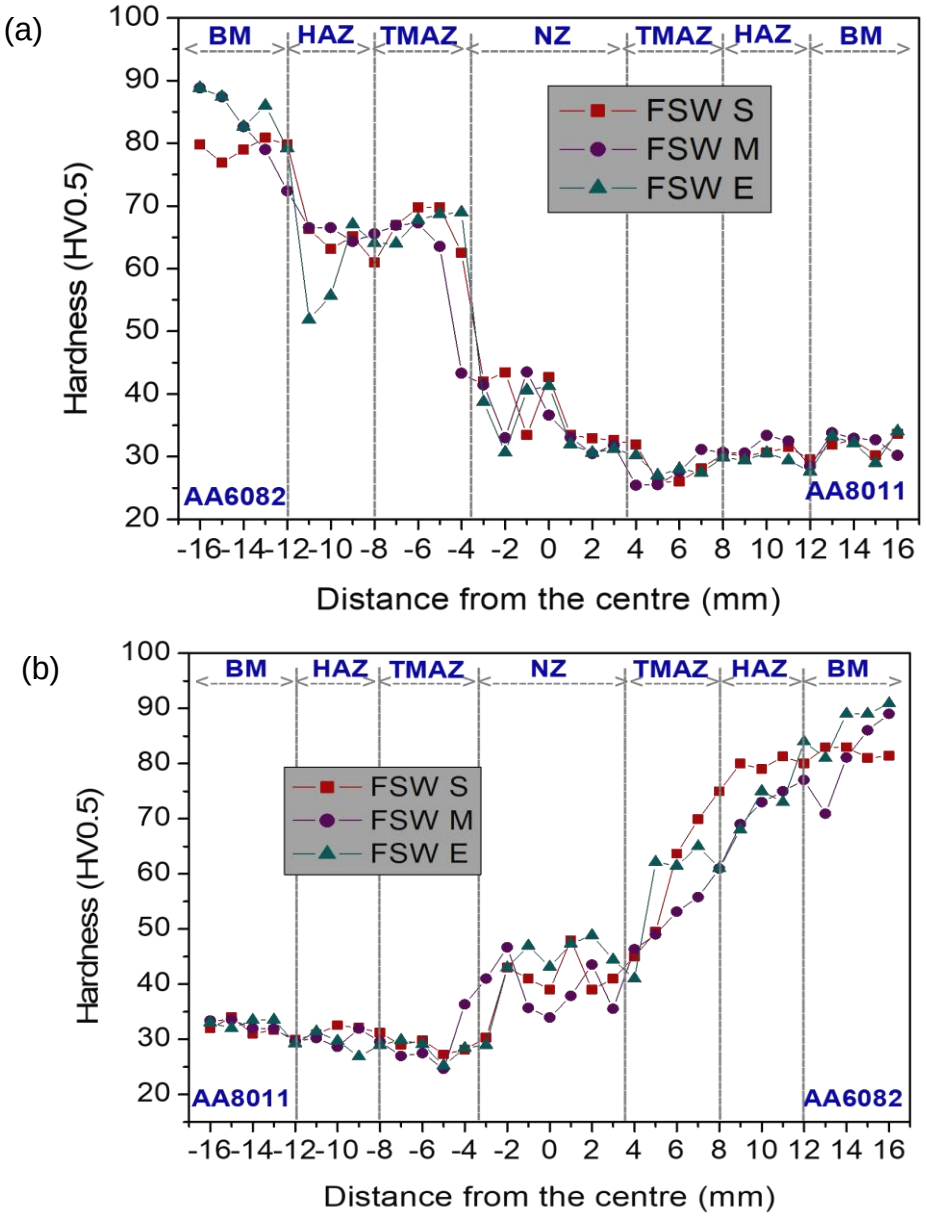

(c)

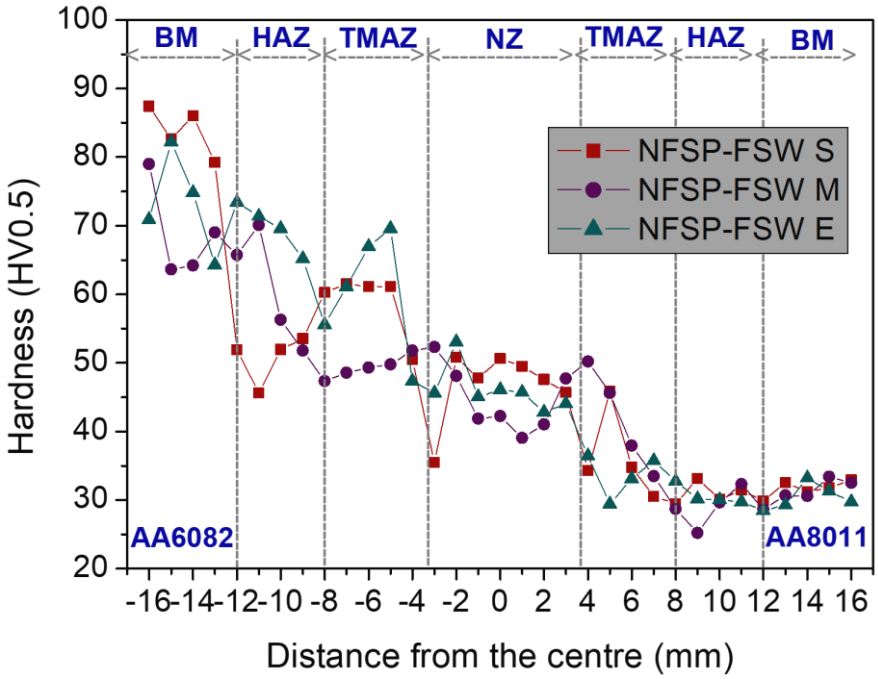
BM
HAZ
TMAZ
NZ
TMAZ
HAZ
BM
NFSP-FSW S
NFSP-FSW M
NFSP-FSW E
Hardness (HV0.5)
AA6082
AA8011
Distance from the centre (mm)

(d)

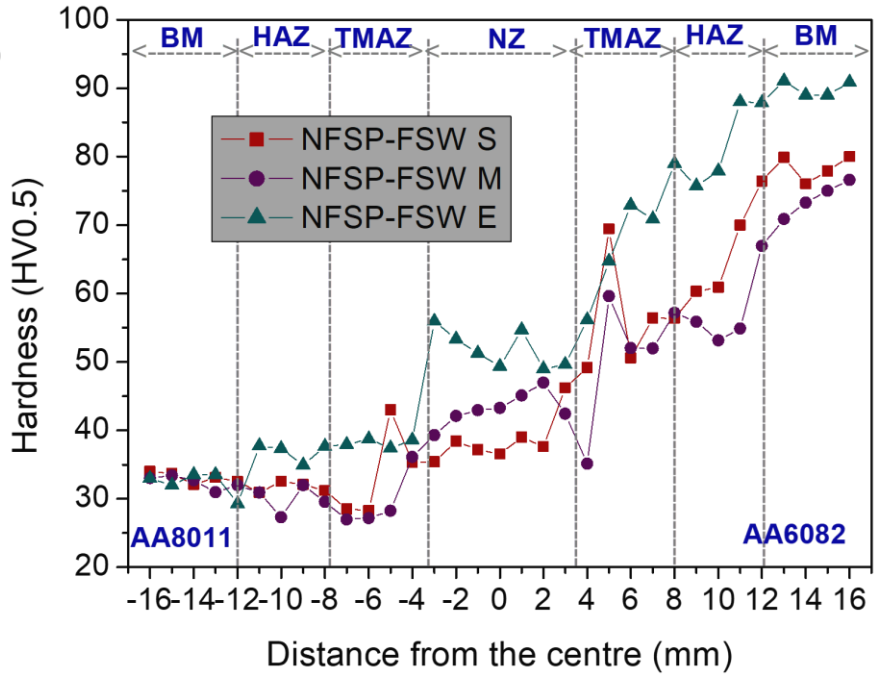
BM
HAZ
TMAZ
NZ
TMAZ
HAZ
BM
NFSP-FSW S
NFSP-FSW M
NFSP-FSW E
Hardness (HV0.5)
AA8011
AA6082
Distance from the centre (mm)

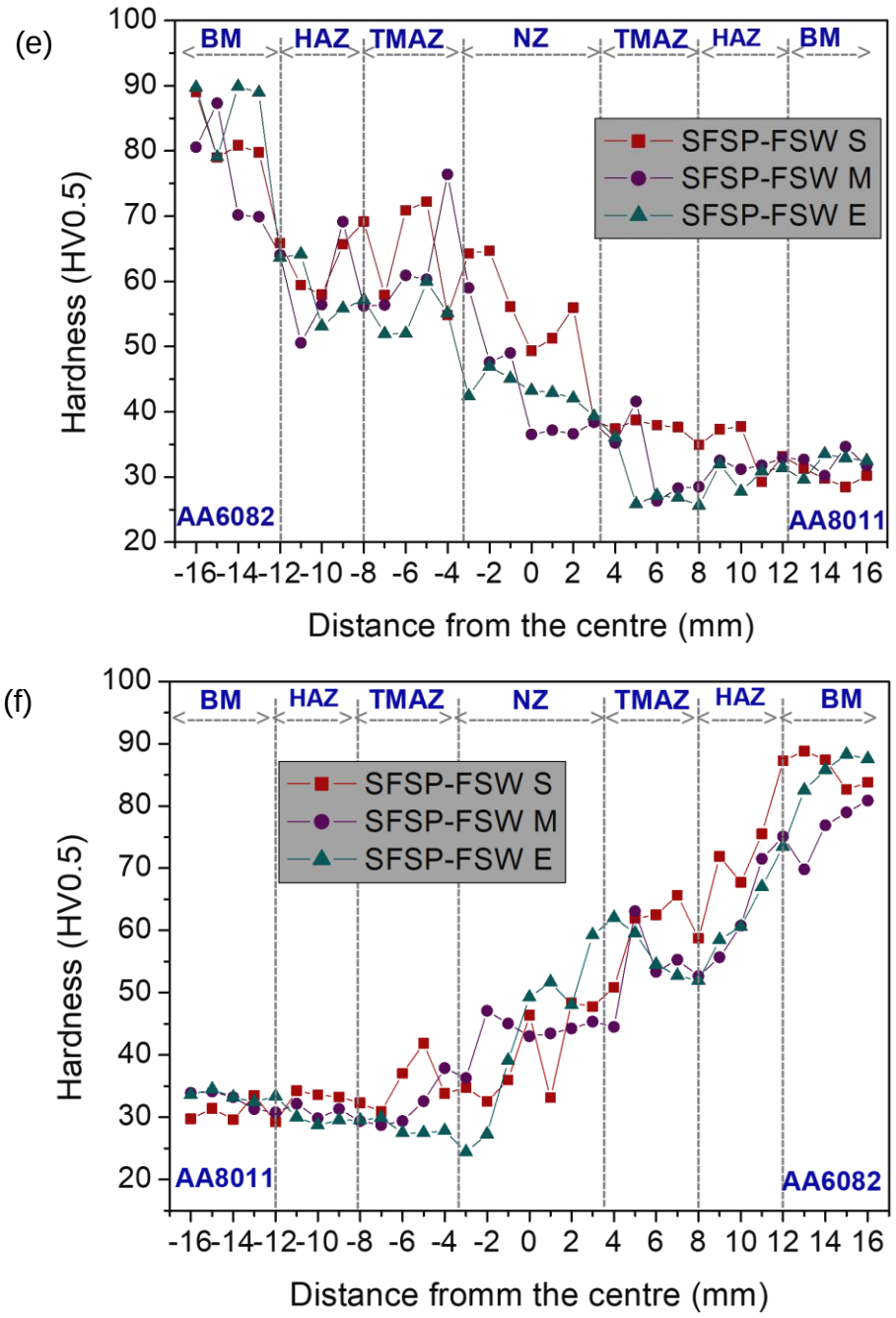

Figure 4.2.7.1: Hardness profiles: (a) FSWed joints AA6082-AS; (b) FSWed joints AA68011; (c) NFSP-FSW AA6082-AS joints; (d) NFSP-FSW AA8011-AS joints; (e) SFSP-FSW AA6082-AS joints; (f) SFSP-FSW AA68011-AS joints.

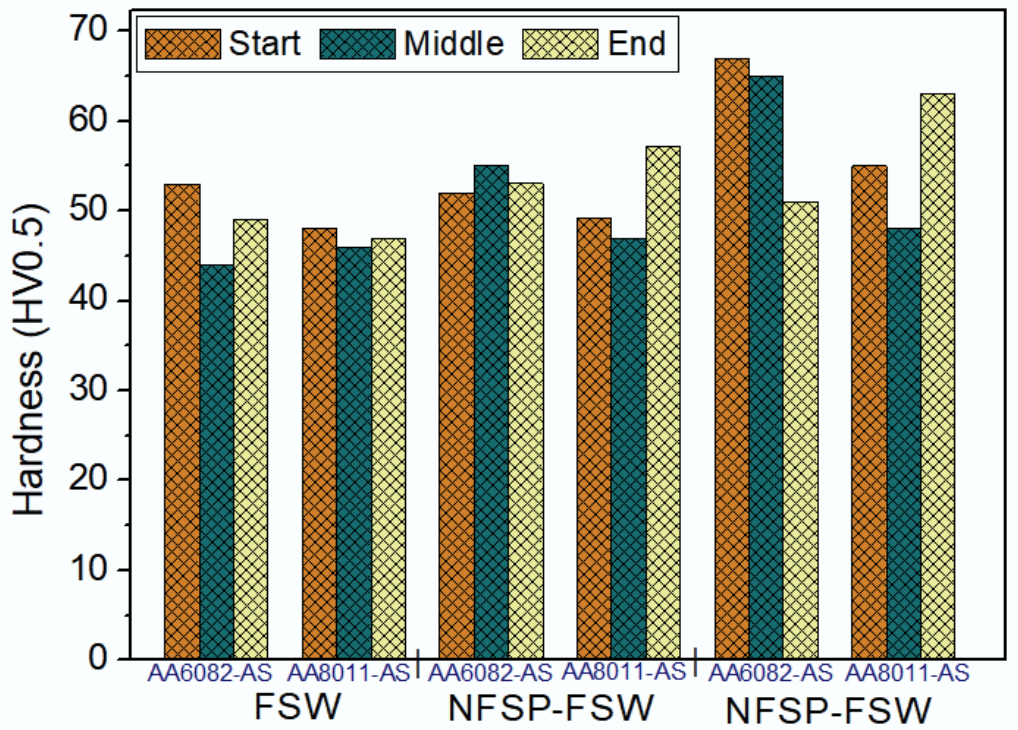

Figure 4.2.7.2: NZ hardness summary.

CHAPTER FIVE

CONCLUSIONS AND RECOMMENDATIONS

5.1 Conclusions

The aim of the study was to develop a new FSP method that can be employed to enhance the mechanical properties of the FSWed and TIG-welded AA6082/AA8011 dissimilar joints. This aim was achieved using predetermined objectives. The objectives included the fabrication of the dissimilar aluminium alloy plates using FSW and TIG welding. The produced welded joints were then friction stir processed under normal and underwater conditions using different material positioning. Afterwards, the influence of the different friction stir processing conditions of the AA6082/AA8011 FSW and TIG-welded joints was studied comparatively through the analysis of metallographic and mechanical tests. The tests included the XRD, macrostructural and microstructural analysis, flexural test, tensile tests, fracture surface morphology and Vickers hardness tests.

The TIG-welded average mean grain sizes before FSP were 23.247 µm and 31.765 µm, respectively. Post-FSP, the results revealed greatly refined grain sizes of 10.373 µm for the NFSP-TIG AA6082-AS and 13.373 µm for the NFSP-TIG AA8011-AS. The SFSP-TIG AA6082 average mean grain size was 4.24 µm, and 4.44 µm was reported for the SFSP-TIG AA8011-AS joints. The FSWed average mean grain size obtained was 23.247 µm. Post-FSP, the average mean grain sizes were significantly decreased to 12.45 for the NFSP-FSW AA6082-AS and 16.566 µm for the NFSP-FSW AA8011-AS joints. The SFSP-FSW AA6082-AS 5.611 µm and 6.321 µm for the SFSP-FSW AA8011-AS refined average mean grain sizes were obtained. The grain sizes of the submerged FSP method resulted in notable grain refinement compared to the normal FSP method. This refinement was due to the high rate of cooling through the underwater environment. Both the FSP of TIG and FSW grain sizes suggest that the AA6082-AS yielded greater grain refinement than the AA8011-AS joints.

The flexural tests for the TIG-welded joints prior to FSP had a UFS of 198.816 MPa with MFS of 46.5% for the specimens tested on the root side of the joint and 166.315 MPa with MFS of 46.2% for the face. The maximum UFS NFSP-TIG were 225.36 MPa (root) and 260.25 MPa (face), while the SFSP-TIG UFS were 211.2 MPa (face) and 300 MPa (root). The MFS for the NFSP-TIG were 43.98 (root) and 44.8% (face). Additionally, the SFSP-TIG MFS for the root was 41.7% and 42.72% for the face. The obtained results suggest that the best results for UFS (face) were obtained for SFSP-TIG and NFSP-TIG for the root, while for the MFS both root and face were obtained on the NFSP-TIG joints. With regards to material positioning for both the NFSP-TIG and SFSP-TIG (face) joints, the best UFS were found on the AA6082-AS joints and for the root, the AA8011-AS showed the most improved results. The NFSP-TIG (root) best MFS was found on the AA6082-AS joints while for the SFSP-TIG (root) the most preferred was the AA8011-AS joints. The AA8011-AS joints yielded better MFS results for both NFSP-TIG and SFSP-TIG (face). The FSWed maximum UFS for face and root prior to FSP were 260.25 MPa and 282.4 MPa, respectively. The MFS obtained for the FSWed joints was 46% for the face and 44.8 for the root. The application of FSP on the FSWed joints resulted in an NFSP-FSW maximum UFS of 327.7 MPa (face) and 307 MPa (face), while 271 MPa (face) and 262.8 MPa (root) were obtained for the SFSP-FSW joints. The MFS of 46.9% (face) and 46.2% (root) were obtained for the NFSP-FSW joints, while 61.6% and 58.8% were obtained for the SFSP-FSW joints. The SFSP-FSW reported best improvement results compared to NFSP-

FSW for the MFS. However, the UFS most improved results were found on the NFSP-FSW compared to the SFSP-FSW. Concerning material positioning, the best MFS results were found on the AA8011-AS regardless of the FSP method employed for both face and root surfaces. Moreover, the UFS best results for the SFSP-FSW were found on the AA8011-AS and AA6082-AS for the NFSP-FSW.

The tensile properties revealed that the FSWed and TIG-welded joints were improved post-FSP application regardless of the FSP conditions applied. The maximum tensile properties obtained for the NFSP-TIG were a UTS of 89.777 MPa, yield strength of 71.822 MPa and a strain rate of 27.994%. The SFSP-TIG maximum tensile properties were a UTS of 90.25 MPa, 72.2 MPa for the yield strength and 28.829% strain rate. The obtained maximum tensile properties for the NFSP-FSW joints included a UTS of 89.611 MPa, yield strength of 71.289 MPa and a strain of 24.609%. The maximum tensile properties obtained for the SFSP-FSW joints were a UTS of 92.511 MPa, yield strength of 74.004 MPa and a strain rate of 25.978%. Comparing the NFSP-TIG and SFSP-TIG average results, the most improved tensile and yield strengths were obtained on the SFSP-TIG joints, while the most improved ductility was noted on the NFSP-TIG joints. Similar behaviour was also noted on the FSP of the FSWed joints, where the SFSP-FSW joints yielded better tensile and yield strength, with NFSP-FSW having higher ductility. The phenomenon responsible was the high rate of cooling on the SFSPed specimens. The obtained tensile results correlate with the grain sizes of the respective joints. The maximum FSPed FSW tensile properties were obtained from the AA6082-AS joints while the FSPed TIG-welded joints were obtained from the AA8011-AS. The fracture surface morphology results suggest that all joints exhibited a ductile failure mode based on the characteristics noted.

The average hardness of the TIG-welded joints prior to FSP was 58.5 HV; post-FSP the NFSP-TIG hardness was 60.5 HV for the AA6082-AS joints and 61.5 HV for the AA68011-AS one. The SFSP-TIG AA6082-AS average was reported at 63 HV and 69 HV for the AA8011-AS joints. The nugget zone average hardness of the FSWed joints prior to FSP was 48 HV for the AA6082-AS joint and 47 HV for the AA8011-AS joint. Post-FSP, the NFSP-FSW average hardness was 53 HV and 52 HV for the AA6082-AS and AA8011-HV joints, respectively. Furthermore, the SFSP-FSW AA6082-AS average hardness was 61 HV and 55 HV for the AA8011-AS joint. While the specimen positioning had no particular sequence, the material positioning was determined to have a minimal effect on the FSW and NFSP-FSW joints but with the SFSP-FSW a notable difference of 6 HV was observed. Both NFSPed and SFSPed joints showed an increase in the hardness of the nugget zone compared to the welded joints, with the SFSPed showing a higher increase compared to the NSFSPed joints. However, for the FSPed TIG specimens, the AA8011-AS joints had a higher increase than the AA6082-AS joints, while on the FSPed FSW joints the AA6082-AS had a higher increase. The hardness results correlated with grain sizes obtained with respect to the Orowam mechanism and Hall-Petch relationship. The different operating conditions had a notable impact on the hardness due to different heat inputs during the FSP of the welded joints.

5.2 Recommendations

Based on the results obtained the following recommendations can be made:

It is recommended that the tool offset be added to the parameters to be optimised for significant enhancement of the mechanical properties of the friction stir processed dissimilar joints under

both conditions employed. In as much as the application of the friction stir processing yielded better results for both material positionings considered, the parameters used do not fully favour both conditions. This is due to the difference in the material melting points and strength. Based on those observations, it is therefore recommended that the processing parameters be optimised for each joint configuration to maximise joint properties.

REFERENCES

1. Drozdov, A. Aluminium: The thirteenth element. RUSAL Library, **2007**. ISBN 978-5-91523-002-5.

2. Richards, J.W. Aluminium: Its history, occurrence, properties, metallurgy and applications, including its alloys . 3 ed. Henry Carey Baird & Co, **1896**.

3. Nappi, C. The global aluminium industry 40 years from 1972 (PDF) (Report). International Aluminium Institute, **2013**.

4. Menzie, W.D.; Barry, J.J.; Bleiwas, D.I; Bray, E.L.; Goonan, T.G.; Grecia, M. The global flow of aluminum from 2006 through 2025. Open-file report 2010–1256. U.S. Department of the Interior U.S. Geological Survey.

5. Totten, G.E.; Mackenzie, D.S. Handbook of aluminum. Vol. 2, Alloy production and materials manufacturing, New York, Basel: Marcel Dekker, **2003**.

6. Sabari, S.S. Evaluation of performance of friction stir welded AA2519-T87 aluminium alloy joints. Doctor Of Philosophy In Manufacturing Engineering Department Of Manufacturing Engineering Faculty Of Engineering And Technology, Tamil Nadu, India, **2016**.

7. Liu, L.; Ren, D.; Liu, F. A review of dissimilar welding techniques for magnesium alloys to aluminum alloys. *Mater.*, 7(5), **2014**, pp. 3735–3757.

8. Lumley R.N.,1 - Introduction to aluminium metallurgy. In Woodhead Publishing Series in Metals and Surface Engineering, Fundamentals of Aluminium Metallurgy, Woodhead Publishing, **2011**, pp. 1-19, I SBN 9781845696542.

9. Yashpal, K.; Jawalkar, C.S.; Kant, S. Review on use of aluminium alloys in aircraft components*. i-manager's J. Mater. Sci.,* 3(3), **2015**, pp. 33-39.

10. Chen, X.; Peng, Y.; Peng, S.; Yao, S.; Chen, C.; Xu, P.; Pi, J. Flow and fracture behavior of aluminum alloy 6082-T6 at different tensile strain rates and triaxialities. *PLoS One,* 12(7), **2017**, e0181983.

11. Liu, H.J.; Fujii, H.; Maeda, M.; Nogi, K. Mechanical properties of friction stir welded joints of 1050 – H24 aluminium alloy. *Sci. Technol. Weld. Join.,* 8(6), **2003**, pp.450-454.

12. Verma, S.; Misra, J.P.; Gupta, M. Chapter 13: Study of temperature distribution during FSW of the aviation-grade AA6082. Manufacturing Engineering: Select Proceedings of CPIE 2018**,** edited by Sharma, V.S.; Dixit, U.S.; Alba-Baena, N. Springer Nature, Singapore, **2019** pp. 185-202.

13. Fayomi, J.; Popoola, A.P.I.; Popoola, O.M.; Oladijo, O.P.; Fayomi, O.S.I. Tribological and microstructural investigation of hybrid AA8011/ZrB2-Si3N4 nanomaterials for service life improvement. *Results in Physics*, 14, **2019**, 102469.

14. Kashaev, N.; Ventzke, V.; Çam, G.;Prospects of laser beam welding and friction stir welding processes for aluminum airframe structural applications. *J. Manuf. Processes*, 36, **2018**, pp. 571-600.

15. Padhy G. K., Wu C. S. and Gao S. Friction stir based welding and processing technologies

- processes, parameters, microstructures and applications: A review. *J. Mater. Sci. Technol*., 34(1), **2018**, pp 1–38.

16. Yeni, C.; Sayer, S.; Pakdil, M. Comparison of mechanical and microstructural behaviour of TIG, MIG and friction stir welded 7075 aluminium alloy. *Kovove Mater.,* 47, **2009,** pp. 341–347.

17. Sabari, S.S. Evaluation of performance of friction stir welded AA2519-T87 aluminium alloy joints. Doctor of Philosophy in Manufacturing Engineering Department Of Manufacturing Engineering Faculty Of Engineering And Technology, Tamil Nadu, India, **2016**.

18. Hou, K.; Baeslack, W. Characterization of the heat-affected zone in gas tungsten arc welded aluminium alloy 2195-T8, J. Mater. Sci. Letters, 15(3), **1996**, pp.239–244.

19. Subbaiah, K.; Jayakumar, C.V. Friction Stir Welding of Al-Mg-Mn Aluminum Alloy Plates: A Review. World Academy of Science, Engineering and Technology, International Journal of Industrial and Manufacturing Engineering 9(1), **2015**, Paris, France, January 23-24.

20. Shanavas, S.; Raja Dhas, J.E. Weldability of AA 5052 H32 aluminium alloy by TIG welding and FSW process – A comparative study. *IOP Conf. Ser.: Mater. Sci. Eng.,* 247, **2017**, pp. 012016.

21. Daniolos, N.M.; Pantelis, D.I. Microstructural and mechanical properties of dissimilar friction stir welds between AA6082-T6 and AA7075-T651. *Int. J. Adv. Manuf. Technol.,* 88, **2017,** pp. 2497–2505.

22. Peng, G.; Ma, Y.; Hu, J.; Jiang, W.; Huan, Y.; Chen, Z.; Zhang, T. Nanoindentation Hardness Distribution and Strain Field and Fracture Evolution in Dissimilar Friction Stir-Welded AA 6061-AA 5A06 Aluminum Alloy Joints. *Adv. Mater. Sci. Eng.*, 4873571, **2018**, pp. 1-11.

23. Mishra, R.S.; Mahoney, M.W. Friction stir processing: A new grain refinement technique to achieve high strain rate superplasticity in commercial alloys. *Mater. Sci. Forum*, 357–359, **2001**, pp. 507–12.

24. Mishra, R.S.; Mahoney, M.W.; McFadden, S.X.; Mara, N.A.; Mukherjee, A.K. High strain rate superplasticity in a friction stir processed 7075 Al alloy. *Scri. Mater.,* 42(2), **2000**, pp. 163–168.

25. Senthilkumar, R.; Prakash, M.; Arun, N.; Jeyakumar, A.A. 2019 The effect of the number of passes in friction stir processing of aluminum alloy (AA6082) and its failure analysis. *Appl. Surf. Sci.,* 491, **2019**, pp. 420–431.

26. Mishra, R.S.; Ma, Z.Y.; Charit, I. 2003 Friction stir processing: a novel technique for fabrication of surface composite. *Mater. Sci. Eng. A,* 341, **2003**, pp. 307–310.

27. Mishra, R.S.; Ma, Z.Y. Friction stir welding and processing. *Mater. Sci. Eng.: R,* **2005**, 50(1-2), pp. 1-78.

28. Ma, Z. Friction stir processing technology: A review. *Metall. Mater. Trans. A,* 39, **2008**, pp. 642–658.

29. WęglowskI, M.S. Friction stir processing –state of the art. *Arch. Civ. Mech. Eng.,* 18, **2018**, pp. 114-129.

30. Saini, N.; Dwivedi, D.K.; Jain, P.K.; Singh, H. Surface modification of cast Al-17%Si alloys using friction stir processing. *Proc. Eng.,* 100, **2015**, pp. 1522–1531.

31. Albakri, A.N.; Aljoaba, S.Z.; Khraisheh, M.K. Modelling of friction stir processing with in

process cooling using computational fluid dynamics analysis Advances in Sustainable Manufacturing ed G Seligeret al, Berlin, Heidelberg: Springer, **2011**, pp.99–105.

32. Sakurada, D.; Katoh, K.; Tokisue, H. Underwater friction welding of 6061 aluminum alloy. *Journal of Japan Institute of Light Metals*, 52(1), **2007**, pp. 2–6.

33.. Hofmann, D.C.; Vecchio, K.S. Submerged friction stir processing (SFSP): An improved method for creating ultra-fine-grained bulk materials. *Mater. Sci. Eng. A*, 402(1–2), **2005**, pp. 234–241.

34. Su, J.Q.; Nelson, T.W.; Sterling, C.J. Friction stir processing of large-area bulk UFG aluminum alloys. *Scr. Mater.,* 52, **2005**, pp. 135–140.

35. Bhargava, G.; Yuan, W.; Webb, S.S.; Mishra, R.S. Influence of texture on mechanical behavior of friction-stir-processed magnesium alloy. *Metall. Mater. Trans. A Phys. Metall. Mater. Sci.,* 41 **2010**, pp. 13–7.

36. Feng, X.; Rui-Dong, F.; Li, Y.; Sang, D. 2020 Effects of nitrogen alloying and friction stir processing on the microstructures and mechanical properties of CoCrFeMnNi high-entropy alloys. *J. Alloy Compd.,* 822, **2020**, 153512.

37. Zhang, H.; Liu,H. Mathematical model and optimization for underwater friction stir welding of a heat-treatable aluminum alloy. *Mater. Des.*, 45, **2013**, pp. 206–211.

38. Ilangovan, M.; Boopathy, S.R.; Balasubramanian, V. Microstructure and tensile properties of friction stir welded dissimilar AA6061-AA5086 aluminium alloy joints*. Trans. Nonferr. Met. Soc. China (English Ed.)*, 25(4), **2015**, pp. 1080–1090.

39. Li, K.; Liu, X.; Zhao, Y. Research status and prospect of friction stir processing technology. *Coatings*, 9, 129, **2019**, pp. 1-14.

40. Karthikeyan, L.; Kumar, V.S. Relationship between process parameters and mechanical properties of friction stir processed AA6063-T6 aluminum alloy. *Mater. Des.*, 32, **2011**, pp. 3085–3091.

41. Sathiskumar, R.; Murugan, N.; Dinaharan, I.; Vijay, S.J. Role of friction stir processing parameters on microstructure and microhardness of boron carbide particulate reinforced copper surface composites. *Sadhana Acad. Proc. Eng. Sci.*, 38, **2013**, pp. 1433–1450.

42. Tamadon, A.; Pons, D.J.; Sued, K.; Clucas, D. Formation mechanisms for entry and exit defects in bobbin friction stir welding. *Met.,* 2018, 8, 33.

43. Mehta, K.P.; Badheka, V.J. Effects of tilt angle on the properties of dissimilar friction stir welding copper to aluminum. *Mater. Manuf. Process*., 31, **2016**, pp. 255–263.

44. Sekban, D.M.; Aktarer, S.M.; Yanar, H.; Alsaran, A.; Purcek, G. Improvement the wear behavior of low carbon steels by friction stir processing. *IOP Conf. Ser.,* 174, **2017**, 012058.

45. Tinubu, O.O.; Das, S.; Dutt, A.; Mogonye, J.E.; Ageha, V.; Xu, R.; Forsdike, J.; Mishra, R.S.; Scharf, T.W. Friction stir processing of A-286 stainless steel: Microstructural evolution during wear. *Wear*, 356–357, **2016**, pp. 94–100.

46. Wang, Y.; Huang, Y.; Meng, X.; Wan, L.; Feng, J. Microstructural evolution and mechanical properties of MgZnYZr alloy during friction stir processing. *J. Alloys Compd.,* 696, **2017**, pp. 875–883.

47. Jin, Y.; Wang, K.; Wang, W.; Peng, P.; Zhou, S.; Huang, L.; Yang, T.; Qiao, K.; Zhang, B.;

Cai, J.; et al. Microstructure and mechanical properties of AE42 rare earth-containing magnesium alloy prepared by friction stir processing. *Mater. Charact*., 150, **2019**, pp. 52–61.

48. Shang, Q.; Ni, D.R.; Xue, P.; Xiao, B.L.; Wang, K.S.; Ma, Z.Y. An approach to enhancement of Mg alloy joint performance by additional pass of friction stir processing. *J. Mater. Process. Technol*., 264, **2019**, pp. 336–345.

49. Barmouz, M.; Besharati Givi, M.K.; Jafari, J. Evaluation of Tensile Deformation Properties of Friction Stir Processed Pure Copper: Effect of Processing Parameters and Pass Number. *J. Mater. Eng. Perform.*, 23, **2014**, pp. 101–107.

50. Luo, P.; McDonald, D.T.; Xu, W.; Palanisamy, S.; Dargusch, M.S.; Xia, K. A modified Hall–Petch relationship in ultrafine-grained titanium recycled from chips by equal channel angular pressing. *Scr. Mater.,* 66, **2012**, pp. 785–788.

51. Pan, L.; Kwok, C.T.; Lo, K.H. Friction-stir processing of AISI 440C high-carbon martensitic stainless steel for improving hardness and corrosion resistance. *J. Mater. Process. Technol.*, 277, **2020**, 116448.

52. Yasavol, N.; Jafari, H. Microstructure, Mechanical and Corrosion Properties of Friction Stir-Processed AISI D2 Tool Steel. *J. Mater. Eng. Perform.,* 24, **2015**, pp. 2151–2157.

53. Kawasaki, M.; Langdon, T.G. Principles of superplasticity in ultrafine-grained materials. *J. Mater. Sci.*, 42, **2007**, pp. 1782–1796.

54. Zhang, W.J.; Ding, H.; Cai, M.H.; Yang, W.J.; Li, J.Z. Ultra-grain refinement and enhanced low-temperature superplasticity in a friction stir-processed Ti-6Al-4V alloy. *Mater. Sci. Eng. A Struct. Mater. Prop. Microstruct. Process.*, 727, **2018**, pp. 90–96.

55. Yang, Y.G.; Zhao, Y.T.; Kai, X.Z.; Tao, R. Superplasticity behavior and deformation mechanism of the in-situ Al3Zr/6063Al composites processed by friction stir processing. *J. Alloy. Compd.*, 710, **2017**, pp. 225–233.

57. Orozco-Caballero, A.; Alvarez-Leal, M.; Hidalgo-Manrique, P.; Cepeda-Jimenez, C.M.; Ruano, O.A.; Carreno, F. Grain size versus microstructural stability in the high strain rate superplastic response of a severely friction stir processed Al-Zn-Mg-Cu alloy. *Mater. Sci. Eng. A Struct. Mater. Prop. Microstruct. Process.,* 680, **2017**, pp. 329–337.

58. Chai, F.; Zhang, D.T.; Li, Y.Y.; Zhang, W.W. High strain rate superplasticity of a fine-grained AZ91 magnesium alloy prepared by submerged friction stir processing. *Mater. Sci. Eng. A Struct. Mater. Prop. Microstruct. Process.,* 568, **2013**, pp. 40–48.

59. Abraham, S.J.; Dinaharan, I.; Selvam, J.D.R.; Akinlabi, E.T. Microstructural characterization of vanadium particles reinforced AA6063 aluminum matrix composites via friction stir processing with improved tensile strength and appreciable ductility. *Compos. Comm.*, *12*, **2019**, pp. 54–58.

60. Bourkhani, R.D.; Eivani, A.R.; Nateghi, H.R. Through-thickness inhomogeneity in microstructure and tensile properties and tribological performance of friction stir processed AA1050-Al2O3 nanocomposite. *Compos. Part B Eng.*, *174*, **2019**, 107061

61. Zahmatkesh, B.; Enayati, M.H. A novel approach for development of surface nanocomposite by friction stir processing. *Mater. Sci. Eng. A*, *527*, **2010**, pp. 6734–6740.

62. Prabhu, M.S.; Perumal, A.E.; Arulvel, S.; Issac, R.F. Friction and wear measurements of friction stir processed aluminium alloy 6082/$CaCO_3$ composite. *Measurement*, *142*, **2019**, pp. 10–20.

63. Reddy, G.M.; Rao, A.S.; Rao, K.S. Friction stir surfacing route: effective strategy for the enhancement of wear resistance of titanium alloy. *Trans. Indian Inst. Met.*, 66, **2013**, pp. 231–238.

64. Nitinkumar, P.; Gaurav, V.; Pandey, R.R.; Shanmugasundaram, T. Fabrication of AA7005/TiB2-B4C surface composite by friction stir processing: Evaluation of ballistic behaviour. *Defence Technol.*, 15(3), **2019**, pp. 363-368.

65. Dhayalan, R.; Kalaiselvan, K.; R. Sathiskumar, R. Characterization of AA6063/SiC-Gr Surface Composites Produced by FSP Technique. *Proc. Eng.*, 97, **2014,** pp. 625-631.

66. Khodabakhshi, F.; Arab, S.M.; Svec, P.; Gerlich, A.P. Fabrication of a new Al-Mg/graphene nanocomposite by multi-pass friction-stir processing: Dispersion, microstructure, stability, and strengthening. *Mater. Charact.*, 132, **2017**, pp. 92–107.

67. Hosseini, S.A.; Ranjbar, K.; Dehmolaei, R.; Amirani, A.R. Fabrication of Al5083 surface composites reinforced by CNTs and cerium oxide nano particles via friction stir processing. *J. Alloy. Compd.,* 622, **2015**, pp. 725–733.

68. Yang, K.; Li, W.Y.; Niu, P.L.; Yang, X.W.; Xu, Y.X. Cold sprayed AA2024/Al2O3 metal matrix composites improved by friction stir processing: Microstructure characterization, mechanical performance and strengthening mechanisms. *J. Alloy. Compd.*, 736, **2018**, pp. 115–123.

69. Zykova, A.P.; Tarasov, S.Y..; Chumaevskiy, A.V.; Kolubaev, E.A. A Review of Friction Stir Processing of Structural Metallic Materials: Process, Properties, and Methods. *Met.*, 10, **2020**, 772.

70. Hsu, C.J.; Kao, P.W.; Ho, N.J. Ultrafine-grained Al-Al2Cu composite produced in situ by friction stir processing. *Scr. Mater*., 53, **2005**, pp. 341–345.

71. You, G.L.; Ho, N.J.; Kao, P.W. The microstructure and mechanical properties of an Al-CuO in-situ composite produced using friction stir processing. *Mater. Lett.*, 90, **2013**, pp. 26–29.

72. You, G.L.; Ho, N.J.; Kao, P.W. Aluminum based in situ nanocomposite produced from Al-Mg-CuO powder mixture by using friction stir processing. *Mater. Lett.*, 100, **2013**, pp. 219–222.

73. Qian, J.W.; Li, J.L.; Xiong, J.T.; Zhang, F.S.; Lin, X. In situ synthesizing Al3Ni for fabrication of intermetallic-reinforced aluminum alloy composites by friction stir processing. *Mater. Sci. Eng. A Struct. Mater. Prop. Microstruct. Process*., 550*,* **2012**, pp. 279–285.

74. Zhang, Q.; Xiao, B.L.; Wang, Q.Z.; Ma, Z.Y. In situ Al3Ti and Al2O3 nanoparticles reinforced Al composites produced by friction stir processing in an Al-TiO2 system. *Mater. Lett.,* 65, **2011**, pp. 2070–2072.

75. Golmohammadi, M.; Atapour, M.; Ashrafi, A. Fabrication and wear characterization of an A413/Ni surface metal matrix composite fabricated via friction stir processing. *Mater. Des.*, 85, **2015**, pp. 471–482.

76. Mahmoud, E.R.I.; Al-qozaim, A.M.A. Fabrication of In-Situ Al--Cu Intermetallics on aluminum surface by friction stir processing. *Arab. J. Sci. Eng.,* 41, **2016**, pp. 1757–1769.

77. Wang, T.; Gwalani, B.; Shukla, S.; Frank, M.; Mishra, R.S. Development of in situ composites via reactive friction stir processing of Ti–B4C system. *Compos. Part B Eng.,* 172, **2019**, pp. 54–60.

78. Miles, M.P.; Gunter, C.; Liu, F.; Nelson, T.W. Friction Stir Processing of 304L Stainless

Steel for Crack Repair. In: Hovanski, Y.; Mishra, R.; Sato, Y.; Upadhyay, P.; Yan, D. (eds) Friction Stir Welding and Processing IX. The Minerals, Metals & Materials Series. Springer, Cham, **2017**.

79. Al-Badour, F.; Zainelabdeen, I.H.; Suleiman, R.K.; Adesina, A. Crack repair using hybrid additive manufacturing and friction stir processing. Proceedings of the conference Volume 6A: Materials and Fabrication. San Antonio, Texas, USA. July 14–19, **2019**. V06AT06A004.

80. Mehdi, H.; Mishra, R.S. Effect of friction stir processing on microstructure and mechanical properties of TIG welded joint of AA6061 and AA7075. *Metallogr. Microstruct. Anal*., 9(3), **2020**, pp. 403–418.

81. Shang, Q.; Ni, D.R.; Xue, P.; Xiao, B.L.; Wang, K.S.; Ma, Z.Y. An approach to enhancement of Mg alloy joint performance by additional pass of friction stir processing. *J. Mater. Process.Technol.*, 264, **2019**, pp. 336-345.

82. Sakurada, D.; Katoh, K.; Tokisue, H. Underwater friction welding of 6061 aluminum alloy. *J. Japan Inst. Light Met.*, 52(1), **2007**, pp. 2–6.

83. Hoffman, D.C.; Kennesh, V. Submerged friction stir processing (SFSP): an improved method for creating ultra-fine-grained bulk materials. *Mater. Sci. Eng. A*, 402 (1–2), **2005**, pp. 234-241.

84. Darras, B. and Kishta, E. Submerged friction stir processing of AZ31 Magnesium alloy. *Mater. Des.,* 47, **2013**, pp. 133–137.

85. Zhang, Y.N.; Cao, X.; Larose, S.; Wanjara, P. Review of tools for friction stir welding and processing. *Canad. Metall. Q.*, 51(3), 2012.

86. Gowthaman, P.S.; Saravanan, B.A. Determination of weldability study on mechanical properties of dissimilar Al-alloys using Friction stir welding process*. Mater. Today: Proc.*, **2020**, https://doi.org/10.1016/j.matpr.2020.08.599.

87. Kailainathan, S.; Sundaram, S.K.; Nijanthan, K. (2014) Influence of friction stir welding parameter on mechanical properties in dissimilar aluminium alloys. *Int. J. Innov. Res. Sci. Eng. Technol.*, 3(8), **2014**, pp. 15691–15695.

88. Sahu, P.K.; Pal, S.; Pal, S.K.; Jain, R. Influence of plate position, tool offset and tool rotational speed on mechanical properties and microstructures of dissimilar Al/Cu friction stir welding joints. *J. Mater. Process. Technol.*, 235, **2016**, pp. 55–57.

89. Karimi, N.; Nourouzi, S.; Shakeri, M.; Habibnia, M.; Dehghani, A. Effect of tool material and offset on friction stir welding of Al alloy to carbon steel. *Adv. Mater. Res.*, 445, **2012**, pp. 747–752.

90. Cavaliere, P.; Panella, F. Effect of tool position on the fatigue properties of dissimilar 2024-7075 sheets joined by friction stir welding. *J. Mater. Process. Technol.,* 206, **2008**, pp. 249–255.

91. Park, S.K.; Hong, S.T.; Park, J.H.; Park, K.Y.; Kwon, Y.J.; Son, H.J. Effect of material locations on properties of friction stir welding joints of dissimilar aluminium alloys. *Sci. Technol. Weld. Join.*, 15(4), **2010**, pp. 331–336.

92. Khanna, N.; Sharma, P.; Bharati, M. *et al.* Friction stir welding of dissimilar aluminium alloys AA 6061-T6 and AA 8011-h14: a novel study. *J Braz. Soc. Mech. Sci. Eng.* 42(7), **2020**, https://doi.org/10.1007/s40430-019-2090-3.

93. Palani, K.; Elanchezhian, C.; Avinash, K.; Karthik, C.; Chaitanya. K.; Sivanur, K.; Reddy. K.Y. Influence of friction stir processing parameters on tensile properties and microstructure of dissimilar AA 8011-h24 and AA 6061-t6 aluminum alloy joints in nugget zone. In: IOP conference series: materials science and engineering of the 3rd international conference on materials and manufacturing engineering, Tamil Nadu, India, **2018**, pp 1–10.

94. Cole, E.G.; Fehrenbacher, A.; Duffie, N.A.; Zinn, M.R.; Pfefferkorn, F.E.; Ferrier, N.J. Weld temperature effects during friction stir welding of dissimilar aluminum alloys 6061-T6 and 7075-T6. *Int. J. Adv. Manuf. Technol.,* 71(1–4), **2014**, pp. 643–652.

95. Rani, N.; Bishnoi, R.N.; Mahendru, A. Effect of tool pin profile on mechanical properties of single pass and double pass friction stir welded aluminium alloys AA6061 & AA8011. *Int. J. Curr. Eng.Technol.,* 5(6), **2015**, pp. 3780–3783.

96. Lee, W.; Yeon, Y.; Jung, S. The joint properties of dissimilar formed Al alloys by friction stir welding according to the fixed location of materials. *Scri. Mater.,* 49(5), **2003**, pp. 423-428.

97. Priya, R.; Subramanya Sarma, V.; Prasad Rao, K. Effect of post weld heat treatment on the microstructure and tensile properties of dissimilar friction stir welded AA 2219 and AA 6061 alloys. *Trans. Indian Inst. Met*., 62, **2009**, pp. 11–19.

98. Mahmoud, E.; Hamed, J.A.; Roohollah, Jamaati. The study of thermomechanical and microstructural issues in dissimilar FSW of AA6061 wrought and A390 cast alloys. *J. Manuf. Process.*, 41, **2019**, pp. 168-176.

99. Dinaharan, I.; Kalaiselvan, K.; Vijay, S.J.; Raja, P. Effect of material location and tool rotational speed on microstructure and tensile strength of dissimilar friction stir welded aluminum alloys. *Arch. Civ. Mech. Eng.,* 12, **2012**, pp. 446-454.

100. Mahdi, M.; Yasser, Z.; Damien, T.; Mohammad, J. Philippe, B. Friction stir welding of AA2024 and AA2198 Aluminum alloys: effect of tool geometry and process parameters. *I*CWNDT2016, Dec **2016**, Tehran, Iran. ffhal-01823809.

101. Simar, A.; Joncheere, C.; Deplus, K.; Pardoen, T.; de Meester, B. Comparing similar and dissimilar friction stir welds of 2017–6005A aluminium alloys. *Sci. Technol. Weld. Join.*, *15*, **2013**, pp. 254–259.

102. Giraud, L.; Robea, H.; Claudina, C.; Desrayaud, C.; Bocherd, P.; Feulvarcha, E. Investigation into the dissimilar friction stir welding of AA7020-T651 and AA6060-T6. *J. Mater. Process. Technol.*, *235*, **2016**, pp. 220–230.

103. El-Hafez, H.A.; El-Megharbel, A. Friction stir welding: Dissimilar aluminum alloys. *World J. Eng. Technol.*, *6*, **2018**, pp. 408–419.

104. Shah, L.H.A.; Sonbolestan, S.; Midawi, A.R.H.; Walbridge, S.; Gerlich, A. Dissimilar friction stir welding of thick plate AA5052-AA6061 aluminum alloys: Effects of material positioning and tool eccentricity. *Int. J. Adv. Manuf. Technol.,* **2019**, *105*, 889–904.

105. Chaudhari, R.; Parekh, R.; Ingle, A. Reliability of Dissimilar Metal Joints Using Fusion Welding: A Review. In Proceedings of the International Conference on Machine Learning, Electrical and Mechanical Engineering (ICMLEME'2014), Dubai, UAE, 8–9 January **2014**.

106. Mabuwa, S.; Msomi, V. Review on friction stir processed TIG and friction stir welded dissimilar alloy joints. *Met.*, 10(1), **2019**, 142.

107. Msomi, V.; Mbana, N.; Mabuwa, S. Microstructural analysis of the friction stir welded 1050-H14 and 5083-H111 aluminium alloys. *Materials Today: Proceedings*, 26(2), **2020**, pp.

189-192.

108. Mabuwa, S.; Msomi, V. The impact of material positioning towards the friction stir welded dissimilar aluminium alloy joints. *Recent Patents on Mech. Eng.*, 14(2), **2020**, pp. 252-259.

109. Yadav, V.D.; Bhatwadekar, S.G. Friction stir welding of dissimilar aluminium alloys AA1100 to AA6101-T6. *Int. J. Res. Aero. Mech. Eng.,* 3(1), **2015**, pp. 1-6.

110. Kumbhar, N.T.; Bhanumurthy, K. Friction StirWelding of Al 5052 with Al 6061 Alloys. *J. Metall.,* **2012**, pp. 1-7.

111. Park, S. K.; Hong, S.T.; Park, J.H.; Park, K.Y.; Kwon, Y.J.; Son, H.J. Effect of material locations on properties of friction stir welding joints of dissimilar aluminium alloys. *Sci. Technol. Weld. Join.,* 15(4), **2010**, pp. 331–336.

112. Khan, N.Z.; Siddiquee, A.N.; Khan, Z.A.; Mukhopadhyay, A.K. Mechanical and microstructural behavior of friction stir welded similar and dissimilar sheets of AA2219 and AA7475 aluminium alloys. *J. Alloys Compd.*, 695, **2017**, pp. 2902–2908.

113. Amancio-Filho, S.T.; Sheikhi, S.; Dos Santos, J.F.; Balfarini, C. Preliminary study on the microstructure and mechanical properties of dissimilar friction stir welds in aircraft aluminium alloys 2024-T351 and 6056-T4. *J. Mater. Process*. *Technol.,* 206, **2008**, 132e142.

114. Da Silva, A.A.M.; Arruti, E.; Janeiro, G.; Aldanondo, E.; Alvarez, P.; Echeverria, A. Material flow and mechanical behaviour of dissimilar AA2024-T3 and AA7075-T6 aluminium alloys friction stir welds. *Mater. Des.,* 32, **2011**, 2021e2027.

115. Cavaliere, P.; Nobile, R.; Panella, F.W.; Squillace, A. Mechanical and microstructural behaviour of 2024–7075 aluminium alloy sheets joined by friction stir welding. *Int. J. Mach. Tools Manuf.,* 46(6), **2006**, pp. 588-594.

116. Niu, P.L.; Li, W.Y.; Chen, D.L. Tensile and cyclic deformation response of friction-stir-welded dissimilar aluminum alloy joints: Strain localization effect. *J. Mater. Sci. Technol.*, 73, **2021**, pp. 91-100.

117. Wang, B.; Lei, B.B.; Zhu, J.X.; Feng, Q.; Wang, L.; Wu, D. EBSD study on microstructure and texture of friction stir welded AA5052-O and AA6061-T6 dissimilar joint. *Mater. Des.*, 87, **2015**, pp. 593-599.

118. EI-Madhoun, Y.; Mohamed, A.; Bassim, M.N. Cyclic stress/strain response and dislocation structures in polycrystalline aluminum. *Mater. Sci. Eng. A*, 359, **2003**, pp. 220-227.

119. Pan, Q.S.; Zhou, H.F.; Lu, Q.H. Gao, H.J.; Lu, L. History-independent cyclic response of nanotwinned metals. *S. N.,* 551, **2017**, pp. 214-217.

120. Feng, A.H.; Chen, D.L.; Ma, Z.Y. Microstructure and cyclic deformation behavior of a friction-stir-welded 7075 Al alloy. *Metall. Mater. Trans. A,* 41 A, **2010**, pp. 957-971.

121. Xu, W.F.; Liu, J.H.; Chen, D.L.; Luan, G.H.; Yao, J.S. Change of microstructure and cyclic deformation behavior along the thickness in a friction-stir-welded aluminum alloy. *Scr. Mater.,* 66, **2012**, pp. 5-8.

122. Shao, S.; Khonsan, M.M.; Wang, J.; Shamsael, N.; Li, N. Original report frequency dependent deformation reversibility during cyclic loading. *Mater. Res. Lett.,* 6, **2018**, pp. 390-397.

123. Bindu, A.H.; Chaitanya, B.S.K.; Ajay, K.; Sudhakar, I.; Investigation on feasibility of

dissimilar welding of AA2124 and AA7075 aluminium alloy using tungsten inert gas welding. *Mater. Today: Proc*., 26(2), **2020**, pp. 2283-2288.

124. Vijay, S.; Rajanarayanan, S.; Ganeshan, G.N. Analysis on mechanical properties of gas tungsten arc welded dissimilar aluminium alloy (Al2024 & Al6063). Materials Today: Proceedings, 21(1), **2020**, pp. 384-391.

125. Wang, W.; Cao, Z.; Liu, K.; Zhang, X.; Zhou, K.; Ou, P. Fabrication and Mechanical Properties of Tungsten Inert Gas Welding Ring Welded Joint of 7A05-T6/5A06-O Dissimilar Aluminum Alloy. *Mater.,* 11(7), **2018**, 1156.

126. Safari, M.; de Sousa, R.A.; Joudaki, J.; Mostaan, H. Experimental Investigation of Weld Quality for Dissimilar Welding of AA6061-T6/AA7075-T6 Aluminum Alloys. *J. Stress Anal.,* 4(2), **2020**, pp. 69-79.

127. Kou, S. Welding Metallurgy, 2nd Ed. John Wiley and Sons Inc., New Jersey, USA, **2003**.

128. Patil, C.; Patil, H.; Patil, H. Experimental investigation of hardness of FSW and TIG joints of aluminium alloys of AA7075 and AA6061. *Frattura ed Integrita Strutturale*, 10(37), **2016**, pp. 325–332.

129. Ishak, M.; Mohd Noordin, N.F.; Ahmad Shah, L.H. Feasibility study on joining dissimilar aluminum alloys AA6061 and AA7075 by Tungsten inert gas (TIG). *Jurnal Teknologi*, 75(7), **2015**, pp. 79–84.

130. Hazari, H.R.; Balubai, M.; Kumar, S.D.; Haq, A.U.I. Experimental investigation of TIG welding on AA 6082 and AA 8011. *Materials Today: Proceedings*, 19(2), **2019**, pp. 818-822.

131. Baghel, P.K.; Nagesh, D.S. Mechanical properties and microstructural characterization of automated pulse TIG welding of dissimilar aluminum alloy. *Int. J. Eng. Mater. Sci.,* 25(2), **2018**, pp.147-154.

132. Sayer, S.; Yeni, C.; ErtugruL, O. Comparison of mechanical and microstructural behaviors of tungsten inert gas welded and friction stir welded dissimilar aluminum alloys AA 2014 and AA 5083. *Metall. Mater.*, 49(2), **2011**, pp. 155–162.

133. Waleed, W.A.; Subbaiah, K. Effect of ER4047 Filler Rod on Tungsten Inert Gas Welding of AA5083-H111 and AA6061-T6 Aluminium Alloys. *J. Chem. Pharm. Sci*., 7, **2017**, pp. 210–213.

134. Ghaffarpour, M.; Kazemi, M.; Mohammadi Sefat, M.J.; Aziz, A.; Dehghani, K. Evaluation of dissimilar joints properties of 5083-H12 and 6061-T6 aluminum alloys produced by tungsten inert gas and friction stir welding. *Proceedings of the Institution of Mechanical Engineers, Part L: Journal of Materials: Design and Applications*., 231(3), **2017**, pp. 262-278.

135. Palanivel, R. et al. Effect of tool rotational speed and pin profile on microstructure and tensile strength of dissimilar friction stir welded AA5083-H111 and AA6351-T6 aluminum alloys. *Mater. Des.*, 40, **2012**, pp. 7–16.

136. Leitao, C.; Louro, R.; Rodrigues, D.M. Analysis of high temperature plastic behavior and its relation with weld ability in friction stir welding for aluminum alloys AA5083-H111 and AA6082-T6. *Mater. Des.,* 37, **2012**, pp. 402-409.

137. Fuller, C.B.; Mahoney, M.W. The effect of friction stir processing on 5083-H321/5356 Al arc welds: Microstructural and mechanical analysis. *Metall. Mater. Trans.,* A 37, **2006**, pp. 3605–3615.

138. Mehdi, H.; R.S. Mishra, R.S. Effect of friction stir processing on mechanical properties and heat transfer of TIG welded joint of AA6061 and AA7075. *Def. Technol.,* **2020**, https://doi.org/10.1016/j.dt.2020.04.014.

139. Devireddy, K.; Devuri, V.; Cheepu, M.; Kumar, B.K. Analysis of the influence of friction stir processing on gas tungsten arc welding of 2024 aluminum alloy weld zone. *IJMPERD*, 8(1), **2018**, pp. 243-252.

140. Msomi, V.; Mabuwa, S. Experimental investigation of bending and tensile strength of friction stir processed TIG-welded AA5083-H111 joint. *Eng. Res. Express,* 2, **2020**, 045005.

141. Mabuwa, S. Msomi, V. The effect of friction stir processing on the friction stir welded AA1050-H14 and AA6082-T6 joints. Materials Today: Proceedings, 26(2), **2020**, pp. 193-199.

142. Msomi, V.; Mabuwa, S. Analysis of material positioning towards microstructure of the friction stir processed AA1050/AA6082 dissimilar joint. Advances in Industrial and Manufacturing Engineering, 1, **2020**, 100002.

143. Mabuwa, S.; Msomi, V. Effect of Friction Stir Processing on Gas Tungsten Arc-Welded and Friction Stir-Welded 5083-H111 Aluminium Alloy Joints. *Adv. Mater. Sci. Eng.,* **2019**, 3510236.

144. da Silva, J.; Costa, J.M.; Loureiro, A.; Ferreira, J.M. Fatigue behaviour of AA6082-T6 MIG welded butt joints improved by friction stir processing. *Mater. Des.*, 51, **2013**, pp. 315-322.

145. Jesus, J.S.; Costa, J.M.; Loureiro, A.; Ferreira, J.M. Fatigue strength improvement of GMAW T-welds in AA 5083 by friction-stir processing. *Int. J. Fatigue*, 97, **2017**, pp. 124-134.

146. Costa, M. Jesus, J.; Loureiro, A.; Ferreira, JJ.A.M.; Borrego, L.P. Fatigue life improvement of MIG welded aluminium T-joints by friction stir processing. *Int. J. Fatigue*, 61, **2014**, pp. 244-254.

147. L.P. Borrego, L.M. Abreu, J.M. Costa, J.M. Ferreira. Analysis of low cycle fatigue in AlMgSi aluminium alloys. *Eng. Fail. Anal.*, 11 (5), **2004**, pp. 715-725.

148. Mehdi, H.; Mishra, R.S. Study of the influence of friction stir processing on tungsten inert gas welding of different aluminum alloy. *SN Appl. Sci.,* 1, **2019**, 712, https://doi.org/10.1007/s42452-019-0712-0.

149. Mehdi, H.; Mishra, R.S. Effect of friction stir processing on mechanical properties and wear resistance of tungsten inert gas welded joint of dissimilar aluminum alloys. *J. Mater.Eng. Perform.,* **2021**, https://doi.org/10.1007/s11665-021-05549-y.

150. Kianezhad, M.; Honarbakhsh, Raouf, A. Improvement of tensile and impact properties of 5083 aluminium weldments using fillers containing nano-Al2O3 and postweld friction stir processing. *J. S. Afr. Inst. Min. Metall.*, 120(4), **2020**, pp. 277-286.

151. Saad, N.A.H.; Hashim, F.A.; Hashim, A.H. Using friction stir process (FSP) to improve the properties of AA7020 aluminum alloy weldments welded by tungsten inert gas (TIG). *J. kerbala Univ.*, 11(1), **2015**, pp. 50-60.

152. Gegesky, M.; Liou, F.; Newkirk, J. Proposed hybrid processes for part building using fusion welding and friction stir processing. Solid Freeform Fabrication 2016: Proceedings of the 26th Annual International Solid Freeform Fabrication Symposium – An Additive Manufacturing Conference. **2016**, pp. 1237-1258.

153. Feng, X.; Liu, H.; Lippold, J.C. Microstructure characterization of the stir zone of

submerged friction stir processed aluminum alloy 2219. *Mater. Charact.*, 82, **2013**, pp. 97-102.

154. Wang, J.; Yalin Lu, Y.; Zhou, D.; Zhang, Y.; Bai, Z.; Xingcheng Li, X. Effects of cooling condition on microstructural evolution and mechanical properties of friction stir processed 2A14 aluminum alloy. *Mater. Res. Express*, 6(12), **2019**, 126577.

155. Patel, V.; Badheka, V.; Wenya Li, Akkireddy, S. Hybrid friction stir processing with active cooling approach to enhance superplastic behavior of AA7075 aluminum alloy. *Arch. Civ. Mech. Eng.*, 19(4), **2019**, pp. 1368-1380.

156. Su, J.Q.; Nelson, T.W.; Sterling, C.J. Grain refinement of aluminum alloys by friction stir processing. *Philos. Mag.,* 86, **2016**, pp. 1–24.

157. Liu, F.C.; Ma, Z.Y. Low-temperature superplasticity of friction stir processed Al-Zn-Mg-Cu alloy*. Scr. Mater.,* 58, **2008**, pp. 667-670.

158. Mirian Mehrian, S.S.; Rahsepar, M.; Khodabakhshi, F.; Gerlich, A.P. Effects of friction stir processing on the microstructure, mechanical and corrosion behaviors of an aluminum-magnesium alloy. *Surface and Coatings Technol.*, 405, **2021**, 126647.

159. Khodabakhshi, F.; Gerlich, A.P.; Simchi, A.; Kokabi, A.H. Cryogenic friction-stir processing of ultrafine-grained Al-Mg-TiO2 nanocomposites. *Mater. Sci. Eng. A,* 620, **2014**, pp. 471-482.

160. Kumar, N.; Mishra, R.S.; Huskamp, C.S.; Sankaran, K.K. Critical grain size for change in deformation behavior in ultrafine grained Al–Mg–Sc alloy. *Scr. Mater., 64,* **2011**, pp. 576-579.

161. Liu, F.C.; Ma, Z.Y. Contribution of grain boundary sliding in low-temperature superplasticity of ultrafine-grained aluminum alloys. *Scr. Mater.,* 62, **2010**, pp. 125-128

162. McNelley, T.R.; Swaminathan, S.; Su, J.Q. Recrystallization mechanisms during friction stir welding/processing of aluminum alloys. *Scr. Mater.,* 58, **2008**, pp. 349-354.

163. Nandan, R.; DebRoy, T.; Bhadeshia, H.K.D.H. Recent advances in friction-stir welding – Process, weldment structure and properties. *Prog. Mater Sci.*, 53, **2008**, pp. 980-155.

164. Liu, H.J.; Zhang, H.J.; Huang, Y.X.; Yu, L. Mechanical properties of underwater friction stir welded 2219 aluminum alloy. *Trans. Nonferr. Met. Soc. China,* 20, **2010**, pp. 1387-1391.

165. Zhang, H.J.; Liu, H.J.; Yu, L. Microstructure and mechanical properties as a function of rotation speed in underwater friction stir welded aluminum alloy joints. *Mater. Des.,* 32, **2011**, pp. 4402-4407.

166. Ebnonnasir, A.; Karimzadeh, F.; Enayati, M.H. Novel artificial neural network model for evaluating hardness of stir zone of submerge friction stir processed Al 6061-T6 plate(Article). *Mater. Sci. Technol.,* 27, **2011**, pp. 990-995.

167. Javad, M.; Salman, N.; Hamed, J.A. The effect of heat treatment and cooling conditions on friction stir processing of A390-10 wt% SiC aluminium matrix composite. *Mater. Chem. Phys.,* 263, **2021,** 124423.

168. Singh, H.; Kumar, P.; Singh, B. Effect of under surface cooling on tensile strength of friction stir processed aluminium alloy 6082. *Asian J. Eng. Appl. Technol.,* 5(1), **2016**, pp. 40–44.

169. Nourbakhsh, S. H. and Atrian, A. Effect of submerged multi-pass friction stir process on the mechanical and microstructural properties of Al7075. *Journal of Stress Analysis*, 2(1),

2017, pp. 51–56.

170. Hughes, S.E. Chapter 3 - Analysis of a Fusion Weld, Editor(s): Hughes, S.E. In Woodhead Publishing Series in Welding and Other Joining Technologies. A quick guide to welding and weld inspection, Woodhead Publishing, **2009**, pp 22-35.

171. Michael J. Troughton. Handbook of Plastics Joining (Second Edition), William Andrew Publishing, **2009**, pp. 577-590.

172. Msomi, V.; Mabuwa, S.; Merdji, A.; Muribwathoho, O.; Motshwanedi, S.S.; Microstructural and mechanical properties of submerged multi-pass friction stir processed AA6082/AA8011 TIG-welded joint. *Materials Today: Proceedings*, 45(6) **2021**, pp. 5702-5705.

173. Mabuwa, S.; Msomi, V. The impact of submerged friction stir processing on the friction stir welded dissimilar joints. *Mater. Res. Express,* 7, **2020**, pp. 096513.

174. Tsai, C.L.; Kim, D.S.; Shim, Y.L.; Feng, Z.; Lee, S. Determination of Residual Stress and Effects in Thick-Section Weldments for Hydraulic Structures. Department of weldning engineering, Ohio State University, Columbus, Ohio. **1992.**

175. Mabuwa, S.; Msomi, V.; Analysis of mechanical properties between submerged and normal multiple-pass friction stir processing of the FSWed dissimilar aluminium joints. *Materials Today: Proceedings*, 45(6), **2021**, pp. 5400-5404.

176. Elangovan, K.; Balasubramanian, V. Influences of tool pin profile and tool shoulder diameter on the formation of friction stir processing zone in AA6061 aluminium alloy. *Mater. Des.,* 29(2), **2008**, pp. 362–373.

177. Gandra, J.; Miranda, R.; Vilaça, P.; Velhinho, A.; Teixeira, J.P. Functionally graded materials produced by friction stir processing. *J. Mater. Processing Technol.,* 211(11), **2011**, pp. 1659–1668.

178. Chen, Y.; Wang, H.; Wang, X. et al., Influence of tool pin eccentricity on microstructural evolution and mechanical properties of friction stir processed Al-5052 alloy. *Mater. Sci. Eng.: A,* 739, **2019**, pp. 272–276, 2019.

179. Muribwathoho, O.; Msomi, V.; Mabuwa, S.; Motshwanedi, S.S. Impact of multi-pass friction stir processing on microhardness of AA1050/AA6082 dissimilar joints. *Materials Today: Proceedings*, 46(1), **2021**, pp. 651-657.

180. Khorsand, S.; Huang, Y. Integrated casting-extrusion (ICE) of an AA6082 aluminium alloy. In: Ratvik A. (eds) Light Metals, **2017**. The Minerals, Metals & Materials Series. Springer, Cham.

181. Pedersen, K.O.; Westermann, I.; Furu, T.; Børvik, T.; Hopperstad, O.S. Influence of microstructure on work-hardening and ductile fracture of aluminium alloys. *Mater. Des.,* 70, **2015**, pp. 31–44.

182. Msomi, V.; Mabuwa, S. Effect of material positioning on fatigue life of the friction stir processed dissimilar joints. *Mater. Res. Express*, 7, **2020**, pp. 106520.

183. Balakrishnan, M.; Dinaharan, I.; Palanivel, R.; Sathiskumar, R. Effect of friction stir processing on microstructure and tensile behavior of AA6061/Al3Fe cast aluminum matrix composites. *J. Allo. Comp.,* 785, **2019**, pp. 531-541

184. Lentz, M.; Laptyeva, G.; Engler, O. Characterization of second phase particles into two aluminium foil alloys. *J. Allo.Comp.,* 660, **2016**, pp. 276-288.

185. Kumar, T.S.; Balasubramanian, V.; Sanavullah, M.Y. Influences of pulsed current tungsten inert gas welding parameters on the tensile properties of AA 6061 aluminium alloy. *Mater. Des.,* 28(7), **2007**, pp. 2080–2092.

186. Muzamil, M.; Wu, J.; Akhtar, M.; Zhang, Z.; Majeed, A.; Yang, J. Modified TIG Welding Joint Process: An Approach to Improve Microstructure and Fracto-Mechanical Behavior by MWCNTs Inducement in Al-Mg-Si Alloy. *Mater.,* 12, **2019**, pp. 1441.

187. Derazkola, H.A.; Eyvazian, A.; Simchi, A. Submerged friction stir welding of dissimilar joints between an Al-Mg alloy and low carbon steel: thermo-mechanical modelling, microstructural features, and mechanical properties. *Manuf. Process.,* 50, **2020**, pp. 68–79.

188. Huang, G.; Wu, J.; Hou, W.; Shen, Y. Microstructure, mechanical properties and strengthening mechanism of titanium particle reinforced aluminum matrix composites produced by submerged friction stir processing. *Mater. Sci. Eng. A*, 734, **2018**, p 353–363.

189. Ramaiyan, S.; Santhanam, S.K.V.; Muthuguru, P. Effect of scroll pin profile and tool rotational speed on mechanical properties of submerged friction stir processed AZ31B magnesium alloy. *Mater. Res.,* 21(3), **2018**, pp. e20170769.

190. Yan, Y.; Li, H.; Zhang, J.; Kong, N. The effect of initial annealing microstructures on the forming characteristics of Ti-4Al-2V titanium alloy. *Met.,* 9(5), **2019**, pp. 576 -589.

191. Thilagham, K.K.T; Muthukumaran, S. Process parameter optimization and characterization studies of dissimilar friction stir welded advancing side AA6082-T6 with retreating side AA2014-T87. *Mater Today: Proceedings,* 27(3), **2020**, pp. 2513-2519.

192. Gou, G.; Zhang, M.; Chen, H.; Chen, J.; Li, P, Yang YP. Efect of humidity on porosity, microstructure, and fatigue strength of A7N01S-T5 aluminum alloy welded joints in high-speed trains. *Mater. Des.,* 85, **2015**, pp. 309–317.

193. Liu, Y.; Wang, W.; Xie, J.; Sun, S.; Wang, L.; Qian, Y.; Meng, Y.; Wei, Y. Microstructure and mechanical properties of aluminum 5083 weldments by gas tungsten arc and gas metal arc welding. *Mater. Sci. Eng. A*, 549, **2012**, pp. 7–13.

194. Mutombo, K.; Toit, M.D. Corrosion fatigue behaviour of aluminium alloy 6061-T651 welded using fully automatic gas metal arc welding and ER5183 fller alloy. *Int. J. Fatigue*, 33(12), **2011**, pp. 1539–1547.

195. Rao, K.P.; Ramanaiah, N.; Viswanathan, N. Partially melted zone cracking in AA6061 welds. *Mater. Des.,* 29(1), **2008**, pp. 179-186,

196. Gupta, M.; Shukla, S.K.; Sharma, V.K.; Kumar, H. Effect of TIG and MIG welding on microstructural and mechanical properties: a state of art. *Int. J. Appl. Eng. Res.*, 13:9(2018), pp. 83–90.

197. Rao, S.R.K.; Reddy, G.M.; Rao, K.P. Effects of thermo-mechanical treatments on mechanical properties of AA2219 gas tungsten arc welds. *J. Mater. Process. Technol.,* 202(1–3), **2008**, pp. 283-289.

198. Çetkin, E.; Çelik, Y.H.; Temiz, S. Efect of welding parameters on microstructure and mechanical properties of AA7075/AA5182 alloys joined by TIG and MIG welding methods. *J. Braz. Soc. Mech. Sci. Eng*., 42(34), **2020**, pp. 1-12.

199. Mathers, G. The welding of aluminum and its alloys, 1st edn. Woodhead Publishing, Cambridge, **2002**.

200. Mironov, S.; Inagaki, K.; Sato, Y.S. et al. Effect of Welding Temperature on Microstructure of Friction-stir Welded Aluminum Alloy 1050. *Metall. Mater. Trans. A,* 46, **2015**, pp. 783–790.

201. Nene, S.S.; Liu, K.; Frank, M.; Mishra, R.S.; Brennan, R.E.; Cho, K.C.; Li, Z.; Raabe, D. Enhanced strength and ductility in a friction stir processing engineered dual phase high entropy alloy. *Sci. Rep.,* 7(1), **2017**, 16167.

202. Fonda, R.W.; Bingert, J.F. Microstructural evolution in the heat-affected zone of a friction stir weld. *Meta. Mater. Trans. A*, 35, **2004**, pp. 1487-1499.

203. Carlone, P.; Palazzo, G.S. Influence of process parameters on microstructure and mechanical properties in AA2024-T3 friction stir welding*. Metallogr. Microstruct. Anal.,* 2, **2013**, pp. 213–222.

204. Li, Y.; Fu, R.; Li, Y.; Peng, Y.; Liu, H. Abnormal Grain Growth in the Heat Affected Zone of Friction Stir Welded Joint of 32Mn-7Cr-1Mo-0.3N Steel during Post-Weld Heat Treatment. *Met.,* 8, **2018**, 254.

205. Mabuwa, S.; Msomi, V. Comparative analysis between normal and submerged friction stir processed friction stir welded dissimilar aluminium alloy joints. J*. Mater. Res. Technol.,* 9(5), **2020**, pp. 9632-9644.

206. Zhao, H.J.; Wang, B.Y.; Liu, G.; Yang, L.; Xiao, W.C. Effect of vacuum annealing on microstructure and mechanical properties of TA15 titanium alloy sheets. *Trans. Nonferr. Met. Soc. China,* 25(6), **2015**, pp. 1881–1888.

207. Dragatogiannis, D.A.; Koumoulos, E.P.; Kartsonakis, I.; Pantelis, D.I.; Karakizis, P.N.; Charitidis, C.A. Dissimilar friction stir welding between 5083 and 6082 Al alloys reinforced with TiC nanoparticles*. Mater. Manuf. Process,* 31, **2016**, pp. 2101-2114.

208. Sameer, M.D.; Birru, A.K. Mechanical and metallurgical properties of friction stir welded dissimilar joints of AZ91 magnesium alloy and AA 6082-T6 aluminium alloy. *J. Mag. Alloys,* 7(2), **2019**, pp. 264-271.

209. Regev, M.; Spigarelli, S. A Study of the metallurgical and mechanical properties of friction-stir-processed Cu. *Met.,* 11, **2021**, pp. 656.

210. Barbini, A.; Carstensen, J.; dos Santos, J.F. Influence of alloys position, rolling and welding directions on properties of AA2024/AA7050 dissimilar butt weld obtained by friction stir welding. *Met.,* 8(4), **2018**, pp. 202.

211. Ghiasvand, A.; Kazemi, M.; Jalilian, M.M.; Rashid, H.A. Effects of tool offset, pin offset, and alloys position on maximum temperature in dissimilar FSW of AA6061 and AA5086. *Int. J. Mech. Mater. Eng.,* 15(6), **2020**, pp.1-14.

212. Msomi, V.; Moni, V. The influence of materials positioning on microstructure and mechanical properties of friction stir welded AA5083/AA6082 dissimilar joint*. Adv. Mater. Processing Technol.*, **2021**, DOI: 10.1080/2374068X.2021.1878732

213. Sorger, G.; Sarikka, T.; Vilaça, P. et al. Effect of processing temperatures on the properties of a high-strength steel welded by FSW. *Weld. World,* 62, **2018**, pp. 1173–1185.

214. Takhakh, A.M. Formability of friction stir welded and processed AA 2024 – O aluminum alloy sheets. *Adv. Natural and Appl. Sci.,* 10(11), **2016**, pp.1998-1090.

215. Si Youcef, Y.; Chemrouk, M. Curvature ductility factor of rectangular sections reinforced concrete beams. *World Academy of Sci. Eng. Technol.*, 6, **2012**, pp.11-20.

216. Msomi, V.; Mbana, N. Mechanical properties of friction stir welded AA1050-H14 and AA5083-H111 Joint: Sampling aspect. *Met.*, 10(2), **2020**, 214.

217. Mabuwa S.; Msomi, V. The effect of FSP conditions towards microstructure and mechanical properties of the AA6082/AA8011 TIG-welded joint. *Mater. Res. Express,* 8, **2021**, 066514.

218. Mabuwa, S.; Msomi, V.; Muribwathoho, O.; Motshwanedi, S.S. The microstructure and mechanical properties of the friction stir processed TIG-welded aerospace dissimilar aluminium alloys. Materials Today: Proceedings, 46(1), **2021**, pp. 658-664.

219. Gopan, V.; Sreekumar, P.S.; Chandran, J.P.; Vijay, W.; Kumar, M.S. Experimental Investigation on the Effect of Process Parameters on Friction Stir Processing Of Aluminium. *Materials Today: Proceedings*, 5(5), Part 2, **2018**, pp. 13674-13681.

220. Derazkola, H.A.; Eyvazian, A.; Simchi, A. Submerged friction stir welding of dissimilar joints between an Al-Mg alloy and low carbon steel: thermo-mechanical modelling, microstructural features, and mechanical properties. *Manuf. Process.*, 50, **2020**, pp. 68–79.

221. Chai, F.; Zhang, D.; Li, Y. Microstructures and tensile properties of submerged friction stir processed AZ91 magnesium alloy. *Journal of Magnesium and Alloys,* 3(3), **2015**, pp. 203-209.

222. García-Bernal, M.A.; Mishra, R.S.; Verma, R.; Hernández-Silva, D. Inhibition of abnormal grain growth during hot deformation behavior of friction stir processed 5083 Al alloys. *Mater. Sci.Eng.: A*, 636, **2015**, pp. 326-330.

223. Sigli, C.; De Geuser, F.; Deschamps, A.; Lepinoux, J.; Perez, M. Recent advances in the metallurgy of aluminum alloys. Part II: Age hardening. *Comptes Rendus Phys.,* 19, **2018**, pp. 688–709.

224. Gupta, A.K.; Lloyd, D.J.; Court, S.A. Precipitation hardening in Al-Mg-Si alloys with and without excess Si. *Mater. Sci. Eng. A*, 316, **2001**, pp. 11–17.

225. Fang, X.; Song, M.; Li, K.; Du, Y. Precipitation Sequence of an Aged Al-Mg-Si Alloy. *J. Min. Met. B,* 46, **2010**, pp. 171–180.

226. Rakhmonov, J.; Liu, K.; Rometsch, P.; Parson, N.; Chen, G. Improving the mechanical response of Al–Mg–Si 6082 structural alloys during high-temperature exposure through dispersoid strengthening. *Met.,* 13, **2020**, pp. 5295.

227. Fathi, J.; Ebrahimzadeh, P.; Farasati, R.; Teimouri, R. Friction stir welding of aluminum 6061-T6 in presence of watercooling: analyzing mechanical properties and residual stress distribution. *I. J. Lightweight Mater. Manuf.,* **2019**, pp. 107–15.

228. Sabari, S., Balasubramanian, V.; Malarvizhi, S.; Reddy, G. Madusudhan. Influences of post weld heat treatment on tensile properties of friction stir welded AA2519-T87 aluminium alloy joints. *J. Mech. Behavior of Materials,* 24(5-6), **2015**, pp. 195-205.

229. Agha Amini Fashami, H.; Bani Mostafa Arab, N.; Hoseinpour Gollo, M. et al. Numerical and experimental investigation of defects formation during friction stir processing on AZ91. *SN Appl. Sci.* 3(108), **2021**. https://doi.org/10.1007/s42452-020-04032-y.

230. Khan, N.Z.; Siddiquee, A.N.; Khan, Z.A.; Shihab, S.K.Investigations on tunneling and kissing bond defects in FSW joints for dissimilar aluminum alloys. *J. Alloys Compd*., 648, **2015**, pp. 360-367.

231. Zand Salimi, S.; Heidarzadeh, A.; Saeid, T. Dissimilar friction-stir welding of 430 stainless

steel and 6061 aluminum alloy: microstructure and mechanical properties of the joints. *Proc. Inst. Mech. Eng. Part (L) J. Mater. Des. Appl.,* 233(9), **2019**, pp. 1791–1801.

232. Habibnia, M.; Shakeri, M.; Nourouzi, S.; Givi, M.B. Microstructural and mechanical properties of friction stir welded 5050 Al alloy and 304 stainless steel plates. *Int. J. Adv. Manu.f Technol.,* 76, **2015**, pp. 819–829.

233. Palani, K.; Elanchezhian, C.; Vijaya Ramnath, B.; Bhaskar, G.B.; Naveen, E. Effect of pin profile and rotational speed on microstructure and tensile strength of dissimilar AA8011, AA01-T6 friction stir welded aluminum alloys. *Materials Today: Proceedings*, 5, **2018**, pp. 24515–24524.

234. Chen, H.B.; Yan, K.; Lin, T.; Chen, S.B.; Jiang, C.Y.; Zhao, Y. The investigation of typical welding defects for 5456 aluminum alloy friction stir welds. *Mater. Sci. Eng. A*, 433, **2006**, pp. 64–69.

235. Mohammadzadeh, H.J.; Farahani, H.; Besharati, M.K.G.; Aghaei, M.V. Study on the effects of friction stir welding process parameters on the microstructure and mechanical properties of 5086-H34 aluminum welded joints. *Int. J. Adv. Manuf. Technol*., 83, **2016**, pp. 611–21.

236. Kah, P.; Rajan, R.; Martikainen, J.; et al. Investigation of weld defects in friction-stir elding and fusion welding of aluminium alloys. *Int. J. Mech. Mater. Eng.,* 10(26), **2015**, pp. 1-10.

237. Oosterkamp, A.; Oosterkamp, L.D.; Nordeide, A. 'KB' phenomena in solid-state welds of aluminum alloys. *Weld. J.,* 83(8), **2004**, pp. 225-231.

238. He, Z.; Peng, Y.; Yin,Z.; Lei, X. Comparison of FSW and TIG welded joints in Al–Mg–Mn–Sc–Zr alloy plates. *Trans. Noferrous Met. Soc. China,* 21, **2011**, pp. 1685–1691.

239. Peng, G.; Yan, Q.; Hu, J.; Chen, P.; Chen, Z.; Zhang, T. Effect of forced air cooling on the microstructures, tensile strength, and hardness distribution of dissimilar friction stir welded AA5A06-AA6061 joints. *Met.,* 9, **2019**, pp. 1–10.

240. Shukla, S.; Komarasamy, M.; Mishra, R.S. 2018 Grain size dependence of fatigue properties of friction stir processed ultrafine-grained Al-5024 alloy. *Int. J. Fatigue,* 109, **2018**, pp. 1–9.

241. Cavaliere, P.; De Santis, A.; Panella, F.; Squillace, A. Effect of welding parameters on mechanical and microstructural properties of dissimilar AA6082–AA2024 joints produced by friction stir welding. *Mater. Des.,* 30, **2009**, pp. 609-616.

242. Kopyściański, M.; Węglowska, A.; Pietras, A.; Hamilton, C.; Dymek, S. Friction stir welding of dissimilar aluminum alloys. *Key Eng. Mater.,* 682, **2016**, pp. 31–7.

243. Imam, M.; Ueji, R.; Fujii, H. Effect of online rapid cooling on microstructure and mechanical properties of friction stir welded medium carbon steel. *J. Mater. Process. Technol.,* 30, **2015**, pp. 62–71.

244. Zhang, Z.; Xiao, B.; Ma, Z. Influence of water cooling on microstructure and mechanical properties of friction stir welded 2014Al-T6 joints. *Mat Sci Eng A: Struct,* 614, **2014**, pp. 6–15.

245. Kalemba-Rec, I.; Kopyściański, M.; Miara, D.; Krasnowski, K. Effect of process parameters on mechanical properties of friction stir welded dissimilar 7075-T651 and 5083-H111 aluminum alloys. *Int. J. Adv. Manuf. Technol.,* 27, **2018**, pp. 2767–2779.

246. Chandrana, R.; Santhanam, S.K.V. Submerged friction stir welding of 6061-T6 aluminium alloy under different water heads. *Mater. Res.,* 21(6), **2018**, pp. 1-12.

247. Chen, Y.C.; Nakata, K. Effect of the surface state of steel on the microstructure and mechanical properties of dissimilar metal lap joints of aluminum and steel by friction stir welding. *Scr. Mater.,* 58, **2007**, pp. 433-436.

248. Cao, X.; Jahazi, M. Friction stir welding of dissimilar Al/Al and Al/non-Al Alloys: a review. *Adv. Manuf. Technol.,* 56, **2009**, pp. 370-376.

249. Rao, P.S.; Dhanis, P.; Mokhtar. A. Microhardness and microstructural studies on underwater friction stir welding of 5052 aluminum alloy Proc. of the ASME 2017 Int. Mechanical Engineering Congress and Exposition: Advanced Manufacturing. Tampa, Florida, USA. November 3–9 Vol. 2, **2017**.

250. Barcellona, A.; Buffa, G.; Fratini, L.; Palmeri, D. On microstructural phenomena occurring in friction stir welding of aluminium alloys. *J. Mat. Proc. Techn*., 177, **2006**, pp. 340– 3.

251. Ravikumar, S.; Seshagiri-Rao, V.; Pranesh, R.V. Effect of welding parameters on macro and microstructure of friction stir welded butt joints between AA7075-T651 and AA6061-T651 alloys. *Proc. Mater. Sci.,* 5, **2014**, pp. 1725–35.